Late Quaternary Changes in Silicate Utilisation and Upwelling Intensity off Peru – Insights from Silicon and Neodymium Isotopes

Dissertation

zur Erlangung des Doktorgrades

Dr. rer. nat.

der Mathematisch-Naturwissenschaftlichen Fakultät

der Christian-Albrechts Universität

zu Kiel

vorgelegt von

Claudia Ehlert

Kiel, 2011

1. Gutachter und Betreuer:	Prof. Dr. Martin Frank
2. Gutachter:	Prof. Dr. Dirk Nürnberg

Eingereicht am:	22. Dezember 2011
Tag der Disputation:	03. Februar 2012
Zum Druck genehmigt:	03. Februar 2012

Gez. (Titel, Vor- und Zuname), Dekan

Erklärung

Hiermit versichere ich an Eides statt, dass ich diese Dissertation selbstständig und nur mit Hilfe der angegebenen Quellen und Hilfsmittel erstellt habe. Ferner versichere ich, dass der Inhalt dieses Dokuments weder in dieser, noch in veränderter Form einer weiteren Prüfungsbehörde vorliegt. Die Arbeit ist unter Einhaltung der Regeln guter wissenschaftlicher Praxis der Deutschen Forschungsgemeinschaft entstanden.

Kiel, 22. Dezember 2011

Claudia Ehlert

Contents

Abstract

The Peruvian coastal upwelling region is characterised by one of the most pronounced oxygen minimum zones in the worlds ocean. The extension and strength of bottom water oxygen depletion has varied in the past as a function of surface water primary productivity and changes in circulation and upwelling intensity. So far, it has proven difficult to disentangle these influences. In this study the stable silicon isotope composition of diatoms ($\delta^{30}Si$) is used to reconstruct surface water silicic acid ($Si(OH)_4$) utilisation during primary productivity. Radiogenic neodymium isotopes (εNd) from Fe-Mn coatings and benthic foraminifers were measured to trace water masses and their mixing, and the detrital fraction was analysed to provide information about sediment provenance, weathering inputs and their transport pathways. Besides the utilisation and water mass mixing effect, other processes such as remineralisation of the diatoms in the water column and in the sediment, influence the signal that is preserved. Here, the first systematic study of the dissolved $\delta^{30}Si$ in the water column ($\delta^{30}Si_{Si(OH)4}$) and in diatoms ($\delta^{30}Si_{opal}$) from the underlying sediments in a coastal upwelling region is carried out to shed light onto the importance of these processes. The results show that the $\delta^{30}Si_{Si(OH)4}$ signature strongly depends on upwelling strength, i.e. supply of new nutrients. Surface waters in the realm of intense upwelling are only weakly fractionated with respect to the subsurface source water signatures, whereas surface waters are more strongly fractionated where upwelling is less pronounced due to higher utilisation of the smaller amounts of available $Si(OH)_4$. The $\delta^{30}Si_{opal}$ values of picked diatoms in the underlying sediments vary within the order of the expected fractionation between surface waters and diatoms and thus serve as a basis for the reliable use of the $\delta^{30}Si_{opal}$ as a proxy for past upwelling conditions. The sediments were also analysed for their εNd and compared to water column measurements from the same area. In general, all phases (seawater, Fe-Mn coatings, benthic foraminifers and detrital material) display a trend from more radiogenic values in the north towards less radiogenic values in the south. This is in agreement with the distribution of the signatures of the Andean hinterland rocks. This is most likely due to extensive exchange between sediments and the

water column, which makes it difficult to use the εNd signatures obtained from Fe-Mn coatings or from benthic foraminiferal carbonate as a water mass tracer. Paleo-reconstructions show, that diatom-related productivity along the Peruvian upwelling area has varied greatly during the past 20 kyr. It was characterised by low fluxes of diatom opal during the last glacial and much higher values thereafter, in particular during the early and the latest Holocene. The combined approach of $\delta^{30}Si_{opal}$ and the radiogenic isotope composition (Nd, Sr) of Fe-Mn coatings of sediment particles and the detrital material itself reveal that this variability has been related to changes in $Si(OH)_4$ utilisation, mostly controlled by the supply of iron and phosphate released from the shelf sediments via upwelling. During the glacial strong upwelling of subsurface waters with an overall low nutrient content significantly diminished primary productivity. During the early and late Holocene oceanographic conditions along the shelf were alternating between stronger and weaker upwelling. Especially the last 2,500 years were characterised by the largest variability of the system of the past 20,000 years, which coincided with the onset of modern El Nino-Southern Oscillation conditions in the Pacific.

The late Holocene was also disrupted by major climatic anomalies, such as the Little Ice Age (LIA). Off Peru, a permanent mean southward migration of the Intertropical Convergence Zone (ITCZ) during the LIA strongly affected the trade wind-driven strength of the upwelling causing permanent El Nino-like conditions. The $\delta^{30}Si_{opal}$ show that productivity and nutrient utilisation were weak. The detrital sediment fraction was dominated by local riverine input of lithogenic material due to higher rainfall in the Andean hinterland. At the end of the LIA, the ITCZ shifted northward, which resulted in a pronounced increase in the strength of upwelling off Peru. Especially $Si(OH)_4$ and Fe remineralisation from the shelf sediments was enhanced causing higher nutrient supply and diatom productivity. The radiogenic isotope record of the detrital shelf sediments indicates increased dust transport due to drier conditions under more persistent non-El Nino conditions. Comparison between $\delta^{30}Si_{opal}$ and bulk $\delta^{15}N$ of organic matter suggests that surface water utilisation has been the predominant factor influencing both signals. The $\delta^{15}N$ signature recorded in the sediment was not, as previously assumed, mainly influenced by subsurface water nitrate reduction processes.

Kurzfassung

Das Peruanische Auftriebsgebiet ist durch eine der weltweit ausgeprägtesten Sauerstoffminimumzonen gekennzeichnet. Ausdehnung und Intensität der Sauerstoffabreicherung im Bodenwasser schwankten in der Vergangenheit durch Veränderungen der Zirkulation und Stärke des Auftriebs und durch die Primärproduktivität im Oberflächenwasser. Bisher war es schwierig, diese verschiedenen Prozesse voneinander zu trennen. Um die Nutzung von Kieselsäure ($Si(OH)_4$) durch Diatomeen während der Primärproduktivität zu bestimmen, werden in dieser Studie stabile Silizium-Isotope genutzt. Radiogene Neodym-Isotope (εNd), die aus authigenen Fe-Mn-Oxid Präzipitaten und benthischen Foraminiferen gewonnen werden, geben Auskunft über Wassermassenzirkulation und –mischung. Das detritische Sedimentmaterial selbst liefert darüber hinaus Informationen über Herkunft, Verwitterung und Transport. Neben Nährstoffnutzung und Wassermassenmischung können auch andere Prozesse wie Auflösung der Diatomeen in der Wassersäule und im Sediment beeinflussen, welches Signal letztlich überliefert wird. Um die Wichtigkeit dieser Prozesse zu untersuchen, wurde hier die erste systematische Vegleichsstudie am gelösten $\delta^{30}Si$ in der Wassersäule ($\delta^{30}Si_{Si(OH)4}$) und an Diatomeen ($\delta^{30}Si_{opal}$) aus den unterliegenden Sedimenten in einem Auftriebgebiet durchgeführt. Die Ergebnisse zeigen, dass $\delta^{30}Si_{Si(OH)4}$ hauptsächlich durch die Stärke des Auftriebs, und damit die Zufuhr von Nährstoffen, bestimmt wird. Wo Auftrieb stark ist, sind die Oberflächenwässer nur schwach fraktioniert im Vergleich zum Ausgangssignal in 50 m bis 150 m Wassertiefe. In Gebieten mit schwächerem Auftrieb dagegen ist, durch die stärkere Nutzung der geringer vorhandenen Menge an Nährstoffen, die Fraktionierung deutlich höher. $\delta^{30}Si_{opal}$ von hand-gepickten Diatomeen aus den unterliegen-den Sedimenten schwankt innerhalb des Rahmens, den man durch Fraktionierung zwischen Oberflächenwasser und Diatomeen erwarten würde, und kann daher als Basis für Paläo-Rekonstruktionen der Auftriebsstärke dienen. An den Sedimenten wurde ebenfalls εNd gemessen und mit den Signaturen in der Wassersäule verglichen. Generell zeigen alle Phasen (Meerwasser, Fe-Mn-Oxid Präzipitate, benthische Foraminiferen und detritisches Material) einen Trend von

radiogeneren Werten im Norden zu weniger radiogenen im Süden. Dies ist im Einklang mit der Signaturverteilung in den Gesteinen der Anden im Peruanischen Hinterland. Grund dafür ist höchstwahrscheinlich intensiver Austausch zwischen den Schelfsedimenten und der Wassersäule, was eine Nutzung von εNd als Wassermassentracer (aus den Präzipitaten und den benthischen Foraminiferen) schwierig macht.

Paläo-Rekonstruktionen haben gezeigt, dass Diatomeen-gesteuerte Primärproduktivität im Peruanischen Auftriebsgebiet während der letzten 20.000 Jahre stark geschwankt hat. Im letzten Glazial waren Produktivität und Flux von Diatomeen sehr gering, während beides im frühen und späten Holozän deutlich anstieg. Der Ansatz $\delta^{30}Si$ und radiogene Isotope (Nd, Sr) kombiniert einzusetzen zeigt, dass diese Variabilität mit der Nutzung von $Si(OH)_4$ zusammenhängt. Diese wird durch die Verfügbarkeit von Eisen und Phosphat gesteuert, welche unter anoxischen Bedingungen aus dem Sediment gelöst werden können. Während des Glazials war der Nährstoffgehalt im aufgetriebenen Wasser gering. Obwohl der Auftrieb stark war, führte der Mangel an Nährstoffen zu einer Abschwächung der Produktivität. Im frühen und späten Holozän dagegen schwankten die ozeanographischen Bedingungen im Peruanischen Gebiet zwischen starkem und schwachem Auftrieb mit variablen Nährstoffgehalten. Besonders die letzten 2.500 Jahre zeigten starke Veränderungen, die stärksten der letzten 20.000 Jahre, was mit dem Einsetzen der modernen ENSO (El Nino-Southern Oscillation) Bedingungen zusammenfällt.

Zusätzlich war das Holozän von kürzeren aber starken Klimaanomalien wie der Kleine Eiszeit (LIA) geprägt. Durch eine permanente Verlagerung der Intertropischen Konvergenzzone (ITCZ) nach Süden während der LIA veränderte sich die Position und Stärke des durch die Passatwinde angetriebene Auftriebs, was zu dauerhaften El Nino-ähnlichen Bedingungen führte. Die $\delta^{30}Si$ Werte zeigen, dass Primärproduktivität und Nährstoffnutzung eher schwach waren. Stärkerer Niederschlag in den Peruanischen Anden führte dazu, dass der Eintrag von Sediment auf den Schelf hauptsächlich durch Flüsse erfolgte. Zum Ende der LIA verlagerte sich die ITCZ nach Norden, was zu einer Verstärkung des Auftriebs vor Peru führte, zu einer verstärkten $Si(OH)_4$- und Eisen-Remineralisation aus den

Sedimenten, und damit zum Anstieg der Produktivität. Durch weniger Niederschlag wurden Partikel nun als Staub eingetragen. Ein erster Vergleich zwischen $\delta^{30}Si$ und $\delta^{15}N$ Signaturen lässt vermuten, dass beide in erster Linie durch die Nährstoffnutzung im Oberflächenwasser beeinflusst werden, und dass $\delta^{15}N$ nicht, im Gegensatz zu früheren Annahmen, die Nitrat-Reduktion in der Wassersäule widerspiegelt.

Danksagung

In erster Linie danke ich meinem Betreuer Prof. Martin Frank. Vielen Dank dass du mir die Chance für diese Arbeit gegeben hast, und dass du immer deinen Optimismus bewahrt hast, auch wenn Paddy und ich den nicht immer teilen konnten. Und natürlich Paddy: Ich bin wirklich froh, dass Martin dich eingestellt hat, ohne die gute Zusammenarbeit hätte vermutlich keine von uns beiden das erreicht, was wir jetzt geschafft haben. Ich wünsche dir viel Spaß und Erfolg weiterhin im SFB und natürlich auch bei der Arbeit mit dem neuen Doktoranden.

Besonders dankbar bin ich Ben Reynolds und Gregory de Souza von der ETH Zürich, die durch ihre selbstlose Hilfe und Unterstützung bei der Silizium-Methode Paddys und meine Arbeit hier in Kiel erst möglich gemacht haben. Ein großer Dank gebührt auch Rainer Gersonde und seiner Gruppe am AWI, insbesondere Birgit Glückselig und Ulrike Böttjer, die mich sehr hilfsbereit in die Geheimnisse der Diatomeen-Trennung eingewiesen haben, und mir auch später mit Rat zur Seite standen.

Natürlich möchte ich auch nicht die vielen Leute hier in Kiel vergessen: Elfi Mollier-Vogel and Tebke Böschen for the profound discussions with you, they really helped to re-think some ideas; Ed Hathorne for the help with the Quadrupole measurements; Stephanie, Annika und Timo für ihre Unterstützung beim schlämmen und picken; Jutta Heinze – du bist wirklich der gute Geist unserer Gruppe, egal was man braucht, du machst es irgendwie möglich; Lisa Bohlen für die gemeinsame Zeit im Kühlschrank auf Meteor; Steffie und Clauschi – wer hätte schon vor mehr als acht (!) Jahren gedacht, dass wir mal in einer Gruppe landen und zusammen unseren Doktor machen, es war eine super Zeit mit euch, die ich niemals vergessen werde; und auch allen anderen nicht namentlich genannten für ihre Unterstützung und die gemeinsame Zeit.

Und natürlich Roland – ich hätte mir niemals vorstellen können mit jemandem zusammen zu arbeiten und auch zusammen zu leben, aber mit dir war es plötzlich ganz selbstverständlich. Vielen Dank dass du mein Leben so vereinfacht und gleichzeitig so bereichert hast.

Chapter 1

Introduction

1.1 Previous Work and Motivation

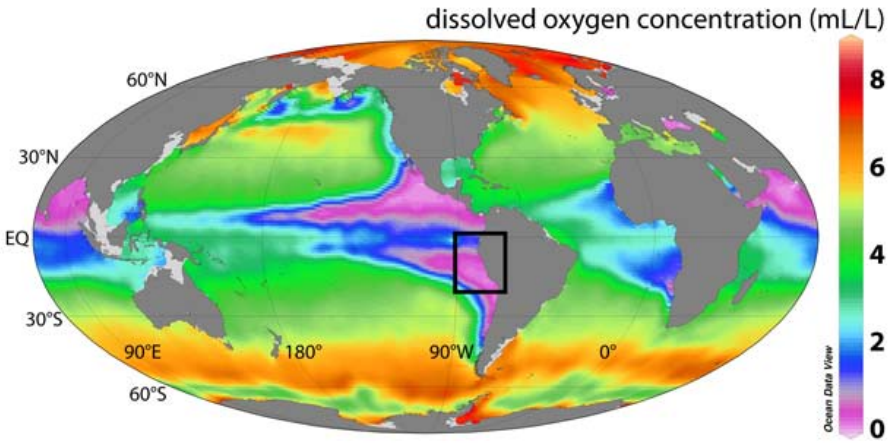

Figure 1.1: Global dissolved oxygen concentrations (mL/L) at 200 m water depth (Garcia et al., 2010a) indicating the extensive oxygen minimum zones in the low latitudes. The black square marks the study area in the eastern equatorial Pacific.

This study is part of the Collaborative Research Centre (SFB) 754 "Climate-Biogeochemistry Interactions in the Tropical Ocean", which investigates the oxygen-depleted areas in the low-latitudes of the global ocean (Fig. 1.1), especially in the Atlantic and Pacific Ocean. Such oxygen minimum zones (OMZs) of the tropics are the key regions of low oxygen in today's ocean. The oxygen concentrations are controlled by the interplay between physics (i.e. water mass circulation, mixing and exchange with the atmosphere) and biology (i.e. oxygen production versus consumption). The sources and sinks of important nutrients, such as nitrogen (N), phosphorus (P) and iron (Fe) are directly controlled by oxygen levels, and experience major changes when oceanic oxygen concentrations decrease below certain threshold levels. Via ocean circulation, these altered nutrient cycle signatures can be transported from the (relatively) small OMZs into the global ocean and affect biogeochemical properties and ecosystems of much larger areas.

Global climate has strong and rapid interactions with oceanographic circulation in the tropical ocean, which is highly sensitive to global changes in

atmospheric forcing as well as local atmospheric and oceanic properties. There are numerous feedbacks between oxygen levels, nutrient cycling and biological productivity. In the past there have been several time periods of globally low oxygen events (e.g. Cretaceous Ocean Anoxic Events) that were associated with warmer climates and higher atmospheric CO_2 levels, conditions that are also expected for the future under anthropogenically induced climate warming. It is therefore necessary to quantitatively evaluate the nature of oxygen-sensitivity as well as to assess consequences for the Ocean's future. This SFB addresses three major questions to understand the coupling of tropical climate variability and circulation with the ocean's oxygen and nutrient balance. They are defined in the proposal as:

1) How does subsurface dissolved oxygen in the tropical ocean respond to changes in ocean circulation and ventilation?
2) What are the sensitivities and feedbacks linking low oxygen levels and key nutrient source and sink mechanisms?
3) **What are the magnitudes, timescales and controlling factors of past, present and likely future variations in oceanic oxygen and nutrient levels?**

This study is part of subproject B7 in the SFB that refers to the third aspect, and that deals with the reconstruction of bottom water oxygen levels and its controlling factors in the coastal upwelling system off Ecuador and Peru between the last glacial maximum and today applying a multidisciplinary approach combining geochemical, micropaleontological and paleoceanographic proxies. It is known that the bottom and pore water oxygen concentrations are mainly controlled by external factors such as surface water bioproductivity (e.g. DeVries and Schrader, 1981; Schrader, 1992; Wolf, 2002; Rein et al., 2004; 2005) as well as changes in circulation and upwelling intensity (e.g. Rein et al., 2005). Productivity itself is a function of nutrient supply controlled by upwelling intensity. The upwelling intensity has been driven by an interplay of the major currents with trade winds and the El Nino-Southern Oscillation (see Chapter 1.3).

Past changes in oceanic productivity, which have influenced and partly controlled the exchange of CO_2 between the atmosphere and the deep sea, have been inferred from the accumulation of biogenic components (organic carbon, calcium carbonate and biogenic silicate (opal, $bSiO_2$)) (Ragueneau et al., 2000). Especially the $bSiO_2$ holds crucial information with respect to the functioning of the biological pump in the present and past ocean. About 3% of the globally produced $bSiO_2$ in the surface water is ultimately preserved in the sediment (Tréguer et al., 1995), which is more than an order of magnitude higher than the preservation efficiency for organic carbon (Westbroeck et al. 1993), making $bSiO_2$ an important paleo-productivity proxy. However, there are several factors that make the quantitative use of $bSiO_2$ difficult (e.g. Nelson et al., 1995; Anderson et al., 1998). Lateral advection of water masses, sediment redistribution and most importantly, the spatial and temporal variations in the preservation efficiency of the $bSiO_2$ (re-dissolution) formed in surface waters all affect the relationship between surface water processes and the burial in underlying sediments (Ragueneau et al., 2000). Therefore, surface water primary productivity and export in the past is very hard to reconstruct but can be improved by the reconstruction of nutrient utilisation with stable silicon (or nitrogen) isotopes. Diatoms, the most important primary producers in the Peruvian upwelling area (Estrada and Blasco, 1985), use dissolved silicate ($Si(OH)_4$) to build their $bSiO_2$ shells. The utilisation of $Si(OH)_4$ should directly reflect its availability in the surface waters and thus the amount of newly supplied $Si(OH)_4$ with upwelled waters. $Si(OH)_4$ utilisation can be measured directly from the isotopic composition of silicon ($\delta^{30}Si$) in diatom shells (see Chapter 1.4.2) (De La Rocha et al., 1998; Brzezinski et al., 2002; Varela et al., 2004; Reynolds et al., 2006). The $\delta^{30}Si$ of diatoms from Peruvian shelf sediments will thus reflect both surface water $Si(OH)_4$ utilisation and water mass mixing by upwelling (De La Rocha et al., 1997, 1998; Brzezinski et al., 2002; Varela et al., 2004; Reynolds et al., 2006). So far, it has proven difficult to disentangle the influences of changes in productivity from those caused by changes in circulation and upwelling intensity. Therefore, another proxy that is independent from biological processes and that is only influenced by water mass advection and vertical mixing is used in this study: radiogenic Nd isotopes (see Chapter 1.5)

(Frank, 2002). The comparison of both proxies will allow the distinction between the different processes that have ultimately influenced past bottom and pore water oxygen conditions.

1.2 Present-day Circulation, Nutrient Distribution and Primary Productivity in the Eastern Equatorial Pacific

1.2.1 Circulation in the Eastern Equatorial Pacific

The circulation in the tropical eastern equatorial Pacific (EEP) has the largest meridional extension of all eastern boundary current systems reaching from ca. 5°S off Peru to at least 42°S off Chile (Karstensen and Ulloa, 2008). It is tightly connected to the zonal equatorial Pacific circulation, and is strongly influenced by the El Nino-Southern Oscillation (ENSO, see Chapter 1.3), the globally strongest form of interannual atmospheric and oceanographic variability (Karstensen and Ulloa, 2008). The EEP circulation is very complex and characterised by a variety of surface, subsurface, intermediate and deep-water currents. Persistent easterly trade and alongshore winds produce offshore Ekman transport of surface waters. In the equatorial region, surface currents, such the South Equatorial Current (SEC) (Fig. 1.2), which is the northern branch of the south Pacific subtropical gyre (Kessler, 2006), are driven westward.

Therefore, warm water accumulates in the western Pacific where it raises sea level by 30–50 cm relative to the eastern Pacific (Wyrtki and Wenzel, 1984). The elevated sea level in turn produces a pressure gradient that is balanced by the eastward flow of the subsurface Equatorial Undercurrent (EUC) (Kessler, 2006), originating from the central Pacific (Brink et al., 1983; Toggweiler et al., 1991) as a mixture of waters of southern and northern Pacific origin (Dugdale et al., 2002). Progressively cooler waters are upwelled to the euphotic zone typically from 50 m to 150 m water depth from the EUC (Brink et al., 1983) both along the equator and most pronounced in the coastal regions, resulting in the low sea surface temperatures in that region (Fig. 1.2) (Kessler, 2006).

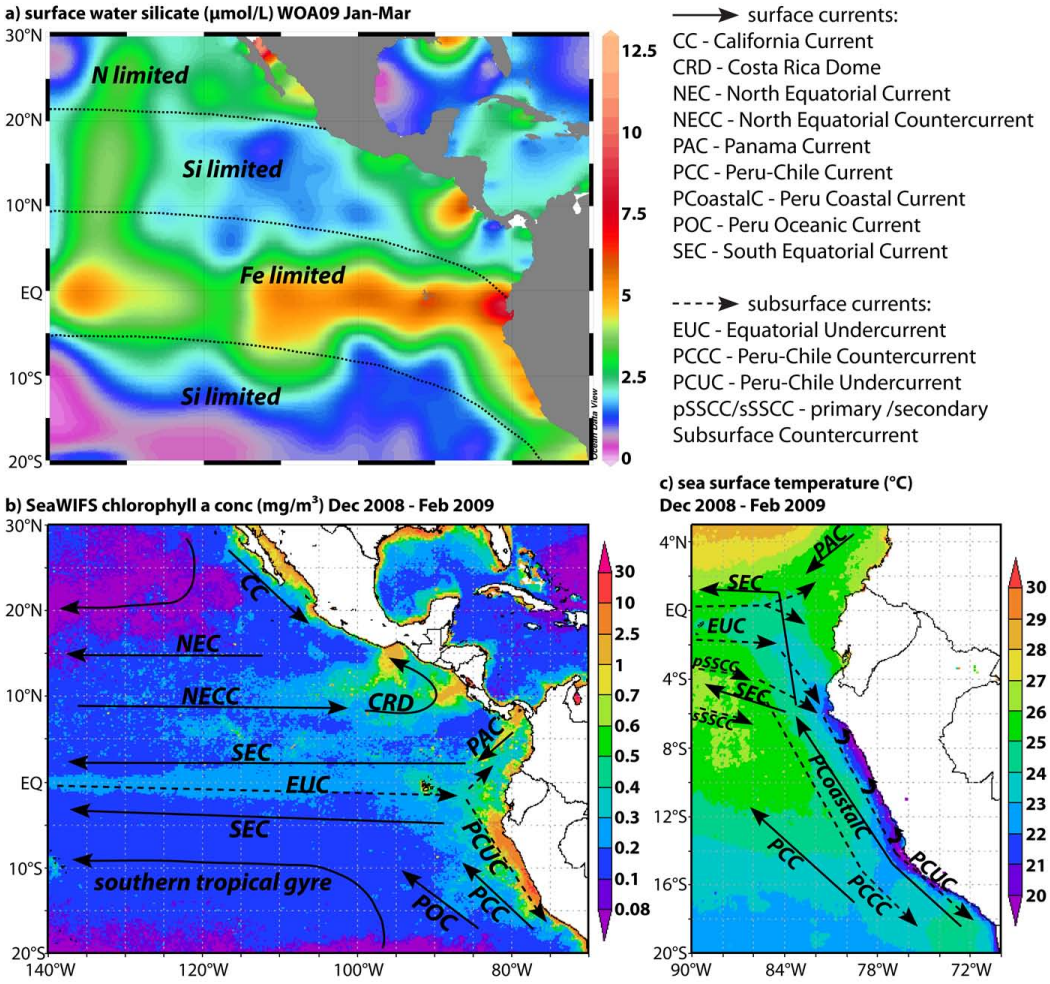

Figure 1.2: Surface water a) mean dissolved silicate (µmol/L) for Austral summer (January to March) (Garcia et al., 2010b) and b) chlorophyll a concentration (mg/m³) between December 2008 and February 2009 derived from SeaWIFS satellite imagery in the EEP. c) Sea surface temperatures (°C) during the same time in the Peruvian upwelling region. The dotted lines in a) indicate the regions of nutrient limitations for N, Si and Fe (after Moore et al., 2004). The solid (surface currents) and dashed (subsurface currents) black arrows in b) and c) mark the schematic main circulation pathways (after Strub et al., 1998; Penven et al., 2005; Kessler, 2006; Ayon et al., 2008; Karstensen and Ulloa, 2008; and ADCP data from Czeschel et al., 2011).

The EUC supplies oxygen-rich waters into the upwelling area (Brink et al., 1983; Toggweiler et al., 1991; Fiedler and Talley, 2006) and therefore splits the eastern Pacific oxygen minimum zone into a northern and a southern hemisphere part (Fig. 1.1). Eastern Pacific intermediate waters mainly consist of three water masses: North Pacific Intermediate water (NPIW), Antarctic Intermediate Water (AAIW), and Equatorial Pacific Intermediate water (Bostock et al., 2010). NPIW is formed in the northwestern subtropical gyre along the Kuroshio and Oyashio Front (Talley, 1993). Antarctic Intermediate Water, which is primarily formed in the southeast Pacific off Chile (Kawabe and Fujio, 2010), flows north- and

westward and is detectable in the EEP to a latitude of approximately 20°S (Talley, 1999). The densest water mass in the Pacific basin is the Lower Circumpolar Deep Water, which is a mixture of Antarctic bottom water and North Atlantic deep water (Wijffels et al., 1996). It is modified by admixture of Upper Circumpolar Deep Water, which flows from the northwest Pacific southward along the continental slope of Central and South America and contributes to the mixture of deep water masses off Peru (Wijffels et al. 1996; Kawabe and Fujio, 2010).

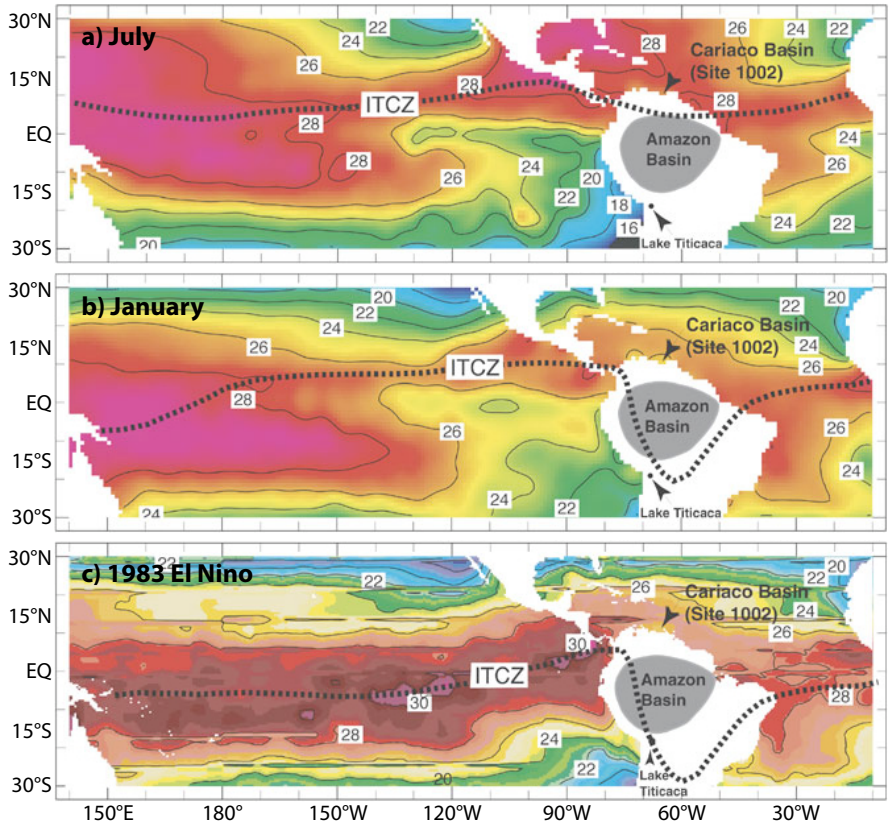

Figure 1.3: Variations in the mean position of the ITCZ during a) July, b) January, and c) during the 1983 El Nino event. Numbers and colors reflect sea surface temperatures (°C, red – warm, blue - cold) (adapted from Haug et al., 2001).

In the Peruvian upwelling region surface circulation is dominated by the northward flowing Peru Oceanic Current (POC), the Peru Coastal Current (PCoastalC) and the Peru Chile Current (PCC), which can be found approximately 100 to 300 km offshore and originate in subantarctic regions (Fig. 1.2) (Strub et al., 1998; Penven et al., 2005; Karstensen and Ulloa, 2008). The EUC, the primary and the secondary Subsurface Countercurrents (SSCC) are the main suppliers of the poleward flowing subsurface Peru-Chile Undercurrent (PCUC) (Fig. 1.2)

representing up to 30% of its volume (Montes et al., 2010). During austral summer 2009, when the samples for this study were taken, the EUC was encountering the western coast of South America at approximately 0°N to 1°N at a depth of 90 m (Czeschel et al., 2011). The PCUC is the ultimate source water mass of the coastal upwelling and is flowing southward along the shelf at approximately 50 m to 150 m water depth (Huyer et al., 1987; Penven et al., 2005; Karstensen and Ulloa, 2008). Upwelling occurs almost year-round because of Peru's low latitude and persistent winds (Chavez, 1995) but is most intense during austral winter (lowest sea surface temperatures in Fig. 1.3a). These seasonal changes are linked to the position of the Intertropical Convergence Zone (ITCZ), which shifts between a more northerly position in austral summer and a more southerly position (associated with stronger trade winds and stronger upwelling off Peru) during austral winter (Fig. 1.3). Also, water masses from the south, such as the Subantarctic Mode Water, the PCC and the PCoastalC can affect the upwelling (Toggweiler et al., 1991; Sarmiento et al., 2004).

1.2.2 Nutrient Distribution and Primary Productivity in the Eastern Equatorial Pacific

Coastal boundary upwelling systems are usually characterised by high rates of primary productivity of phytoplankton (as indicated by the chlorophyll a concentration in Fig. 1.2) (Chavez and Barber, 1987; Chavez, 1995; Fiedler, 2002; Fiedler and Talley, 2006). Compared to the oligotrophic subtropical gyres, the concentration of surface chlorophyll across the equatorial upwelling region is high. This band of high bioproductivity extends westwards from the Galapagos islands to beyond 140°W. Phytoplankton biomass is generally maximal on or near the equator, but is also enhanced south of the equator in the eastern Pacific (95°W to the coast of South America) due to influx of the SEC from the Peruvian coastal upwelling region bringing in nutrients, especially nitrate (NO_3^-) (Fig. 1.2). The Peruvian coastal upwelling region is extremely rich in chlorophyll and this biomass production extends westwards up to 1000 km offshore (Pennington et al., 2006). This high productivity can only occur due to thermocline shoaling and local wind-driven upwelling of subsurface waters, which provide nutrients, such as

dissolved silicate ($Si(OH)_4$) (Fig. 1.2), to the euphotic zone. Due to the regional differences in upwelling strength, nutrient supply and consumption, different zones of limitation occur (Fig. 1.2). In the equatorial upwelling region dissolved NO_3^-, phosphate (P) and $Si(OH)_4$ concentrations are high relative to the surrounding oceanic regions (Fig. 1.2). Subsurface NO_3^- reduction processes (denitrification, anammox) consume NO_3^- in the upwelling source waters, so that surface NO_3^- becomes exhausted before P (Penningon et al., 2006). In some regions of the EEP dissolved $Si(OH)_4$ has been suggested to be the limiting macronutrient for diatom growth (Dugdale and Wilkerson, 2001; Dugdale et al., 2011). Offshore, and in particular in regions of the narrow continental shelves, phytoplankton productivity is also limited by the micronutrient iron (Fe) (Fig. 1.2) (Hutchins et al., 2002; Moore et al., 2004; Brzezinski et al., 2011). In the Peruvian upwelling region Fe is mainly supplied to the euphotic zone via remineralisation from the shelf sediments (Froelich et al., 1988; Noffke et al., unpublished, 2011), which occurs under oxygen-depleted conditions in the bottom waters (McManus et al., 1997).

Primary productivity in the EEP is strongly seasonal. Despite the fact that highest upwelling rates occur during austral winter, highest levels of productivity occur during austral summer and fall (Chavez, 1995). The phytoplankton community in the coastal upwelling region is dominated by larger species such as diatoms, whereas further offshore more open-ocean type smaller plankton, such as cyanobacteria and prochlorophytes, are predominant (Chavez, 2005). Although primary productivity is high all along the shelf region off Peru, there are local areas of extremely high productivity, which are mostly associated with the shape of the coastline, i.e. capes and adjacent bay areas, at 6°S, 9°S, 12°S and 15°S (Rojas de Mendiola, 1981; Thomas, 2001). Organic matter produced in the euphotic zone sinks to deeper water, and is captured by the PCUC where it decays. This process is strongly enhanced by bacterial activity and converts organic compounds into inorganic nutrients, by which oxygen is consumed. The high export of organic matter produces the large oxygen minimum zone beneath the thermocline (Fiedler and Talley, 2006).

1.3 Temporal Variability in the Eastern Equatorial Pacific: El Nino-Southern Oscillation and Pacific Decadal Oscillation

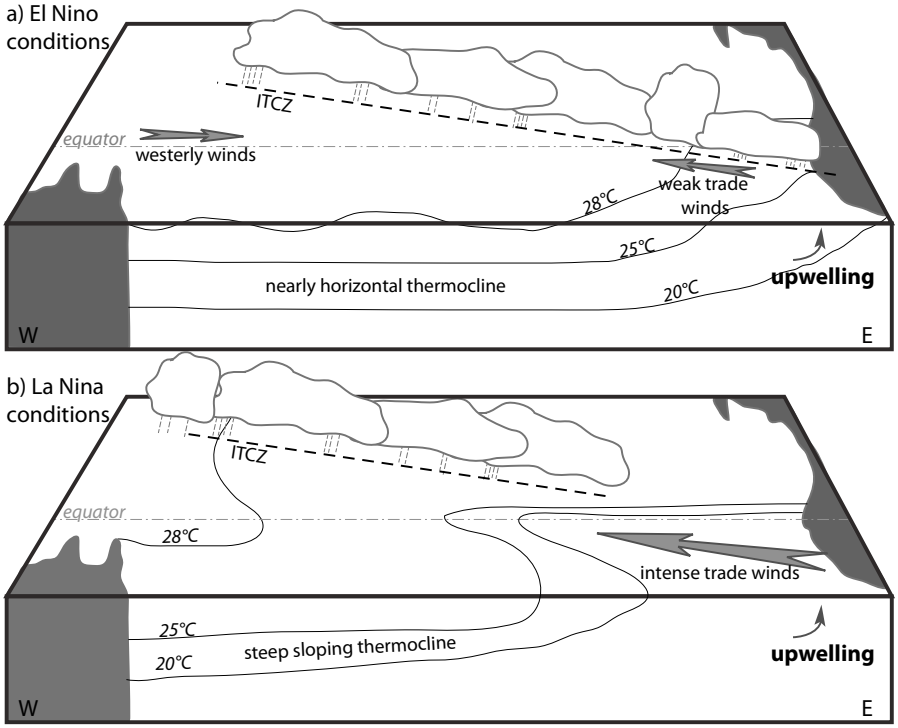

Figure 1.4: Schematic view of a) El Nino and b) La Nina conditions in the Pacific Ocean (after Philander, 1999) indicating the change in sea surface temperatures and thermocline depth in relation to trade wind strength.

The ocean environment in the tropical Pacific has varied on seasonal, interannual and longer time-scales in the past. El Nino events are the strongest source of temporal variability in the eastern tropical Pacific Ocean and are part of a coupled ocean-atmosphere heat flux interaction of the El Nino-Southern Oscillation (ENSO) in the equatorial Pacific Ocean and global atmosphere (Philander, 1999). Events of varying strength occur every two to seven years and last for 6 to 18 months. During El Nino events the ITCZ is shifted southward (Fig. 1.3c and 1.4) causing a weakening or even reversal of the eastward trade winds in the western Pacific, which reduces the east-west tilt in thermocline depth and enhances the redistribution of warm surface water into the EEP (causing much higher sea surface temperatures, Fig. 1.3c) (Fiedler, 2002). El Ninos thus affect the eastern tropical Pacific most strongly in the equatorial and coastal upwelling regions. (Wang et al., 2004; Fiedler and Talley, 2006). There, the thermocline deepens and the SEC and EUC weaken or disappear. Enhanced rainfall episodes

occur along the Ecuadorian and Peruvian coastal regions (Fig. 1.5) (Rossel and Cadier, 2009). Most importantly to biological production, the thermocline deepening results in substantial decrease of nutrient supply to the euphotic zone (Barber and Chavez, 1983). Even in those regions where wind-driven upwelling continues, low nutrient waters from above the thermocline are often brought to the surface (Fig. 1.4a) (Huyer et al., 1987). In contrast to El Nino, the opposite phase La Nina is characterised by strong trade winds, a shallow thermocline, and cool sea surface temperatures (Fig 1.4b) (Fiedler, 2002). Nutrient supply is strongly increased which fuels primary productivity. During El Nino events, off Peru and Chile the layer of oxygen-depleted water deepens along with the thermocline thereby oxygenating the shelf and upper continental slope and thus altering levels of denitrification and the export flux of organic matter as well as the remineralisation of nutrients such as Fe from the shelf sediments (Morales et al., 1999). Consequently, warmer surface waters and lower nutrient concentrations favour a switch in the phytoplankton community from high-nutrient demanding diatoms to smaller cyanobacteria and prochlorophytes adapted to lower nutrients (Chavez, 2005). Phytoplankton communities become dominated by species of diatoms, dinoflagellates, and coccolithophores that are usually found offshore in warm subtropical waters (Rojas de Mendiola, 1981). At 30°S sediment traps have recorded markedly lower (by 75%) diatom fluxes and an increased contribution of taxa typical of warm open ocean conditions during El Ninos (Romero et al., 2001).

On longer, multi-decadal timescales the entire Pacific, especially the north Pacific region, is affected by persistent climate conditions, which is called the Pacific Decadal Oscillation (PDO) (Mantua and Hare, 2002). It is characterised by several years of warmer conditions (called El Viejo) alternating with years of colder conditions (La Vieja) (Chavez, 2005). PDO variance has two broadband peaks at periods of 15-25 years and 50-70 years (Fiedler, 2002). El Viejo and La Vieja appear analogous to El Nino and La Nina in that both types of fluctuation have similar effects on basin-wide SST and thermocline depth (Mantua and Hare, 2002; Chavez, 2005) although the absolute magnitude of PDO variability in the EEP is smaller than ENSO, but may have large cumulative effects on biological productivity due to their long duration (Alheit and Niquen, 2004; Chavez, 2005).

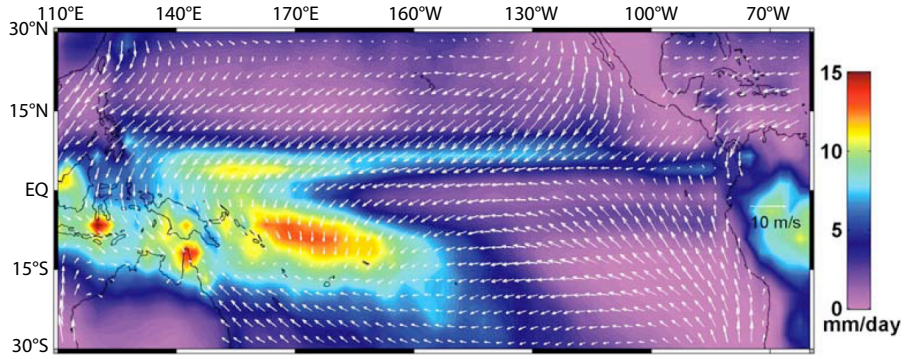

Figure 1.5: Austral summer (JFM) versus 1997–1998 El Nino (JFM) precipitation (colors) and wind (arrows) patterns across the Tropical Pacific indicating that the southward displacement of the ITCZ is coupled with weaker southerly trade winds in the tropical South Eastern Pacific, as well as with wet conditions both in the Indo Pacific and in the central Peruvian Andes (from Gutierrez et al., 2009).

Paleo-reconstructions from the EEP have shown major variability of ENSO strength since the last glacial maximum. The background climate state and the physical mechanisms for this change in ENSO have remained poorly constrained and controversial. In the Pacific a critical factor has been the sea surface temperature gradient across the ocean along the equator. During the Holocene, temperatures in the western Pacific have not changed much (Tudhope et al., 2001), so the east to west gradient has depended only on changes that occurred in the EEP. During the deglacial time prior to 11.5 ka enhanced La Nina-like conditions were prevailing that were still influenced by (weakened) glacial boundary conditions (Makou et al., 2010). Although strong El Nino-like events occurred during the early Holocene (Carré et al., 2005), the climatic state varied on frequencies of about 15 years between 15 and 7 ka, much longer than present-day El Nino variations (Rodbell et al., 1999). Extremely warm El Nino events were less frequent and smaller in amplitude during the mid-Holocene (Clement et al., 2000). In more recent time, especially after 5 ka BP, modern type ENSO activity became active triggered by stronger trade winds causing steeper zonal sea surface temperature gradients (Sandweiss et al., 2001; Rodbell et al., 1999; Loubere et al., 2003) with concomitant increases in both El Nino and La Nina amplitude during the past 2 kyr (Makou et al., 2010). These changing conditions also affected the human cultural development in the region. Only after 5 ka BP, when the Peruvian coastal region experienced moderate rainfall events more frequently, monument temple building constructions and the formation of cities were performed, which

were abandoned again after ca. 3 ka when El Nino frequency strengthened (Sandweiss et al., 2001).

1.4 The Marine Silicon Cycle

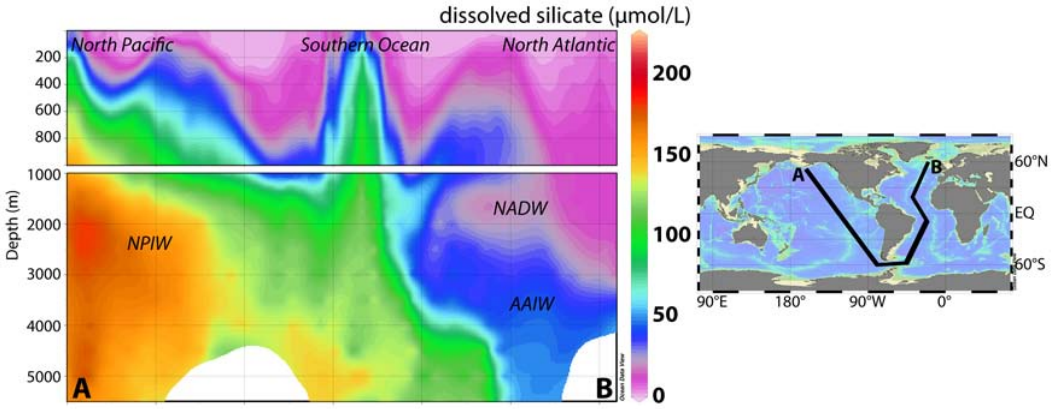

Figure 1.6: Global depth section of dissolved silicate concentration (µmol/L) (Garcia et al., 2010b) from the North Pacific (left) to the North Atlantic (right) indicating the main differences in $Si(OH)_4$ concentrations between both ocean basins.

Silicon enters the ocean in dissolved form via rivers sourced from weathering of siliceous rocks, via atmospheric dust deposition and subsequent dissolution and via low-temperature alteration of sea-floor basalts (Tréguer et al., 1995). During transport from the weathering sites until ultimately ending in the ocean Si is involved in various biogeochemical processes, such as precipitation of weathering products (formation of clay minerals, biogenic silicate, e.g. in phytoliths and freshwater diatoms) (Ding et al., 1996; De La Rocha et al., 2000; Basile-Doelsch, 2006; Georg et al., 2009). Si has a residence time in the ocean of about 15,000 years (Tréguer et al., 1995; DeMaster, 2002) and, in total, a global ocean content of about 10^{17} moles dissolved Si with an average concentration of 71 µM (Tréguer et al., 1995). As a consequence of ocean circulation $Si(OH)_4$ is fractionated between the different oceanic basins (Ragueneau et al., 2000) ranging from less than 1 µM in the low latitude surface waters to more than 170 µM in the intermediate North Pacific (Fig. 1.6) (Garcia et al., 2010b). Unlike NO_3^-, $Si(OH)_4$ concentrations remain low throughout the upper 1,000 m in the water column, except for the equatorial and northern Pacific and the Southern Ocean (Fig. 1.6). Also, the lateral increase in $Si(OH)_4$ concentration within the oceanic basins is much stronger than the increase of NO_3^-, which must be linked to differences in

biogeochemical processes between Si and other nutrients. In seawater, $Si(OH)_4$ is one of the major nutrients for phytoplankton growth (Ragueneau et al., 2000). There are large differences in N and Si regeneration in the ocean. NO_3^- concentrations increase rapidly with depth and reach a maximum at relatively shallow depth to stay essentially constant below. In contrast, the $Si(OH)_4$ concentration increases more slowly and almost all the way to the bottom of the ocean (Dugdale and Wilkerson, 2001). In the ocean $Si(OH)_4$ is almost exclusively used by diatoms, which build $bSiO_2$ shells. NO_3^- in organic matter is degraded and actively oxidised by bacteria in very shallow depths, whereas the diatom shells, and therefore the Si is more slowly re-dissolved mostly by chemical processes while the particles sink down (Dugdale and Wilkerson, 2001). The flux of biogenic silicate from the surface ocean into deeper layers and its recycling was estimated to be around 120 x 10^{12} M/yr and with that to be 20 times larger than the flux of Si into the ocean (Nelson et al., 1995; Tréguer et al., 1995).

1.4.1 Diatoms

Diatoms are a group of microscopic, eukaryotic phytoplankton, which make up to 25% of the annual global photosynthesis (Nelson et al., 1995). They are the most diverse group of phytoplankton with more than 200,000 estimated different species (Armbrust et al., 2009), ranging in size from a few µm to several mm consisting of single cells or chains of connected cells (e.g. *Chaetoceros*) (Armbrust et al., 2009). The genera *Chaetoceros*, *Coscinodiscus* and *Thalassionema* (Fig. 1.7) are considered to have the highest species diversity and widest distribution (Sunesen et al., 2008). Traditionally the identification at species level has been based on morphological features observed by light microscopy. The oldest diatom fossils are 190 Myr old, although molecular studies suggest that the first diatoms appeared around 250 Myr ago together with the dinoflagellates and coccolithophorites resulting in a major global biogeochemical shift in global carbon cycling, a decline in atmospheric CO_2, and an increase in O_2 concentrations (Sims et al., 2006). Reproduction of diatoms occurs mostly via mitotic division of the cells, which is only infrequently interrupted by sexual reproduction events. Diatoms can bloom very quickly and increase their cell number by many orders of magnitudes

within a few days (Armbrust, 2009). The organic carbon produced by diatoms serves as the basis for the marine food webs. One of the most important features of diatoms are their cell walls (called frustules) made of amorphous silicate (SiO_2*nH_2O) (Mortlock and Froelich, 1989) taken up from the surrounding seawater either as $Si(OH)_4$ or as $Si(OH)_3^-$.

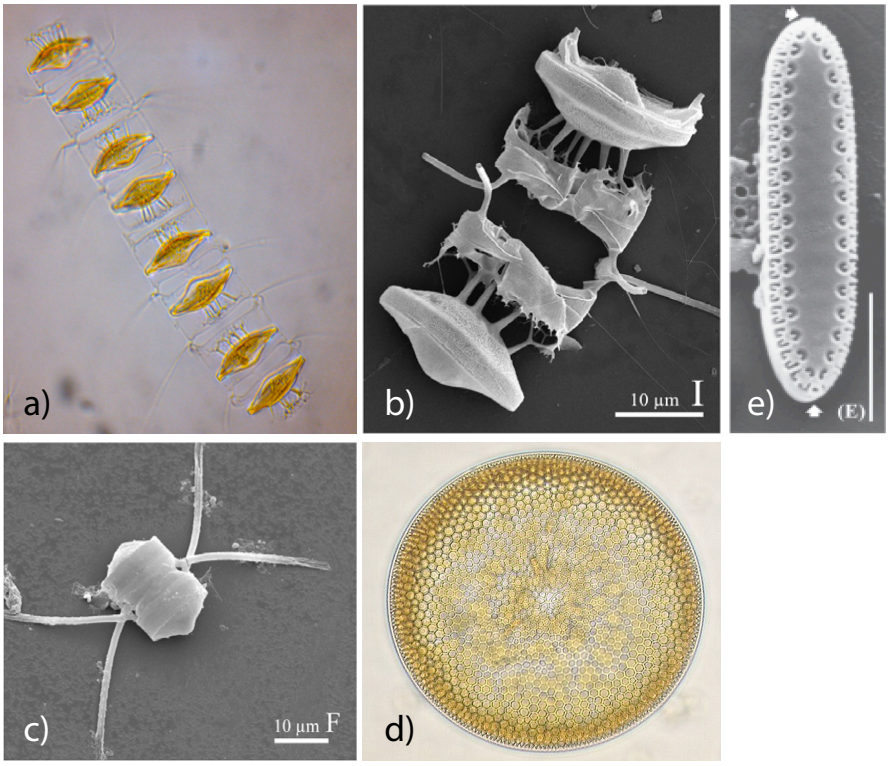

Figure 1.7: SEM and light microscopy imgages of the most abundant diatom species from the Peruvian upwelling area: a) and b) Chaetoceros diadema (a) chain of resting spores, picture from Richard A. Ingebrigtsen, Department of Arctic and Marine Biology, University of Tromsø, b) from Sunesen et al., 2008, scale is 10 µm), c) Chaetoceros didymus (Sunesen et al., 2008, scale is 10 µm), d) Coscinodiscus radiatus (from www.awi.de), e) Thalassionema nitzschioides, scale is 5 µm (Sar et al., 2007).

The frustules are produced in an acidic silicate-deposition vesicle and encased in an organic matrix that is rich in proteins and sugars, preventing the biogenic silicate from dissolving in sea water, which is usually undersaturated with respect to $Si(OH)_4$. Consumption of this matrix by bacteria, e.g. within the oxygen minimum layer off Peru, accelerates the recycling of silicate within the water column (Bidle et al., 2002). In creating these walls from $Si(OH)_4$ dissolved the sea water, diatoms control the biogenic cycling of silicon in the world's oceans (Nelson et al., 1995; Ragueneau et al., 2000) to such an extent that every atom of silicon entering the ocean is incorporated into a diatom cell wall on average 39 times

before being buried on the sea floor (Tréguer, 1995). Diatoms can increase their $Si(OH)_4$ uptake and specific cell division rate when extracellular silicate concentration in the surrounding surface water increases (Wilken et al., 2011), but they can also maintain cell division rates under decreased $Si(OH)_4$ concentrations, e.g. in the open ocean, by producing thinner frustules (Brzezinski et al., 1990). The disadvantage is that thinner frustules may make such cells more susceptible to destruction by dissolution or grazing, decreasing the chance of their preservation in the sediments (Lewin, 1961).

The contribution of diatoms to the total production varies from one system to the other, depending on physical (e.g. seasonality), chemical (nutrient availability) and biological (formation of blooms) processes (Ragueneau et al. 2000). Diatoms, such as dinoflagellates, belong to the large phytoplankton with a small surface to volume ratio. Therefore, they require environments with high nutrient concentrations (Ragueneau et al., 2000). Diatoms are found worldwide, but they tend to dominate phytoplankton communities within well-mixed equatorial divergences (Dugdale and Wilkerson, 1998) and coastal upwelling regions (Rojas de Mendiola, 1981), where sufficient light, inorganic NO_3^-, P, $Si(OH)_4$ and trace elements are available (Morel and Price, 2003). Primary productivity in 30–40% of the global oceans is limited by the availability of Fe, in particular in open-ocean regions of the Southern Ocean, equatorial Pacific Ocean (Fig. 1.2) and north Pacific Ocean (Moore et al., 2002). These high-nutrient, low-chlorophyll (HNLC) regions are characterized by low concentrations of Fe and high concentrations of the major nutrients (NO_3^-, P, $Si(OH)_4$). Limitation of nutrients other than $Si(OH)_4$ can lead to a heavier silicification of the frustules (Hutchins and Bruland, 1998; Takeda, 1998). Interactions between nutrient availability and $Si(OH)_4$ utilisation by diatoms in the Southern Ocean are thought to explain, at least in part, the reduction in atmospheric CO_2 during the glacial periods when Fe concentrations were higher mainly due to higher dust supply (Siegenthaler et al. 2005). Under Fe-replete conditions, diatom communities use less silicate relative to nitrogen. This leaves excess silicate in the surface waters, which can be transported via ocean circulation into other regions of the ocean, e.g. the subtropics. Here, it favours diatom rather than coccolithophorid productivity,

which can have a great impact on the atmospheric CO_2 concentration (the so-called Silicic Acid Leakage Hypothesis (SALH)) (Matsumoto and Sarmiento, 2008; Brzezinski et al., 2002).

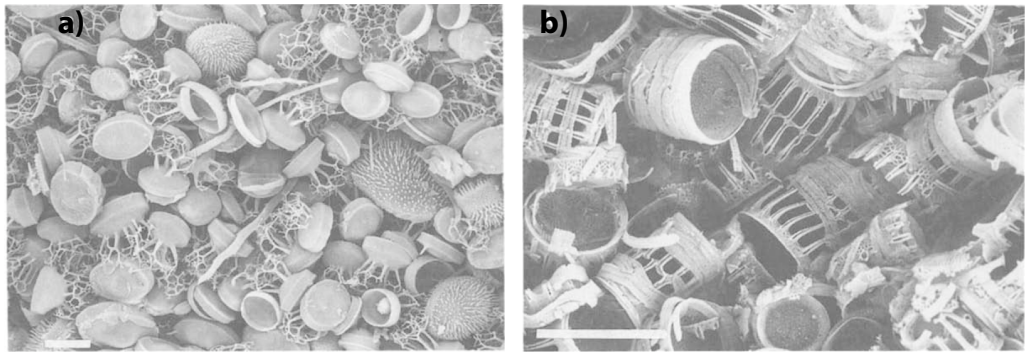

Figure 1.8: SEM images from a) Chaetoceros resting spores, mainly of Chaetoceros diadema, and b) Skeletonema sp., scale bars are 10 µm (from Brodie and Kemp, 1994).

Along the Peruvian upwelling area, neritic bloom-forming diatom species dominate the phytoplankton community, especially many species of *Chaetoceros* and its resting spores can be found (Fig. 1.8) (Rojas de Mendiola, 1981, Abrantes et al. 2007). Together with *Thalassionema nitzschioides*, the second most abundant species (Abrantes et al., 2007), *Chaetoceros* is mostly abundant during spring upwelling events (Rojas de Mendiola, 1981). Other species, such as *Skeletonema costatum* (Fig. 1.8), which is presently mostly abundant at 35°S off Chile, was enriched in the area under changed upwelling and nutrient conditions, e.g. at the end of the Little Ice Age (see Chapter 5). Several studies have shown that dissolution selectively destroys fragile species in the water column, at the sediment-water interface, and within the sediments (Nelson and Goering, 1977; Koning et al., 2001; Romero et al., 2001; Abrantes et al., 2002). As a result, many of the fragile forms of the diatoms, such as *Chaetoceros*, are found rarely in the sediment. The sedimentary record of those fragile genera is thus mainly composed of the resting spores that are formed as part of a survival strategy (Abrantes et al., 2007). More resistant and abundant upwelling species such as *Thalassionema nitzschioides* are found in their normal life forms (Koning et al., 2001; Romero et al., 2001; Abrantes et al., 2002, 2007).

1.4.2 Stable Silicon Isotopes

Silicon (Si) is, after oxygen, the second most abundant element on earth. It has three stable isotopes, ^{28}Si, ^{29}Si and ^{30}Si, with abundances of 92.2%, 4.7% and 3.1%, respectively, and one naturally occurring but radioactive isotope (^{32}Si), which is of cosmogenic origin. The Si isotope composition is expressed in the delta-notation giving the deviation of the measured ^{30}Si/^{28}Si ratio in a sample from the international standard NBS28 in parts per thousand (‰):

$$\delta^{30}Si = \left[\frac{{}^{30}Si/{}^{28}Si_{sample}}{{}^{30}Si/{}^{28}Si_{NBS28}} - 1 \right] * 1{,}000$$

Alternatively, in some studies the δ^{29}Si is given, which is defined by the ^{29}Si/^{28}Si ratio and can be translated into the δ^{30}Si ratio (due to strictly mass dependent fractionation). The isotopic composition of Si varies because of mass dependent isotope fractionation based on isotope exchange reactions (equilibrium isotope fractionation) and kinetic effects (kinetic isotope fractionation). The δ^{30}Si varies between different silicate materials on earth due to these mass-dependent fractionation processes. The δ^{30}Si of bulk earth was estimated to be -0.29‰ ± 0.08‰ (Fitoussi et al., 2009; Savage et al., 2010). Endogenous rocks have δ^{30}Si between -1.1‰ to +0.7‰ (Douthitt, 1982; Ding et al., 1996). Secondary clay minerals that are produced during weathering range between -2.3‰ and +0.1‰ in δ^{30}Si (Ding et al., 1996; De La Rocha et al., 2000; Georg et al., 2009), and silcretes have very low δ^{30}Si of up to -6‰ (Basile-Doelsch, 2006). The dissolved pools are usually enriched in the heavier isotopes. River water has δ^{30}Si values between +0.4‰ and +3.4‰ (De La Rocha et al., 2000; Georg et al., 2006a; Ding et al., 20011), whereas seawater usually ranges between +0.6‰ and +3.1‰ (De La Rocha et al., 2000; Varela et al., 2004; Cardinal et al., 2005), with surface water having generally the higher δ^{30}Si values due to biological productivity and utilisation. Biogenic silica shows the largest range in δ^{30}Si in nature. Siliceous sponges are the most ^{30}Si-depleted organisms with δ^{30}Si up to -4‰ (Douthitt, 1982; De La Rocha, 2003; Hendry et al., 2010). Diatoms are enriched in ^{30}Si and

range from -0.3‰ to +2.6‰ (De La Rocha et al., 1998; Varela et al., 2004; Reynolds et al., 2008).

Isotope signatures vary in the ocean due to the three following different processes: 1) Diatoms preferentially take up the lighter isotope from the surrounding dissolved pool, leaving the residual surface seawater enriched in the heavier isotopes. This fractionation process was found to occur with a fractionation factor of -1.1‰ (De La Rocha et al., 1997; Milligan et al., 2004; Varela et al., 2004), which was found in culturing experiments independent of diatom species (three marine species: *Skeletonema costatum*, *Thalassiosira weissflogii*, and *Thalassiosira* sp.) or temperature (12-22°C range) (De La Rocha et al., 1997) or growth rate (Milligan et al., 2004). Due to the high abundance of diatoms in the ocean this is the most important factor controlling the seawater $\delta^{30}Si$ values. 2) Demarest et al. (2009) found an isotope effect due to the partial dissolution of the diatom frustules of -0.55‰ that counteracts the fractionation during the formation of the frustules and releases primarily the lighter isotopes back into seawater. 3) Si uptake and spicule formation by marine benthic siliceous sponges fractionates the $\delta^{30}Si$ by up to -4‰ (De La Rocha et al., 2003; Hendry et al., 2010; Wille et al., 2010), which has primarily an effect on the deep water isotope composition.

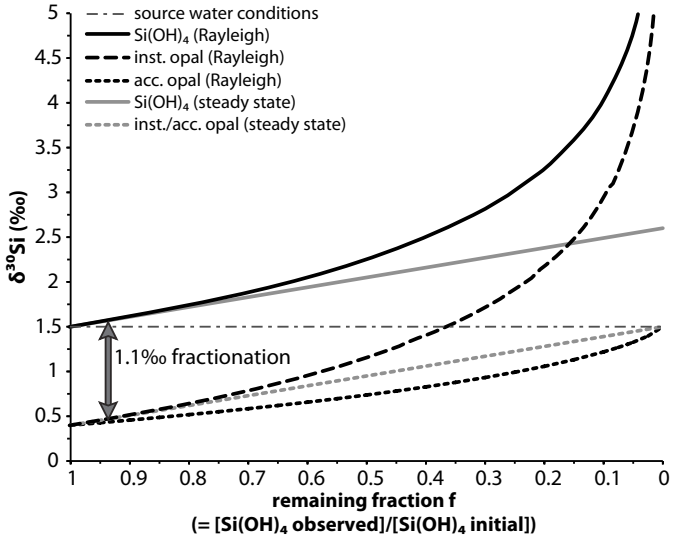

Figure 1.9: Simulation of Si isotope fractionation during opal precipitation by diatoms for Rayleigh-type (closed system, black curves) and steady state-type (open system, grey curves) model conditions as a function of f (remaining $Si(OH)_4$ from the initially available nutrient pool). In this case, the source water has a $\delta^{30}Si_{Si(OH)4}$ of +1.5‰.

Long- and short-term imbalances in the global budget of the silica cycle could have an influence on the average marine $\delta^{30}Si$ composition, and therefore also on the composition of diatoms, which would affect the reconstruction of $Si(OH)_4$ utilisation (De La Rocha and Bickle, 2005). Such changes could arise from a sustained change in the riverine flux of Si, e.g. if the discharge is reduced by 50% this might alter the average $\delta^{30}Si$ up to a few tenths of per mille. Such a variation could be reconstructed by analysing the $\delta^{30}Si$ composition of the deep sea, for example by sponges.

Two different models can be used to describe the evolution of the $\delta^{30}Si$ composition of surface waters during biologically induced fractionation by diatoms: a steady-state model (continuous supply of nutrients and export of the produced $bSiO_2$ at a constant rate causing a dynamic equilibrium of the $Si(OH)_4$ content), and a Rayleigh-type model (a fixed input followed by fractional loss or export of $bSiO_2$ causing an increase of the $\delta^{30}Si$ of the remaining waters and the newly formed diatoms and finally the complete utilisation of the available $Si(OH)_4$) (Fig. 1.9) (De La Rocha et al., 1997; Cardinal et al., 2005; Reynolds et al., 2006). The first one was used to explain biological fractionation of Si in open ocean waters (Varela et al., 2004; Cardinal et al., 2005), whereas the second one is usually used to explain laboratory culturing experiments given that such closed system conditions rarely ever occur in a natural system (Douthitt, 1982; De La Rocha et al., 1997; Basile-Doelsch, 2006; Reynolds et al., 2006). The two models can be described and approximated by the following equations:

Steady-state model:

$$\delta^{30}Si_{Si(OH)_4\ observed} = \delta^{30}Si_{Si(OH)4\ initial} - \varepsilon * (1 - f)$$

$$f = \frac{Si(OH)_{4\ observed}}{Si(OH)_{4\ initial}}$$

Under assumed steady state conditions the effective net $bSiO_2$ production (e.g. during one year) is equal to the net $Si(OH)_4$ supply (Fripiat et al., 2011a).

Rayleigh-type model:

$$\delta^{30}Si_{Si(OH)_4\ observed} = \delta^{30}Si_{Si(OH)_4\ initial} + \varepsilon * (\ln f)$$

$$\delta^{30}Si_{diatom_{inst}} = \delta^{30}Si_{Si(OH)_4\ observed} + \varepsilon$$

$$\delta^{30}Si_{diatom_{accumulated}} = \delta^{30}Si_{Si(OH)_4\ initial} - \varepsilon * \left(\frac{f \ln f}{1-f} \right)$$

where $\delta^{30}Si_{Si(OH)4\ initial}$ is the Si isotope composition of $Si(OH)_4$ in the surface water before biological utilisation starts to fractionate the Si isotopes, $\delta^{30}Si_{Si(OH)4\ observed}$ is the Si isotope composition measured in the surface water, *f* is the depletion factor describing the fraction of the initial $Si(OH)_4$ concentration that remains, ε is the fractionation factor between the $Si(OH)_4$ and the diatoms produced, $\delta^{30}Si_{diatom\ inst}$ is the Si isotope composition of the instantaneously produced diatoms at any time and $\delta^{30}Si_{diatom\ accumulated}$ is the silicon isotope composition of the accumulated diatoms and integrates over time of the growth period. Both models assume a constant fractionation factor. The remaining fraction f of the available $Si(OH)_4$ is directly proportional to the utilisation of $Si(OH)_4$ in the surface water by diatoms:

$$utilisation[\%] = (1-f) * 100$$

Although diatoms are the most important primary producers in the ocean and they largely control the cycling of the major nutrient Si, there are few possibilities to reconstruct the history of diatom productivity and the marine Si cycling, and thus to explore potential contributions to past changes in biogeochemical cycling (De La Rocha et al., 2008). As described above, $bSiO_2$ accumulation records are often biased, e.g. by current-driven sediment redistribution of the sediment or by dissolution of the $bSiO_2$ (Ragueneau et al., 2000). Since the diatoms, that are produced in the surface water and that are buried in the sediment, reflect the signal of the surface water, the analysis of $\delta^{30}Si$ of diatom $bSiO_2$ can provide information on the $Si(OH)_4$ utilisation at the time of frustule formation, also in the geological past (De La Rocha et al., 1998; Wischmeyer et al., 2003), which is potentially unbiased by dissolution effects (De La Rocha et al., 1998). Such a tracer is of particular use in those areas of the global ocean, where calcareous sediments are rare and where siliceous sediments preferentially accumulate (Tréguer et al., 1995). Therefore, paleo-studies of silicon

isotope composition in diatom opal have so far mostly focused on the high latitudes in the Southern Ocean (De La Rocha et al., 1998; Brzezinski et al., 2002; De La Rocha, 2006) and the North Pacific (Reynolds et al., 2008), whereas only one study so far was conducted in the low latitudes in the tropical eastern Pacific Ocean (Pichevin et al., 2009).

1.5 Radiogenic Neodymium and Strontium Isotopes

Physical oceanographers use tools, such as temperature and salinity, which are conservative in the ocean, and nutrient concentrations (e.g. of N, P, Si) to characterise certain water masses and their mixing. However, such parameters are not preserved in the paleo-record at the required precision to reconstruct past water column properties. Therefore, other proxies such as the stable carbon isotope composition ($\delta^{13}C$) (e.g. Raymo et al., 1992; Ravelo and Andreasen, 2000), cadmium to calcium ratios (Cd/Ca) (Boyle and Keigwin, 1985) and the radiogenic isotope composition of trace metals are applied to reconstruct changes in water mass circulation in the past.

Radiogenic isotopes are produced by radioactive decay of a parent isotope. During geological processes such as internal differentiation in the earth mantle and the crust the different parent and daughter elements are fractionated due to their distinct chemical properties and are enriched either in the liquid or in the residual, therefore producing distinguishable differences of the radiogenic isotope ratios in the respective mantle-derived and continental crust-derived rocks. Thus, radiogenic isotope compositions of rocks are a function of rock type (chemical differentiation) and their age (radioactive decay) leading to significant variations in the isotopic composition that can be used to trace geochemical processes on different time scales including continental weathering and oceanic water mass mixing.

Through weathering and erosion the source rocks release their signatures either as particles (rivers, eolian dust input) or in dissolved form (rivers) into the ocean. Thereby they transfer the radiogenic isotope signature of the continental source rocks to the ambient water masses. Additional sources in the ocean can be boundary exchange with the shelf sediments and hydrothermal inputs (Palmer and

Edmond, 1989; Lacan and Jeandel., 2005). Various archives can provide radiogenic isotope compositions of different water masses, e.g. ferromanganese (Fe-Mn) crusts, foraminifers and fish teeth (Abouchami et al., 1999; Martin and Scher, 2004; Klevenz et al., 2008). Under oxic conditions in the pore waters, bottom water isotopic compositions (present and past) are also preserved in early diagenetic, authigenic Fe-Mn oxyhydroxide coatings of sediment particles that can be directly extracted from bulk sediments (Rutberg et al., 2000; Gutjahr et al., 2007; Stumpf et al., 2010). In unoxic sediments, however, the reduction of solid Fe-oxides releases also the trace elements from sedimentary coatings (Haley et al., 2004). In contrast, benthic foraminifers are clearly formed from local bottom water, and the recorded signature is not influenced by the surrounding redox conditions (Klevenz et al., 2008).

The most important advantage of radiogenic isotopes is their independence of fractionation induced by biological processes or evaporation. As a consequence, changes in the radiogenic isotope composition of a water mass can only occur by addition (e.g. by riverine or eolian input or by mixing of different water masses) of the respective trace metal from a reservoir with a different isotopic composition (Frank, 2002). Through weathering and erosion continental source rocks release and supply particles of distinct isotopic signatures. Hence, the radiogenic isotope systems of Nd and Sr of sediment particles have successfully been applied to reconstruct source areas of deposited particles that have either been transported by rivers and oceanic water masses or via the atmosphere (e.g. Goldstein et al., 1984; Dia et al., 1992; Fagel et al., 2004; Ehlert et al., 2011).

1.5.1 Neodymium Isotopes

Neodymium (Nd) belongs to the light rare earth elements (LREEs) and has seven different naturally occurring isotopes (^{142}Nd, ^{143}Nd, ^{144}Nd, ^{145}Nd, ^{146}Nd, ^{148}Nd and ^{150}Nd) with abundances of 27.1%, 12.2%, 23.9%, 8.3%, 17.2%, 5.7% and 5.6%, respectively. The radiogenic ^{143}Nd is produced by α-decay from the radioactive ^{147}Sm, which has a half-life of 106 Gyr:

$$^{147}_{62}Sm \rightarrow ^{143}_{60}Nd + \alpha + E$$

where E is the total decay energy. The isotopic composition of Nd is expressed by the $^{143}Nd/^{144}Nd$ ratio, and is, due to the small variations which are mostly at the fourth or even fifth decimal place, given in the ε-notation as the deviation from the **Ch**ondritic **U**niform **R**eservoir (CHUR, which has presently a $^{143}Nd/^{144}Nd$ of 0.512638 (Jacobsen & Wasserburg, 1980)) in parts per 10,000:

$$\varepsilon Nd = \left[\frac{^{143}Nd/^{144}Nd_{sample}}{^{143}Nd/^{144}Nd_{CHUR}} - 1 \right] * 10{,}000$$

Although Sm and Nd are both LREEs with similar ionic radii, their physical and chemical behaviour is different enough to enable fractionation. Nd is preferentially concentrated in the liquid phase during partial melting of silicate minerals, while Sm remains in the residual solids. This results in basaltic magmas having a lower Sm/Nd ratio than its source rocks. All rock types that characterise the continental crust, such as granites, granulites, shales, graywackes, sandstones and limestones, have a lower Sm/Nd ratio than mafic, mantle-derived igneous rocks, such as tholeeite basalts, gabbros, and ultramafic rocks. The continental crust is enriched in Nd relative to Sm compared to the residual rocks in the lithospheric mantle. The mantle is thus enriched in radiogenic ^{143}Nd compared to the continental crust, because more ^{147}Sm has been available to decay. Consequently volcanic rocks have high Sm/Nd ratios and high εNd (called "radiogenic"), whereas older continental crust rocks have a low Sm/Nd and low εNd. The Nd isotopic composition of the continental crust is very heterogeneous ranging in εNd between -56 in old granitic cratons in Greenland and +12 in recent mid-ocean ridge basalts (Goldstein and Hemming, 2003; Jeandel et al., 2007). Nd is mobilised through weathering and delivered to the ocean via rivers, eolian input and boundary exchange processes along the continental shelf regions (Frank, 2002; Lacan and Jeandel, 2005), but hydrothermal input does not play a role as a source. Dissolved Nd in the hydrothermal solutions is immediately adsorbed and scavenged to the hydrothermal sediments by precipitation (German et al., 1990).

The residence time of Nd in seawater is between 400 to 2000 years (Tachikawa et al., 1999; Arsouze et al., 2009) and Nd isotopes can therefore be used to trace water mass mixing on ocean basin scales.

1.5.2 Strontium Isotopes

Strontium (Sr) has four naturally occurring isotopes (^{84}Sr, ^{86}Sr, ^{87}Sr and ^{88}Sr) with abundances of 82.5%, 7.0%, 9.9% and 0.6%, respectively. The radiogenic isotope ^{87}Sr is produced from radioactive ^{87}Rb by β^- -decay with a half-life of 48.8 Gyr:

$$^{87}_{37}Rb \rightarrow ^{87}_{38}Sr + \beta^- + \bar{\upsilon} + E$$

where $\bar{\upsilon}$ is an antineutrino and E is the total decay energy. The Sr isotopic composition is given as the ratio of the radiogenic ^{87}Sr to the primordial ^{86}Sr. In contrast to the Sm/Nd system, the parent element Rb is more compatible and is enriched in the liquid during crust formation. Therefore, older continental rocks have a high Rb/Sr and a high ^{87}Sr/^{86}Sr (radiogenic), whereas mantle-derived volcanic rocks have a low Rb/Sr and a low ^{87}Sr/^{86}Sr.

Sr in seawater is mainly derived from riverine inputs. The signature can be strongly influenced by old carbonates in the drainage area, which are easily dissolved and have a radiogenic isotope signature similar to seawater. Another significant source are mantle derived high-temperature hydrothermal inputs at the mid-ocean ridges, which have unradiogenic ^{87}Sr/^{86}Sr ratios (Palmer and Edmond, 1989). Remobilisation of Sr from shelf sediments via the pore waters is another small but significant source for Sr in the oceans. They have average isotope compositions similar to present-day seawater. The residence time of Sr in the ocean is in the order of several million years, which is the reason why it is homogenously distributed in seawater. The present-day ^{87}Sr/^{86}Sr ratio is 0.70916 (Palmer & Edmond, 1989). Due to this long residence time paleo radiogenic Sr isotope compositions extracted from Fe-Mn oxyhydroxide coatings of marine sediments cannot be used to trace water masses throughout the latest Quaternary. However, the radiogenic Sr isotope composition in the ocean has changed significantly over longer time-scales throughout the Phanerozoic due to increased

hydrothermal inputs during continental break up phases or changes in continental weathering contributions as a function of higher orogenies (Veizer et al., 1999).

During weathering and erosion processes the radiogenic isotope composition of the product can become decoupled from that of the parent rock resulting in signatures that vary with grain size. In the case of Sr, the parent element Rb is enriched in clay minerals, where it substitutes potassium. This leads to higher Rb/Sr and higher $^{87}Sr/^{86}Sr$ ratios in fine-grained weathering products. These incongruent weathering processes clearly affect the Sr isotope but not strongly the Nd isotope compositions (Tütken et al., 2002).

1.6 Outline of the Thesis

Coastal upwelling areas are characterised by high rates of phytoplankton primary productivity, especially diatoms. Changes in productivity, e.g. due to changed nutrient conditions, can strongly impact the export of organic carbon to the deep sea, and ultimately influence the global carbon cycle (e.g. Brzezinski et al., 2002). This is the first study focusing on the distribution and evolution of nutrient utilisation by diatoms in such an environment using stable Si isotopes. $\delta^{30}Si$ of diatom opal is supposed to reflect surface water $Si(OH)_4$ utilisation. However, so far no study has been carried out that showed that the surface water signal is reliably preserved in the underlying sediments. In particular in a coastal upwelling regime, which is influenced by a high variability in physical and biological properties, it is necessary to carefully examine the processes that influence the $\delta^{30}Si$ signal archived by the diatoms.

Thus, Chapter 3 focuses on the comparison between measurements of dissolved $\delta^{30}Si_{Si(OH)4}$ in the water column along the Peruvian shelf (conducted by P. Grasse) and the $\delta^{30}Si$ of diatoms in the underlying shelf sediments. The dissolved $\delta^{30}Si_{Si(OH)4}$ is compared with measured chemical and physical water mass properties (such as $Si(OH)_4$ concentration, temperature and salinity) to evaluate utilisation versus water mass mixing effects and the influence of remineralisation processes to show which factors mainly control the $\delta^{30}Si_{Si(OH)4}$ and how large the ultimate variability is. The $\delta^{30}Si$ of the surface sediment diatoms, which actually integrate the surface water signal over a longer time period, are then compared to

the surface water $\delta^{30}Si_{Si(OH)4}$ signatures to examine to which extent the processes influencing the utilisation signal are preserved. In addition, this study can also provide information on how effective the commonly applied methods for diatom separation from the sediment are, and if the methods have to be adapted to the conditions of the study area.

In order to reconstruct the changes in nutrient utilisation and upwelling intensity off Peru since the last glacial maximum, Si, Nd and Sr isotopic compositions are measured in a core from the upwelling region for the time between 20,000 years ago and present. Chapter 3 provides the necessary background information and calibration of the $\delta^{30}Si$ signatures to the present-day situation for the overall goal of this project addressed in Chapter 4. The $\delta^{30}Si$ signal of the past has been influenced by $Si(OH)_4$ utilisation but also strongly by water mass mixing. Therefore, in Chapter 4 the silicon isotope signatures of the diatoms are supported by measurements of radiogenic Nd and Sr isotopes from authigenic Fe-Mn bulk sedimentary coatings, benthic foraminifers and from the detrital fraction. A core-top study, similar to the $\delta^{30}Si$ conducted in Chapter 3, compared the sedimentary radiogenic isotope signatures with those measured dissolved in the water column (measurements conducted by P. Grasse) in order to characterise distinct water masses influencing the bottom waters along the shelf. Also the detrital signal is compared to source provenances in the South American hinterland to define weathering inputs and transport pathways.

In Chapter 5, finally, the Si, Nd and Sr isotopic compositions of two shorter cores covering the period of time since the Little Ice Age until present are determined. Previous studies showed that this time period was characterised by major biogeochemical regime shifts along the Peruvian region. The main goal of Chapter 5 is the reconstruction of the factors that have controlled the dynamics of $Si(OH)_4$ and other nutrients and oxygen, in particular in comparison with the nitrogen isotope composition ($\delta^{15}N$) of sedimentary organic matter. This study shows the major benefit of $\delta^{30}Si$ measurements, which are, in contrast to the $\delta^{15}N$, not strongly influenced by oxygen-dependent water-column processes.

Chapter 2
Methodology

2.1 Material Selection and Age Models

During the SFB-related cruises M77/1 & 2 in 2008 with the German research vessel Meteor multicorer (MUC) samples were taken between 1°N and 18°S in water depths between 60 m and 2600 m (Table A.2 and A.3)). These were used for the surface sediment calibration of $\delta^{30}Si_{opal}$, εNd_{foram} from benthic foraminifers and the radiogenic isotope compositions of Nd in Fe-Mn coatings to the isotopic composition of Si and Nd in the water column measured by P. Grasse (Chapters 3 and 4). In addition, the Nd and Sr isotope composition of the detrital material was determined.

Piston core SO147-106KL, which was used for the reconstruction of surface water $Si(OH)_4$ utilisation and upwelling intensity along the Peruvian shelf during the past 20 kyr (Chapter 4), was recovered on the central Peruvian shelf at 12°03' S, 77°39.8' W in a water depth of 184 m during the cruise SO147 with the German research vessel Sonne in the year 2000 (Dullo et al., 2000). It was recovered from a small basin, which is sheltered by a landward ridge against erosion and sediment re-deposition. The core is 18.75 m long and consists mostly finely laminated diatomaceous ooze and silty clay interrupted by unlaminated foraminiferal sands (Wolf, 2002). The age determination of the uppermost part of the core was obtained by radioactive ^{137}Cs and excess ^{210}Pb profiling, whereas the stratigraphy of the upper 10 m is based on 45 AMS ^{14}C measurements of the bulk organic carbon fraction (Rein et al., 2004, 2005). The oldest radiocarbon age measured on a prominent mollusc layer was 19.6 kyr BP and the age model of the core is based on linearly interpolated ages between the calibrated radiocarbon ages.

For the reconstruction of surface water $Si(OH)_4$ utilisation and upwelling intensity during the past few hundred years covering the time between the Little Ice age and present, two shorter cores were analysed (Chapter 5). The first one, B0405-6, is a Soutar box core and was taken from the upper slope off Pisco at 14°07' S, 76°30' W in a water depth of 299 m with the Peruvian R/V José Olaya

Balandra in 2004 (Gutierrez et al., 2006). The core consists of finely laminated material. The age model for the past 135 years relies on downcore profiling of ^{241}Am and excess ^{210}Pb. Radiocarbon ages from bulk organic sedimentary carbon where used to constrain the chronology of the whole record, which was shown to cover the past ~600 years (Gutierrez et al., 2009). The second core, MUC M77/1-470, was taken during cruise M77/1 at 11° S, 77°56.6' W in 145 m water depth. At the time of writing of this thesis samples for the age determination of this core were still in progress. The preliminary age model is therefore based on visual correlation of the $bSiO_2$ record with the record of core B0405-6. A prominent increase in $bSiO_2$ from minimum to maximum values, which is also reflected in the organic carbon content, is observed in both cores and corresponds to an age of 1820 to 1850 years AD in the Pisco core (Gutierrez et al., 2009). The age model will be completed in the near future and, similar to core B0405-6, will be based on excess ^{210}Pb profiling and radiocarbon ages of bulk organic carbon for the deeper part of the core.

2.2 Stable Silicon Isotopes

2.2.1 Diatom Separation

A contamination with detrital grain, especially from clays, can considerably influence the silicon isotope composition of a diatom sample because clays are usually significantly lighter in their $\delta^{30}Si$ composition than diatoms (De La Rocha et al., 2000). Therefore, an extensive cleaning protocol was applied for all bulk diatom samples in order to ensure an as complete as possible separation of the diatom fraction from the residual material. The method applied here follows the method of Morley et al. (2004) (Fig. 2.1).

In a first step, about 250 to 500 mg of freeze-dried sediment were transferred into a 50 mL centrifuge tube. Several mL of H_2O_2 (30%) and HCl (35%) was added to the sediment and left overnight for reaction to remove the organic matter and the carbonates. The exact amount and ratio between the two reagents depends on the amount of organic matter and carbonates in the sample, but should usually be around 1:1 or 1:2 H_2O_2-HCl. Afterwards the sediment was rinsed three

times with MQ. Treatment with these reagents had to be repeated until no more reaction could be observed.

In the second step the sediment was then wet-sieved to obtain a single size fraction between 11 and 32 µm, which mostly consists of diatoms whereas radiolarians are rare. First the samples were placed in an ultrasonic bath for approximately 10 minutes and then immediately washed through the 32 µm sieve into a 5 L container. This container was placed again in the ultrasonic bath for another 5 minutes and the sample was then stepwise washed through the 11 µm sieve. The sieve then contained the $bSiO_2$ sample whereas the clay fraction was near quantitatively removed. The $bSiO_2$ was then transferred into a new 50 mL centrifuge tube, was centrifuged for 10 minutes at maximum speed, and the supernatant water was decanted.

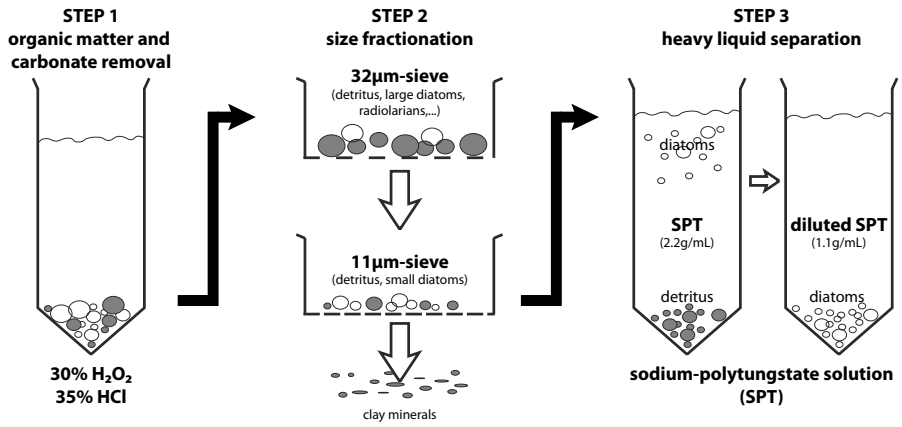

Figure 2.1: Flow diagram showing the applied cleaning method for separating and concentrating diatoms from sediments (after Morley et al., 2004). The grey circles indicate detrital material, whereas the white circles represent the $bSiO_2$ fraction.

The third step consisted of the separation of the $bSiO_2$ from the residual detrital material with a heavy liquid solution, in this study sodium-polytungstate (SPT). The density of this solution can be varied by dilution through adding MQ or by evaporation. At first, 50 mL of the SPT with a density of 2.2 g/mL was added to the sample, which was then shaken and placed in an ultrasonic bath for 15 minutes. Afterwards the sample was immediately centrifuged for 25 minutes at 2500 rpm. The liquid contained the $bSiO_2$ sample whereas the denser detrital material was concentrated at the bottom of the tube. The supernatant solution was split and transferred into two other 50 mL centrifuge tubes in equal proportions and was filled up with MQ to 50 mL to dilute the solution. After centrifuging the

sample again at 2500 rpm for 10 minutes the $bSiO_2$ was concentrated at the bottom of the tubes, and could be transferred into a single tube using MQ. The SPT solution was decanted by rinsing through a paper filter (and after evaporation was used again). The $bSiO_2$ fraction had to be rinsed with MQ, either by centrifuging it several times or by washing it again through the 11 µm sieve. The result of this cleaning process was visually checked via light-microscopy. If the sample still contained too much clay or other detrital material the respective steps of the cleaning process had to be repeated. Finally the $bSiO_2$ sample was stored dry or covered with a small amount of MQ (not more than 150 µL, to produce a $bSiO_2$-MQ mix which could be easily transferred with a pipette into a teflon vial) before further dissolution.

In addition to the separated $bSiO_2$ from the 11 to 32 µm fraction, larger diatoms were hand-picked. Therefore, the same samples as for benthic foraminifer separation were used (section 2.4.1). The large diatoms were part of each size fraction but were most abundant in the 125 to 250 µm fraction. About 200 diatom specimens (non species specific, but mostly centric diatoms) were picked under a binocular with a very small wet brush and transferred into 7 mL teflon vials for dissolution.

2.2.2 Dissolution, Concentration Measurements and Chromatographic Separation

Dissolution of the Standards and Samples:

The dissolution of the diatom samples and the preparation of the standard material is based on the method described by Georg et al. (2006b), which uses NaOH to transform solid siliceous samples into an aqueous (and HF-free) solution. The standards, generally in a powder form (ca. 20 mg standard powder), were fused with NaOH-pellets (ca. 200 mg for 20 mg of standard material) in silver-crucibles at ~730°C for ca. 8 minutes in a muffle furnace and immediately afterwards transferred into MQ, diluted to concentrations around 10ppm Si and were then acidified with HCl (35%) to pH 2 to 3.

For the dissolution of the diatom-samples the method of Reynolds et al. (2008) was applied. About 75 µL of the diatom-MQ mixture was transferred into a

7 mL teflon vial and dried down on a hotplate. To each sample 1 mL 0.1 M NaOH was added and left overnight at 130°C on a hotplate. After cooling down, the samples were transferred into 1.5 mL centrifuge vials, centrifuged at maximum speed for 10 minutes, and the supernatant solution was transferred into new 7 mL teflon vials. 200 µL H_2O_2 (30%) was added to each sample to remove the last remainders of contained organic matter. After most of the reaction had ended (usually after 30 to 60 min) the samples were dried down and then re-dissolved again overnight in 1 mL 0.1 M NaOH at 130°C. While the samples were still hot they were diluted with 4 mL MQ and were then neutralised with 0.1 mL 1M HCl. The Si concentration was then near 50 ppm. The hand-picked diatoms were dissolved in the same way except that the amount of the chemicals was always halved to make sure that the concentration of the final sample solution was not too low. Dissolution of about 200 specimens generally resulted in concentrations of 3 to 4 ppm Si. In neutralised form, the samples can be stored for several months. K. Hendry (pers. communication) mentioned that Si samples might not be stable over a time period of several months due to unpredictable Si-complex formation in the solution, which may alter the concentration and isotopic composition (the solution might behave differently from the original solution during column chemistry and measurements). However, a change in the concentration or isotope ratio was not observed for any of the samples in this study although some of them were measured repeatedly over a period of more than a year. Care should nevertheless been taken that the Si concentration in the samples is not too high. Samples with >50 ppm Si should be further diluted with MQ for longer storage.

Concentration Measurements:

The Si concentrations were measurements colorimetrically on a photospectrometer (Hansen and Koroleff, 1999) at a wavelength of 810 nm. Typically, Si samples were diluted 1:10 before analysis. 0.5 mL of the standards and samples were diluted with 2.5 mL MQ and 0.2 mL molybdate-solution. After 30 minutes 200 µL oxalic acid and 200 µL ascorbic acid were added. The oxalic acid prevents the reduction of the excess molybdate and eliminates the influence of phosphate in the solution. The ascorbic acid works as a reductant and is added to

stabilise the molybdate-oxalic acid solution. The blue silico-molybdate complex is formed within 30 minutes and is stable for several hours for measurements.

Table 2.1: Applied chromatographic treatment of the diatom samples and standard solutions. The grey shading indicates stages of sample loading or collection.

1 mL BioRad AG50W-X8 (200-400 mesh size)			
step	**stage**	**chemical**	**amount (mL)**
1	clean resin	3M HCl	2
		6M HCl	2
		HNO_3 (65%)	0.1
		6M HCl	2
		3M HCl	2
		6M HCl	2
		3M HCl	2
		MQ	3 x 2
2	check pH (≥6)		
3	**load sample**	**2-3ppm**	**1**
4	**dilute and elute**	**MQ**	**min. 2mL**

Chromatographic Separation and Purification:

The chromatographic separation of the Si solutions was adapted from Georg et al. (2006b). For a pH range between 2 and 8 Si is mainly present as the non-ionic $Si(OH)_4$ or the anionic $H_3SiO_4^-$, which will not be retained on a column loaded with cation exchange resin. The cation exchange resin used (BioRad AG50W-X8) had been pre-cleaned with MQ and 6 M HCl. For the chemical purification 1 mL of the resin was filled into a BioRad column, and rinsed in several steps with HCl and HNO_3 at variable concentrations and then rinsed with MQ to ensure neutral pH before loading the samples (Table 2.1). Both samples and standards were treated in the same way on the columns, and were generally loaded in 1 mL with 2 ppm Si concentration. Elution was achieved with at least 2 mL MQ (double volume of the resin bed) to ensure 100% yield of the Si and thus to prevent any isotopic fractionation of Si on the column.

2.2.3 MC-ICPMS Analyses

2.2.3.1 Al/Si and Ti/Si Ratio Measurements

Following the method described by Reynolds et al. (2008) no aggressive cleaning of the diatom frustules was carried out before dissolution in order to

remove trace metals, because this is not required for the analysis of Si isotope ratios from $bSiO_2$. However, if the trace metal content in the solution is high this can be a sign of the presence of a contaminant phase, such as clay minerals. As described in Chapter 1.4, clay minerals have usually a lighter Si isotope composition than diatoms due to fractionation processes during weathering (Ding et al., 1996; De La Rocha et al., 2000; Georg et al., 2009), and large amounts of remaining clays could significantly alter the $\delta^{30}Si$ measurements in shifting the ratios towards lighter values. With the applied separation method after Morley et al. (2004) clay minerals are removed by wet sieving the samples through an 11 µm sieve. This does not always remove 100% of the clay fraction. Especially in the pores of the diatoms material can withstand the cleaning procedures.

In order to exclude significant contributions from such sources, trace element concentrations of aluminium (Al) and titanium (Ti) in the dissolved diatom-solution where measured on an *Agillent 7500 Series* quadrupole ICPMS at IFM-GEOMAR. The ratios are given in Table A.2 in the Appendix and are further discussed in Chapter 3.

2.2.3.2 Stable Silicon Isotope Measurements

The Si isotope measurements following the method described by Georg et al. (2006b) were performed on a *Nu Plasma HR* MC-ICPMS at IFM-GEOMAR in Kiel. A complete separation of the Si beams from interferences is not possible with the achievable resolution on this instrument. Therefore, measurements were, in contrast to the radiogenic isotope measurements, not conducted out on the peak centre but on the flat top of the peak shoulder (Fig. 2.2).

This mass spectrometer has three different sets of adjustable slits at various positions of the instrument (Fig. 2.3), of which the source defining slit and the alpha slits are most important for silicon isotope measurements in that they enable true high resolution capabilities. The source defining slit, positioned at the end of the transfer box, has three selectable settings of 0.3 (low resolution), 0.05 (medium- high resolution, used for the determination of Si isotopes) and 0.03 mm (high resolution) width. The alpha slits, positioned in front of the ESA unit, are fully adjustable from 0 to 7 mm. Matching the width of these slits allows clipping of the

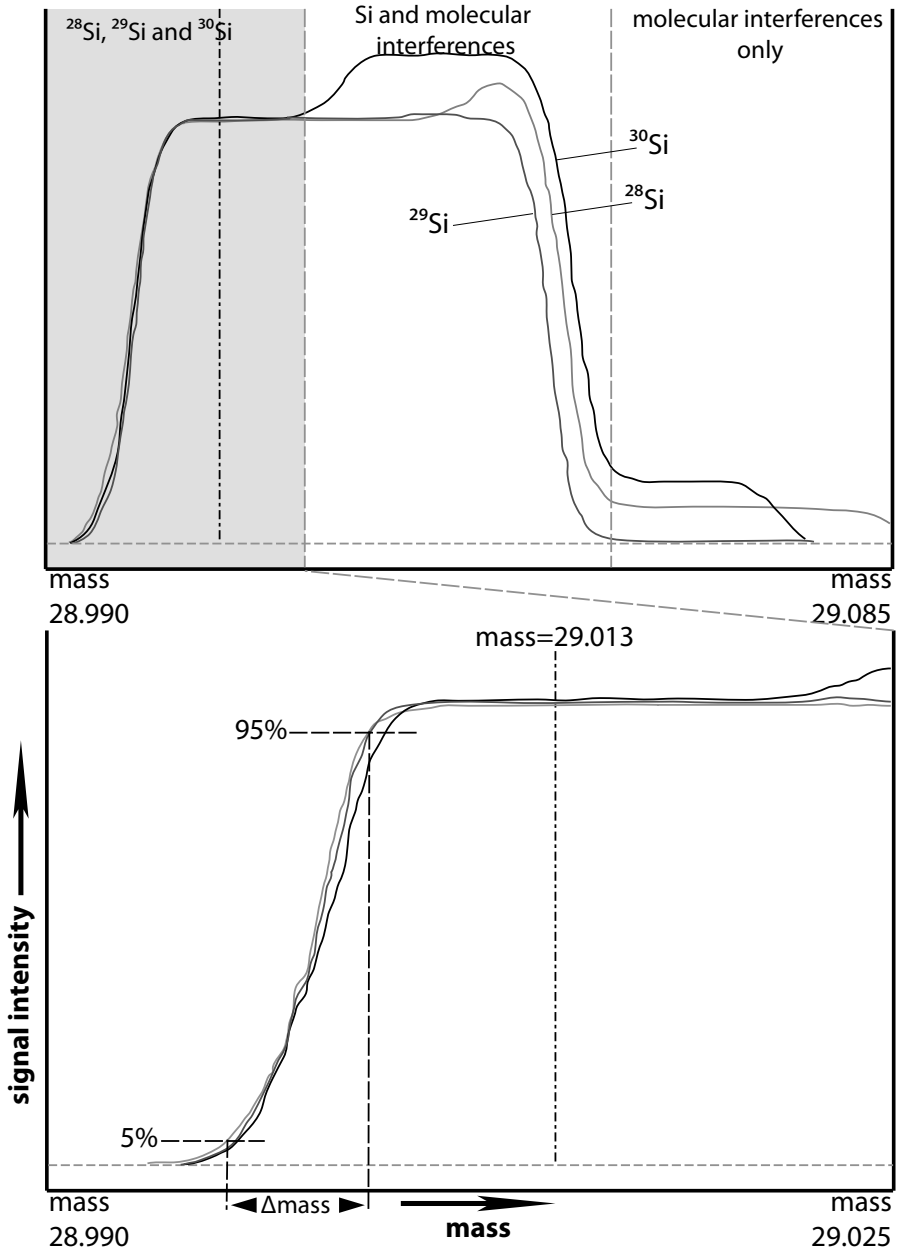

Figure 2.2: Instrumental magnet scan indicating the polyatomic interferences (upper plot) and peak position of the three Si peaks with medium resolution, the dashed line marks the ideal position of the exact axial mass for measurements on the peak shoulder (here 29.011). Resolution power is calculated from the mass difference at 95% and 5% of total beam intensity.

Table 2.2: Configuration of the detector Faraday cups for Si isotope analyses on a Nu Plasma HR MC-ICPMS. Examples for polyatomic interferences are given in brackets.

Cup	H6	H5	H4	H3	H2	H1	Ax	L1	L2	L2	L4	L5
Zero (OPZ)	^{30}Si	-	-	-	-	-	^{29}Si	-	-	-	-	^{28}Si
Mass (Si)	^{30}Si (^{14}N^{14}N^{+})	-	-	-	-	-	^{29}Si (^{14}N^{14}N^{1}H^{+})	-	-	-	-	^{28}Si (^{14}N^{16}O^{+})

ion beam on one side. This allows the separation of the three Si peaks (^{28}Si, ^{29}Si and ^{30}Si) from polyatomic interferences such as CO^+, N_2^+, NO^+, SiH^+ and especially the large interference of $^{14}N^{16}O^+$ on the ^{30}Si peak possible (Fig. 2.2). The source defining slit is made of thin metal only, and the slit positions are „used up“ after some time due to erosion from the permanent contact with the argon beam. This results in loss of resolution. which can alter the measured isotopic ratios. In order to avoid these effects, the resolution power was checked regularly (see below).

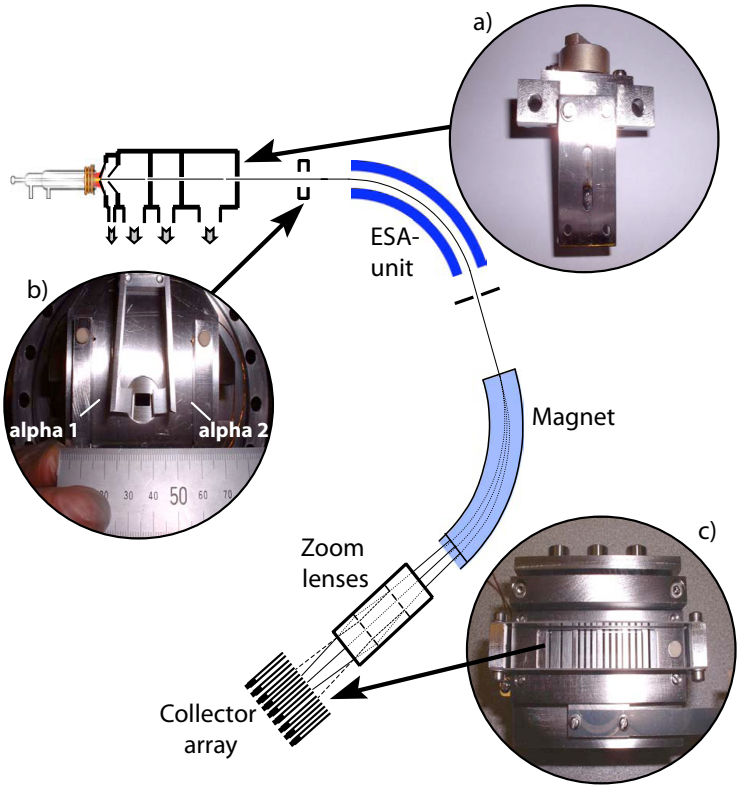

Figure 2.3: Location of the a) source defining slit, b) alpha slits, and c) collector slits on a Nu Plasma HR MC-ICPMS (adapted from the Nu Instruments manual).

For Nd isotope measurements, for example, zeros are measured by “deflect ESA“, which is the most common method for obtaining zero measurements on the *NU Plasma HR* MC-ICPMS. Using this method, the software deflects the beam away from the collector region by applying an additional 10 V to the ESA voltage during the zero measurement sequence. This is possible because for Nd no blank (i.e. no background Nd in the matrix solutions) has to be subtracted. In contrast, all used solutions (i.e. MQ, and the used HCl/HNO_3-acids) contain a certain amount of Si, which have to be corrected for. For analysis settings that need to determine zeros to correct for blanks or possible molecular interferences, the “On Peak Zero (OPZ)“

method is normally used. The zero measurement for OPZ is performed by a dedicated analysis routine that is run before sample analysis. It is generally carried out with a blank acid solution being aspirated (here MQ, because all samples/standards were always diluted with MQ). For this study blanks were usually two orders of magnitude lower than the signal of the samples/standards. Although the masses are allocated for the different collectors in the Measure Zeros routine (Table 2.2), the magnet position will not be adjusted by centring the beam during the measurements. Therefore, the exact mass required has to be set in the Magnet Scan window prior to the OPZ measurements.

A complete separation of the different Si peaks from the isobaric interferences is not possible with the *NuPlasma HR*, but in the medium resolution mode (or pseudo-high resolution mode) the separation is generally sufficient for precise measurements. For a completely resolved peak the resolution is calculated as:

$$R = \frac{m}{\Delta m}$$

where R is the resolution power, m is the atomic mass and Δm is the maximum peak width at 5% of the maximum peak height. This can not be used in the „pseudo-high mass resolution mode“. There, Δm is the difference between the masses where the beam intensity amounts to 95% and 5% of the maximum signal intensity, respectively (Fig. 2.2) (Vanhaecke and Moens, 2004). For Si isotope measurements the resolution power has to be at least 2500 (van den Boorn et al., 2006), but values around 4000 are easily reached. A reliable indicator for data quality is the mass fractionation determined during measurements (Fig. 2.4) because if interferences are not sufficiently resolved they will cause isotope ratios to be shifted away from a mass dependent fractionation line. The slope of the mean fractionation line for kinetic and equilibrium fractionation for Si isotopes is 0.5135 (Reynolds et al., 2006), and the mean fractionation for samples and standards in this study is 0.5095 (Fig. 2.4), which is within precision indistinguishable indicating that the mass separation during isotope measurements was efficient.

The configuration of the Faraday cups with the corresponding isotopic masses and typical parameter settings can be found in Tables 2.2 and 2.3. Measurements were achieved in a standard-sample-standard bracketing method

(Albarède et al, 2004). All solutions were checked for the concentration directly prior to the isotopic measurements, and were measured at a Si concentration of 14-21 µmol/kg depending on the performance of the instrument on the respective measurement day. Solutions were introduced into the plasma via a Cetac Aridus II desolvating nebulizer system equipped with a PFA nebulizer yielding a 60 to 80 µL/min uptake rate.

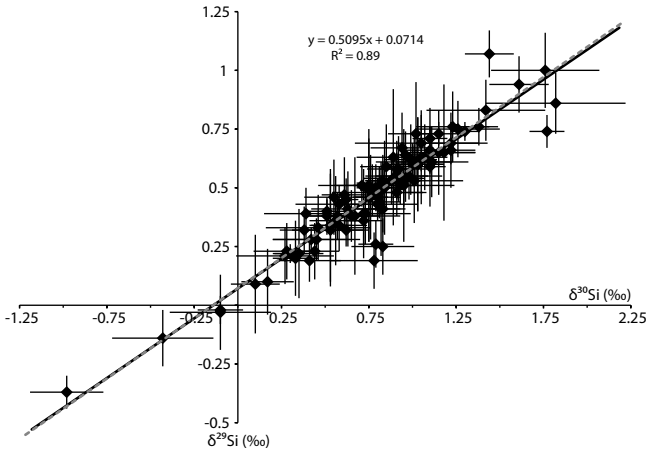

Figure 2.4: Cross plot of $\delta^{30}Si$ versus $\delta^{29}Si$ from all sedimentary diatom samples obtained in this study. Error bars represent $2\sigma_{(sd)}$ of repeated sample measurements. The black solid curve marks the mass dependent fractionation line for this study (= 0.5095x), whereas the grey dashed curve marks the mean mass dependent fractionation line for kinetic and equilibrium fractionation (= 0.5135x).

Table 2.3: Typical operating conditions used for the NU Plasma HR MC-ICPMS.

Parameter	**settings**
RF power	1300 W
1st acceleration potential	4 kV
torch	(semi-demountable sapphire torch or) normal glass torch
Coolant flow rate (Ar)	13 L/min
Auxiliary flow rate (Ar)	0.9-1.1 L/min
Nebuliser	Self aspiring microflow PFA (Elemental Scientific)
uptake rate	60-80 µL/min
Cup configuration	L5 (^{28}Si)
	Ax (^{29}Si)
	H6 (^{30}Si)
Desolvator	Cetac Aridus II
	(Ar-gas supply only)

Repeated measurements of the reference materials IRMM018 and Big Batch during the time of this thesis gave average $\delta^{30}Si$ values of -1.58 ± 0.31‰ ($2\sigma_{sd}$) and -10.78 ± 0.31‰ ($2\sigma_{sd}$), respectively, which are in good agreement with values obtained by other laboratories (Reynolds et al., 2007). Samples were measured

three to five times within one session (during one day), which generally resulted in uncertainties between 0.04‰ and 0.30‰ ($2\sigma_{sd}$). Replicate measurements of an in-house diatom matrix standard over longer periods of time (n = 20 sessions within one year) gave an external reproducibility of 0.25‰ ($2\sigma_{sd}$).

2.3 Determination of Biogenic Opal Concentrations

The $bSiO_2$ content in the sediment of core SO147-106KL (Wolf, 2002), in surface sediments and in cores MUC M77/1-470 and B0405-6 (this study) were measured following the sequential leaching methods described by DeMaster (1981) and Müller and Schneider (1993). About 20 mg of freeze-dried and fine-ground sediment material is leached at 85°C in 100 mL 1 M NaOH. In an automated procedure different chemicals (sodium-molybdat, oxalic acid, ascorbic acid and sulphuric acid) are added to the silicate solution. Measurement of one sample/standard takes about 45 minutes. Similar to the concentration measurements of dissolved $Si(OH)_4$ (section 2.3.2) the determination of the concentration is based on the formation of a blue silico-molybdate complex, which is being measured colorimetrically on a photometer.

2.4 Radiogenic Neodymium and Strontium Isotopes

2.4.1 Sample Preparation

Past bottom water dissolved radiogenic Nd isotope compositions were extracted from two different phases in the sediment: early diagenetic authigenic Fe-Mn oxyhydroxide coatings and benthic foraminifers. The detailed methods are described in the following (schematic overview in Fig. 2.5). Furthermore, the residual lithogenic material was completely dissolved to obtain the detrital radiogenic Nd and Sr isotope signal.

Fe-Mn Oxyhydroxide Coatings:

The method applied in this study was published by Stumpf et al. (2010), and is a slightly modified version of the method of Gutjahr et al. (2007). For the extraction of the authigenic Fe-Mn oxyhydroxide coatings ~3 g of dried, coarsely ground bulk sediment was rinsed twice with MQ-water. The sedimentary

carbonate fraction was removed using a 15%-acetic acid/1 M Na-acetate buffer, followed by a triple rinse with de-ionised water. The coatings themselves were then dissolved by leaching with a 0.05 M hydroxylamine hydrochloride/15% acetic acid solution buffered to pH 3.6 with NaOH for 3 hours in a shaker. The supernatant, which contained the dissolved seawater fraction, was separated by centrifugation for further chemical separation and purification. The residual detrital fraction was again mixed with the 1:1 diluted leach solution for at least 12 h to achieve a complete removal of the coatings, followed by a triple rinse with de-ionised water.

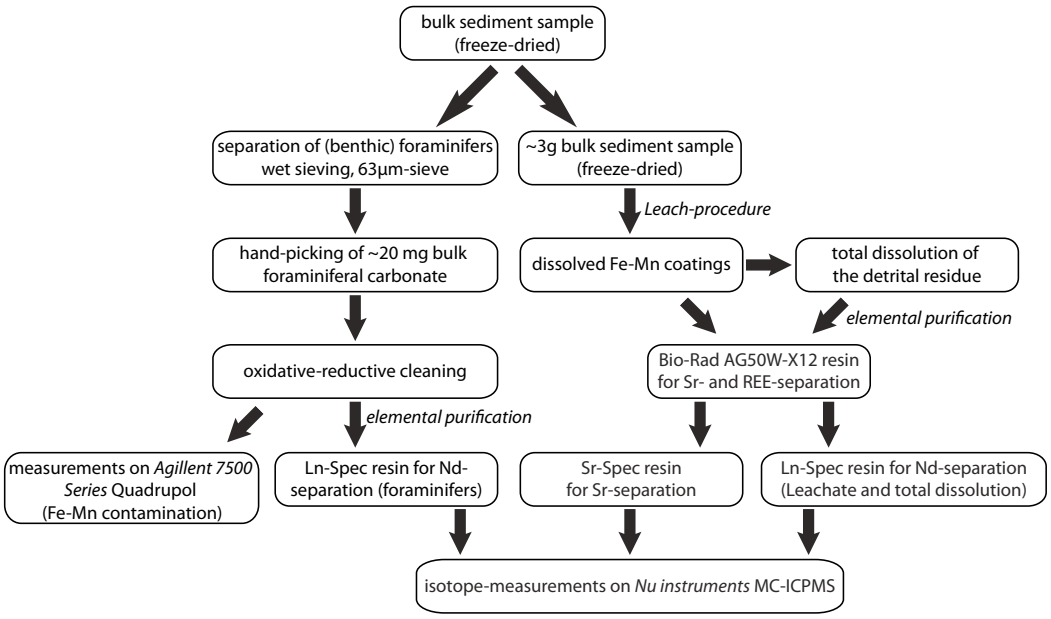

Figure 2.5: Schematic overview of the successive sample preparation for benthic foraminifers, Fe-Mn coatings and detrital material.

Benthic Foraminifers:

For the separation of benthic foraminifers the sediment was first freeze-dried, and then washed through a 63 µm sieve. In some samples a quick wet-sieving was not possible because the material sticked together too tightly. Those samples were then treated for maximum 10 minutes with a weak (< 5%) H_2O_2 solution to achieve separation of the particles of the material. The sieved samples were dried, and dry-sieved into commonly used size fractions (>400 µm, 250-400 µm, 125-250 µm, <125 µm). The benthic foraminifers were then hand-picked under a binocular. Due to the fact that the amount of foraminiferal carbonate was very low in most of the samples, picking had to be non-species specific and was

performed on all size fractions. About 20 mg of foraminifers were picked and the shells were then cracked, whereby any obvious contaminants such as mineral grains were removed. Afterwards the samples were transferred into 15 mL centrifuge tubes.

Table 2.4: Applied cleaning procedure for benthic foraminifers, based on the methods by Boyle (1981), Vance and Burton (1999) and Vance et al. (2004).

step	stage	chemical	amount (mL)	repetition	90°C water bath (total time in min)	ultrasonic bath (total time in sec)
1	clay removal	MQ	5	3	-	20-30
2		methanol	2	2	-	20
3		MQ	5	3	-	-
4	oxidative cleaning	H_2O_2 (30%), NaOH (0.1N)	10	-	30	1min every 10min
5	rinse	MQ	10-15	3	-	-
6	reductive cleaning	ammonium-hydroxide (25%), citric acid, hydrazinium-hydroxide	10	-	30	20sec every 2min
7	rinse	MQ	10-15	3	-	-
8	transfer in 1.5mL centrifuge vials					
9	dissolution	0.6 mL MQ + HNO_3 (0.5M)	until dissolution is completed			

Cleaning of the foraminifers followed the methods described by Boyle (1981), Vance and Burton (1999) and Vance et al. (2004) (Table 2.4). First, any contained clay material was removed from the samples by adding MQ or ethanol and ultrasonication of the sample. Floating particles were removed with a water-jet pump or with a pipette. Oxidative cleaning was achieved with a 30% H_2O_2/0.1 N NaOH solution in a water bath heated to 90°C for 30 minutes, and ultrasonicating the samples in between for one minute every ten minutes. After rinsing the samples carefully, a reductive cleaning step was applied using a 25% ammonium-hydroxide/citric acid/hydrazinium-hydroxide solution. The samples were treated with this solution for 30 minutes in the 90°C warm water bath, and were in between ultrasonicated for 20 seconds every two minutes. Afterwards the

Table 2.5: Applied chromatographic treatment of the leachate and total dissolution samples. The shading represents stages of sample loading or collection, a) cation exchange, b) Sr separation, c) Nd separation.

a) Cation column extraction, 0.8mL BioRad AG50W-X12 (200-400 mesh size) for Sr-REE-separation

step	stage	chemical	amount (mL)
1	clean resin	6M HCl	8
2	condition resin	1M HCl	1.5
3	**load sample**	**1M HCl**	**0.5**
4	wash-in	1M HCl	3 x 0.6
5	elute matrix	3M HCl	5
6	**collect Sr**	**3M HCl**	**5**
7	change acid	MQ	2 x 1
8	elute Ba	2.5M HNO3	8
9	**collect REE**	**6M HNO3**	**6**
10	clean resin	6M HNO3	6
11	change acid	MQ	2 x 1
12	storage	1M HCl	1

b) 50µL Sr-Spec for Sr-separation

step	stage	chemical	amount (µL)
1	clean column	0.1M H_2SO_4	1 x 1 reservoir
		MQ	2 x 1 reservoir
2	load resin	resin fill	50
3	clean resin	0.1M H_2SO_4	1x 1 reservoir
		MQ	2 x 1 reservoir
4	condition resin	3M HNO3	2 x 50
		3M HNO3	2 x 75
5	**load sample**	**3M HNO3**	**50µL**
6	elute	3M HNO3	2 x 50
		3M HNO3	300
7	**collect Sr**	**MQ**	**500**

c) 2mL Eichrom®LN-Spec (50-100 mesh-size) for Nd-separation

step	stage	chemical	amount (mL)
1	clean resin	6M HCl	8
2	condition resin	0.1M HCl	1.5
3	**load sample**	**0.1M HCl**	**0.5**
4	wash-in/elute Ba	0.1M HCl	0.5
5	elute LREE	0.25M HCl	7.5
6	**collect Nd**	**0.25M HCl**	**5**
7	clean resin	6M HCl	8
8	pass and storage	0.3M HCl	2

samples were again rinsed carefully, and transferred into a 1.5 mL centrifuge vial with a pipette. 0.6 mL MQ was added to each sample and then slowly acidified using a 0.5 M HNO_3 solution and ultrasonicating repeatedly for several minutes to dissolve the foraminifers in an as weak as possible solution.

Detrital Material

About 30 mg of the dried residual detrital material remained from the leaching procedure were transferred into 15 mL teflon vials. The first dissolution step was achieved with a mixture of 4 mL HF (40%)/1 mL HNO_3 (65%) at 140°C in closed vials on a hotplate. After 2 days the solution was left open for evaporation, and treated then with 4 mL aqua regia at 130°C for another 1-2 days. After evaporating to dryness, 1mL HNO_3 (65%)/200 µL H_2O_2 (30%) were added for further removal of any remaining organic matter. After a final evaporation step, the sample was dissolved in 1 mL HNO_3 (65%), transferred into 1.5 mL centrifuge vials, and centrifuged at max. speed for 10 minutes. The supernatant was transferred into clean 7 mL teflon vials for further chemical separation and purification.

2.4.2 Chromatographic Separation and Purification

Leachate and Total Dissolution Samples:

Separation and purification of the respective elements in the leachates and the dissolved detritus followed previously published standard procedures for Nd (Cohen et al.,1988; Barrat et al., 1996; Le Fèvre and Pin, 2005) and for Sr (Horwitz et al., 1992; Bayon et al., 2002). After separation of the alkaline elements from the rare earth elements on cation exchange columns (0.8 mL AG50W-X12 resin, mesh 200-400, Table 2.5), Sr was purified on columns with 50 mL Sr Spec resin (mesh 50-100, Table 2.5), while Nd was separated from the other REEs on columns containing 2 mL Ln Spec resin (mesh 50-100, Table 2.5).

Benthic Foraminifers:

Separation of foraminiferal Nd from major elements and other REEs is based on a single column filled with 3.14 mL Ln-SPEC resin. This was possible due

to the small amount of matrix and Nd in the foraminiferal carbonate, and to prevent unnecessary loss of Nd during the two column procedures. (Kraft et al., unpublished, 2011). The elution scheme is given in Table 2.6.

Table 2.6: Applied chromatographic procedure for the separation of Nd from foraminiferal carbonate. The shading represents stages of sample loading or collection.

3.14mL Eichrom®LN-Spec (50-100 mesh size) for Nd-separation

step	stage	chemical	amount (mL)
1	clean resin	6M HCl	8
2	condition resin	0.1M HCl	1.5
3	**load sample**	**0.1M HCl**	**0.5**
4	wash-in	0.1M HCl	0.5
5	elute	0.25M HCl	10
		0.3M HCl	2
6	**collect Nd**	**0.3M HCl**	**6**
7	clean resin	6M HCl	8
8	pass and storage	0.3M HCl	2

2.4.3 MC-ICPMS Isotope Analyses

All radiogenic isotope measurements were performed on the *NuPlasma HR* MC-ICPMS (Nu Instruments) at IFM-GEOMAR, Kiel. Configuration of the detector cups for Nd and Sr isotopes are given in Tables 2.7. Similar to the Si isotope measurements, Sr requires OPZ measurements due to interferences of krypton (Kr). All purified Nd and Sr samples were adjusted to approximately the same concentration in 1 ml HNO_3 (2%) by performing a concentration test prior to the isotope batch runs in order to achieve comparable beam sizes during the isotope analyses of all samples and the standards.

Measured Nd isotope compositions were corrected for instrumental mass bias using a $^{146}Nd/^{144}Nd$ of 0.7219 and were normalised to the JNdi-1 standard with an accepted literature value for $^{143}Nd/^{144}Nd$ of 0.512115 (Tanaka et al., 2000). Samples with low concentrations (≤10 ng Nd) were measured in time-resolved mode. During time-resolved measurements, the complete sample is aspired to obtain as much Nd as possible. The internal reproducibilities were in the order of 2 to $9x10^{-6}$ ($1\sigma_{(sd)}$) for auto run measurements, and between $4x10^{-6}$ and $3x10^{-5}$ ($1\sigma_{(sd)}$) for time-resolved samples. External reproducibility was estimated by repeated measurements of the JNdi-1 standard and was always better than 34

ppm for normal auto-run sessions, and between 39 to 104 ppm for time-resolved sessions ($2\sigma_{(sd)}$).

Measured $^{87}Sr/^{86}Sr$ ratios were corrected for instrumental mass bias using $^{88}Sr/^{86}Sr = 8.3752$ and were normalised to the accepted value for NIST SRM987 of 0.710245. Internal reproducibilities were between 5 to $9x10^{-6}$ ($1\sigma_{(sd)}$). The $2\sigma_{(sd)}$ external reproducibility of repeated standard measurements was always better than 36 ppm ($2\sigma_{(sd)}$). Procedural Nd and Sr blanks for leachates and total dissolution of the detrital material were ≤83 pg and 2.1 ng, respectively, which is negligible compared to sample concentrations.

Table 2.7: Configuration of the detector cups for Nd isotope analyses and Sr isotope analyses on a Nu Plasma MC-ICPMS. Interfering masses are given in brackets.

Cup	H5	H4	H3	H2	H1	Ax	L1	L2	L3	L4
Mass (Nd)	^{150}Nd (^{150}Sm)	^{148}Nd (^{148}Sm)	^{147}Sm	^{146}Nd	^{145}Nd	^{144}Nd (^{144}Sm)	^{143}Nd	^{142}Nd (^{142}Ce)	^{140}Ce	^{138}Ba (^{138}Ce)
Sr (OPZ)	-	^{88}Sr	-	^{87}Sr	-	^{86}Sr	-	^{85}Rb	^{84}Sr	^{83}Kr
Mass (Sr)	-	^{88}Sr	-	^{87}Sr (^{87}Rb)	-	^{86}Sr (^{86}Kr)	-	^{85}Rb	^{84}Sr (^{84}Kr)	^{83}Kr

Chapter 3

Silicon Isotope Distribution in Waters and Surface Sediments of the Peruvian Coastal Upwelling

Abstract

We present the first systematic study of the dissolved silicon isotope composition in the water column ($\delta^{30}Si_{Si(OH)4}$) and in diatoms ($\delta^{30}Si_{diatom}$) from the underlying surface sediments in a coastal upwelling region. The surface waters upwelling on the shelf off Peru are mainly fed by southward flowing subsurface waters along the coast, which show a mean $\delta^{30}Si_{Si(OH)4}$ of +1.5‰. The concentration of dissolved silicic acid ($Si(OH)_4$) increases towards the south and with increasing water depth documenting intense remineralisation of particulate biogenic silica ($bSiO_2$) in the water column and in the surface sediments. Surface waters in the realm of intense upwelling between 10°S and 15°S are only weakly fractionated with respect to dissolved Si isotope composition ($\delta^{30}Si_{Si(OH)4}$=+1.7‰), whereas further north and south, where upwelling is less pronounced, surface waters are more strongly fractionated ($\delta^{30}Si_{Si(OH)4}$ up to +2.8‰) due to the higher utilisation of the smaller amounts of available $Si(OH)_4$. The estimated degree of $Si(OH)_4$ utilisation in the surface water along the shelf ranges between 51% and 93%.

The $\delta^{30}Si_{diatom}$ values of picked diatoms in the underlying sediments vary from +0.6‰ to +2.0‰, which is within the order of the expected fractionation between surface waters and diatoms. The fractionation signal produced during formation of the diatoms in the surface water is recorded by $\delta^{30}Si_{diatom}$ values in the underlying sediments. Consistent with the distribution in the surface waters

---

This chapter is going to be submitted to Geochimica et Cosmochimica Acta as:

Ehlert, C., P. Grasse, E. Mollier-Vogel, T. Böschen, J. Franz, G. F. de Souza, B. C. Reynolds, L. Stramma, & M. Frank. Silicon Isotope Distribution in Waters and Surface Sediments of the Peruvian Coastal Upwelling.

the diatoms have the lowest $\delta^{30}Si_{diatom}$ values in the main upwelling region. The silicon isotope compositions of bulk biogenic opal $bSiO_2$ ($\delta^{30}Si_{bSiO2}$) signatures from the same sediment samples are generally much lower than the $\delta^{30}Si_{diatom}$, indicating a significant contamination of the $bSiO_2$ with biogenic siliceous material other than diatoms, such as sponge spicules. This shift towards much lighter values by up to -1.3‰ for samples with low $bSiO_2$ concentrations potentially biases the interpretation of paleo-$\delta^{30}Si$ records and the reconstruction of past $Si(OH)_4$ utilisation in surface waters.

3.1 Introduction

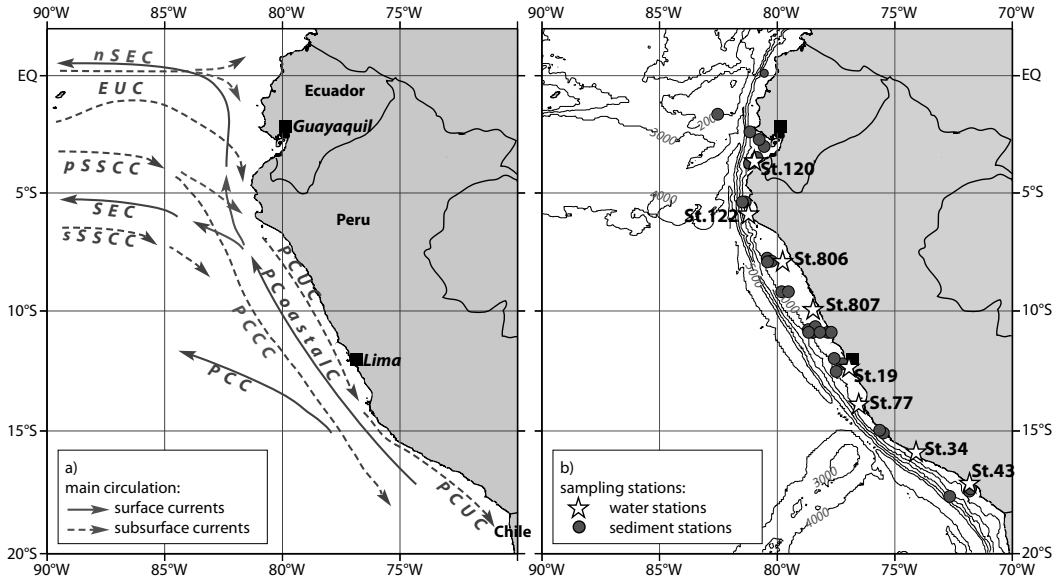

Figure 3.1: Maps showing the a) generalised circulation pathways of currents influencing the near-coastal areas (after Ayon et al., 2008; Kessler, 2006; Penven et al, 2005; and ADCP data according to Czeschel et al., 2011). Surface currents (solid line): SEC South Equatorial Current, nSEC northern South Equatorial Current, PCC Peru-Chile Current, PCoastalC Peru Coastal Current, subsurface currents (dashed line): EUC Equatorial Undercurrent, pSSCC and sSSCC primary and secondary Southern Subsurface Countercurrent, PCUC Peru-Chile Undercurrent, PCCC Peru Chile Countercurrent. b) Location of the CTD stations (white stars with station numbers) and surface sediment stations (grey dots). The bathymetry is given for 0 to 5000 m water depth in 1000 m increments.

The Peruvian coastal upwelling region is characterised by extremely high rates of primary productivity (Thiede and Suess, 1983; Berger et al., 1989; Pennington et al., 2006). Persistent easterly trade and alongshore winds produce offshore Ekman transport of surface water, which is replaced by upwelled, nutrient-rich subsurface waters. The main water mass supplying the Peruvian upwelling system are the southward flowing Peru-Chile Countercurrent (PCCC)

and the Peru-Chile Undercurrent (PCUC) (Brink et al., 1983), which prevails between 50 m and 150 m water depth (Huyer et al., 1987; Karstensen and Ulloa, 2008). These currents are fed by the eastward flowing high salinity and oxygen enriched waters of the Equatorial Undercurrent (EUC) (Lukas, 1986; Penven et al., 2005; Kessler, 2006) and the Southern Subsurface Countercurrent (SSCC), both originating from the central Pacific (Brink et al., 1983; Toggweiler et al., 1991) (Fig. 3.1a). Near the shelf, the northward flowing Peru Coastal Current (PCoastalC) shows usually a strong seasonality and is strong in September and October (Strub et al., 1998), while it was weaker and showed a strong subsurface component in January 2009 (Czeschel et al., 2011).

Upwelling intensity is generally high during most of the year (Strub et al., 1998; Gunther, 1936), which results in year-round high nutrient concentrations in the surface waters (Pennington et al., 2006) and very high primary productivity, generally dominated by diatoms (Estrada and Blasco 1985; Abrantes et al., 2007). The amount of primary productivity off Peru is so high that these decomposition processes cause one of the most pronounced Oxygen Minimum Zones (OMZs) of the world's ocean (e.g. Karstensen et al., 2008; Fuenzalida et al., 2009).

From reconstructions based on sedimentary records it has been inferred that most of the changes in bottom water oxygen levels under the coastal upwelling system off Peru have been related to changes in surface water productivity (e.g. DeVries and Schrader, 1981; Schrader, 1992; Rein et al., 2005). So far, it has proven difficult to disentangle the influences of changes in productivity from those caused by changes in circulation and upwelling intensity. The isotopic composition of stable silicon Si (expressed as $\delta^{30}Si$) is a powerful tool to investigate changes of silicic acid ($Si(OH)_4$) utilisation, as well as nutrient dynamics and productivity in the present and past ocean (De La Rocha et al., 1998, Brzezinski et al., 2002; Reynolds et al., 2008). Diatoms take up dissolved ($Si(OH)_4$) to form their opaline frustules (Tréguer et al., 1995), whereby Si isotopes are fractionated. The lighter isotopes are preferentially incorporated into the diatom frustules and leave the residual surface water enriched in the heavier isotopes (high $\delta^{30}Si$ values). The fractionation factor between seawater and diatoms is about -1.1‰ (De La Rocha et al., 1997; Milligan et al., 2004; Varela et al., 2004;

Reynolds et al., 2006; Beucher et al., 2008). In areas of strong upwelling the degree of utilisation and therefore the dissolved $\delta^{30}Si_{Si(OH)4}$ in the surface water is expected to be low due to continuous supply of large amounts of less fractionated $Si(OH)_4$ from subsurface waters. In contrast, in areas of weak upwelling the $Si(OH)_4$ in the surface waters will be almost completely utilised, which means that due to the degree of enrichment $\delta^{30}Si_{Si(OH)4}$ will correspondingly be very high. The $\delta^{30}Si_{Si(OH)4}$ distribution in surface waters therefore directly reflects $Si(OH)_4$ availability (Varela et al., 2004; Cardinal et al., 2005; Reynolds et al., 2006) and thus the amount of newly supplied nutrients with upwelled waters. Changes in $Si(OH)_4$ utilisation by diatoms due to changes in $Si(OH)_4$ supply and upwelling intensity are therefore expected to be reflected by the Si isotope composition of surface water ($\delta^{30}Si_{Si(OH)4}$) and that of the diatoms growing in them ($\delta^{30}Si_{bSiO2}$ for bulk biogenic silica ($bSiO_2$) material and $\delta^{30}Si_{diatom}$ for hand-picked diatoms).

A large fraction of the diatom $bSiO_2$ produced in surface waters re-dissolves in the upper water column because seawater is undersaturated with respect to silicate. On average only about 3% of the $bSiO_2$ produced is ultimately deposited and preserved in the sediment (Tréguer et al., 1995). These remineralisation processes are, however, highly variable and depend on the marine setting. In oligotrophic open ocean gyres 50-100% of the $bSiO_2$ produced in the surface water redissolves in the upper 100m of the water column, whereas in coastal diatom bloom areas preservation rates can be much higher (Nelson and Goering, 1977; Nelson et al., 1995). The dissolution of $bSiO_2$ is strongly influenced by physical parameters, such as temperature and pH (Lewin, 1961), and bacterial activity can lead to higher dissolution rates (Bidle and Azam, 1999; Bidle et al., 2002). A consistent fractionation of Si isotopes during dissolution of $bSiO_2$ of -0.55‰ has been reported (Demarest et al., 2009), which leaves partially-dissolved diatoms with a higher than initial $\delta^{30}Si$. Ignoring this fractionation effect may result in an overestimation of the level of past $Si(OH)_4$ utilisation in surface waters and an underestimating of the calculated fractionation factor.

In this study, we present new water column profiles of the Si isotope composition of dissolved $Si(OH)_4$ for eight shallow water stations together with isotopic analyses of diatoms extracted from the underlying surface sediments

along the Peruvian shelf between the equator and 17.5°S, which covers the major gradients of coastal upwelling intensity. The main goal of this study is to determine the factors controlling the $\delta^{30}Si$ of dissolved $Si(OH)_4$ in the surface waters and how these signatures are recorded by the corresponding sedimentary diatoms as a function of upwelling intensity and diatom productivity. The influence of $Si(OH)_4$ utilisation versus effects of water mass mixing is evaluated including the influence of remineralisation processes on the $\delta^{30}Si_{Si(OH)4}$ distribution, which will serve as a basis for the reliable use of the $\delta^{30}Si_{diatom}$ as a proxy for past upwelling conditions.

3.2 Material and Methods

All samples were collected during cruises M77/1 to 4 with the German RV Meteor between October 2008 and February 2009 in the frame of Collaborative Research Centre (SFB) 754: Climate - Biogeochemistry Interactions in the Tropical Ocean. All sampling stations are located on the Ecuadorian and Peruvian shelf between the equator and 17.5°S (Fig. 3.1b, Table A.1 and A.2).

The water samples for the whole water column, including bottom water, were collected using a rosette with 24 Niskin bottles (10 L each) equipped with a SeaBird CTD. Subsamples for $Si(OH)_4$ concentration measurements were frozen onboard immediately after sampling to be measured at the Max-Planck Institute (MPI) for Marine Microbiology in Bremen, Germany. $Si(OH)_4$ concentrations of frozen samples were compared to selected filtered and acidified (non frozen) seawater samples. Reproducibility between both was within 5 to 10% (no systematic variations). Oxygen concentrations were determined with the O_2-sensor of the CTD and were later calibrated with bottle data obtained by Winkler titration (Winkler, 1888). $BSiO_2$ in the water column was sampled by filtration through nitrocellulose acetate filters (0.65 µm pore size) at low vacuum pressure (< 200 mbar) on-board and was stored frozen at -20°C. For analysis, the filters with the samples were treated with 25 ml NaOH (0.1 M) in Nalgene bottles and were shaken in a water bath at 85°C for 2h 15 min. After cooling, analysis of the samples was conducted according to the method for determination of inorganic silicate by Hansen and Koroleff (1999).

Seawater samples for $\delta^{30}Si_{SiOH4}$ analysis (500 to 2000 ml) were immediately filtered on board through nitrocellulose acetate filters (0.45 µm pore size), acidified to pH 2 with concentrated Teflon-distilled HCl (1 mL HCl per litre of seawater), and stored in acid cleaned polyethylene bottles. In the clean laboratory of IFM-GEOMAR Si was separated from the water samples using a brucite-coprecipitation method (following Reynolds et al. (2006), after Karl and Tien (1992)). Given that incomplete precipitation would lead to isotopic fractionation of the Si in the sample, recovery was checked for every sample, and only those with >97% yield were used for isotopic measurements. Depending on the $Si(OH)_4$ concentration of the samples, 10 to 300 mL of previously neutralized seawater was precipitated at pH 10 by adding 1M NaOH (10 µl/ml). The precipitate was dissolved in 6M HCl resulting in a pH of 2-3. Water samples with concentrations of less than 4 µmol/kg $Si(OH)_4$ were preconcentrated through additional precipitation steps applying the same method to ensure that at least 43 nmol Si were processed through ion-exchange chromatography.

The sediment samples were collected using a multicorer. For this study only the uppermost centimetre of each core was used. The content of $bSiO_2$ was measured following DeMaster (1981) and Müller and Schneider (1993). The extraction of diatoms from the sediment samples for Si isotope analyses followed the procedure by Morley et al. (2004). Approximately 300 µg of freeze-dried sediment was treated with concentrated H_2O_2 and HCl to remove organic matter and carbonates and was then wet sieved to extract the 11-32 µm fraction. $BSiO_2$ was separated from detrital material in multiple steps using a sodium polytungstate solution with a density of 2.1-2.2 g/mL. For dissolution of the diatom frustules the method of Reynolds et al. (2008) was applied and extended by an additional step for oxidation of organic matter. For this purpose, 200 µL concentrated H_2O_2 (suprapure) was added to each sample, which was then dried and redissolved in 0.1 M NaOH. Tests demonstrated that this step does not affect the Si isotope results but significantly increases the stability of the beam during mass spectrometry and improves the reproducibility of the measurements. The Si concentrations in both seawater and diatom samples were measured colorimetrically using a photospectrometer (Hansen and Koroleff, 1999). Al/Si and

Ti/Si ratios were measured in aliquots of the dissolved $bSiO_2$ samples prepared for Si isotope analyses using an *Agillent 7500 Series* quadrupole ICPMS at IFM-GEOMAR in Kiel to check for potential contamination by clays (Table A.2).

From selected samples large diatoms were hand-picked to obtain a pure diatom $\delta^{30}Si_{diatom}$ value not influenced by other potentially present $bSiO_2$ phases. These samples were wet sieved through a 63 µm sieve, dried and sieved into different size fractions. Between 100 and 200 individual diatom specimens (non species-specific) were hand-picked from the 125-250 µm fraction, which resulted in concentrations of about 100 to 150 µmol/kg Si after dissolution in 2.5 ml of solution performed with the same method as for the bulk $bSiO_2$.

For Si isotope measurements, all samples were chromatographically purified following the method described by Georg et al. (2006b). Si isotope ratios were measured on a *NuPlasma HR* MC-ICPMS (Nu Instruments) at IFM-GEOMAR, which is equipped with an adjustable source-defining slit set to medium resolution to ensure peak separation of the ^{30}Si peak and molecular interferences. Measurements were carried out with a standard-sample bracketing method (Albarède et al., 2004). All solutions were measured at a Si concentration of 14-21 µmol/kg depending on the performance of the instrument and were introduced into the plasma via a Cetac Aridus II desolvator equipped with a PFA nebulizer at a 60 to 80 µL/min uptake rate. Si isotope compositions are reported in the $\delta^{30}Si$ notation of deviations of the measured $^{30}Si/^{28}Si$ from the international Si standard NBS28 in parts per thousand (‰) (Chapter 1). Repeated measurements of the reference materials IRMM018 and Big Batch gave average $\delta^{30}Si$ values of -1.55 ± 0.28‰ ($2\sigma_{sd}$, n = 38) and -10.80 ± 0.22‰ ($2\sigma_{sd}$, n = 38), respectively, which are in good agreement with values obtained by other laboratories (Reynolds et al., 2007). Samples were measured three to five times within one run, which generally resulted in uncertainties between 0.07 and 0.40‰ ($2\sigma_{sd}$), with one sample having a $2\sigma_{sd}$ of 0.48‰ (Table A.1 and A.2). Replicate measurements of in-house matrix standards for both seawater and diatom samples over longer periods of time gave a reproducibility of 0.25‰ ($2\sigma_{sd}$), which corresponds to all error bars of the Si isotope compositions in the figures.

3.3 Results

3.3.1 Water Stations

3.3.1.1 Subsurface and Bottom Waters

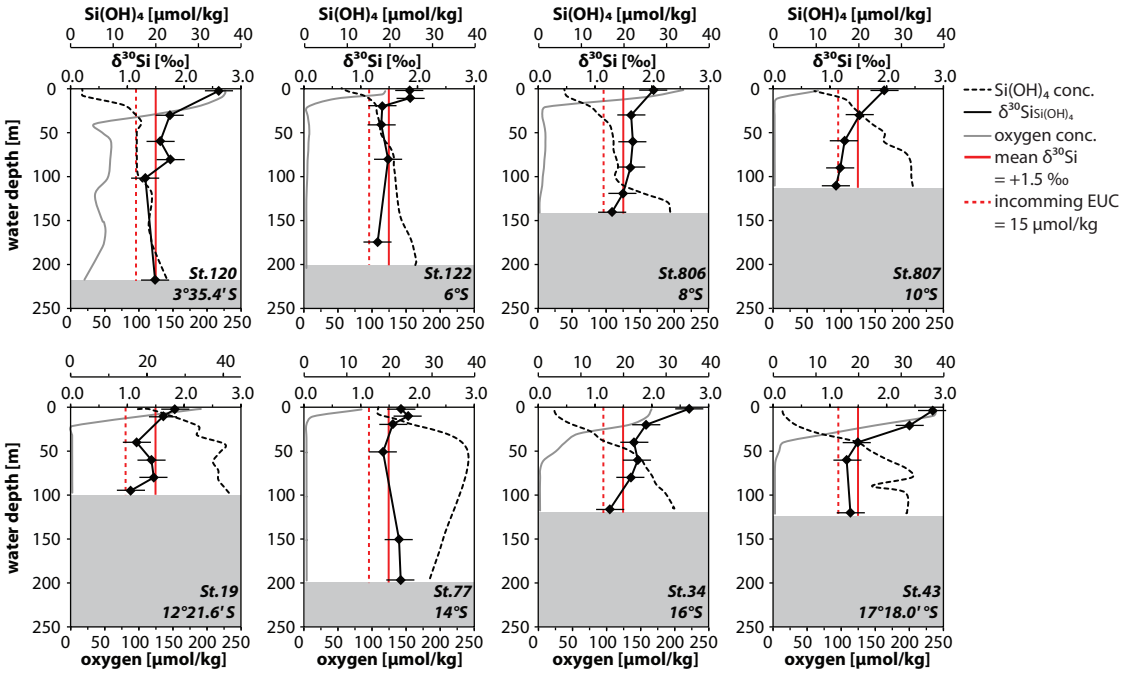

Figure 3.2: Water column profiles for 8 stations along the Ecuadorian and Peruvian shelf from north (top, left) to south (bottom, right) (see Fig. 3.1). The grey shading indicates the bottom. For all stations the $\delta^{30}Si_{Si(OH)4}$ (‰, solid black line) and the $Si(OH)_4$ concentrations (µmol/kg, dashed black line) are shown. The grey solid line indicates the dissolved oxygen concentration (µmol/kg). The solid and dashed red lines mark the mean subsurface $\delta^{30}Si_{Si(OH)4}$ of +1.5‰ (50-150 m water depth of all 8 stations) and the $Si(OH)_4$ concentration of ~15 µmol/kg of the incoming EUC. Please note the slightly different scale for $Si(OH)_4$ concentration for St. 19. Error bars represent 0.25‰ $2\sigma_{sd}$ long-term reproducibility of repeated sample measurements.

The water column profiles (Fig. 3.2, Table A.1) show a general increase in $Si(OH)_4$ concentrations with water depth. Only at St. 77 the highest concentration (40 µmol/kg) was found at 50 m depth and then decreased again to 30 µmol/kg near the bottom of the profile. The subsurface waters (50 m to 150 m water depth) flow southward along the shelf. In the northernmost St. 120, the concentration is influenced by the incoming EUC, which has a $Si(OH)_4$ concentration of 15 µmol/kg (red dashed line in Fig. 3.2). Towards the south the $Si(OH)_4$ concentration in this water depth range increases. The highest subsurface $Si(OH)_4$ concentrations are found at St. 19 and St. 77 between 12°S and 14°S (~40 µmol/kg). Further to the south concentrations decrease again (~30 µmol/kg). The $\delta^{30}Si_{Si(OH)4}$ of all water column profiles mirrors the $Si(OH)_4$ concentrations in that it decreases with

increasing water depth and $Si(OH)_4$ concentration. The mean $\delta^{30}Si_{Si(OH)4}$ between 50 m and 150 m water depth, which corresponds to the source depth of the upwelling, is +1.5 ± 0.2‰ ($1\sigma_{sd}$) (marked by the red solid line in Fig. 3.2). At most of the stations the deepest samples represent bottom waters and their $\delta^{30}Si_{Si(OH)4}$ was also found to be near +1.5‰. Only at St. 807 and St. 19 between 10 and 12°S the isotopic composition of the bottom waters is somewhat lower with values of +1.1‰.

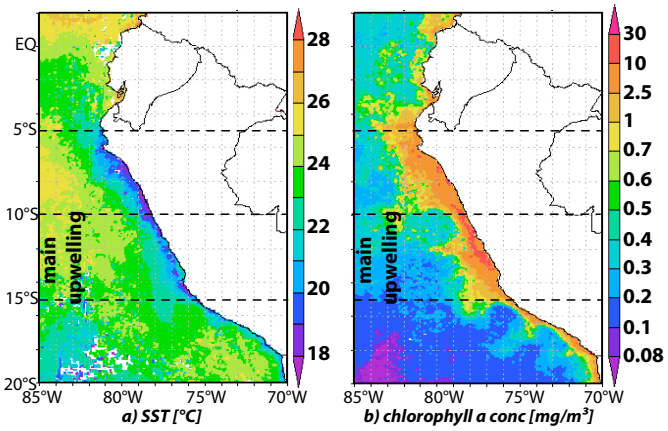

Figure 3.3: Distribution of a) surface water temperature SST (°C) and b) chlorophyll a concentration (mg/m³) to indicate the area of the strongest upwelling intensity (lowest SST and highest chlorophyll concentration). Data were available from NASA Giovanni (http://disc.sci.gsfc.nasa.gov/giovanni/overview/index.html).

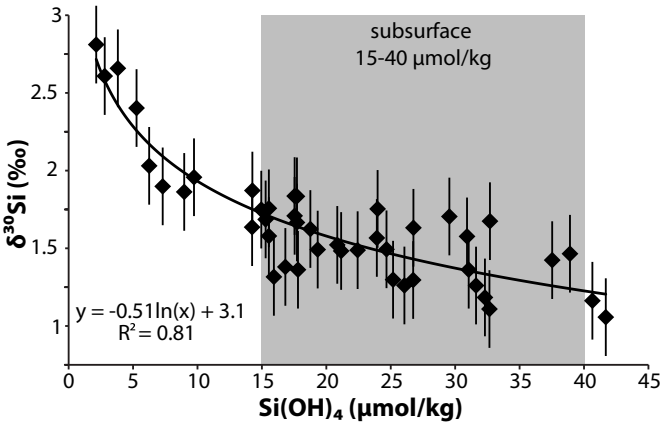

Figure 3.4: Correlation between dissolved $\delta^{30}Si_{Si(OH)4}$ (‰) and $Si(OH)_4$ concentrations (µmol/kg) for all seawater samples. The grey bar indicates the range of subsurface water $Si(OH)_4$ concentrations (50-150m water depth) between 15-40 µmol/kg. Error bars represent 0.25‰ $2\sigma_{(sd)}$ long-term reproducibility of repeated sample measurements.

3.3.1.2 Surface Waters

In the surface waters the concentration of $Si(OH)_4$ varies widely with latitude and upwelling intensity. The highest concentrations of $Si(OH)_4$ (17.72 µmol/kg, Fig. 3.2, Table A.1) are found close to the coast between 10° to 15°S, where the upwelling is most intense as evidenced by very low sea surface temperatures (SSTs) (Fig. 3.3a). To the north and south of this, the concentrations of $Si(OH)_4$ are lower at minimum values of 2.14 µmol/kg. The surface waters show

higher $\delta^{30}Si_{Si(OH)4}$ values than the subsurface waters in all profiles, ranging from +1.7‰ to +2.8‰ (Fig. 3.2). The highest $\delta^{30}Si_{Si(OH)4}$ values between +2.6‰ and +2.8‰ were found at the northernmost station (St. 120, 4°S) and at the stations south of 15°S (St. 34, St. 43). Low $\delta^{30}Si_{Si(OH)4}$ in surface waters ranging between +1.7‰ and +2.0‰ were found along the shelf at St. 122, 806, 807, 19 and St. 77 (between 6°S to 15°S), with the latter showing the minimum value. The $\delta^{30}Si_{Si(OH)4}$ values of the surface waters show a clear negative correlation with $Si(OH)_4$ contents (Fig. 3.4, see Table A.1). Subsurface water $\delta^{30}Si_{Si(OH)4}$ and $Si(OH)_4$ (marked with the grey shading in Fig. 3.4) show a larger scatter than surface water values.

3.3.2 Surface Sediments

The distribution of $bSiO_2$ concentrations in the surface sediment reflects primary productivity in the surface waters (Fig. 3.3b and 3.5b). The highest concentrations of up to 21 wt% are found close to the coast between 10 and 15°S. North and south of this area the fraction of $bSiO_2$ in the shelf sediments is much lower and reaches values as low as 0.24 wt% at 3°S. The $\delta^{30}Si_{bSiO2}$ values range between -1.0‰ and +1.1‰, with the highest values found at 15°S (Fig. 3.5a, Table A.2). Along the shelf between 5° and 10°S where the upwelling is weaker and $bSiO_2$ concentrations are lower the values range between +0.3‰ and +0.8‰. Samples (n = 2) from the Gulf of Guayaquil display even lower $\delta^{30}Si_{bSiO2}$ ratios (-0.1‰). The $\delta^{30}Si_{diatom}$ values of the hand-picked diatoms are generally significantly higher than those of the $bSiO_2$ in the same samples with $\delta^{30}Si_{diatom}$ ranging between +0.6‰ to +2.0‰ (Fig. 3.5a, Table A.2). Al/Si and Ti/Si ratios of $bSiO_2$-samples range between 1 to 235 mmol/mol and 31 to 125 µmol/mol (Table A.2).

3.4 Discussion

3.4.1 Silicon Isotope Distribution in the Water Column

3.4.1.1 Subsurface and Bottom Waters

Upwelling along the Peruvian shelf occurs from the subsurface waters of the PCUC and the PCCC (Fig. 3.1), which mainly originate from the EUC and SSCC (Brink et al., 1983; Penven et al., 2005; Kessler; 2006). During January and February 2009, when the samples were taken, the PCUC was clearly detectable

with ADCP along the shelf between 50 m to 150 m water depth at 6°S. At 14°S the southward directed PCCC joined the PCUC and they were no longer distinguishable (Czeschel et al., 2011). Subsurface waters between 50 m and 150 m, reflecting the main source for the upwelling (Huyer et al., 1987; Karstensen and Ulloa, 2008; Czeschel et al., 2011) are characterized by a mean $\delta^{30}Si_{Si(OH)4}$ signature of +1.5 ± 0.2 ($1\sigma_{(sd)}$, Fig. 3.2). The incoming $Si(OH)_4$ concentration at the northerly stations lies around 15 µmol/kg (Fig. 3.2). The $Si(OH)_4$ concentrations within the subsurface waters do increase significantly from 15 to 40 µmol/kg along the southward flowpath, which indicates extensive remineralisation processes occurring both in the water column and most likely also from the shelf sediments. Settling diatoms are (partially) dissolved in the water column, and after sedimentation further dissolution is promoted, by physical parameters (temperature, pressure) and biological activity (Nelson et al., 1995; Dugdale and Wilkerson, 1998). Bacterial activity can also enhance dissolution rates by degrading the organic matrix that protects the diatom frustules (Bidle and Azam, 1999; Bidle et al., 2002). Dissolution of $bSiO_2$ is expected to lead to lower $\delta^{30}Si_{Si(OH)4}$ values in the water column (Demarest et al., 2009). However, it is only in some bottom water samples close to the sediment-water interface (St. 807, 19) where direct indications for dissolution are found ($\delta^{30}Si_{Si(OH)4}$ shows a slight shift to values as low as +1.1‰, Fig. 3.2). A possible explanation for the relatively uniform $\delta^{30}Si_{Si(OH)4}$ of the subsurface waters are efficient vertical water mass mixing due to upwelling, but also horizontal mixing processes and eddy formation, which all together reduce any possible latitudinal effects of remineralisation. Fig. 3.4 shows that the subsurface waters (characterised by $Si(OH)_4$ concentrations between 15 to 40 µmol/kg) display a much larger scatter than the surface waters, which is an indicator for water mass mixing processes but also dissolution of $bSiO_2$. Upwelled water masses near the coast are transported offshore and downwelled further west. These water masses are mixed again with central Pacific water masses and would thus transport subsurface waters with higher $\delta^{30}Si_{Si(OH)4}$ values back to the shelf. Therefore, a continuous supply of waters with higher $\delta^{30}Si_{Si(OH)4}$ signatures would be mixed with the lower $\delta^{30}Si_{Si(OH)4}$ of the source waters of the upwelling. This would lead to higher $\delta^{30}Si_{Si(OH)4}$ than expected from

the southward increasing $Si(OH)_4$ concentrations. In addition, south of 14°S the influence of the PCoastalC is detectable by lower $Si(OH)_4$ concentrations. According to ADCP data of Czeschel et al. (2011) this current flows northward close to the shelf at approximately 50 m to 100 m depth and can thus also influence the isotope signal of the subsurface source waters of the upwelling given that it is derived from subsurface waters of southern origin. North of 14°S the PCoastalC is subducted to a depth of approximately 200 m and therefore does not influence the upwelling source waters any more.

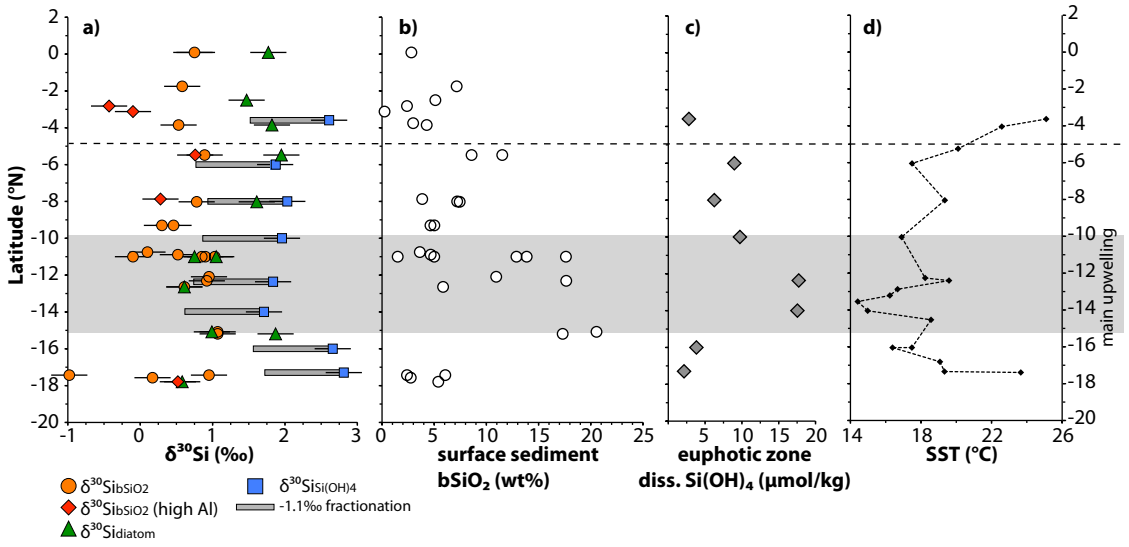

Figure 3.5: Latitudinal distribution of a) $\delta^{30}Si$ (‰) (orange circles: $bSiO_2$ samples, red diamonds: $bSiO_2$ samples with high Al/Si ratios, green triangles: picked diatoms, blue squares: surface water samples), the horizontal grey bars mark the -1.1‰ for fractionation between water and diatoms, error bars represent 0.25‰ $2\sigma_{(sd)}$ long-term reproducibility of repeated sample measurements, b) surface sediment $bSiO_2$ concentration (wt%), c) surface water $Si(OH)_4$ concentrations (µmol/kg), e) surface water temperature for all shelf stations (°C). The horizontal black dashed line and grey shading indicates the same latitudinal areas as in Fig. 3.3.

3.4.1.2 Surface Waters

The surface waters along the Peruvian shelf can be separated into different latitudinal regions due to their different physical (SSTs) and biological (chlorophyll a concentration) properties (Fig. 3.3). The high chlorophyll a concentrations are derived from diatom blooms (Bruland et al., 2005), which imply that primary productivity is driven by diatoms. $Si(OH)_4$ concentrations in surface waters of the coastal upwelling area off Peru are high where strong upwelling promotes continuous supply of deeper waters feeding the surface water pool. Conversely,

they are lower in those areas where the delivery through upwelling is not as strong and primary productivity utilises the nutrients in the surface water more completely. The $\delta^{30}Si_{Si(OH)4}$ difference between the subsurface source waters and the surface waters above, which reflects the utilisation of $Si(OH)_4$, amounts to only about 0.3‰ within the main upwelling zone between 10°S and 15°S (Fig. 3.2). Along the northern part of the shelf between 3°S to 8°S the difference is about 0.6‰, and reaches up to 1.2‰ south of 15°S, where upwelling is far less intense (higher SSTs in Fig. 3.3a and 3.5d). The surface water $\delta^{30}Si_{Si(OH)4}$ values directly reflect the availability of $Si(OH)_4$ in the euphotic zone (Fig. 3.5a, c). Higher $Si(OH)_4$ concentrations in the surface water are associated with higher primary productivity (as indicated by the surface water chlorophyll a concentration, Fig. 3.5c and 3.3b) (Bruland et al., 2005), but lower $\delta^{30}Si_{Si(OH)4}$ values (Fig. 3.5a). So, in the surface waters outside of the upwelling region there is a higher degree of utilisation of $Si(OH)_4$ due to phytoplankton productivity, but at the same time $bSiO_2$ productivity is lower (Fig. 3.5a, c). Even within the main upwelling region, nearly continuous re-supply $Si(OH)_4$ to the surface cannot prevent at least a slight Si isotope fractionation of the $Si(OH)_4$ in the surface waters. However, even the maximum difference between surface and deep Si isotope composition of 1.2‰ is still low compared with areas of highly depleted surface $Si(OH)_4$ concentrations, such as in open ocean gyres (Reynolds et al., 2006).

3.4.1.3 Silicon Isotope Fractionation Models

The Si isotope fractionation factor for the formation of diatom silica from seawater assessed by culture experiments is -1.1‰ in $\delta^{30}Si$ (De La Rocha et al., 1997). Two different models can describe the evolution of the $\delta^{30}Si$ composition of surface waters during biologically induced fractionation: a steady-state model, wherein a continuous supply of nutrients causes a dynamic equilibrium of the $Si(OH)_4$ content, and a Rayleigh-type model, in which no additional nutrients are newly supplied to the system (De La Rocha et al., 1997; Cardinal et al., 2005; Reynolds et al., 2006). The two models can be described and approximated by simple equations (see Chapter 1.4.2):

Steady-state system:

$$\delta^{30}Si_{Si(OH)_4\ obs} = \delta^{30}Si_{Si(OH)_4\ init} - \varepsilon * (1 - f)$$

$$f = Si(OH)_{4\,obs} / Si(OH)_{4\,init}$$

Under assumed steady state conditions the effective net $bSiO_2$ production (e.g. during one year) is equal to the net $Si(OH)_4$ supply (Fripiat et al., 2011a).

Rayleigh-type system:

$$\delta^{30}Si_{Si(OH)_4\ obs} = \delta^{30}Si_{Si(OH)_4\ init} + \varepsilon * (\ln f)$$

$$\delta^{30}Si_{diatom_{inst}} = \delta^{30}Si_{Si(OH)_4\ obs} + \varepsilon$$

$$\delta^{30}Si_{diatom_{acc}} = \delta^{30}Si_{Si(OH)_4\ init} - \varepsilon * (f \ln f / 1 - f)$$

where $\delta^{30}Si_{Si(OH)4\ init}$ is the Si isotope composition of $Si(OH)_4$ in the surface water before biological utilisation starts to fractionate the Si isotopes, $\delta^{30}Si_{Si(OH)4\ obs}$ is the Si isotope composition measured in the surface water, *f* is the depletion factor describing the fraction of the initial $Si(OH)_4$ concentration that remains, ε is the fractionation factor between the $Si(OH)_4$ and the diatoms produced, $\delta^{30}Si_{diatom\ inst}$ is the Si isotope composition of the instantaneously produced diatoms at each time and $\delta^{30}Si_{diatom\ acc}$ is the silicon isotope composition of the diatoms which accumulated and integrate over time. Both models assume a constant fractionation factor. The value of ε is given by the slope of the linear regression between $\delta^{30}Si_{Si(OH)4\ obs}$ and *f* for the steady-state model, and between $\delta^{30}Si_{Si(OH)4\ obs}$ and ln*f* for the Rayleigh-type system model (Fig. 3.6).

Due to the fact, that upwelling is supplied from the subsurface waters, the tightly defined mean $Si(OH)_4$ concentration for the depth between 50 m to 150 m, or bottom water where water depth is less than this, is employed as initial concentration of the upwelling source waters at each station (Huyer et al., 1987; Karstensen and Ulloa, 2008) (Table A.1). These waters show a relatively uniform $\delta^{30}Si$ of +1.5‰, which was defined as the source water signature (Fig. 3.6). Both models were applied for the $\delta^{30}Si_{Si(OH)4}$ from the euphotic zone (defined by the oxycline, which mostly fits also well with the nutricline for $Si(OH)_4$, Fig. 3.2, 3.6a, c) as well as for surface water samples only (Fig. 3.6b, d). The fractionation factors calculated from our data range between -2.7‰ (steady-state, surface water only) and -0.5‰ (Rayleigh, euphotic zone data) (Fig. 3.6), and thus deviate from the experimentally determined fractionation factor of -1.1‰ (De La Rocha et al.,

1997). Applying the steady state model for all measured $\delta^{30}Si_{Si(OH)4}$ from the euphotic zone results in a calculated fractionation factor of -1.3‰, which is very

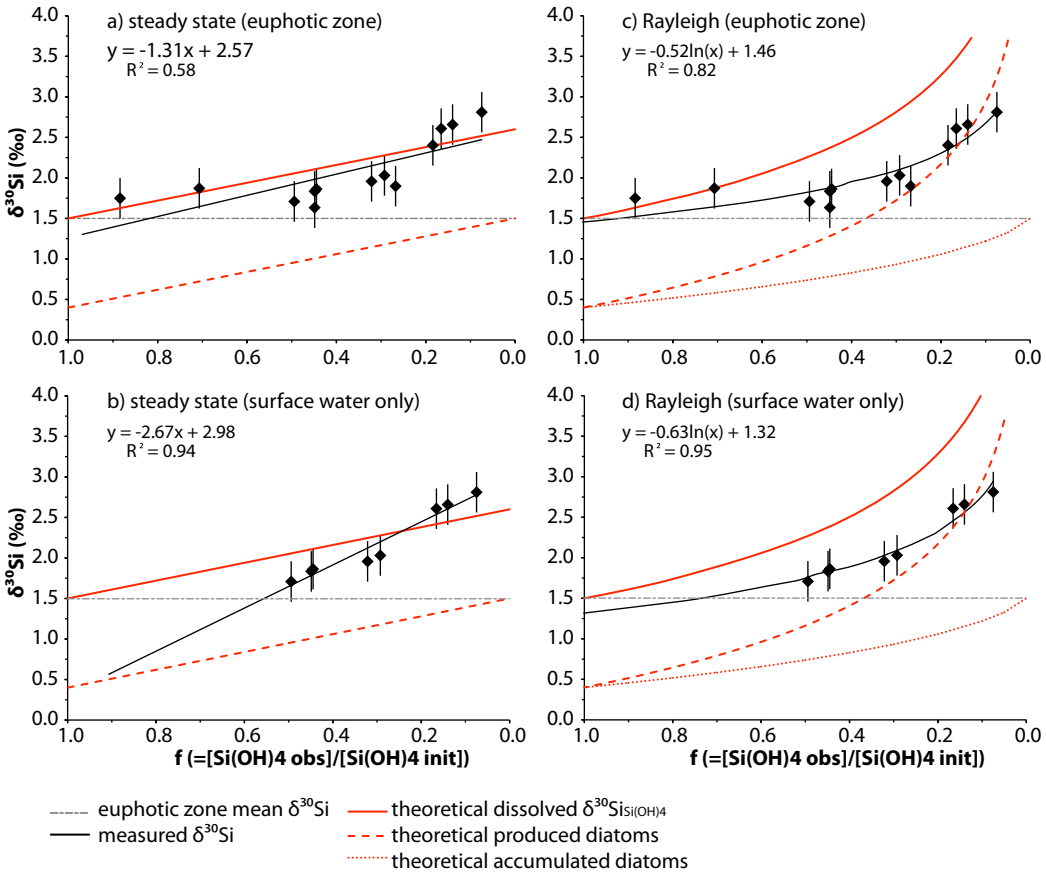

Figure 3.6: $\delta^{30}Si_{Si(OH)4}$ (‰) versus f (remaining $Si(OH)_4$ from the available pool) indicating the fractionation factor for steady state-type (a, b) and Rayleigh-type conditions (c, d, using a logarithmic function) (black curves). The bold red lines in the graphs indicate the fractionation curve of $Si(OH)_4$ for a -1.1‰ fractionation, assuming an initial value of 1.5‰ (grey dashed line), whereas the dashed red line indicates the expected fractionation curve for the produced diatoms as a result of a -1.1‰ fractionation, and the red dotted line indicates the accumulated diatoms under Rayleigh-type conditions. Error bars represent 0.25‰ $2\sigma_{sd}$ long-term reproducibility of repeated sample measurements.

close to the experimentally derived from De La Rocha et al. (1997). Using all data from the euphotic zone, however, usually results in an underestimation of the fractionation factor due to dissolution of the diatoms (Beucher et al., 2011; Demarest et al., 2011). During dissolution the lighter isotopes are released to the surrounding seawater, which leads to lowers $\delta^{30}Si_{Si(OH)4}$ values and an increase in $Si(OH)_4$ concentration, and consequently to lower calculated utilisation rates. Also, the discrepancies in the calculated fractionation factors are not surprising and arise from the fact that the estimation of the fractionation factor is easily biased by

extensive mixing (Reynolds et al., 2006; Fripiat et al., 2011b). The steady-state model fits the water data much better. This is a reasonable result for an upwelling area, which is not expected to be a Rayleigh-type system due to the continuous re-supply of upwelled nutrients. The calculated utilisation (for steady state conditions) of available $Si(OH)_4$ in surface waters on the shelf ranges from about 51% in the main upwelling region to up to 93% further south (utilisation [%] = (1-*f*)*100).

3.4.2 Surface Sediments

The distribution of $bSiO_2$ in surface sediments and surface waters agrees quite well in that the highest concentrations are found at those locations where the upwelling is most intense (Fig. 3.5b). This is also where the $\delta^{30}Si_{Si(OH)4}$ of the surface water indicates the weakest fractionation (Fig. 3.5a). Correspondingly, diatoms deposited in the underlying surface sediments should also have the lowest $\delta^{30}Si$ ratios between 10°S to 15°S. In fact, off Peru, the $\delta^{30}Si_{bSiO2}$ values show no distinct variability (Fig. 3.5), and are mostly isotopically to low when compared to the $\delta^{30}Si_{Si(OH)4}$. Overall, the highest values are found in the area of the strongest upwelling. The concentration of $bSiO_2$ and $\delta^{30}Si_{bSiO2}$ show together a positive trend (Fig. 3.7), which is opposite to the expected correlation in an upwelling area: high $bSiO_2$ concentrations are expected to prevail where the highest delivery of nutrients occurs and where correspondingly only weak Si isotope fractionation occurs. This discrepancy cannot be explained by fractionation processes.

Instead, the measured $\delta^{30}Si_{bSiO2}$ may not reflect diatoms alone but may be a mixture of silicate from different sources. The most obvious would be a contamination with clay. If the cleaning process was not sufficient, remaining and (partially) dissolved clays in the sample solution would shift the measured $\delta^{30}Si_{bSiO2}$ towards lighter values (Ding et al., 1996; De La Rocha et al., 2000; Georg et al., 2009). Therefore, Al/Si and Ti/Si ratios were measured for most of the samples in order to exclude significant contributions from such sources (Table A.2). The ratios range between 1 and 235 mmol/mol for Al/Si ratios and between 31 and 125 µmol/mol for Ti/Si ratios. Both elements are present as trace elements in diatom frustules (Ellwood and Hunter, 1999) but more importantly are major

elements in clay minerals at much higher concentrations (Al/Si ratios in clays is ~1). It is very difficult to demonstrate complete removal off all clays from the diatoms (Shemesh et al., 1988). If all contamination would arise from clay minerals, Ti and Al should be correlated with each other. However, the poor correlation between Al/Si and Ti/Si ratios (Fig. 3.8a) basically excludes a systematic contamination with clays. The Al content of living diatoms is generally less than 1% (Lewin, 1961; Shemesh et al., 1988; van Bennekom et al., 1989). The concentration of trace metals in the $bSiO_2$ depends on the concentration of the medium they grew from (Ellwood and Hunter, 1999), i.e. higher concentration in the seawater leads to higher concentration in the $bSiO_2$. Additionally, Al can be passively incorporated in $bSiO_2$ immediately after deposition at the sediment–water interface (van Cappellen and Qiu, 1997; Dixit et al., 2001, Ragueneau et al., 2005), leading to an enrichment of Al in the $bSiO_2$, which can alter the interpretation of trace metal measurements.

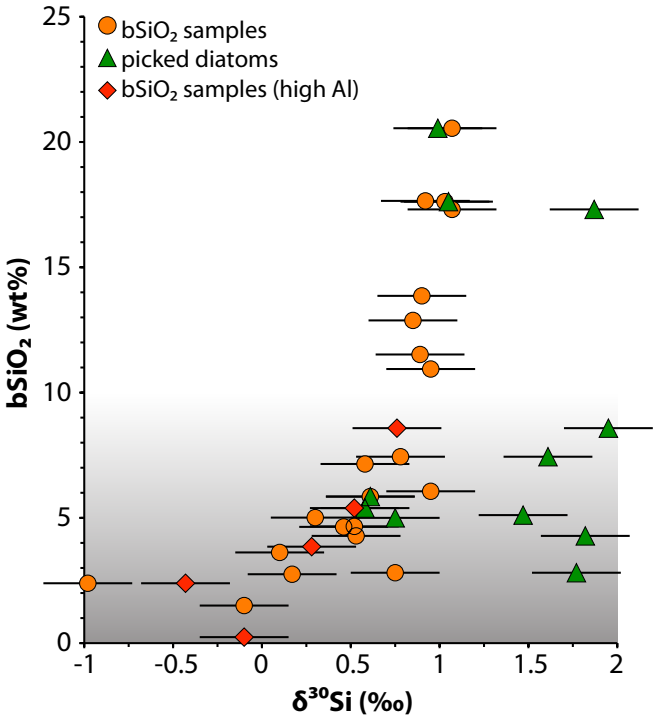

Figure 3.7: Correlation between $bSiO_2$ (wt.%) and $\delta^{30}Si$ (‰) of $bSiO_2$ (orange circles) and of hand-picked diatoms (green triangles) in the surface sediments. The red diamonds mark $bSiO_2$ samples, which have Al/Si ratios >50. The grey shading indicates samples with $bSiO_2$ concentration <10 wt%, which is assumed to be a critical with respect to possible contaminations. Error bars represent 0.25‰ $2\sigma_{sd}$ long-term reproducibility of repeated sample measurements.

Typically, the Al/Si ratio of diatoms in sediments should be between 25 and 50 mmol/mol (Hurd, 1973; van Bennekom et al., 1988), which is one order of magnitude lower than corresponding Al/Si ratios in silicate minerals (Ragueneau

et al., 2005). Of the checked $bSiO_2$ samples in this study, most had Al/Si ratios <50, usually much lower. Only five samples had a Al/Si ratio >50 (Fig. 3.8b). These are potentially contaminated with clay mineral-derived silicate, and the respective $\delta^{30}Si_{bSiO2}$ values are excluded from the further interpretation. However, there are several samples, which were considered to be clean (Al/Si <50) and which still revealed very low $\delta^{30}Si_{bSiO2}$ values (Fig. 3.5, 3.7, 3.8). Reason for this must be another contaminant source. For example, siliceous sponge spicules have very light isotope ratios of about -3‰ $\delta^{30}Si$ (Douthitt, 1982; De La Rocha, 2003; Hendry et al., 2010), and radiolarians can be isotopically light as well. A bias to more negative $\delta^{30}Si_{bSiO2}$ ratios due to a contamination with non diatom $bSiO_2$ is the most likely explanation for the overall too low $\delta^{30}Si_{bSiO2}$ values, which is supported by the fact that the highest offset from expected values occurs in those sediments containing the lowest amounts of $bSiO_2$, especially along the northern part of the shelf region (Fig. 3.5 and 3.7). A separation of diatoms from $bSiO_2$ of different origin is not possible with the applied heavy liquid separation method, and sponge spicules and diatoms do not show a difference in resistivity to dissolution processes during the preparation for Si isotope analyses.

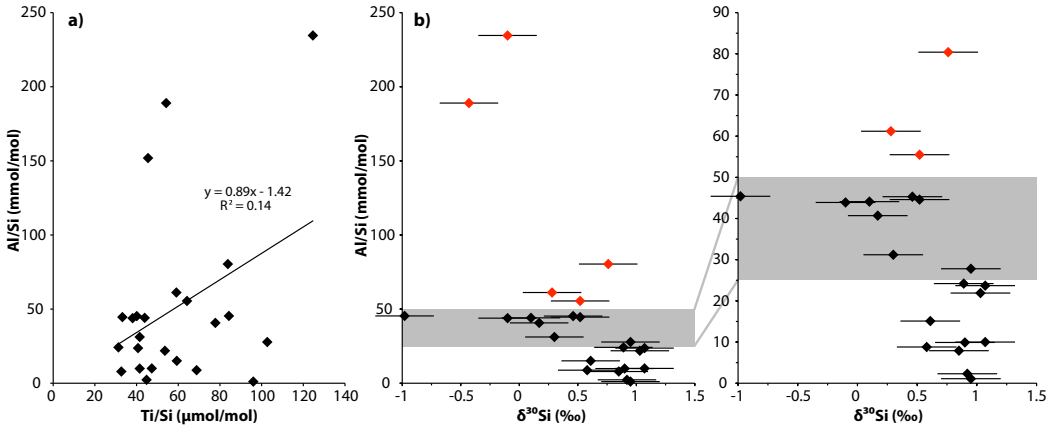

Figure 3.8: a) Ti/Si (µmol/mol) versus Al/Si (mmol/mol) ratios for $bSiO_2$ samples. (Not measured in picked diatoms) b) $\delta^{30}Si_{bSiO2}$ (‰) versus Al/Si ratios (mmol/mol). The grey shading indicates Al/Si ratios between 25 and 50 mmol/mol, samples with higher ratios (marked in red) are potentially contaminated with clay material.

In order to test the contamination hypothesis, large diatoms were hand-picked from the same sediment samples. As far as currently known, all diatoms fractionate $Si(OH)_4$ in the same way, independent of species, temperature (De La

Rocha et al., 1997) and salinity (Alleman et al., 2005). However, the picked diatom $\delta^{30}Si_{diatom}$ values are significantly different from bulk $\delta^{30}Si_{bSiO2}$ and range from +0.6‰ to +2.0‰ (Fig. 3.5, Table A.2). Different diatom assemblages might represent different times of upwelling season, and can therefore be influenced by different source water signatures. The $bSiO_2$-fraction probably consists mostly of specimens of *Chaetoceros* (resting spores) and *Thalassionema*, the two most abundant species along the Peruvian shelf (Abrantes et al., 2007), which are both indicative of strong upwelling conditions (Schrader and Sorknes, 1991; Abrantes et al., 2007). The large fraction probably mostly contained specimens of *Coscinodiscus*, large-centric diatoms which are especially abundant in tropical-oceanic (low-nutrient) waters or when upwelling is weaker (which would be an explanation for the higher $\delta^{30}Si_{diatom}$ values) (De Vries and Schrader, 1981; Brodie and Kemp, 1994). Sedimentation rates along the Peruvian shelf are highly variable. At 12°S, mostly characterized by strong upwelling it accounts for ca. 0.13 cm/yr (Munoz et al., 2004). On average, the first cm of the sediment, which is always used here, will probably integrate the utilisation signal over ca. 10 years/growing seasons. Within the main upwelling region between 10 to 15°S, where $bSiO_2$ concentrations are highest (Fig. 3.5b), $\delta^{30}Si_{bSiO2}$ and $\delta^{30}Si_{diatom}$ agree very well (Fig. 3.5a). Even if both assemblages reflect different growing seasons, the source water conditions in that area obviously do not change significantly throughout the whole year. Further to the north, especially north of 5°S, there is a general offset of up to 1.3‰ between both sedimentary phases (Fig. 3.5), and only the $\delta^{30}Si_{diatom}$ seem to reflect measured surface water $\delta^{30}Si_{Si(OH)4}$ (Fig. 3.5a). Here, $bSiO_2$ concentrations are lowest (Fig. 3.5b), and a potential contamination is most likely. The offset could, however, also be the reflection of the different growing conditions. For the samples north of 5°S having a mean $\delta^{30}Si_{bSiO2}$ of +0.6‰ this would indicate surface water $\delta^{30}Si_{Si(OH)4}$ of around +1.7‰ (assuming a fractionation between both phases of -1.1‰ (De La Rocha et al., 1997)). This is a very low signature comparable to the values measured in the main upwelling region, but the northerly region does not experience such strong upwelling and nutrient supply (Karstensen and Ulloa, 2008). Another interesting feature are the low $\delta^{30}Si$ values in both $bSiO_2$ and in the picked diatoms south of 15°S, which, except for one $bSiO_2$ sample, do not differ

significantly from a value of about +0.6‰. In contrast, the present day surface waters in that area have high $\delta^{30}Si_{Si(OH)4}$ values of about +2.7‰. South of 14°S the northward flowing PCoastalC may have had an influence on the $\delta^{30}Si_{diatom}$ and $\delta^{30}Si_{bSiO2}$ signatures. This current originates in the south, and is characterised by lower $Si(OH)_4$ concentrations. A lighter $\delta^{30}Si_{Si(OH)4}$ signature of this current is possible, although not clearly detectable in the water column (Fig. 3.2), but may have influenced the isotopic signature of the diatoms over a longer time scale. Furthermore, a transport of isotopically lighter diatoms within the PCoastalC is also a possible scenario.

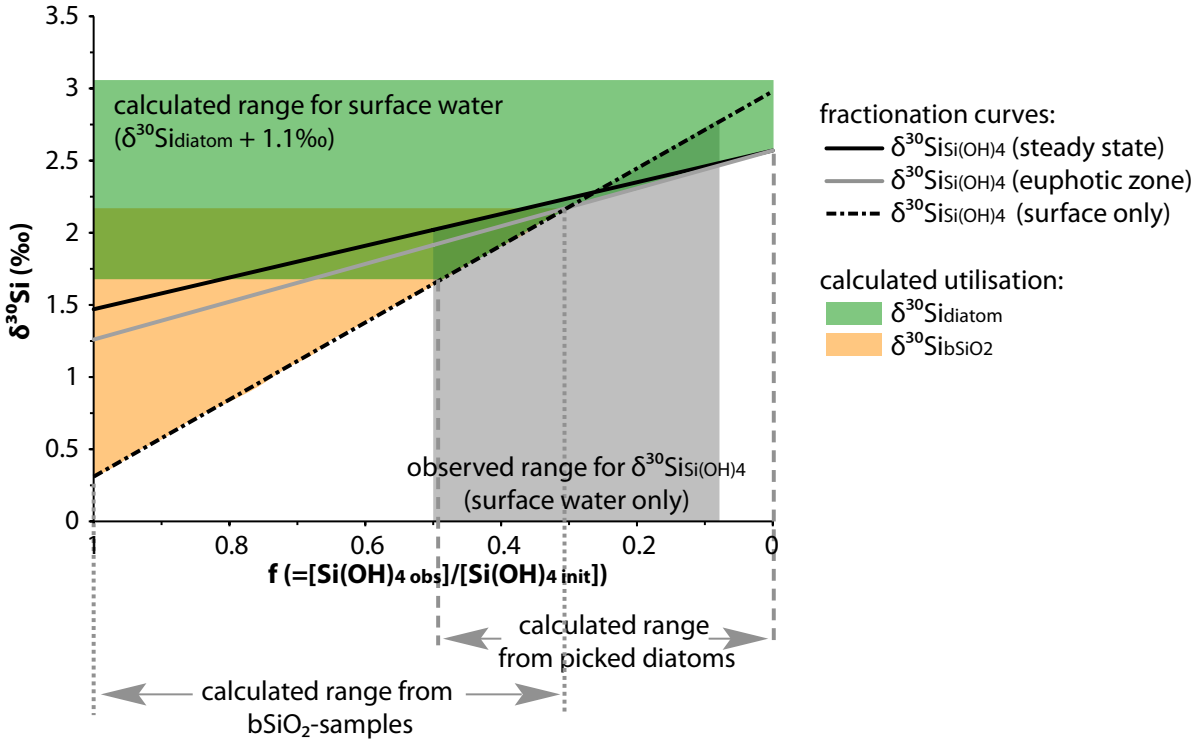

Figure 3.9: $\delta^{30}Si$ (‰) versus f. The curves indicate the fractionation behaviour for steady state-type conditions for surface water for a theoretical fractionation of -1.1‰ (solid black), where the dashed black curve and the solid grey curve indicate the fractionation behaviour for surface water samples only (fractionation factor -2.7‰) and for the euphotic zone (fractionation factor -1.3‰) from measurements in the euphotic zone (see Fig. 6a and b). The grey shading indicates the observed range of measurements in the surface water, whereas the green and orange shadings indicate the theoretical surface water conditions calculated from picked diatoms and $bSiO_2$ surface sediment samples (measured $\delta^{30}Si$ + 1.1‰).

Overall, the $\delta^{30}Si_{diatom}$ samples seem to preserve the utilisation signal much better and more reliably. The $\delta^{30}Si_{diatom}$ data show almost the same distribution pattern as the $\delta^{30}Si_{Si(OH)4}$ in the surface waters. They are low in the main upwelling region, and show much higher values along the northern part of the shelf between

5°S to 10°S. The sedimentary diatoms can be used to reconstruct past-surface water utilisation rates. Therefore, the fractionation factor of -1.1‰ between diatoms and surface water is applied (Fig. 3.9). Hand-picked diatoms, which have $\delta^{30}Si_{diatom}$ values ranging between +0.6‰ and +2.0‰, reflect surface water $\delta^{30}Si_{Si(OH)4}$ values between +1.7‰ and +3.1‰. Under steady state conditions this requires surface water utilisation rates between 50 and ca. 100%. In contrast, the $\delta^{30}Si_{bSiO2}$ range between -1.0‰ and +1.1‰, indicating surface water $\delta^{30}Si_{Si(OH)4}$ values between +0.1‰ and +2.2‰. For these samples, the utilisation rates range between 0 to 70% (Fig. 3.9). That is much lower than the present-day observed one. Such low utilisation rates might occur during different times of the year, but is not very likely that it is a persistent feature.

Although the actual values indicate a transfer of the surface water signal into the sediment, the picked diatoms integrate the surface water signal over the whole growing season as well as many years, and (partial) dissolution, along-shelf transport, as well as different conditions during single years (e.g. El Nino events) are very likely to influence the deposited signature, which has to be taken into account for interpretations of past upwelling conditions. Even if we assume a higher fractionation of $Si(OH)_4$ in the surface water during El Nino conditions due to diminished upwelling (Feldman, 1984, Fiedler, 2002), this signature is obviously not preserved in these sediments given that the highest $\delta^{30}Si_{Si(OH)4}$ in surface water and the $\delta^{30}Si_{diatom}$ values from hand-picked surface sediment diatoms agree relatively well (Fig. 3.5a and 3.9). The reason for this is probably that the majority of the diatoms grow under “normal” conditions, and that under e.g. El Nino conditions no significant amounts of diatoms are produced at the surface that could transfer the surface water fractionation signal into the underlying sediments.

The general assumption for all paleo-studies using Si isotopes as a paleo-proxy for $Si(OH)_4$ utilisation is that the major fraction of the $bSiO_2$ in the sediment consists of diatoms (De La Rocha et al., 1998; Brzezinski et al., 2002; Beucher et al., 2007; Reynolds et al., 2008). This is probably justified for studies of the Southern Ocean or the Subpolar North Pacific where $bSiO_2$ concentrations are usually higher than 10-20 wt%. However, the surface sediment distribution of $bSiO_2$ off Peru today (Fig. 3.5b) shows strong latitudinal gradients between high and low silica

concentrations due to differences in upwelling intensity and nutrient supply. Paleo-studies in this area will focus on questions related to how upwelling intensity changed in the past. During times of overall low upwelling, the concentration of $bSiO_2$ will have also been low in areas where it is high today. In this case, a significant influence of non-diatom $bSiO_2$ cannot be excluded, unless all samples are hand-picked to avoid contamination. Correlations between $bSiO_2$ concentration in the sediment, $\delta^{30}Si_{bSiO2}$, and $\delta^{30}Si_{diatom}$ indicate that off Peru a minimum concentration of 5-10 wt% $bSiO_2$ is necessary to ensure that sufficient amounts of diatoms are present in the sediment to exclude a significant influence of non diatom $bSiO_2$ material.

3.5 Conclusions

Subsurface waters, which feed the coastal upwelling off Peru display a mean $\delta^{30}Si_{Si(OH)4}$ signature of +1.5 ± 0.2‰ all along the Peruvian shelf, whereas the $Si(OH)_4$ concentration increases with latitude towards the south as a function of water mass mixing and the remineralisation of $bSiO_2$ in the water column and in the sediments, as indicated by significant increases in $Si(OH)_4$ concentrations in the bottom waters above the shelf. The $\delta^{30}Si_{Si(OH)4}$ distribution in the surface waters along the Peruvian shelf is controlled by the upwelling intensity, i.e. an interplay between the supply of $Si(OH)_4$ and water mass mixing. In the area of the strongest upwelling and re-supply of $Si(OH)_4$, where the degree of utilisation of $Si(OH)_4$ is overall low (about 50%), the increase in surface water $\delta^{30}Si_{Si(OH)4}$ compared to the subsurface source waters is small, only 0.2-0.3‰. Higher degrees of $Si(OH)_4$ utilisation (up to 93%) in surface waters outside the main upwelling area result in higher $\delta^{30}Si_{Si(OH)4}$ values of up to 2.8‰, corresponding to a difference of up to 1.2 ‰ from the source water.

The calculation of the fractionation factor ε based on our data gives values between -0.5‰ and -2.7‰ for Rayleigh-type and steady-state system conditions, respectively. This is a large deviation from the experimentally derived value of -1.1‰, which is caused by the strong influence of water mass mixing in this highly dynamic environment. However, all euphotic zone $\delta^{30}Si_{Si(OH)4}$ reveal a fractionation factor of -1.3‰ for steady state conditions, which is very similar to the

experimental one, and which also seems realistic given the environmental conditions. Comparison of $\delta^{30}Si_{diatom}$ compositions obtained from hand-picked diatoms from the underlying sediments, which range from +0.6‰ to +2.0‰, shows the same overall distribution as that of $\delta^{30}Si_{Si(OH)4}$. The silicate of these diatoms exhibits lower $\delta^{30}Si_{diatom}$ values in the main upwelling region, where productivity is highest. Along the northern shelf between 5°S to 10°S, where upwelling and productivity are lower, the $\delta^{30}Si_{diatom}$ values are higher.

A comparison between $\delta^{30}Si_{bSiO2}$ signatures obtained from bulk $bSiO_2$ in the sediment, which was extracted applying commonly used methods, and $\delta^{30}Si_{diatom}$ from hand-picked diatoms indicates that in samples with low $bSiO_2$ concentrations a contamination with isotopically lighter siliceous material, such as sponge spicules or radiolarians, occurs. This observation has important implications for the general interpretation of paleo-$\delta^{30}Si$ records at locations with low $bSiO_2$ content and suggests that for sediments containing such low amounts of $bSiO_2$ significant biases of the $\delta^{30}Si$ records can only be excluded if it can be demonstrated that a pure diatom fraction was extracted.

Acknowledgments

This work is a contribution of the Sonderforschungsbereich 754 "Climate - Biogeochemistry Interactions in the Tropical Ocean" (www.sfb754.de), which is supported by the Deutsche Forschungsgemeinschaft. Special thank goes to the crew of the RV Meteor. Many thanks also go to Birgit Glückselig, Ulrike Böttjer, and Rainer Gersonde from AWI, Bremerhaven, who helped to establish the diatom separation methods. Analyses and visualisations used in this study were produced with the Giovanni online data system, developed and maintained by the NASA GES DISC.

Chapter 4

Changes in Silicate Utilisation and Upwelling Intensity off Peru Since the LGM – Insights from Silicon and Neodymium Isotopes

Abstract

Diatom-related primary productivity along the Peruvian upwelling area showed large variations during the past 20 kyr, which were characterized by low fluxes of biogenic opal ($bSiO_2$) during the last glacial and much higher values thereafter, in particular during the early and the latest Holocene. Combined records of the stable silicon isotope composition of diatom-opal ($\delta^{30}Si_{opal}$) and the radiogenic isotope composition (Nd, Sr) of Fe-Mn coatings of the sediment particles and the detrital material itself reveal that this variability has been related to changes in silicic acid ($Si(OH)_4$) utilisation, mostly controlled by the supply of iron (Fe) and phosphate (P) via upwelling. $Si(OH)_4$ utilisation documented by $\delta^{30}Si_{opal}$ was low (+0.4‰) during the last glacial, whereas the detrital material showed highly radiogenic signatures of $\varepsilon Nd_{detritus}$ of -1.5. This suggests that the area off Peru has been characterised by strong upwelling of subsurface waters with an overall low nutrient content. For the early Holocene the record showed much higher values for $\delta^{30}Si_{opal}$ (+1.2‰) and $Si(OH)_4$ utilisation (50-60%). The $\varepsilon Nd_{detritus}$ at the same time showed a trend from less radiogenic values around -2.5 towards more radiogenic values around -1.5. This implies relatively variable oceanographic conditions along the shelf alternating between stronger and weaker upwelling conditions. The late Holocene has been characterised by the largest variability of the system of the past 20 kyr. $\delta^{30}Si_{opal}$ (+1.4‰) and $Si(OH)_4$ utilisa-

---

This chapter is going to be submitted to Paleoceanography as:

Ehlert, C., P. Grasse, & M. Frank. Changes in silicate utilisation and upwelling intensity off Peru since the LGM – insights from silicon and neodymium isotopes.

tion (60-90%) were highest, whereas the $\varepsilon Nd_{detritus}$ decreased from -1.5 to values around -4.5 between 5 and 1.2 ka BP, indicating the predominant local origin of material input. These changes correlate with the onset of modern El Nino-Southern Oscillation conditions in the Pacific during the latest Holocene.

4.1 Introduction

The Peruvian continental margin is characterized by one of the most pronounced Oxygen Minimum Zone (OMZ) in the world's ocean (e.g. Karstensen et al., 2008; Fuenzalida et al., 2009). The effects of oxygen-dependent nutrient cycling (e.g. for nitrogen, phosphorus and iron) in this region are distributed via currents and exert a far-reaching influence, partly affecting the global ocean. Past oxygen variability in the Peru region has primarily been considered as a function of upwelling intensity driven by an interplay of major currents with trade winds and the El Nino-Southern Oscillation (ENSO) (Brink et al., 1983; Karstensen and Ulloa, 2008) and surface water bioproductivity (e.g. De Vries and Schrader, 1981; Thiede and Suess, 1983; Rein et al., 2004, 2005). In the Peruvian upwelling system primary productivity is mainly dominated by diatoms (Estrada and Blasco 1985; Abrantes et al., 2007), which build their opaline frustules from dissolved silicic acid ($Si(OH)_4$) (Tréguer et al., 1995). The nutrients feeding the productivity are mainly supplied via upwelling of the southward flowing subsurface waters of the Peru-Chile Undercurrent (PCUC) (Fig. 4.1) (Brink et al., 1983). This current is partly fed by the eastward flowing oxygen enriched waters of the Equatorial Undercurrent (EUC) (Lukas, 1986; Penven et al., 2005; Kessler, 2006) originating from the central Pacific (Brink et al., 1983; Toggweiler et al., 1991) as a mixture of waters of southern and northern Pacific origin (Dugdale et al., 2002). Also, water masses from the south, like the Subantarctic Mode Water (SAMW), the Peru-Chile Current (PCC) and the Peru Coastal Current (PCoastalC) affect the upwelling (Toggweiler et al., 1991; Sarmiento et al., 2004). As a result, past changes in $Si(OH)_4$ concentrations in the high latitudes should affect tropical $Si(OH)_4$ supply and diatom productivity, as proposed by the silicic acid leakage hypothesis (e.g. Nozaki and Yamamoto, 2001; Brzezinski et al., 2002), and thus ultimately the extent and strength of the OMZ.

However, downcore changes in the record of biogenic opal ($bSiO_2$) content cannot unambiguously be attributed to variations of productivity but may also be influenced by changes in preservation (De Vries and Schrader, 1981) or the strength of silicification of the diatoms. Under iron (Fe) depleted conditions the Si:N and Si:C ratio in the diatom frustules increases, i.e. they build thicker frustules and therefore the export of $bSiO_2$ from surface to deep waters can be enhanced without an increase in export productivity (Takeda, 1998).

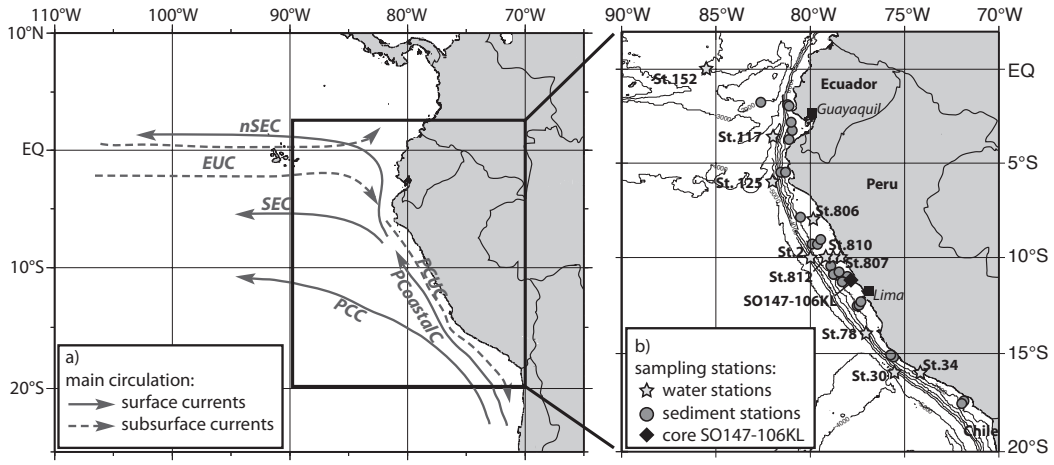

Figure 4.1: a) Schematic ocean circulation and main currents in the EEP: Surface currents (solid lines): (n)SEC (northern) South Equatorial Current, PCC Peru-Chile Current, PCoastalC Peru Coastal Current, subsurface currents (dashed lines): EUC Equatorial Undercurrent, PCUC Peru-Chile Undercurrent (after Strub et al., 1998; Penven et al., 2005; Kessler, 2006; Ayon et al., 2008; Karstensen and Ulloa, 2008; and ADCP data from Czeschel et al., 2011), b) Station map for water column stations (light grey stars), surface sediments (grey dots) and the location of core SO147-106KL (black diamond). The bathymetry is given for 0 to 5000 m water depth in 1000 m increments.

The stable silicon isotopic composition (expressed as $\delta^{30}Si$, which is the measured $^{30}Si/^{28}Si$, normalised to that of the international standard NBS28, multiplied by 1,000) of the diatom frustules ($\delta^{30}Si_{opal}$) is a powerful tool to investigate changes of $Si(OH)_4$ utilisation, as well as nutrient dynamics and productivity in the present and past ocean (De La Rocha et al., 1998, Brzezinski et al., 2002; Reynolds et al., 2008). Diatoms preferentially incorporate the lighter ^{28}Si during opal formation, which leaves the residual seawater enriched in the heavy isotopes. The fractionation between seawater and diatoms accompanying that process is -1.1‰ (De La Rocha et al., 1997; Milligan et al., 2004; Varela et al., 2004; Reynolds et al., 2006; Beucher et al., 2008). Correspondingly, when upwelling is strong along the Peruvian coast the degree of utilisation of $Si(OH)_4$ is weak and the

dissolved and diatom-$\delta^{30}Si$ will be low, whereas under weaker upwelling conditions the diatoms utilise the available $Si(OH)_4$ more completely, which leads to a stronger fractionation and thus higher $\delta^{30}Si$ values (see Chapter 3). However, the $\delta^{30}Si$ signatures are not only controlled by $Si(OH)_4$ utilisation but are also strongly influenced by upwelling intensity and water mass advection (Reynolds et al., 2006; Beucher et al., 2011), two processes that are difficult to disentangle in the paleo-record.

Information on past changes in water mass advection and vertical mixing can be gained from radiogenic Nd isotopes. Water masses acquire their Nd isotope composition (expressed as εNd, which corresponds to the measured $^{143}Nd/^{144}Nd$, normalised to the Chondritic Uniform Reservoir CHUR (0.512638), multiplied by 10,000) in their source regions through weathering of continental rocks with distinct isotopic signatures, which are supplied to the oceans via rivers, eolian inputs or through shelf exchange processes (e.g. Frank, 2002; Lacan and Jeandel, 2005). In the Eastern Equatorial Pacific (EEP) two main endmembers dominate the Nd isotope signal. Waters with Southern Ocean origin have less radiogenic signatures between -5 and -9 (Piepgras and Jacobsen, 1988) whereas more radiogenic signatures reflect contributions from the central Pacific, such as the EUC, which have εNd values between -1.6 and -3.5 (Lacan and Jeandel, 2001; Grasse et al., unpublished, 2011). Past bottom water isotopic compositions are preserved either in early diagenetic, authigenic ferromanganese oxyhydroxide coatings of the sediment particles ($\varepsilon Nd_{coating}$) that can be extracted from bulk sediments (Rutberg et al., 2000; Gutjahr et al., 2007) or from the carbonate fraction of benthic foraminifers (Klevenz et al., 2008). Additionally, lithogenic particles in the sediment, which are delivered to the shelf via weathering of continental source rocks of different origin and age, have distinct radiogenic isotope signatures ($\varepsilon Nd_{detritus}$), which can be used to trace their source areas (Goldstein et al., 1984; Dia et al., 1992; Fagel et al., 2004). Changes in $\varepsilon Nd_{detritus}$ are generally closely related to climatic changes causing variations transport pathways from the respective source areas (Grousset et al., 1988; Fagel et al., 2004; Ehlert et al., 2011; Stumpf et al., 2011). The major goal of this study is to reconstruct silicate utilisation and upwelling intensity by means of combined Si isotope compositions

in diatoms and water mass mixing based on Nd isotope compositions of authigenic fractions (Mn-Fe coatings of particles and benthic foraminifers) and detrital material at the centres of coastal upwelling on the Peruvian shelf during the past 20,000 years. Periods of weaker upwelling (e.g. prolonged El Nino-like phases) result in a diminished nutrient supply to the euphotic zone (Barber and Chavez, 1983). Subsurface waters are replaced by more oligotrophic surface waters and in particular the flowpath of the northward flowing Peru Coastal Current (PCoastalC) is shifted more closely to the coast (Huyer et al., 1987; Fiedler and Talley, 2006), resulting in a general decrease of primary productivity and a change in phytoplankton assemblages (Feldman et al., 1984; Chavez, 2005). Those drastic changes should be reflected in the sediment record.

4.2 Material and Methods

4.2.1 Core Location, Age Model and Sampling

Surface sediment samples for Nd isotope analyses were taken onboard RV Meteor during cruises M77/1 and 2 along the Ecuadorian and Peruvian shelf between 2°S to 18°S at water depths between 114 m and 2600 m in the year 2008 (Fig. 4.1, Table A.3). Nd and Si isotope measurements for the reconstruction of past conditions were conducted on core SO147-106KL, which was recovered during RV Sonne cruise SO147 along the central Peruvian shelf in 184 m water depth at 12°03' S, 77°39.8' W in 2000 (Fig. 4.1, Table A.4) (Dullo et al., 2000). The age determination of the upper 11 m of the core is based on caesium and lead isotope profiling and 45 AMS ^{14}C measurements of the bulk organic carbon fraction (Rein et al., 2004, 2005). The oldest radiocarbon age is 19.6 ka BP and the age model of the core is based on linearly interpolated ages between the calibrated radiocarbon ages (all ages in the following are given in ka B.P.).

4.2.2 Biogenic Opal and Silicon Isotope Analyses

The $bSiO_2$ content in the sediment (Wolf, 2002) was measured following the sequential leaching methods described by DeMaster (1981) and Müller and Schneider (1993). For silicon isotope measurements diatoms were extracted from the sediment in two different ways. For the size fraction 11-32 µm the procedures

described by Morley et al. (2004) were applied. Approximately 300 mg sediment were treated with 30% H_2O_2 and 35% HCl to remove the organic and carbonate fractions. Afterwards the sediment was wet sieved to separate the 11 to 32 µm fraction. In the last step a heavy-liquid solution (sodium-polytungstate, 2.1-2.2 g/mL) was applied to separate diatoms from the detrital lithic silicate material. For the alternative procedure the diatoms were hand-picked from the size fraction 125-250 µm (as described in Chapter 2 and 3). For dissolution of the diatom frustules the samples were treated with 0.1 M NaOH at 130°C on a hotplate for several hours (Reynolds et al., 2008). Si concentrations of the dissolved diatom samples were measured colorimetrically using a photospectrometer (Hansen and Koroleff, 1999). All sample solutions were chromatographically purified with 1mL pre-cleaned AG50W-X8 cation exchange resin (BioRad®, mesh 200-400) following the method described by Georg et al. (2006b). Si isotope ratios were measured on a *NuPlasma HR* MC-ICPMS (Nu Instruments) at IFM-GEOMAR, equipped with an adjustable source-defining slit set to medium resolution to ensure separation of the ^{30}Si peak and molecular interferences. The measurements were carried out applying a standard-sample bracketing method (Albarède et al., 2004). All solutions were measured at a Si concentration of 14-21 µmol/kg depending on the sensitivity of the instrument on the respective measurement day and were introduced into the plasma via a Cetac Aridus II desolvating nebulizer system equipped with a PFA nebulizer yielding a 60 to 80 µL/min uptake rate. Repeated measurements of the reference materials IRMM018 and Big Batch gave average $\delta^{30}Si$ values of -1.56 ± 0.17‰ ($2\sigma_{sd}$) and -10.81 ± 0.17‰ ($2\sigma_{sd}$), respectively, which are in agreement with values obtained by other laboratories (Reynolds et al., 2007). Samples were measured on at least two separate days and three to five times within one session (during one day), which generally resulted in uncertainties between 0.07 and 0.30‰ ($2\sigma_{sd}$) (Table A.4). All error bars provided in the figures correspond to that reproducibilities. Replicate measurements of an in-house diatom matrix standard over longer periods of time (n= 20 sessions within one year) gave an external reproducibility of 0.25‰ ($2\sigma_{sd}$).

4.2.3 Neodymium and Strontium Isotope Analyses

For Nd and Sr isotope analyses, in a first step the carbonate fraction was removed from the freeze-dried and homogenized sediment samples using a 15%-acetic acid/1 M Na-acetate buffer solution. Thereafter, the authigenic Fe-Mn oxyhydroxide fraction was extracted from the sediment by leaching with a 0.05 M hydroxylamine hydrochloride/15%-acetic acid solution buffered to pH 3.8 with NaOH (Gutjahr et al., 2007; Stumpf et al., 2010). After removal of the authigenic fraction 30 mg of the residual bulk fraction of the dried sediment was treated with a mixture of concentrated HF-HNO_3-HCl until total dissolution for the extraction of the detrital radiogenic isotope signal. The elemental separation and purification of the leachates and of the completely dissolved detrital material followed previously published procedures for Sr (Horwitz et al., 1992) and Nd (Cohen et al., 1988) applying ion exchange chromatography for cation separation (0.8 mL AG50W-X12 resin, BioRad®, mesh 200-400) and subsequent separation of Sr from Rb (50 µL Sr-Spec resin, mesh 50-100), as well as separation of Nd from the other REEs (2 mL Eichrom® Ln-Spec resin, mesh 50-100). The benthic foraminifers (bulk species) were picked in all size fractions >63 µm, because foraminiferal carbonate is scarce in this area of high diatom productivity. About 20 mg of benthic foraminiferal carbonate resulted in 5 ng to 10 ng of purified Nd for mass spectrometric analyses. The cleaning applying oxidative and reductive cleaning procedures was carried out following the methods described by Boyle (1981), Vance and Burton (1999) and Vance et al. (2004). Due to the small amount of Nd in the foraminiferal carbonate the chemical purification of Nd was achieved on a single column (3.14 mL Eichrom® Ln-Spec resin, mesh 50-100) (Kraft et al., unpublished, 2011). All radiogenic isotope measurements were performed on the *NuPlasma HR* MC-ICPMS (Nu Instruments) at IFM-GEOMAR. Measured Nd isotope compositions were corrected for instrumental mass bias using a $^{146}Nd/^{144}Nd$ of 0.7219 and were normalised to the JNdi-1 standard with an accepted literature value for $^{143}Nd/^{144}Nd$ of 0.512115 (Tanaka et al., 2000). External reproducibility was estimated by repeated measurements of the JNdi-1 standard and was usually between 15 and 55 ppm ($2\sigma_{(sd)}$, Table A.3 and A.4). Measured $^{87}Sr/^{86}Sr$ ratios were corrected for instrumental mass bias using $^{88}Sr/^{86}Sr$ = 8.3752 and were normalised to the accepted value for NIST SRM987 of 0.710245. The $2\sigma_{(sd)}$ external

reproducibility of repeated standard measurements was always better than 36 ppm ($2\sigma_{(sd)}$, Table A.3 and A.4). Total procedural Nd and Sr blanks for leachates and total dissolution of the detrital material were ≤ 83 pg and 2.1 ng, respectively, which was negligible compared to sample concentrations.

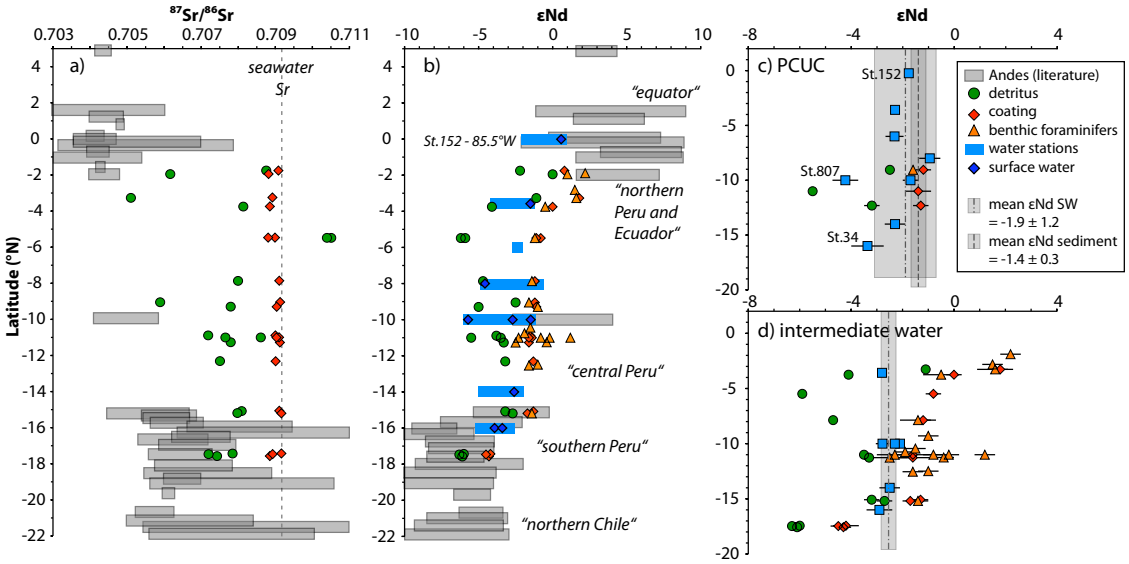

Figure 4.2: Distribution of a) $^{87}Sr/^{86}Sr$ and b) εNd in waters and surface sediments along the Peruvian shelf: water column dissolved εNd (blue boxes, Grasse et al., unpublished (2011)), Fe-Mn coatings (red diamonds), benthic foraminifers (orange triangles), and detrital material (green circles). The error bars represent $2\sigma_{(sd)}$ external reproducibilities. The grey boxes mark the range of bulk rocks in the Andean hinterland (Sarbas and Nohl, 2009). c) and d) show the latitudinal distribution within the subsurface PCUC (between 50 m to 200 m water depth) and intermediate water (200 m to 1000 m water depth), respectively. The dashed line and grey shading indicates the mean and 2 standard deviation range for the values of the coating/ benthic foraminifera (mean sed.) and for the seawater (mean SW, excluding St. 807 and 34, see text).

4.3 Results

4.3.1 εNd Signatures Extracted from Surface Sediments

The Nd isotope composition was measured in surface sediments from water depths ranging from 114 m to 2607 m along the Ecuadorian and Peruvian shelf between 2°S and 18°S (Fig. 4.1, Table A.3). The εNd signature in Fe-Mn coatings and benthic foraminifers from the same samples are mostly within error indistinguishable from each other. In the coatings, the $\varepsilon Nd_{coating}$ signatures range from +1.8 at 2°S to -4.5 at 18°S (Fig. 4.2b). Benthic foraminifera show εNd_{foram} values between +2.2 at 2°S and -2.5 at 11°S. South of 15°S no benthic foraminiferal εNd could be measured because the amount of available specimen in the sediments was too low. In the detrital material $\varepsilon Nd_{detritus}$ shows a range between 0 at 2°S and

-6.3 at 17°S. The εNd signature of the Fe-Mn coatings and the benthic foraminifers is always about 2 to 3 εNd units more radiogenic than the respective detrital signal, whereas the detrital signal and the dissolved εNd in the surface waters tend to agree very well with each other as a function of latitude.

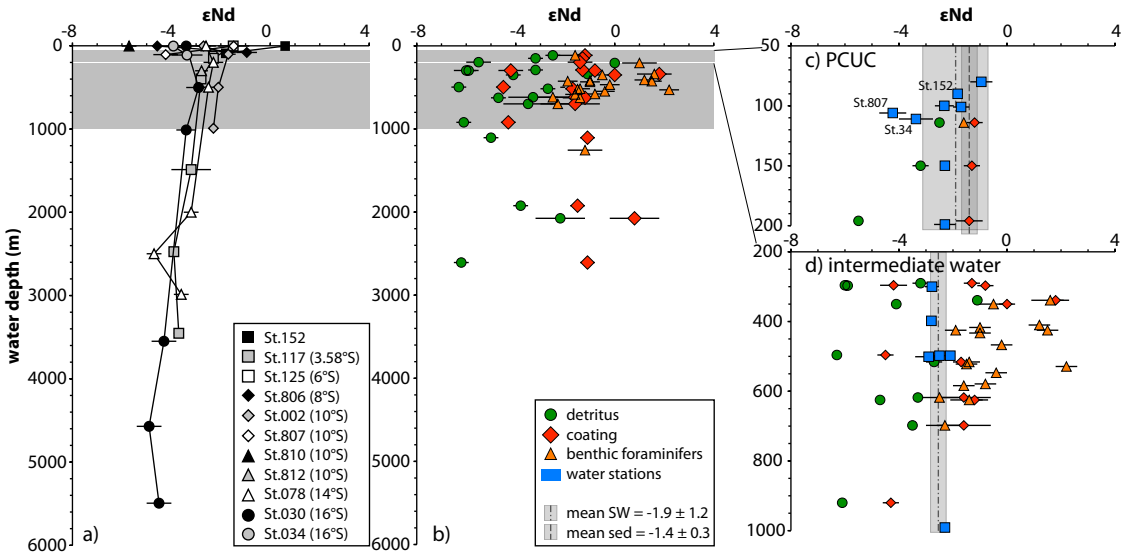

Figure 4.3: εNd versus water depth for a) dissolved εNd, b) Fe-Mn coatings (red diamonds), benthic foraminifers (orange triangles) and detrital material (green circles). The error bars represent $2\sigma_{(sd)}$ external reproducibilities. c) and d) represent the distribution within the PCUC layer (50 m to 200 m water depth) and intermediate waters (200 m to 1000 m water depth). The vertical dashed lines and grey shading indicates the mean and 2 standard deviation range for the values of the coating and benthic foraminifers (mean sed.) and for the seawater (mean SW) (same as in Fig. 4.2).

The εNd in the Fe-Mn coatings and benthic foraminifers from the subsurface waters (EUC/PCUC, 50 m to 200 m water depth) are all very close to each other with a mean value of -1.4 ± 0.3 (Fig. 4.2c). This is, within error, in good agreement with dissolved seawater measurements of the EUC further offshore at the equator (εNd = -1.8 ± 0.1, Grasse et al., unpublished, 2011) and also with the mean value (εNd = -1.9 ± 1.2) obtained for subsurface water samples between 50 m to 200 m water depths (Fig. 4.2c) (Table A.5). Only two water stations (St. 807 and 34), which are located very close to the coast, show less radiogenic εNd values between -3 and -4. In the intermediate water between 200 m and 1000 m water depth, however, the εNd signature in the water column is relatively homogenous (mean εNd = -2.6 ± 0.3) (Fig. 4.2d), whereas the εNd signatures in the Fe-Mn coatings, benthic foraminifera and detrital material are all highly radiogenic in the

northern part of the Peruvian shelf, and show a continuous trend towards less radiogenic values in the south.

Comparison between surface sediments and water depth illustrates the large range of the measured εNd values (Fig. 4.3). The present day water column near the coast only shows a small Nd isotope variability and a weak trend towards less radiogenic isotope compositions with water depth (Fig. 4.3a) (Table A.5). In general, and as described above for the latitudinal distribution, the Nd isotope signatures of the water column and the detrital fractions are less radiogenic than the Fe-Mn coatings and foraminiferal data, which also show a large range in all water depths (Fig. 4.3b). Again, within the subsurface water between 50 m to 200 m water depth, dissolved εNd signatures and those extracted from Fe-Mn coatings and benthic foraminifera agree relatively well (Fig. 4.3c). Below, within intermediate water depths between 200 m to 1000 m, the dissolved εNd is rather homogenous, but the Fe-Mn coatings, benthic foraminifers and detrital material scatter widely (Fig. 4.3d).

4.3.2 Downcore records

4.3.2.1 Biogenic Opal and Silicon Isotope Composition

In core SO147-106KL the $bSiO_2$ concentration shows a large variability and ranges between 3 wt% and 31 wt% (Fig. 4.4) (Wolf, 2002). The diatom flux shows peak values for the early Holocene between 10 to 8 ka and during the late Holocene between 2.5 ka and present. Marked minimum $bSiO_2$ contents occurred during the LGM/deglacial and during the late Holocene between 5 and 2.5 ka.

$\delta^{30}Si_{opal}$ ranges from 0.3‰ to 1.3‰ for $bSiO_2$, and from 0.4‰ to 1.4‰ for hand-picked diatoms (Table A.4). Both methods show the same overall trend and are mostly within error of each other with one exception around 10.5 ka, where $\delta^{30}Si_{bSiO2}$ was low (+0.4‰)and $\delta^{30}Si_{diatom}$ was high (+1.3‰). The lowest $\delta^{30}Si_{opal}$ signatures occurred during the LGM (+0.3‰) and during the early Holocene (around +0.4‰), whereas the early and late Holocene were characterised by higher values up to +1.4‰. The concentrations of $bSiO_2$ and $\delta^{30}Si_{opal}$ are overall positively correlated.

4.3.2.2 Neodymium and Strontium Isotope Signatures

The downcore Nd isotope composition extracted from the Fe-Mn coatings range between -2.1 and -0.9 (Table A.4). The variability has been low with no significant trends or excursions during the past 20 kyr (Fig. 4.4). In contrast, the $\varepsilon Nd_{detritus}$ signatures range between -4.5 and -0.7 and show a trend from more radiogenic values during the LGM and the deglacial to less radiogenic values during the late Holocene. The least radiogenic values occurred around 10 ka and in particular during the past 2.5 kyr, which represents the most pronounced change of the whole record. The $^{87}Sr/^{86}Sr_{detritus}$ signature of the detrital fraction ranged between 0.70620 to 0.70849, and shows a variability closely following that of the $\varepsilon Nd_{detritus}$ record.

4.4 Discussion

4.4.1 Surface sediments

4.4.1.1 Neodymium and Strontium Isotope Composition in Surface Sediments

Along the Peruvian shelf the εNd signature of the authigenic Fe-Mn coatings, the benthic foraminifers, both of which are supposed to represent the isotopic composition of past bottom waters, and the detrital fraction all show a trend from more radiogenic values in the north to less radiogenic values in the south (Fig. 4.2b), which is similar to the distribution of the dissolved surface water εNd signature (Grasse et al., unpublished, 2011, and this study). The detrital particles carry Nd isotope signatures similar to those of the hinterland rocks in the Andes (Fig. 4.2b), which are characterised by highly radiogenic values between +4 and +7 near the equator and less radiogenic values of up to -6 in central and southern Peru and northern Chile (source regions are defined here as: equator 0-5°N, northern Peru and Ecuador 0-5°S, central Peru 5-15°S, southern Peru 15-18°S, and northern Chile 18-22°S) (Sarbas and Nohl, 2009). All sedimentary phases display a relatively large scatter of εNd signatures with water depth, which makes a clear distinction between subsurface, intermediate and deep waters very difficult (Fig. 4.3). There are a number of possible reasons for the observed patterns:

a) The Nd isotope composition of all water masses is within error indistinguishable. In general, the water masses in the EEP are dominated by two

main endmembers for the Nd isotope signal. Waters originating in the Southern Ocean are characterized by less radiogenic signatures between -5 and -9 (Piepgras and Jacobsen, 1988) and more radiogenic signatures reflect contributions from the northern and especially the central Pacific, such as the EUC, which has εNd values between -1.6 and -3.5 (Lacan and Jeandel, 2001; Grasse et al., unpublished, 2011). Along the continental margin the water column profiles show comparably radiogenic values around -1.9 within the subsurface layer representing the EUC/PCUC (Fig. 4.2c and 4.3c) but below only a slight trend towards less radiogenic values with water depth is observable (Fig 4.2d and 4.3d), which does not allow the identification of characteristic signatures for different water masses.

b) Boundary exchange with the underlying sediments, continuous eolian or riverine material input from the Andean hinterland, and dissolution and mixing with the advected dissolved isotopic signatures (Tachikawa et al., 2004; Lacan and Jeandel, 2005; Grasse et al., unpublished, 2011) overprint the local water mass signatures. Especially the anoxic sediments of the Peruvian coast have to be considered as a source for Nd (Elderfield and Sholkovitz, 1987; Haley et al., 2004), whereas the trend in the detrital Sr isotopic composition is far less pronounced (Fig. 4.2a). Material input along the Peruvian shelf is dominated by riverine input, whereas dust deposition does not play a major role (Scheidegger and Krissek, 1982; Bruland et al., 2005) and is delivered from the arid Peruvian Andes and, to a lower extent, from the Atacama desert (Molina-Cruz, 1977). The surface water dissolved εNd signatures display a wide range (Fig. 4.2b and 4.3b), which closely mirror the hinterland geology (Fig. 4.2b). However, the water column, Fe-Mn coatings and benthic foraminifers from the surface sediments in the area where the subsurface waters of the PCUC are in contact with the shelf do not indicate significant exchange with the detrital material (Fig. 4.2c and 4.3c). Consequently, at least in the subsurface water (50 m to 200 m water depth), where current speeds are high, isotopic exchange between detrital material and the water column seems to be limited. The Fe-Mn coatings and the benthic foraminifers reflect the dissolved εNd signature from the PCUC. Water station 34, which is located at 16°S, has slightly less radiogenic signatures. ADCP profiles from January 2009 at that latitude indicate a stronger than normal influence of the northward directed

PCoastalC, which is usually defined as a surface current, in that water depth (Czeschel et al., 2011). This might have influenced the signature in the water column, but is not reflected in the sediments, which integrate the signal over longer timescales. For intermediate water depths the sedimentary phases show a clear north-south trend (Fig. 4.2d), whereas the water column is only slightly less radiogenic than the EUC layer (Fig. 4.3c, d). Especially in anoxic sediments Fe-oxides are re-dissolved and are expected to release the detrital geochemical and isotopic signature into the bottom water (Elderfield and Sholkovitz, 1987; Landing and Bruland, 1987; Haley et al., 2004). Anoxic conditions occur along the Peruvian shelf usually in water depths between 150 m and 800 m between 5°S and 13°S, whereas north and south of this area their vertical extension decreases (Fuenzalida et al., 2009).

c) Downslope transport of particles occur during earthquakes (Dorbath et al., 1990; Reinhardt et al., 2002) or more constantly within a nepheloid layer along the steep continental margin as has been observed elsewhere before (Gutjahr et al., 2008; Stumpf et al., 2010). This process can significantly influence the Fe-Mn coatings, but not the benthic foraminifers. Most likely a combined effect of the mixing-induced diminishing influence of the incoming central Pacific surface waters, that have highly positive εNd values (Lacan and Jeandel, 2001; Grasse et al., unpublished, 2011) and exchange with the detrital fraction of the shelf sediments combined with minor effects of downslope transport of particles explains the observed distributions.

Provenance analyses show that the trend in detrital εNd of all surface sediment samples can be very well explained by southwards increasing contributions of central and southern Peruvian origin (Fig. 4.2 and 4.5), which have significantly less radiogenic εNd and more radiogenic $^{87}Sr/^{86}Sr$ isotope signa tures than the source rocks further in the North around the equator. However, the distribution can also be interpreted that the $^{87}Sr/^{86}Sr_{detritus}$ shows an offset towards more radiogenic values from the given Nd isotope signal of the hinterland rocks (Fig. 4.5). A possible explanation could therefore also be incongruent weathering processes, which affects the Sr but not the Nd isotope composition (Tütken et al., 2002). During chemical weathering clay-size particles are produced

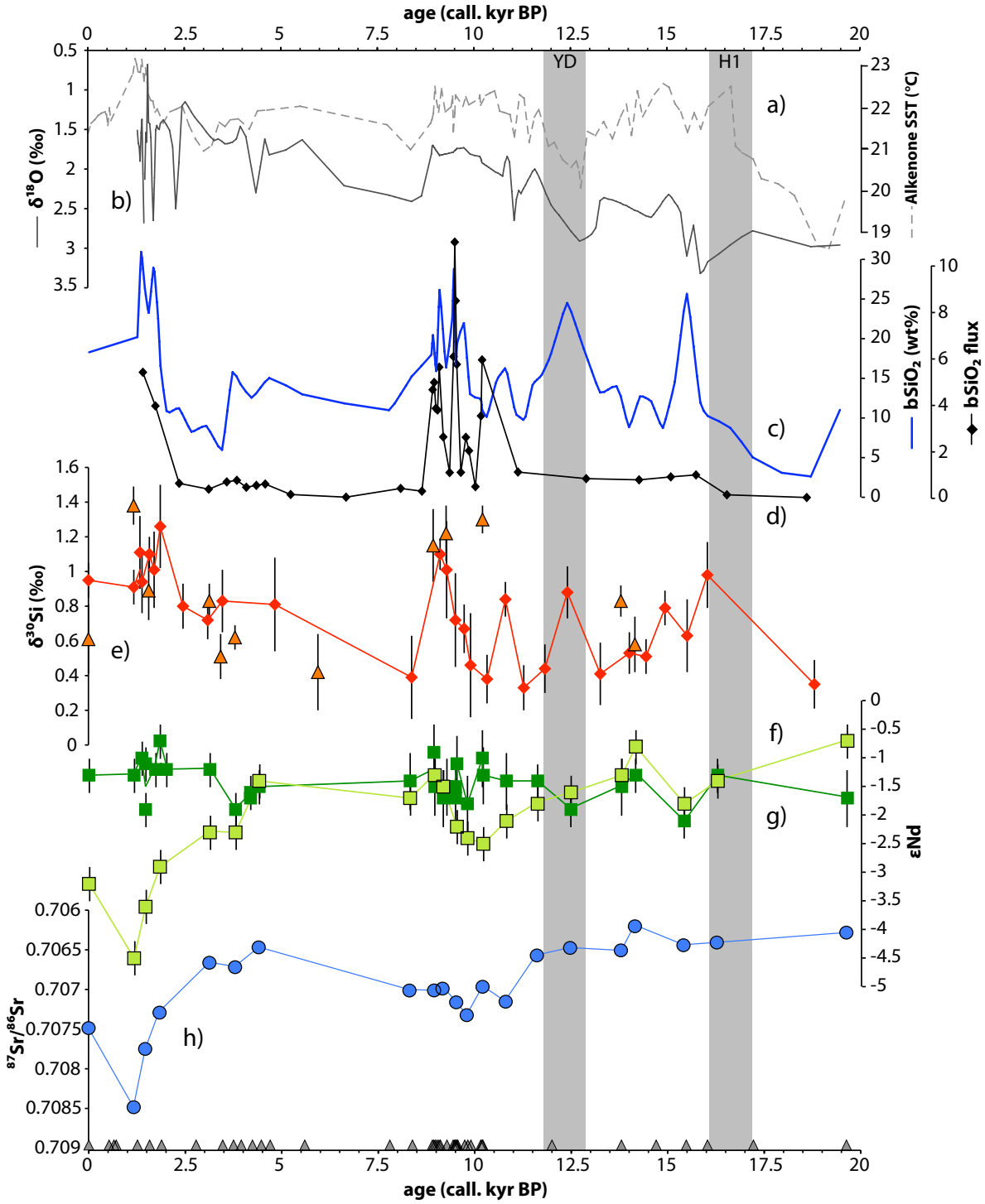

Figure 4.4: Downcore records of core SO147-106KL. a) alkenone derived sea surface temperatures (°C) (Rein et al., 2005) b) benthic (B. seminuda) $\delta^{18}O$ (‰) (Wolf, 2002), c) $bSiO_2$ concentration (wt%) (Wolf, 2002), d) $bSiO_2$ flux, e) $\delta^{30}Si$ (‰) of $bSiO_2$ (red diamonds) and hand-picked diatoms (orange triangles), error bars represent $2\sigma_{(sd)}$ external reproducibilities of repeated sample measurements, f) $\varepsilon Nd_{detritus}$ (light green squares) and g) $\varepsilon Nd_{coating}$ (dark green squares), error bars represent $2\sigma_{(sd)}$ external reproducibilities of repeated standard measurements, and h) $^{87}Sr/^{86}Sr_{detritus}$ (light blue circles, scale is reversed). The grey triangles represent calibrated AMS ^{14}C dates (Rein et al., 2004, 2005).

which have a higher Rb/Sr ratio than larger particles, and therefore have a higher $^{87}Sr/^{86}Sr$ than the parent bulk rock material. Changes in the $^{87}Sr/^{86}Sr$ can therefore reflect both a shift in the provenance or a variation in the climatic regime. A clear statement can only be given when the same sediment size fraction is analysed in all samples, which is not the case here.

4.4.1.2 Silicon Isotope Composition in Surface Sediments

The silicon isotope composition of the surface waters in the Eastern Equatorial Pacific (EEP) can be extracted from diatoms from the surface sediments and is mainly influenced by silicic acid utilisation by diatoms and upwelling intensity (see Chapter 3). Today, under conditions of strong upwelling in the area between 10 to 15°S, the rates of re-supply of the surface waters with isotopically less fractionated $Si(OH)_4$ from the upwelled subsurface waters is high and thus the degree of surface water silicate utilisation by the diatoms is low. Therefore the $\delta^{30}Si$ both in surface water and diatoms produced from these waters is low. In contrast, under weaker upwelling conditions the diatoms utilise the available $Si(OH)_4$ more completely, which leads to higher silicon isotope ratios in both the surface waters and the diatoms that grew from them. The distribution of $\delta^{30}Si$ and $Si(OH)_4$ concentration in the water column documents the strong influence of water mass mixing on both the dissolved Si isotope compositions at a particular location and their vertical and horizontal gradients.

4.4.2 Environmental Conditions on the Central Peruvian Shelf during the Past 20 kyr

4.4.2.1 Past Silicic Acid Utilisation in the Surface Waters

In the EEP the availability of $Si(OH)_4$ in surface waters is considered to be the major controlling factor of $bSiO_2$ productivity (Dugdale and Wilkerson, 1998). The time series presented here for core 106KL does not only reveal a markedly lower $bSiO_2$ content in the glacial sediments, but also a large variability during the past 20 kyr (Fig. 4.4). The content of $bSiO_2$ was high (>20 wt%) during the late Holocene, the early Holocene, the Younger Dryas (YD) and immediately after Heinrich event 1 (H1). When considering $bSiO_2$ fluxes, the curve looks somewhat

different and reveals enhanced diatom accumulation only during the early and late Holocene. The $\delta^{30}Si$ records for both bulk $bSiO_2$ and hand-picked diatoms show a variability very similar to the $bSiO_2$ content, which is in contrast to the expected relationship inferred from the calibration of surface sediment data to present day surface water signatures, as described above (Chapter 3). Applying the surface sediment relationship (high $bSiO_2$ – low $\delta^{30}Si_{opal}$) to the downcore record indicates that either the $bSiO_2$ record does not reflect changes in diatom productivity or the $\delta^{30}Si_{opal}$ record has been influenced by processes other than $Si(OH)_4$ utilisation. Downcore changes in the $bSiO_2$ record do not necessarily have to be attributed to changes in productivity, but can also have been related to changes in preservation (De Vries and Schrader, 1981). Settling diatoms are (partially) dissolved in the water column and in the sediment as a function of physical and chemical parameters (temperature, pressure, trace metal content) and biological activity (species assemblage, dead diatom percentages, grazing, bacterial degradation of the protecting organic matrix around the diatom frustules) (Bidle and Azam, 1999; Ragueneau et al., 2000; Bidle et al., 2002). Dissolution of $bSiO_2$ is expected to lead to a decrease of dissolved $\delta^{30}Si_{Si(OH)4}$ values in the water column (Demarest et al., 2009) leaving the diatoms relatively enriched in heavy ^{30}Si. Such excursions (low $bSiO_2$ – high $\delta^{30}Si_{opal}$) are not observed in the record, which essentially rules out $bSiO_2$ dissolution as the main reason for the observed variability.

The theoretical relationship between the degree of surface water $Si(OH)_4$ utilisation and the Si isotope composition can be described assuming either Rayleigh-type (fixed input followed by fractional loss or export) or steady state (constant supply and export at equilibrium) fractionation behaviour (Fig. 4.6). The lighter isotopes are preferentially incorporated into the diatom frustules leaving the dissolved fraction enriched in the heavier isotopes (Douthitt, 1982; De La Rocha et al., 1997). Assuming that all recorded $\delta^{30}Si_{opal}$ variations are only a function of $Si(OH)_4$ utilisation in the surface water would imply that the highest $\delta^{30}Si_{opal}$ occurred when there was near complete utilisation of $Si(OH)_4$ (Reynolds et al., 2008). With complete utilisation the $\delta^{30}Si_{opal}$ would be equal to the dissolved $\delta^{30}Si_{Si(OH)4}$ in the source water (= +1.4‰) (Fig. 4.6). This value is in good

agreement with actual measurements of $\delta^{30}Si_{Si(OH)4}$ from the upwelling subsurface source waters ($\delta^{30}Si_{Si(OH)4}$ = +1.5‰ (Chapter 3)).

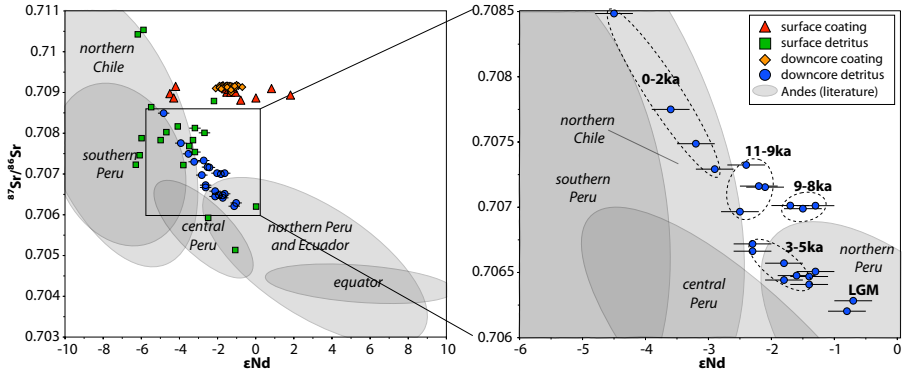

Figure 4.5: $^{87}Sr/^{86}Sr$ versus εNd for surface sediment and downcore data together with potential source endmembers indicating the provenance of the detrital and dissolved material (same data source as for Fig. 4.2; Sarbas and Nohl, 2009). Error bars represent $2\sigma_{(sd)}$ external reproducibilities. The dashed circles mark time periods of significant changes in the radiogenic isotope composition discussed in the text.

Present day surface waters in the area of the core location (between 10°S to 14°S) have relatively low $\delta^{30}Si_{Si(OH)4}$ between +1.7‰ to 2‰, because the re-supply of $Si(OH)_4$ via upwelling is relatively constant, and the fractionation due to limitation is low. The degree of $Si(OH)_4$ utilisation is only between 20 to 45% (Fig. 4.6). The $\delta^{30}Si_{opal}$ record shows a large variability, whereby the highest values (+1.4‰) are in good agreement with values found today in the region of moderate upwelling. They indicate surface water $\delta^{30}Si_{Si(OH)4}$ values of +2.5‰, assuming a fractionation factor between diatoms and seawater of -1.1‰ (De La Rocha et al., 1997), and a utilisation of $Si(OH)_4$ between 60% (for Rayleigh-type fractionation) and 90% (for steady state-type fractionation) (Fig. 4.6). The lowest $\delta^{30}Si_{opal}$ values (+0.3‰) in the downcore record, which were accompanied by minima in $bSiO_2$ content, require lower surface water dissolved $\delta^{30}Si_{Si(OH)4}$ values of about +1.4‰. The low values correspond to the value of the subsurface source water, and are only insignificantly lower than what is found today in the areas of strongest upwelling along the Peruvian shelf (Chapter 3). This corresponds to an almost absent utilisation of $Si(OH)_4$ in the surface water for both types of fractionation (Fig. 4.6).

This is, however, contrary to the observed present day distribution because low $bSiO_2$ accumulation would have been expected to occur due to a limitation of $Si(OH)_4$ supply, which would then have caused a higher fractionation in $\delta^{30}Si$ (De La Rocha et al., 1998). Thus the observed correlation between low $bSiO_2$ content and low $\delta^{30}Si_{opal}$ rather indicates that diatom growth along the Peruvian upwelling area in the past was not ultimately limited by $Si(OH)_4$ supply, as also proposed by Dugdale and Wilkerson (1998), but that other micro- or macronutrients, such as Fe or P, controlled diatom productivity (see also Moore et al., 2004; Pichevin et al., 2009; Brzezinski et al., 2011). Diatoms have a high demand of Fe and P for their growth (Sunda and Huntsman, 1995). In the EEP the major inputs of Fe and P do not originate from dust supply (Brink et al., 1983) but their main source is remineralisation from the shelf sediments (Froelich et al., 1988; Noffke et al., unpublished, 2011). This source is most efficient under strongly oxygen-depleted bottom water conditions (Ingall and Jahnke, 1994; McManus et al., 1997). Several studies (Gutierrez et al., 2008; Fuenzalida et al., 2009) have shown that the upper vertical boundary of the OMZ has changed over time, mostly related to pronounced El Nino events, during which the upwelling-driven nutrient supply to the euphotic zone along the Peruvian shelf has been reduced (Huyer et al., 1987). This has led to a decrease in primary productivity (Feldman et al., 1984; Chavez et al., 2005), less oxygen consumption through decay of organic matter, which in turn has led to decreased Fe and P supply from the underlying sediments. Under Fe-limited conditions, however, diatoms reveal a higher Si:N uptake ratio (are more strongly silicified, but also more likely $Si(OH)_4$ limited) (Takeda, 1998; Hutchins et al., 2002; Baines et al., 2010) which leads to an increased export of Si (from $bSiO_2$), relative to N and P, and which consequently affects the interpretation of the $bSiO_2$ record in terms of nutrient utilisation. This means that the phases of highest $bSiO_2$ content in the sediment in the late and the early Holocene were the only periods of time, during which upwelling was at least temporarily reduced (due to El-Nino like conditions) resulting in a reduced Fe-supply and enhanced $Si(OH)_4$ limitation because of the increased Si-demand under Fe-limiting conditions. Comparison with alkenone-derived sea surface temperatures (SSTs) supports this idea (Fig. 4.4) (Rein et al., 2005). The highest SSTs indicating weakest upwelling occur

during the late Holocene, whereas a more invariant record of the surface temperatures was found for the early Holocene.

4.4.2.2 Past Changes in Circulation and Weathering Inputs

The $\varepsilon Nd_{coating}$ signature in the record has not varied significantly over the past 20 kyr. At the shallow site of core 106KL a significant change in circulation should have been related to changes in upwelling intensity. Under strong upwelling conditions the strongest influence by the southward flowing subsurface PCUC is expected. Under weaker upwelling conditions, associated with a widening of the thermocline, the influence of northward directed surface currents, such as the PCC or the PCoastalC may have been increased (Huyer et al., 1987). However, Grasse et al. (unpublished, 2011) have shown that along the coast the surface waters display a wide range in εNd but the water masses below do not differ significantly from each other in their εNd signature, which is supported by Fig. 4.3c also not indicating significant variations. Therefore, a change in $\varepsilon Nd_{coating}$ may not expected even if changes in mixing relationships between these water masses occurred.

In contrast, the $\varepsilon Nd_{detritus}$ signature has varied strongly over the past 20 kyr, in particular during the late Holocene. This indicator of provenance change of transported material provides more robust insights into circulation changes of the past than $\varepsilon Nd_{coating}$ or $\delta^{30}Si$. More radiogenic $\varepsilon Nd_{detritus}$ values are related to a more northerly source region in the Peruvian hinterland (Fig. 3.2b and 3.5), whereas less radiogenic values are ascribed to a more local origin from central or southern Peruvian sources. As described for the surface sediments, the $\varepsilon Nd_{detritus}$ can be used to trace provenance because the isotope composition is not affected by chemical weathering or grain-size sorting, whereas the radiogenic $^{87}Sr/^{86}Sr_{detritus}$ is strongly influenced by grain-size effects during chemical weathering (Tütken et al., 2002). Stronger offsets from source signatures towards higher $^{87}Sr/^{86}Sr_{detritus}$ can therefore also be a reflection of stronger incongruent chemical weathering effects, most likely due to stronger rainfall in the hinterland, which mainly occurred during El Nino events (Waylen and Caviedes, 1984; Bendix, 2000). In the following,

the paleoenvironmental reconstruction for three different timeslices, the glacial, the early Holocene and the late Holocene will be discussed in more detail.

4.4.2.3 Reconstruction of the Last Glacial

Several studies have proposed that during the last glacial period unused $Si(OH)_4$ from the Southern Ocean was transported into the tropical upwelling areas via Subantarctic Mode Water, where it supposedly promoted enhanced diatom productivity (Silicic Acid Leakage Hypothesis) (e.g. Nozaki and Yamamoto, 2001; Brzezinski et al., 2002). This, however, contradicts tropical Pacific records, which do not indicate increased $bSiO_2$ content or fluxes during the last glacial (Pichevin et al., 2009; Dubois et al., 2010; this study).

Others argued that the low glacial $bSiO_2$ productivity may have occurred due to persistent El Nino-like conditions in the tropical Pacific (Bradtmiller et al., 2006), which weakened upwelling and therefore decreased Fe and $Si(OH)_4$ supply to the euphotic zone. Alternatively, the missing increase in low latitude opal productivity may indicate a Pacific-wide overall reduced nutrient supply to the tropics within thermocline waters during the last glacial due to reduced vertical mixing in the Southern Ocean (Loubere et al., 2011), which would have limited productivity independent of the strength of upwelling. Such conditions would, however, favour a higher degree of utilisation of $Si(OH)_4$ by diatoms, which would result in higher $\delta^{30}Si_{opal}$ values. This is not observed in the glacial records of the EEP. In contrast to the present situation, where most of the Fe and P is supplied into the surface waters via remineralisation and upwelling of subsurface water, dust-related Fe input in the EEP was at least 30% higher during the glacial (McGee et al., 2007), which contributed to weaker silicification of the diatoms and thus also lower $Si(OH)_4$ utilisation.

Today the $\delta^{30}Si$ source signature delivered, among other, via the EUC has a $\delta^{30}Si_{Si(OH)4}$ signature of +1.5‰ (Beucher et al., 2008; Chapter 3). During the glacial, however, this source signature may have been different due to changes in the preformed $Si(OH)_4$ concentration and origin of the source water (Brzezinski et al., 2002), a changed utilisation or remineralisation processes along the EUC flowpath, or a reorganisation of the circulation in the region (Mohtadi et al., 2008). Therefore

much lower values are reasonable and are consistent with an overall reduced productivity and $Si(OH)_4$ utilisation. Assuming the same source signature for the source waters would indicate very low $Si(OH)_4$ utilisation, because $\delta^{30}Si_{opal}$ was only +0.4‰, and consequently the surface water $\delta^{30}Si_{Si(OH)4}$ above was only +1.5‰, indicating almost zero $Si(OH)_4$ utilisation (Fig. 4.6) (Chapter 3).

The isotope signature of the glacial detritus was most radiogenic for $\varepsilon Nd_{detritus}$ and least radiogenic for $^{87}Sr/^{86}Sr_{detritus}$, indicating contributions from northern Peru (Fig. 4.5). Possible El Nino like conditions would have resulted in enhanced rainfall, which would then have delivered larger amounts of local detrital material with less radiogenic $\varepsilon Nd_{detritus}$ signatures and a higher $^{87}Sr/^{86}Sr_{detritus}$ (Fig. 4.2a, b) to the shelf. Indications for such a process are, however, missing during the last glacial. Therefore, we propose that the Peruvian shelf was not influenced by El Nino-like conditions but rather characterised by stronger upwelling.

4.4.2.4 The Early Holocene off Peru

In contrast to the LGM, the $bSiO_2$ flux and content (20 wt%) were very high during the early Holocene at the location of the core (Fig. 4.4). At the same time, the $\delta^{30}Si_{opal}$ increased to higher values around 1.2‰, which is slightly higher than the values measured in surface sediments in that area ($\delta^{30}Si \sim +0.9‰$) (Chapter 3). De Vries and Schrader (1981) argued that the high diatom concentration along the Peruvian shelf during the late Pleistocene may have been related to a change in diatom assemblage towards more dissolution-resistant species (due to a slight northward shift of the upwelling cell from 14-16°S to 12-14°S, in which the diatoms are more dissolution-resistant). However, the relatively high $\delta^{30}Si_{opal}$ values prove that the change in $bSiO_2$ content in the record was related to a change in $Si(OH)_4$ utilisation and was not a consequence of enhanced preservation. Increased $bSiO_2$ accumulation and high $\delta^{30}Si_{opal}$ values at the same time indicate higher nutrient concentrations in the water column but also higher $Si(OH)_4$ utilisation during the early Holocene. During that time, the SSTs were higher, but also less variable than during the remainder of the record (Fig. 4.4) (Rein et al., 2005) indicating periodically weaker upwelling.

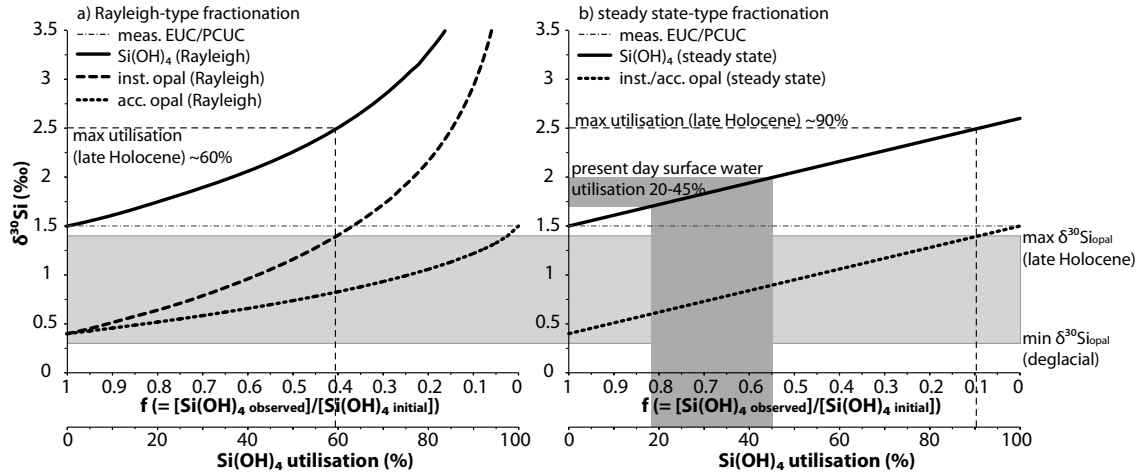

Figure 4.6: Theoretical changes in $\delta^{30}Si$ values of seawater (solid lines) and instantaneous and accumulated $bSiO_2$ (dashed and pointed lines) as a function of f (remaining $Si(OH)_4$ from the available pool) with an initial $\delta^{30}Si$ value of +1.5‰. Precipitation of opal follows either a) a Rayleigh-type fractionation model or b) a steady state system behaviour applying a fractionation factor of -1.1‰ (De La Rocha et al., 1997). The light grey shaded area marks the range of observed $\delta^{30}Si_{opal}$ values in the downcore record between +0.3‰ during the deglacial and +1.4‰ during the late Holocene. The dark grey shading in b) represents theoretical present day surface water utilisation in the area between 10°S to 14°S ranging up to 45% (Chapter 3). Vertical dashed lines mark calculated maximum (late Holocene) surface water $\delta^{30}Si_{Si(OH)4}$ values of +2.5‰ and respective $Si(OH)_4$ utilisation of 60% (a) and 90% (b). Minimum utilisation is 0%.

Prior to the early Holocene, the $\varepsilon Nd_{detritus}$ showed a trend towards less radiogenic signatures reaching values as low as of -2.5 (Fig. 4.4). At the same time the $^{87}Sr/^{86}Sr_{detritus}$ moderately increased. During the subsequent early Holocene, however, the trend reversed and the $\varepsilon Nd_{detritus}$ returned to values around -1.5, whereas the $^{87}Sr/^{86}Sr_{detritus}$ remained at the same level. These trends indicate a change of the atmospheric circulation. Alternating El Nino- and La Nina-like conditions must have prevailed causing periodically higher local material input with less radiogenic $\varepsilon Nd_{detritus}$ signatures and stronger chemical weathering due to enhanced rainfall causing higher $^{87}Sr/^{86}Sr_{detritus}$ values. Although the SSTs were high, the trend in $\varepsilon Nd_{detritus}$ from less radiogenic towards more radiogenic values between 10 to 9 ka most likely resulted from a shift from more El Nino-like towards more La Nina-like conditions with stronger upwelling accompanied by a subsurface current strengthening and a shift of the provenance from more southern towards more central Peruvian origin (Fig. 4.5). Under stronger upwelling conditions, the material transport within the southward directed currents (PCUC) was obviously enhanced.

Similar to our observations, and in contrast to the results by Rein et al. (2005), Carré et al. (2005) found that SSTs were about 3°C colder during the early Holocene compared to the late Holocene, indicating stronger upwelling conditions during that time. Vargas et al. (2006) on the other hand found several debris flows in southernmost Peru dated for the time period 12.9 to 8.4 ka BP, which were interpreted to be associated with intense rainfall episodes that must have occurred during non-El Nino conditions, concomitant with intensified coastal upwelling. These different findings indicate the high variability during the early Holocene with warm SSTs (Fig. 4.4), variable marine bioproductivity and strong El Nino related flooding events.

4.4.2.5 The Late Holocene off Peru

All proxies document a highly variable environment along the Peruvian shelf during the late Holocene. The $bSiO_2$ flux increased strongly around 2 ka resulting in high contents reaching up to 20-30 wt%. This was accompanied by the highest $\delta^{30}Si_{opal}$ signatures of up to +1.4‰. Calculating surface water $\delta^{30}Si_{Si(OH)4}$ values of +2.5‰ results in estimates for $Si(OH)_4$ utilisation between 60 to 90% (Fig. 4.6), which is the highest during the past 20 kyr. 90% utilisation can be found today in the areas of weaker upwelling and lower nutrient re-supply to the surface water (Chapter 3). The $\varepsilon Nd_{detritus}$ signal showed the largest variability within the past 20 kyr. It was characterised by a pronounced decrease from -1.5 to values around -4.5 between 4 and 1.2 ka. The surface sediment in that area is also characterised by less radiogenic $\varepsilon Nd_{detritus}$ values around -3.2 compared to the areas further north. In particular, the signatures of the last 2 kyr have been very different from the rest of the record. The highly unradiogenic $\varepsilon Nd_{detritus}$ and radiogenic $^{87}Sr/^{86}Sr_{detritus}$ could be derived via dust input from the Atacama desert in southern Peru and northern Chile (Molina-Cruz, 1977). However, climatic reconstructions indicate a general southward shift in the mean position of the Intertropical Convergence Zone (ITCZ) during the Holocene (Haug et al., 2001), which caused higher precipitation in the Peruvian region (Bendix, 2000; Baker et al., 2001) and a more local input of material. The strong offset in $^{87}Sr/^{86}Sr_{detritus}$ from these source area signatures (Fig. 4.5) indicate stronger weathering and

material transport from the hinterland due to higher rainfall activity related to strong El Nino conditions. At the same time high $bSiO_2$ content and high $Si(OH)_4$ utilisation require stronger upwelling of nutrient-rich subsurface waters, which usually occurs during La Nina-like conditions. These conditions alternating on a seasonal and interannual time scales left their signal in the sedimentary record. The observed timing in our record confirms that ENSO patterns only operated during the second half of the Holocene and that the onset modern ENSO conditions did not occur before 5.5 kyr BP, with increased frequency of major events only during recent times (Loubere et al., 2003; Carré et al., 2005; Vargas et al., 2006). It was only during the latest late Holocene in the past 2 to 3 kyr that the Peruvian shelf area experienced persistently more moderate productivity conditions, with shorter periods of increased productivity (Agnihotri et al., 2008).

4.5 Conclusions

Surface sediments along the Peruvian margin were analysed for their radiogenic Nd isotope composition, and compared to water column measurements from the same area. In general, all phases (seawater, Fe-Mn coatings, benthic foraminifers and detrital material) display a trend from more radiogenic values in the north towards less radiogenic values in the south, which is in good agreement with the distribution of the signatures of the outcropping rocks of the Andean hinterland. This indicates that there has been extensive exchange between sediments and water column, which makes it difficult to use the εNd signatures obtained from Fe-Mn coatings or from benthic foraminiferal carbonate as a water mass tracer. However, the εNd in the coatings and in the benthic foraminifers from within the subsurface water of the PCUC (50 m to 200 m water depth) are in good agreement with the water column measurements and do not show a trend with latitude, whereas the detrital material from the same samples is significantly less radiogenic. This indicates that the shallow sites are less affected by any sediment-water column exchange processes.

Combined $\delta^{30}Si_{opal}$ and εNd and $^{87}Sr/^{86}Sr$ in coatings and detrital material have been analysed to reconstruct surface water $Si(OH)_4$ utilisation by diatoms and upwelling intensity during the past 20 kyr. The $\delta^{30}Si_{opal}$ varied between low

values of +0.3‰, indicating almost no $Si(OH)_4$ utilisation, and +1.4‰, which corresponds to a utilisation of 60 to 90%. Most of the time both $bSiO_2$ flux and $\delta^{30}Si_{opal}$ were low, which is attributed to the fact that diatom productivity along the Peruvian shelf was ultimately not limited by $Si(OH)_4$ availability, but by Fe and P supply. During times of weaker upwelling (e.g. the early Holocene but also during the late Holocene) Fe remineralisation from the sediments was low causing Fe-stress for diatoms. Under such conditions their demand for $Si(OH)_4$ increased which caused a higher degree of utilisation. Accordingly, the early and the late Holocene, although being characterised by the highest $bSiO_2$ content in the sediment, were the times of periodically weaker upwelling (and probably also the weakest OMZ). The Nd and Sr isotope signatures of the detrital material support this interpretation. Both time periods were characterised by relatively unradiogenic εNd and high $^{87}Sr/^{86}Sr$ signatures characteristic for material input from the close hinterland. This input mainly occurred via riverine discharge during El Nino (like) conditions, when rainfall was high and upwelling intensity was low. Both, $\delta^{30}Si_{opal}$ and the radiogenic Nd and Sr isotope compositions of the detrital material document that strongest El Nino conditions of the past 20 kyr were operating only during the late Holocene during the past 5 kyr.

Acknowledgments

This work is a contribution of the Sonderforschungsbereich 754 "Climate - Biogeochemistry Interactions in the Tropical Ocean" (www.sfb754.de) which is supported by the Deutsche Forschungsgemeinschaft.

Chapter 5

Evolution of Nutrient Utilisation and Weathering Inputs in the Peruvian Upwelling Since the Little Ice Age

Abstract

For this study two cores from the Peruvian shelf covering the period of time between the Little Ice Age (LIA) and present were examined. Both indicate weak primary productivity (diatom opal productivity) during the LIA. The stable silicon isotope composition of diatom opal ($\delta^{30}Si_{opal}$) show moderate degrees of utilisation of silicic acid ($Si(OH)_4$) in the surface waters during that time. Additionally, the radiogenic isotope composition of Nd and Sr (εNd and $^{87}Sr/^{86}Sr$) of the detrital sediment fraction were predominantly influenced by local riverine input of lithogenic material due to higher rainfall in the Andean hinterland. These patterns can only be caused by permanent El Nino-like conditions, diminished upwelling and low nutrient supply. At the end of the LIA (between ca. 1800 and 1820 AD) upwelling strength increased. Especially $Si(OH)_4$ and iron (Fe) remineralisation from the shelf sediments was enhanced causing higher nutrient supply and biological productivity. The time period between 1820 and 1865 AD was characterised by recurring periods of upwelling relaxation. Productivity was still high at that time causing the strongest degrees of nutrient utilisation during the past ~600 years. After 1865 AD until present utilisation remained high but the utilisation was somewhat lower indicating that much more nutrients were available. In contrast to the LIA, the detrital εNd and $^{87}Sr/^{86}Sr$ signatures indicate increased material supply to the shelf via dust due to drier conditions under more persistent non-El Nino conditions irregularly interrupted by strong El-Nino years. The comparison between $\delta^{30}Si_{opal}$ and bulk $\delta^{15}N$ of organic matter suggests that

---

This chapter is going to be submitted as:

Ehlert, C., P. Grasse, D. Gutierrez, R. Salvatecci, & M. Frank. Evolution of nutrient utilisation and weathering inputs in the Peruvian Upwelling since the Little Ice Age.

the $\delta^{15}N$ signature recorded in the sediment has primarily been influenced by surface water utilisation processes and not, as previously assumed, by subsurface water nitrate reduction processes.

5.1 Introduction

The global climate of the late Holocene was disrupted by major anomalies, such as the Little Ice Age (LIA) between ca. 1400 to 1850 AD (Lamb, 1965; Grove, 2001). During that time a southward shift in the mean position of the Intertropical Convergence Zone (ITCZ) compared to today's position (Haug et al., 2001; Koutavas and Lynch-Stieglitz, 2004; Mann et al., 2005; Newton et al., 2006) caused cooling and large expansions of mountain glaciers in the northern hemisphere (Broecker, 2000; Cronin et al., 2003), as well as pronounced changes in rainfall patterns in the tropics (Haug et al., 2001; Rein et al, 2004; Newton et al., 2006; Graham et al., 2007, 2010). The Peruvian region is in particular influenced by El Nino Southern Oscillation (ENSO), which exerts control on circulation, biological productivity and ecosystem structure (Alheit and Niquen, 2004; Pennington et al., 2006). During El Nino events the Pacific region also experiences a mean southward shift of the ITCZ (Fedorov and Philander, 2000). Consequences are weaker trade winds and reduced coastal upwelling of nutrient-rich subsurface waters along the Peruvian shelf causing a reduction in primary productivity (Barber and Chavez, 1983; Fiedler, 2002) and higher precipitation in the Andean hinterland (Bendix, 2000; Baker et al., 2001)

Sediments from the Peruvian shelf, which cover the period of time from the LIA until present, indicate that the marine realm was characterised by an abrupt biogeochemical regime shift at the end of the LIA between ca. 1820 to 1870 AD. While low productivity and a more oxygenated water column prevailed during the LIA, markedly increased biological productivity and pronounced oxygen depletion over wide areas of the shelf have characterised the system from the end of the LIA until present day (Vargas et al., 2007; Sifeddine et al., 2008; Gutierrez et al., 2009).

In this study the stable silicon isotope composition of diatoms ($\delta^{30}Si_{opal}$) in sediments covering the period of time from the LIA to the present were analysed. The main goal was the reconstruction of the factors that have controlled the

dynamics of silicate and other nutrients and oxygen in the Peruvian upwelling, in particular in comparison with the nitrogen isotope composition ($\delta^{15}N$) of sedimentary organic matter. Both $\delta^{30}Si$ and $\delta^{15}N$ provide information about utilisation of silicic acid ($Si(OH)_4$) and nitrate (NO_3^-) during primary productivity, e.g. during the formation of diatom frustules (Altabet and Francois, 1994; De La Rocha et al., 1997, 1998).

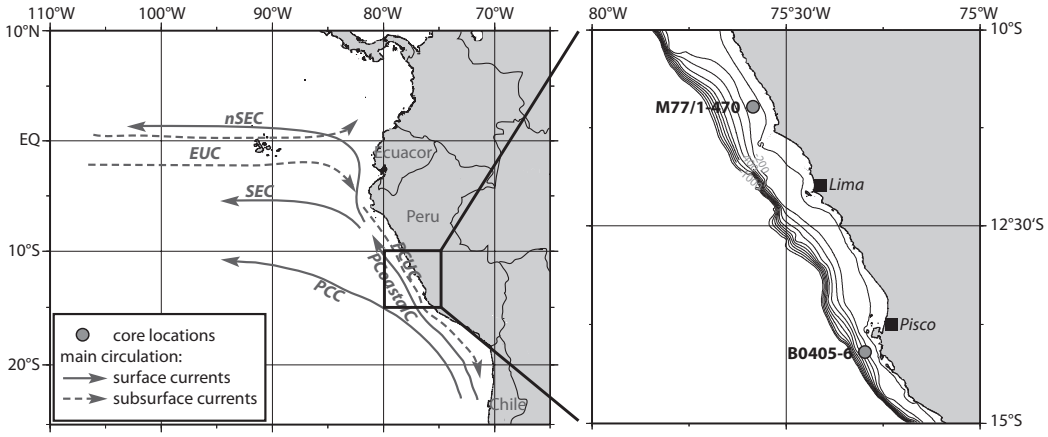

Figure 5.1: Schematic main circulation in the eastern equatorial Pacific, surface currents (solid lines): (n)SEC (northern) South Equatorial Current, PCC Peru-Chile Current, PCoastalC Peru Coastal Current, subsurface currents (dashed lines): EUC Equatorial Undercurrent, PCUC Peru-Chile Undercurrent (after Strub et al., 1998; Kessler, 2006; Karstensen and Ulloa, 2008; and ADCP data according to Czeschel et al., 2011), the inset marks the location of the two cores M77/1-470 and B0405-6 (grey dots). The bathymetry is given for 0 to 1000 m water depth in 100 m increments.

Diatoms preferentially incorporate the lighter isotopes from the dissolved nutrient pool leaving the residual waters enriched in the heavier isotopes (Wada and Hattori, 1978; Altabet et al., 1991; De La Rocha et al., 1997). For the $\delta^{30}Si_{opal}$ this fractionation process is mainly controlled by the availability of $Si(OH)_4$. (Chapter 3). The $\delta^{15}N$ of dissolved nitrate is partly controlled by NO_3^- utilisation during biological production but is also affected by NO_3^- reduction processes in the water column (denitrification, anammox) (Codispoti et al., 2001; Dalsgaard et al., 2003), resulting in a marked enrichment of the upwelling source waters in the heavier ^{15}N (Liu and Kaplan, 1989; Brandes et al., 1998). Therefore, sedimentary $\delta^{15}N$ from an area with oxygen-depleted waters is usually interpreted to reflect changes in the intensity of subsurface NO_3^- reduction and the extent of oxygen depletion (De Pol-Holz et al., 2007, 2009; Agnihotri et al., 2008; Gutierrez et al.,

2009). Comparison of both isotope systems provides information about the degree of utilisation of nitrate and silicate versus the influence of NO_3^- reduction.

In addition, the radiogenic isotope compositions of neodymium (εNd) and strontium ($^{87}Sr/^{86}Sr$) in authigenic ferromanganese (Fe-Mn) oxyhydroxide coatings and in the detrital fraction of the sediment were used to detect changes in transport, provenance and input mechanisms of terrigenous material as a function of changes in precipitation on land and in surface circulation. Past bottom water isotopic compositions can be reconstructed from Fe-Mn coatings of the bulk sediments particles ($\varepsilon Nd_{coating}$) (Rutberg et al., 2000; Gutjahr et al., 2007). Water masses can be traced by their Nd isotope composition due to weathering of continental rocks with distinct isotopic signatures in their source regions. These signatures are supplied to the oceans via rivers, eolian inputs or through shelf exchange processes (e.g. Frank, 2002; Lacan and Jeandel, 2005). Source regions for water masses influencing the Eastern Equatorial Pacific (EEP) are the Southern Ocean, which supplies less radiogenic signatures between -5 and -9 (Piepgras and Jacobsen, 1988), and the northern and central Pacific, delivering more radiogenic signatures around -2 (Lacan and Jeandel, 2001; Grasse et al., unpublished, 2011). Additionally, weathering of continental source rocks also delivers lithogenic particles to the shelf with different origin and age, which have distinct radiogenic isotope signatures ($\varepsilon Nd_{detritus}$, $^{87}Sr/^{86}Sr_{detritus}$), which can be used to trace their source areas (Goldstein et al., 1984; Dia et al., 1992; Fagel et al., 2004) (Chapter 4). Changes in detrital material input and transport pathways are generally closely related to climatic changes causing variations in the respective source areas (Grousset et al., 1988; Fagel et al., 2004; Ehlert et al., 2011; Stumpf et al., 2011).

5.2 Material and Methods

5.2.1 Core Locations, Age Models and Sampling

For the reconstruction of surface water $Si(OH)_4$ utilisation and material transport during the past few hundred years between the LIA and present two short cores were analysed. Box core B0405-6 was recovered from the upper slope off Pisco at 14°07.9' S, 76°30.1' W in a water depth of 299 m with the Peruvian R/V José Olaya Balandra in 2004 (Fig. 5.1) (Gutierrez et al., 2006). The age model was

previously published by Gutierrez et al. (2009) and is based on downcore profiling of ^{241}Am and excess ^{210}Pb and radiocarbon ages obtained from bulk organic sedimentary carbon, which demonstrate that the core covers the past ~600 years. The second core, multicorer M77/1-470, was taken at 11° S, 77°56.6' W in 145 m water depth (Fig. 5.1). At the time of writing of this manuscript samples for the age determination of this core were still in progress. The preliminary age model of core M77/1-470 is therefore based on cross-correlation with the record of core B0405-6. The prominent increase in $bSiO_2$ to maximum values (Fig. 5.2a, e), which is also reflected by the organic carbon content (not shown), is obvious in both cores and corresponds to an age of 1820 to 1850 AD in the Pisco core (Gutierrez et al., 2009).

5.2.2 Methods

5.2.2.1 Biogenic Opal and Silicon Isotope Analyses

The $bSiO_2$ contents in both cores were measured following the sequential leaching techniques described by DeMaster (1981) and Müller and Schneider (1993). Silicon isotope analyses were performed on the 11-23 µm diatom-fraction that was extracted from the sediment applying the procedures described by Morley et al. (2004). In the first step ~300 mg of the previously freeze-dried sediment was treated with 30% H_2O_2 and 35% HCl to remove the organic and carbonate fractions. Afterwards the sediment was washed through 32 µm and 11 µm sieves and in a third step the diatoms were separated from the detrital mineral fraction using a heavy-liquid separation (sodium-polytungstate, 2.1-2.2 g/mL). The cleaned diatoms were then dissolved in a 0.1 M NaOH at 130°C on a hotplate for several hours (Reynolds et al., 2008). Si concentrations of the dissolved diatom samples were measured colorimetrically using a photospectrometer (Hansen and Koroleff, 1999). Chromatographic separation and purification of the Si was achieved with 1mL pre-cleaned AG50W-X8 cation exchange resin (mesh 200-400) (Georg et al., 2006b). Si isotope ratios were measured on a *NuPlasma HR* MC-ICPMS (Nu Instruments) at IFM-GEOMAR, Kiel, equipped with an adjustable source-defining slit, which can be set to medium resolution to ensure peak separation of the ^{30}Si peak and molecular interferences. The measurements were

carried out applying a standard-sample bracketing method (Albarède et al., 2004). All solutions were measured at a Si concentration of 14-21 µmol/kg depending on the performance of the instrument on the respective measurement day and were introduced into the plasma via a Cetac Aridus II desolvating nebulizer system equipped with a PFA nebulizer yielding a 60 to 80 µL/min uptake rate. Si isotope compositions are reported in the $\delta^{30}Si$ notation giving the deviations of the measured $^{30}Si/^{28}Si$ from the international Si standard NBS28 in parts per thousand (‰). Repeated measurements of the reference materials IRMM018 and Big Batch gave average $\delta^{30}Si$ values of -1.52 ± 0.18‰ ($2\sigma_{(sd)}$) and -10.84 ± 0.18‰ ($2\sigma_{(sd)}$), respectively, which are in agreement with values obtained by other laboratories (Reynolds et al., 2007). Samples were measured on at least two separate sessions, and three to five times within one session (during one day), which generally resulted in uncertainties between 0.04 and 0.23‰ ($2\sigma_{(sd)}$) (Tables A.6 and A.7). All error bars for Si isotope compositions provided in the figures correspond to that reproducibilities. Replicate measurements of an in-house diatom matrix standard over longer periods of time (n = 20 sessions within one year) gave an external reproducibility of 0.25‰ ($2\sigma_{(sd)}$).

5.2.2.2 Neodymium and Strontium Isotope Analyses

To obtain the radiogenic isotope composition of past seawater above the sites of the sediment cores from the early diagenetic Fe-Mn coatings of the sediment particles, previously published methods were applied (Gutjahr et al., 2007; Stumpf et al., 2010). First, the carbonate fraction was removed from the freeze-dried and homogenized sediment samples using a 15%-acetic acid/1 M Na-acetate buffer solution. Afterwards, the authigenic Fe-Mn oxyhydroxide fraction was leached from the sediment with a 0.05 M hydroxylamine hydrochloride/15%-acetic acid solution buffered to pH 3.8 with NaOH. After repeated leaching, the detrital isotope signal was extracted from the residual dried bulk fraction of the sediments, which was treated with a mixture of concentrated HF-HNO_3-HCl until total dissolution. The separation and purification of Nd and Sr in the leachates and in the completely dissolved detrital sediment fraction followed previously published procedures for Nd (Cohen et al., 1988) and Sr (Horwitz et al., 1992)

applying ion exchange columns for cation separation (0.8 mL AG50W-X12 resin, mesh 200-400) and subsequent separation of Sr from Rb (50 µL Sr-Spec resin, mesh 50-100), and separation of Nd from the other REEs (2 mL Eichrom Ln-Spec resin, mesh 50-100). All radiogenic isotope measurements were performed on the *NuPlasma HR* MC-ICPMS (Nu Instruments) at IFM-GEOMAR. Measured Nd isotope compositions were corrected for instrumental mass bias using a $^{146}Nd/^{144}Nd$ of 0.7219 and were normalised to the JNdi-1 standard with an accepted literature value for $^{143}Nd/^{144}Nd$ of 0.512115 (Tanaka et al., 2000). All values are given as εNd, which corresponds to the measured $^{143}Nd/^{144}Nd$, normalised to the Chondritic Uniform Reservoir CHUR (0.512638), multiplied by 10,000. The external reproducibility was estimated by repeated measurements of the JNdi-1 standard and was always better than 20 ppm ($2\sigma_{(sd)}$, Tables A.6 and A.7). Measured $^{87}Sr/^{86}Sr$ ratios were corrected for instrumental mass bias using $^{88}Sr/^{86}Sr = 8.3752$ and were normalised to the accepted value for NIST SRM987 of 0.710245. The $2\sigma_{(sd)}$ external reproducibility of repeated standard measurements was always better than 36 ppm ($2\sigma_{(sd)}$, Tables A.6 and A.7). Procedural Nd and Sr blanks for leachates and total dissolutions of the detrital material were ≤ 83 pg and 2.1 ng, respectively, which was negligible compared to sample concentrations.

5.3 Results

5.3.1 Core M77/1-470

The sediment of core M77/1-470, which is located at 11°S in 145 m water depth, is characterised by $bSiO_2$ concentrations ranging between 10.1 to 26.9 wt% (Fig. 5.2a, Table A.6), whereby the lowest values occurred near the proposed end of the LIA and the maximum values were found immediately after its end. The $\delta^{30}Si_{opal}$ varies between 0.6‰ and 1.1‰ and correlates well with $bSiO_2$ concentrations (Fig. 5.3a) with the maximum and minimum values corresponding to the same samples as for $bSiO_2$ concentrations. The $\varepsilon Nd_{coating}$ record only shows a small variability ranging from -1.2 to -2.3 with a mean value of -1.7 ± 0.7 ($2\sigma_{(sd)}$) and no significant trends are observable. The $\varepsilon Nd_{detritus}$ is characterised by less radiogenic values than the coatings between -3.6 and -5.2 with a mean value of -4.5 ± 1.0 ($2\sigma_{(sd)}$) (Table A.6). The $^{87}Sr/^{86}Sr_{detritus}$ signature in the same samples ranges

between 0.70647 and 0.70936. The variability of $\varepsilon Nd_{detritus}$ and $^{87}Sr/^{86}Sr_{detritus}$ is very similar in that both show a trend from less radiogenic $\varepsilon Nd_{detritus}$ and more radiogenic $^{87}Sr/^{86}Sr_{detritus}$ values at the beginning of the LIA towards more radiogenic values in $\varepsilon Nd_{detritus}$ and less radiogenic $^{87}Sr/^{86}Sr_{detritus}$ at the end of the LIA. Right after the LIA the trends in both records show a marked reversal, more pronounced in the Sr isotope than in the Nd isotope data, resulting in the youngest samples having the least radiogenic $\varepsilon Nd_{detritus}$ and the most radiogenic $^{87}Sr/^{86}Sr_{detritus}$ signatures. Surface sediments along the Peruvian shelf show highly variable signatures, which have more radiogenic εNd values in the North and much less radiogenic εNd values in the South off southern Peru and northern Chile (Chapter 4). This north-south trend is due to southward increasing contributions of material input from the adjacent Andean hinterland rocks, which show a similar trend in the signatures. The observed range, especially in $^{87}Sr/^{86}Sr_{detritus}$, in core M77/1-470 is large, and is comparable to the complete glacial-interglacial range in core SO-147-106KL (Chapter 4, Fig. 4.5 and 5.5).

5.3.2 Core B0405-6

In core B0405-6, which is located near 14°S in 299 m water depth, the range of $bSiO_2$ concentrations and maximum value are higher than in core M77/1-470 and vary between 12.6 to 37.7 wt% (Fig. 5.2e, Table A.7). The trend is nevertheless very similar to that of core M77/1-470 and correlates closely with the silica and diatom fluxes (Fig. 5.2e). The lowest values occurred at the end of the LIA and the highest values are found right after the end of the LIA. The $\delta^{30}Si_{opal}$ record shows the same range from 0.6‰ to 1.1‰ as core M77/1-470 and the same trend with the lowest values at the end of the LIA and the highest values right thereafter. No $\varepsilon Nd_{coating}$ signature was measured on that core because the available amount of sediment material was not sufficient any more. The $\varepsilon Nd_{detritus}$ signatures are characterised by slightly more radiogenic values than in core M77/1-470 ranging between -4.1 to -2.5 but the variability is essentially insignificant (mean value -3.2 ± 0.9, $2\sigma_{(sd)}$ excluding the value at 1761 AD, which is considered an outlier). The $^{87}Sr/^{86}Sr_{detritus}$ values range between 0.70711 and 0.70796, which is somewhat lower than in core M77/1-470. Similar to core M77/1-470 the main feature

observed is a pronounced trend from less radiogenic values in $^{87}Sr/^{86}Sr_{detritus}$ during the LIA towards more radiogenic values thereafter.

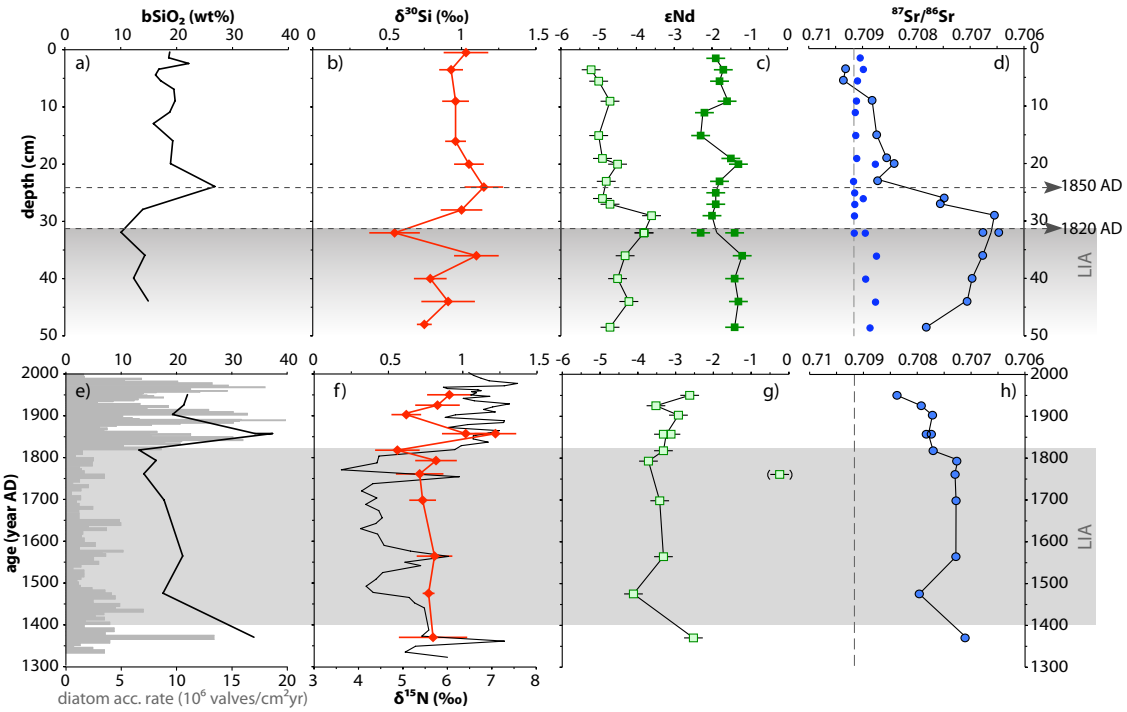

Figure 5.2: Downcore records for core M77/1-470 (upper panel) and core B0405-6 (lower panel), the grey bars indicate the time range of the LIA between ca. 1400 to 1820 AD (which is most likely not completely covered by core M77/1-470), and the grey dashed lines in the upper panel mark minimum and maximum $bSiO_2$ values corresponding to ages of ca. 1820 and 1850 AD in core B0405-6, a/e) $bSiO_2$ content (black curves), and diatom flux (grey bars) (Gutierrez et al., 2009), b/f) $\delta^{30}Si_{opal}$ (red diamonds) and bulk sediment $\delta^{15}N$ (black curve) (Gutierrez et al., 2009), c/g) εNd of Fe-Mn coatings (dark green squares) and detrital material (light green squares), d/h) $^{87}Sr/^{86}Sr$ of Fe-Mn coatings (dark blue dots) and detrital material (light blue dots), the dashed line marks the present-day seawater $^{87}Sr/^{86}Sr$ isotope composition (=0.70916). Error bars represent $2\sigma_{(sd)}$ external reproducibilities.

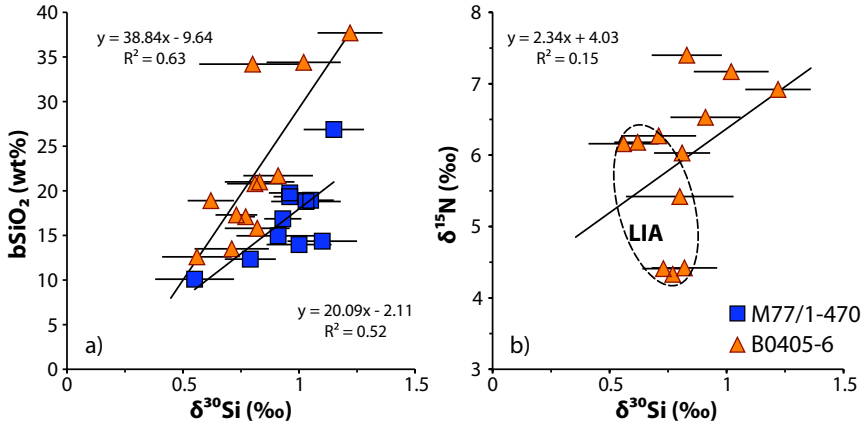

Figure 5.3: a) $\delta^{30}Si_{opal}$ versus $bSiO_2$ and b) $\delta^{30}Si_{opal}$ versus bulk sedimentary $\delta^{15}N$ for core M77/1-470 (blue squares) and B0405-6 (orange triangles). Error bars represent $2\sigma_{(sd)}$ external reproducibilities.

5.4 Discussion

Sediments from the Peruvian shelf, which cover the past few hundred years, indicate that the marine regime was characterised by an abrupt biogeochemical shift between ca. 1820 to 1870 AD (Vargas et al., 2007; Sifeddine et al., 2008; Gutierrez et al., 2009). The LIA between 1400 and 1820 AD was accompanied by a southward displacement of the ITCZ and the associated precipitation belt (Haug et al., 2001). El Nino-like warming (Bird et al., 2011a, b) and intensified South American summer monsoon precipitation in the tropical Pacific occurred, which was about 10 to 30% higher than today (Rabatel et al., 2008; Reuter et al., 2009) causing an extension of the Andean glaciers (Vuille et al., 2008) and allowing human settlements in the southern Peruvian Andes (Unkel et al., 2007). In the upwelling areas off Peru and along the western South American shelf regions the main consequence of these climatic conditions was a reduction in wind-driven coastal upwelling and a strong decrease in biological productivity (Vargas et al., 2007; Valdés et al., 2008; Gutierrez et al., 2009).

After 1820 AD, the mean position of the ITCZ shifted northward (Haug et al., 2001) causing intensification of coastal winds and upwelling strength and a decrease in precipitation (Rabatel et al., 2008; Bird et al., 2011a, b) and sea surface temperatures (Vargas et al., 2007). Records of productivity, denitrification and redox conditions, such as $\delta^{15}N$ or the Mo and Cd content of the sediments, indicated a rapid change in the source waters towards markedly different biogeochemical conditions characterised by lower subsurface oxygen and higher nutrient concentrations causing higher biological productivity, which have lasted until present day (Sifeddine et al., 2008; Gutierrez et al., 2009). This shift after the end of the LIA was a major anomaly in late Holocene climate in the eastern Pacific and of the same order of magnitude as the changes in conditions off Chile during the Younger Dryas (De Pol-Holz et al., 2006). This study focuses on two short cores from the Peruvian shelf, which cover the LIA and the time after, to reconstruct changes in nutrient utilisation and the factors influencing it.

5.4.1 Surface Water Nutrient Utilisation During and After the LIA

The pronounced change in the biogeochemical regime from low productivity during the LIA towards higher productivity thereafter, which could be observed in several cores from the EEP region (Vargas et al., 2007; Agnihotri et al., 2008; Sifeddine et al., 2008; Gutierrez et al., 2009), can also be observed in the two records studied here. The $bSiO_2$ content varies between 10 and 12 wt% before 1820 AD, and increases to values around 27 wt% in M77/1-470 and 38 wt% in B0405-6 after the end of the LIA (Fig. 5.2a, e, Tables A.6 and A.7). This increase in $bSiO_2$ correlates well with the increase in silica and diatom flux in core B0405-6 (Fig. 5.2e) (Gutierrez et al., 2009). Similar to the bSiO2, $\delta^{30}Si_{opal}$ in both cores is characterised by low values around +0.6‰ before the regime shift just before 1820 AD, and shows the highest values around +1.1‰ around 1850 AD. The correspondence between $bSiO_2$ content and $\delta^{30}Si_{opal}$ is more pronounced for core B0405-6 (Fig. 5.3a), which is probably due to its higher $bSiO_2$ variability.

Sedimentary $\delta^{15}N$ data, which are only available for core B0405-6, show a shift from lower values around +5‰ during the LIA to higher values around +7‰ after the end of the LIA at 1800 to 1850 AD and have remain at that level until present time (Fig. 5.2f) (Gutierrez et al., 2009). These values are in agreement with surface sediment $\delta^{15}N$ measured in the region ranging from +6‰ to +9‰ (Mollier-Vogel et al., unpublished, 2011). Bulk $\delta^{15}N$ signatures measured in a core at 11°S in 186 m water depth, which is very close to the location of core M77/1-470, showed very similar values and variability (Agnihotri et al., 2008). In contrast to the $\delta^{15}N$, the $\delta^{30}Si_{opal}$ signature is not only characterised by a simple increase at the end of the LIA. Instead, both $\delta^{30}Si_{opal}$ records show intermediate $\delta^{30}Si_{opal}$ signatures between +0.8‰ and +0.9‰ during the LIA, a pronounced short-term decrease to 0.6‰ at the end of the LIA followed by a marked increase right after the end of the LIA to values around +1.1‰, and finally return to intermediate values between +0.8‰ and +1.0‰ in the youngest part of the record. This difference in the trends in $\delta^{30}Si_{opal}$ and $\delta^{15}N$ is also reflected in the poor correlation coefficient between both proxies (Fig. 5.3b). Especially the samples from the LIA show a large deviation between $\delta^{15}N$ and $\delta^{30}Si_{opal}$ signatures.

The theoretical relationship between the degree of surface water nutrient utilisation and the stable isotopic composition of Si and N can be described

assuming either Rayleigh-type (fixed input followed by fractional loss or export) or steady state (constant supply and export at equilibrium) fractionation behaviour (Fig. 5.4). The lighter isotopes are preferentially incorporated into the diatom frustules and the organic matter, respectively, leaving the dissolved fraction enriched in the heavier isotopes (Wada and Hattori, 1978; Altabet et al., 1991; De La Rocha et al., 1997). The fractionation between $\delta^{30}Si$ in seawater and $\delta^{30}Si$ in the produced diatom opal is -1.1‰ (De La Rocha et al., 1997) and between $\delta^{15}N$ in seawater and $\delta^{15}N$ in organic matter is usually between -3‰ to -10‰ (Horn et al., 2011), and is assumed here to be -6‰ (Reynolds et al., 2008; Mollier-Vogel et al., unpublished, 2011). The $\delta^{30}Si_{opal}$ is only influenced by surface water diatom productivity and $Si(OH)_4$ utilisation and to some extent by advection of the different surface water masses. The $\delta^{15}N$ of the organic matter is influenced by NO_3^- uptake by phytoplankton. This NO_3^- supplied to the surface waters has, however, been enriched in ^{15}N due to upwelling from oxygen-depleted subsurface waters, which have undergone significant NO_3^- reduction (mostly denitrification, but also anammox processes) (Liu and Kaplan, 1989; Brandes et al., 1998; Altabet et al., 1999) and bulk sediment $\delta^{15}N$ from an area with oxygen depleted waters is therefore usually interpreted to reflect changes in the intensity of subsurface NO_3^- reduction and the extension of the oxygen minimum zone (Altabet et al., 1999; De Pol-Holz et al., 2007; Agnihotri et al., 2008; Gutierrez et al., 2009). Comparison of $\delta^{30}Si$ and $\delta^{15}N$ should therefore provide insight into the strength of NO_3^- reduction. Along the Peruvian shelf region biological productivity in the euphotic zone is driven by the upwelling of nutrients from subsurface waters. For the calculation of the utilisation of these nutrients, an initial $\delta^{30}Si_{Si(OH)4}$ of +1.5‰ (Chapter 3) and an initial $\delta^{15}N$ of +10‰ for those upwelled water masses at 14°S was assumed (Fig. 5.4) (Ryabenko, 2011; Mollier-Vogel et al., unpublished, 2011). The lowest $\delta^{30}Si_{opal}$ signatures of +0.6‰, which were measured at both locations for the end of the LIA (Fig. 5.2b, f), require surface water $\delta^{30}Si_{Si(OH)4}$ of +1.7‰. This is on the order of surface water $\delta^{30}Si_{Si(OH)4}$ measured today in the area of the strongest upwelling (Chapter 3), and corresponds to a calculated $Si(OH)_4$ utilisation of less than 20%, for both Rayleigh-type and steady state-type fractionation behaviour. The highest measured $\delta^{30}Si_{opal}$ signatures of +1.1‰ which occurred during the transition time

at the end of the LIA between 1845 to 1865 AD (Fig. 5.2b, f) correspond to a surface water $\delta^{30}Si_{Si(OH)4}$ of +2.2‰ and a degree of utilisation of 50 to 65% for Rayleigh-type and steady state-type fractionation, respectively (Fig. 5.4). Within a period of a few decades, the utilisation of available $Si(OH)_4$ had more than doubled, whereas the diatom flux increased by about a factor of 3 (Fig. 5.2e). The $\delta^{15}N$ of the organic matter changed at the same time from values around +5‰, reflecting a NO_3^- utilisation of 15%, to values around +7‰, which corresponds to 40 to 50% NO_3^- utilisation, depending on which fractionation model is applied (Fig. 5.4). These changes in $Si(OH)_4$ and NO_3^- utilisation are in the same order of magnitude and reflect low nutrient utilisation during the LIA and much higher degree of utilisation in the time after the LIA. These high levels of utilisation are still relatively low and are comparable to the centres of coastal upwelling today (Chapter 3; Mollier-Vogel et al., unpublished, 2011). The large shift in $\delta^{15}N$ after 1820 AD has been interpreted to reflect an expansion of the nutrient-rich, oxygen-poor subsurface waters (Gutierrez et al., 2009). However, comparison with $\delta^{30}Si_{opal}$ shows that indeed the extension of the oxygen minimum zone during recent times (Gutierrez et al., 2009) has not been reflected by the higher $\delta^{15}N$ values, but the increase only reflects higher surface water utilisation. As Mollier-Vogel et al. (unpublished, 2011) have shown, the subsurface enrichment of $\delta^{15}N_{NO3-}$ by NO_3^- reduction is only reflected in the sediments under near-complete surface water NO_3^- utilisation, which did obviously not occur at the studied sites and which is not expected to occur in this environmental setting.

5.4.2 Factors Influencing the Utilisation Signals

The similarity of the $\delta^{30}Si_{opal}$ signatures around 0.8‰ to 1.0‰ during the LIA and in the youngest part of the records shows that the utilisation of $Si(OH)_4$ was overall the same, although the amount of produced diatoms was much higher after the LIA (Fig. 5.2). This documents that the overall nutrient concentrations in the upwelled subsurface source waters were lower during the LIA than they are today. The LIA off Peru was characterised by a mean southward migration of the ITCZ (Haug et al., 2001). Recent El Nino events, which are a major climatic phenomenon in this region, are also accompanied by such southward shifts,

although on much shorter timescales (Fedorov and Philander, 2000). During such events, the zone of strong trade winds is also shifted southward causing a southward advection of surface nutrient poor equatorial and tropical water masses and a weakening of the associated coastal upwelling off Peru. The consequently reduced nutrient supply to the euphotic zone from subsurface waters and sediments results in decreased biological productivity, and organic matter degradation in the water column is less intense. Therefore, the extension of the oxygen-depletion in the water column is reduced. A lower $Si(OH)_4$ availability in the surface water is usually thought to cause a higher degree of utilisation, e.g. higher $\delta^{30}Si$ in the water and in the diatom opal (Chapter 3), which has obviously not been the case at the sites of our study. As shown before (Chapter 4), the Fe supply under such conditions is also strongly limited. Especially Fe, which is an important micronutrient for phytoplankton growth, is delivered to the surface waters along the Peruvian shelf via upwelling of subsurface waters and not via eolian or riverine input (Bruland et al. 2005; Noffke et al., unpublished, 2011). By the end of the LIA before 1820 AD upwelling strongly increased causing extensive vertical supply of remineralised nutrients from the underlying shelf sediments. This strong input of Fe caused a phytoplankton bloom. Under Fe-replete conditions the Si:N ratio in diatom frustules is lower (Sarthou et al., 2005; Wilken et al., 2011), which causes a lower $Si(OH)_4$ and a higher NO_3^- utilisation and consequently a lower $\delta^{30}Si_{opal}$ in the sediment and an earlier increase in $\delta^{15}N$, as observed in our records (Fig. 5.2f).

Under present day conditions the most abundant diatom species are *Chaetoceros sp*. (resting spores) and *Thalassionema nitzschioides* (Abrantes et al., 2007), both species indicative of strong upwelling (Koning et al., 2001; Abrantes et al., 2007). Analyses of the downcore diatom assemblage have shown that the high diatom and silica flux in core B0405-6 during the period between 1845 to 1865 AD, which corresponds to the highest $\delta^{30}Si_{opal}$ values, was dominated by high abundances of *Skeletonema costatum* (Gutierrez et al., 2009). This is a species, which blooms during relaxation of upwelling (Alvarez-Salgado et al., 2005) and which is today only highly abundant along the southern Chile margin (Abrantes et al., 2007). Thus during the transition time after the end of the LIA periodic

stratification events caused a reduction in nutrient and Fe supply causing higher utilisation in both $Si(OH)_4$ and NO_3^-.

The calculation of surface water nutrient utilisation depends on the assumed source water conditions. The assumed source water $\delta^{30}Si_{Si(OH)4}$ and $\delta^{15}N_{NO3-}$ values of +1.5‰ and +10‰, respectively, were measured in the present day subsurface waters under strong upwelling conditions supplying high amounts of nutrients to the euphotic zone. Under strong upwelling conditions the bottom waters on the shallow shelf are today dominated by the southward directed Peru-Chile Undercurrent (PCUC) (Fig. 5.1) (Brink et al., 1983), whereas under more El Nino-like conditions the influence of the PCUC diminishes and the northward directed surface currents of the Peru Coastal Current (PCoastalC) and Peru-Chile Current (PCC) expand both latitudinally and vertically in the water column (Kessler, 2006). This might change the source water signature, and would therefore change the calculated degrees of utilisation. However, there is no information to date how the source signature during times of weaker upwelling changed. Assuming a lower source water signature (e.g. due to weaker subsurface NO_3^- reduction and weaker ^{15}N enrichment) would result in a theoretical calculation of higher utilisation. On the other hand, a southward shift of the ITCZ causing weaker productivity off Peru also causes stronger upwelling and higher productivity further south (Mann et al., 2009). Here, the northward flowing surface waters underwent extensive utilisation, and transported therefore a pre-formed isotope signature to the Peruvian upwelling region. Such water masses would have a higher source signature, which would then result in even lower calculated degrees of utilisation in the surface waters during the LIA.

5.4.3 Changes in Detrital Material Input and Transport

Early diagentic Fe-Mn coatings in marine sediments have been shown to archive the dissolved εNd signature of (bottom) water masses. The signature is aquired in the source regions of water masses via weathering of continental rocks with distinct isotopic signatures and supply to the ocean by rivers, eolian input or through shelf exchange processes (Frank, 2002; Lacan and Jeandel, 2005). The eastern equatorial Pacific is influenced by two main different water mass sources.

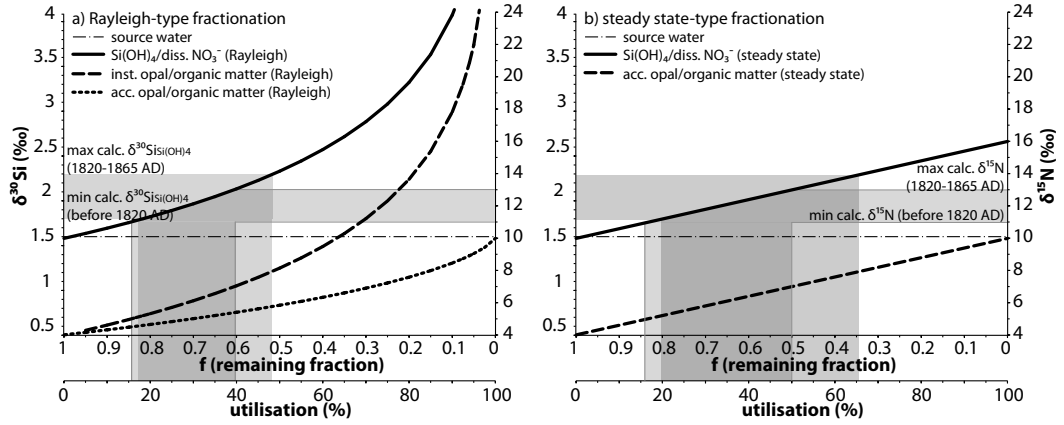

Figure 5.4: Theoretical changes in $\delta^{30}Si$ and $\delta^{15}N$ values of seawater (solid lines) and instantaneous and accumulated biogenic opal (dashed and pointed lines) as a function of f (remaining nutrients from the available pool = [$nutrient_{observed}$]/[$nutrient_{initial}$]) with an initial $\delta^{30}Si_{Si(OH)4}$ value of +1.5‰ and $\delta^{15}N_{NO3-}$ of +10‰. Precipitation of opal follows either a) Rayleigh-type fractionation or b) a steady state-type fractionation behaviour, with fractionation factors of -1.1‰ ($\delta^{30}Si$) and -6‰ ($\delta^{15}N$). The grey bars mark the maximum (min. = end-LIA, max. = post-LIA) range of calculated $\delta^{30}Si$ and $\delta^{15}N$ for surface waters and respective nutrient utilisation.

The central Pacific is characterised by more radiogenic signatures around -2 and waters of this origin are supplied to the EEP via the EUC/PCUC (Lacan and Jeandel, 2001; Grasse et al., unpublished, 2011). In contrast, the water masses of Southern Ocean origin are characterised by less radiogenic signatures around -8 (Piepgras and Jacobsen, 1988; Grasse et al., unpublished, 2011). Core M77/1-470 is located in 145 m water depth, which is in the core depth of the PCUC (Fig. 5.1) (Brink et al., 1983). The $\varepsilon Nd_{coating}$ signature in core M77/1-470 ranges between -1.2 and -2.3 (Fig. 5.2c, Table A.6). The data seem to show a slight trend from more radiogenic values in the older LIA part of the record towards less radiogenic values in the younger part. However, this trend is not strong and the data rather suggest that the signature of the past 400 years with its mean $\varepsilon Nd_{coating}$ is -1.7 ± 0.7 ($2\sigma_{(sd)}$), has not deviated significantly from the composition of the present-day PCUC itself (Grasse et al., unpublished, 2011; Chapter 4). As described above, the PCUC is the predominant current influencing the bottom water under normal conditions when upwelling is strong. Under changed conditions the PCoastalC and the PCC can expand and might impact the bottom water signatures. However, as described in Chapter 4, the variability in $\varepsilon Nd_{coating}$ is not necessarily only related to a change in the prevalent current regime but more to the exchange between bottom waters with the underlying sediments and the pore waters, especially under sedimentary oxygen-depleted conditions (Haley et al., 2004; Lacan and Jeandel, 2005), which

prevents a quantitative assessment of water mass mixing based on the Nd isotope composition of the coatings.

The radiogenic isotope composition of the lithogenic particle fraction of the sediment has been widely used to trace changes in source provenance and input mechanisms (Goldstein et al., 1984; Fagel et al., 2004), which are mostly related to climatic changes (Grousset et al., 1988; Fagel et al., 2004; Ehlert et al., 2011; see also Chapter 4). The Andean rocks along the northwestern South American region display a wide range in εNd and $^{87}Sr/^{86}Sr$ (Fig. 5a) (Sarbas and Nohl, 2009) varying from highly radiogenic εNd and unradiogenic $^{87}Sr/^{86}Sr$ values in equatorial region and in northern Peru to very unradiogenic εNd and radiogenic $^{87}Sr/^{86}Sr$ isotopic compositions in southern Peru and northern Chile. The sedimentary records for $\varepsilon Nd_{detritus}$ and $^{87}Sr/^{86}Sr_{detritus}$ for both cores show broad similarities but also some differences. Core M77/1-470 has overall slightly less radiogenic $\varepsilon Nd_{detritus}$ values than core B0405-6 (Fig. 5.2c, g). Moreover, it shows a trend from less radiogenic towards more radiogenic values during the LIA, and afterwards a step of 1.5 εNd units towards less radiogenic values, which then remain at that level. The $\varepsilon Nd_{detritus}$ record of core B0405-6 does not display any significant trend, the values remain at the same level around -3. If at all, core B0405-6 shows a slight trend towards less radiogenic values in the younger part of the record, which is the opposite pattern to core M77/1-470.

The $^{87}Sr/^{86}Sr_{detritus}$ in both cores is mainly characterised by a rapid shift towards more radiogenic values after the end of the LIA, whereby the change is much more pronounced in core M77/1-470, and the trend towards more radiogenic values has continued until the present day (Fig. 5.2d, h). The youngest samples are in good agreement with measurements of surface sediments from the same area (Fig. 5.5) (Chapter 4). The trends in core M77/1-470 are relatively large and display the same magnitude as the complete glacial-interglacial variation in core SO147-106KL, which is located at 12°S off Lima (Fig. 5.5) (Chapter 4). All data of both M77/1-470 and B0405-6 plot within the provenance fields of southern Peru and northern Chile, whereas the samples from the LIA in core M77/1-470 may have been also influenced by material input from central Peru (Fig. 5.5b). Today, material input along the Peruvian shelf occurs mostly via eolian and

riverine input (Molina-Cruz, 1977; Scheidegger and Krissek, 1982; Bruland et al., 2005).

The LIA was characterised by more intense rainfall (Haug et al., 2001; Gutierrez et al., 2009) due to the mean southward migration of the ITCZ and the associated precipitation belt. This caused more intense rainfall in the Andean hinterland (Bendix, 2000; Baker et al., 2001). Clay minerals are the dominant weathering product and show an increase in flux during the LIA (Sifeddine et al., 2008). Most terrigenous particles from the LIA show indications of riverine transport and discharge (Sifeddine et al., 2008). Clay minerals have a high Rb/Sr ratio, and therefore a high $^{87}Sr/^{86}Sr$. Enhanced weathering intensity may therefore be represented by more radiogenic $^{87}Sr/^{86}Sr_{detritus}$ (Tütken et al., 2002). However, both cores show the less radiogenic values during the LIA before 1850 AD, and the time after the LIA shows the more radiogenic values (Fig. 5.5b). An explanation for this somewhat unexpected pattern may be that material input during the LIA was dominated by more local sources due to the higher river discharge. That would explain why core M77-1/470, which is located at 11°S, recorded a higher influence of more radiogenic $\varepsilon Nd_{detritus}$ and less radiogenic $^{87}Sr/^{86}Sr_{detritus}$ signatures of central Peruvian origin. After the LIA, when the climate became drier, eolian dust input became predominant. The wind-blown dust has mainly originated from the Atacama desert located in the southern Peruvian and northern Chilean Andes (Molina-Cruz, 1977). This material has less radiogenic εNd and much more radiogenic $^{87}Sr/^{86}Sr$ values (Fig. 5.5) (Sarbas and Nohl, 2009) and therefore represents a suitable source contribution for the sediment during the LIA. The difference between river-derived input during the LIA and dust-derived input in more recent times is much clearer observable in core M77/1-470. This core is located at 11°S, which is much further north than core B0405-6 located at 14°S. In the more northern position riverine input drains the area of central Peru, whereas the dust comes from a more southerly source. For core B0405-6 this difference is much less pronounced because both riverine and dust material input have the same source region in southern Peru.

Both $\delta^{30}Si_{opal}$ and the detrial radiogenic signatures indicate, that the LIA must have been controlled by persistent El Nino like conditions. Nutrient supply,

productivity and utilisation were low, because upwelling was diminished. Although more material was delivered locally via rivers, this was not sufficient to compensate the lack of nutrients. In contrast, the strong remineralisation of nutrients from the shelf sediments from subsurface waters fuelling the enhanced productivity was only possible due to an increase in trade wind strength causing also higher dust supply.

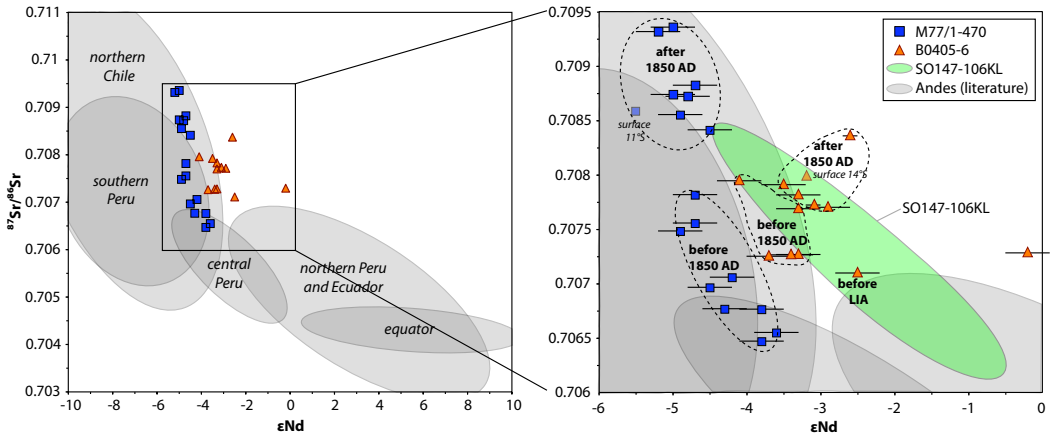

Figure 5.5: $\varepsilon Nd_{detritus}$ versus $^{87}Sr/^{86}Sr_{detritus}$ for core M77/1-470 (blue squares) and B0405-6 (orange triangles). Error bars represent $2\sigma_{(sd)}$ external reproducibilities. The green shading represent the complete glacial-interglacial range recorded in core SO147-106KL from 12°S (Ehlert et al., unpublished, 2011b) and the grey shading indicates potential source endmembers indicating the provenance of the detrital material (Sarbas and Nohl, 2009).

5.5 Conclusions

The $\delta^{30}Si_{opal}$ from two cores from the Peruvian shelf recorded large changes in surface water $Si(OH)_4$ utilisation due to changes in upwelling intensity and nutrient supply during the LIA and the time thereafter. During the LIA the overall nutrient content in the water column was low because the upwelling strength was reduced. Reason for this was a shift of the mean position of the ITCZ southward strongly influencing the atmospheric and oceanographic circulation regime. The Peruvian regime was during that time characterised by persistent El Nino-like conditions, which significantly reduced the primary productivity. The stronger rainfall associated with El Nino conditions were recorded by the radiogenic isotope composition of the detrital material along the shelf, which was mainly transported via rivers from the Andean hinterland. At the end of the LIA, before 1820 AD, The ITCZ was shifted northward, which resulted in a rapid increase in

upwelling strength, nutrient supply and productivity. However, the utilisation of $Si(OH)_4$ by was low, because the demand by diatoms was reduced due to a natural Fe-fertilisation. Between 1820 to 1865 AD periodically occurring stratification and weaker upwelling/nutrient, as indicated by the diatom assemblage, caused a $Si(OH)_4$ utilisation that was three times higher than before 1820 AD, and that was also higher than present day utilisation. After 1865 AD more persistent non-El Nino conditions, which were only irregularly interrupted by El Nino events, favoured a high productivity with moderate utilisation of nutrients. The northward migration of the ITCZ after the end of the LIA was associated with drier conditions and stronger trade winds, which can be traced in the detrital sediments. The radiogenic isotope compositions of the particles indicate the predominant dust transport.

The comparison between $\delta^{30}Si_{opal}$ and $\delta^{15}N$ in the same sediment samples provided some very interesting results. Most paleo-studies from coastal upwelling regions have argued so far that the $\delta^{15}N$ record must have been influenced by both the utilisation of nitrate in the surface water but also the nitrate reduction processes in the water column, and would therefore reflect the extension of oxygen-depleted subsurface waters. However, our data indicate that the denitrification processes, although definitely occurring in such an environment, are not preserved in the sediment, but that mainly the utilisation signal is recorded.

Acknowledgements

This work is a contribution of Sonderforschungsbereich 754 "Climate - Biogeochemistry Interactions in the Tropical Ocean" (www.sfb754.de), which is supported by the Deutsche Forschungsgemeinschaft. We would like to acknowledge the help of Jutta Heinze in the laboratory for the biogenic opal concentration measurements.

Chapter 6
Summary and Outlook

6.1 General Conclusions

Being part of the SFB 754 the main goal of this study was the reconstruction of external factors controlling bottom water oxygen concentrations, and therefore the extension and strength of the oxygen minimum zone, along the Peruvian shelf region during the past ~20,000 years by tracing silicate utilisation, upwelling intensity, and water mass mixing, as well as weathering inputs and transport pathways of weathering products.

The stable silicon isotope composition of diatoms ($\delta^{30}Si_{opal}$) is a powerful tool providing information about surface water nutrient utilisation by diatoms. However, it is also greatly influenced by water mass mixing and redissolution effects, which also influence the signal in the paleo-record. To apply the $\delta^{30}Si_{opal}$ as a paleo-tracer it was necessary to constrain the variability of dissolved silicon isotope compositions in the present-day ocean, and to validate how well this variability is actually preserved in the underlying sediments. This work represents the first comprehensive investigation and comparison of the silicon isotope distributon and its controlling factors in the water column and the surface sediments in a coastal upwelling area. Measurements of the dissolved $\delta^{30}Si_{Si(OH)4}$ in water profiles all along the Peruvian shelf region between 3°S and 17°S reveal that subsurface waters, which feed the coastal upwelling, all display a mean $\delta^{30}Si_{Si(OH)4}$ signature of +1.5‰. In contrast, the silicic acid ($Si(OH)_4$) concentration increases with latitude towards the south. This is a combined effect of vertical and horizontal water mass mixing in the subsurface waters, as well as remineralisation of biogenic opal in the water column and in the sediments. In the surface waters, the $\delta^{30}Si_{Si(OH)4}$ distribution is controlled by the upwelling intensity, i.e. an interplay between the supply of $Si(OH)_4$ and water mass mixing. In the area of the strongest upwelling (between 10 and 15°S), where the re-supply of $Si(OH)_4$ is high, the degree of utilisation of $Si(OH)_4$ is overall low (about 50%). Consequently, the increase in surface water $\delta^{30}Si_{Si(OH)4}$ compared to the subsurface source waters is small (only 0.2-0.3‰). Higher degrees of $Si(OH)_4$ utilisation (up to 93%) in surface

waters outside the main upwelling area result in higher $\delta^{30}Si_{Si(OH)4}$ values of up to 2.8‰, corresponding to a difference of up to 1.2 ‰ from the source water. Comparison of $\delta^{30}Si_{diatom}$ compositions obtained from hand-picked diatoms from the underlying sediments, which range from 0.58‰ to 1.95‰, shows a distribution very similar to that of surface water $\delta^{30}Si_{Si(OH)4}$. Within the main upwelling region, where productivity is highest, the diatom opal exhibits lower $\delta^{30}Si_{diatom}$ values, whereas further to the north between 5°S to 10°S, where upwelling intensity and productivity are lower, the $\delta^{30}Si_{diatom}$ values increase.

Comparison between $\delta^{30}Si_{bSiO2}$ signatures obtained from bulk opal in the sediment, which was extracted applying commonly used methods, and $\delta^{30}Si_{diatom}$ from hand-picked diatoms indicates that in samples with low $bSiO_2$ concentrations a contamination with isotopically lighter biosiliceous material, such as sponge spicules or radiolarians occurs. This observation has important implications for the general interpretation of paleo-$\delta^{30}Si$ records at locations with low $bSiO_2$ content and suggests that for sediments containing such low amounts of $bSiO_2$ significant biases of the $\delta^{30}Si$ records can only be excluded if extraction of a pure diatom fraction can be demonstrated.

Similar to the silicon isotopes, a comparison of water column and surface sediment signatures was also achieved for radiogenic neodymium isotopes (εNd) in order to calibrate this proxy for circulation changes. In the sediment, εNd was measured in authigenic Fe-Mn coatings and in benthic foraminiferal carbonate. In addition, the radiogenic isotope signatures of the detrital fraction were determined to detect differences in provenance and material input mechanisms. In general, all sedimentary signatures display a north-south trend to less radiogenic εNd values, which is similar to the surface water εNd distribution and reflects the Andean hinterland geology of Peru and Ecuador, but does not allow a distinction of different bottom water currents based on εNd from Fe-Mn coatings or benthic foraminifers. This is probably a combined effect of a diminishing influence of the signatures of incoming central Pacific surface waters due to mixing with other water masses, and exchange of the bottom waters with the detrital fraction of the shelf sediments. These two core-top calibration studies provide the basis for the

investigation of changes in nutrient utilisation, upwelling intensity and productivity in the past.

During the past 20,000 years primary productivity has varied largely off Peru. In Chapter 4, $\delta^{30}Si_{opal}$ (both bulk and picked diatoms, which provided indistinguishable signatures throughout the record), $\varepsilon Nd_{coating}$ and the radiogenic isotope composition (Nd and Sr) of the detrital fraction were applied to reconstruct the controlling factors and the amplitude of this variability from a core retrieved from one of the centres of present day coastal upwelling. During the LGM and deglacial period $bSiO_2$ accumulation was very low. The $\delta^{30}Si_{opal}$ signatures indicate that the utilisation of available $Si(OH)_4$ in the surface water was very low, whereas e.g. during the late Holocene both $bSiO_2$ flux and $\delta^{30}Si_{opal}$ were much higher. The utilisation of $Si(OH)_4$ was around 2.5 ka, similar to today, between 60 to 90%. In contrast to expectations arising from the surface sediment calibration obtained in Chapter 3, $bSiO_2$ content and $\delta^{30}Si_{opal}$ were overall positively correlated over the entire period of time covered. This would not have been the case if $Si(OH)_4$ had been the only driver of utilisation by diatoms. Consequently, diatom productivity along the Peruvian shelf was ultimately not limited by $Si(OH)_4$ availability. Instead, dissolved Fe and P remineralisation from the shelf sediments were the controlling parameters. During times of at least periodically weaker upwelling and a smaller extension of the OMZ (e.g. the early and the late Holocene) diminished Fe and P supply to the euphotic zone caused stress for the diatoms, which resulted in a heavier silicification of the frustules. This explains the higher export of $bSiO_2$ to the sediments and also the stronger utilisation of $Si(OH)_4$. The Nd and Sr isotope signatures of the detrital fraction of the sediment are in agreement with that interpretation. Times of weaker upwelling were characterised by increased river transported material input from the nearby hinterland. This happened mostly during El Nino like conditions causing weaker upwelling and enhanced rainfall in the Peruvian Andes. The phase of strongest El Nino-like conditions of the past 20,000 years has only occurred in the late Holocene during the past 5,000 years.

However, the atmospheric and oceanographic regime off Peru did not only vary on glacial-interglacial timescales but has also been characterised by decadal

to centennial-scale variability (Chapter 5). The last pronounced regime shift occured at the end of the LIA (ca. 1850 AD) when the ITCZ shifted from a more southerly position towards the North. This had a large impact on the biogeochemical regime along the Peruvian upwelling regime. During the LIA, which was characterised by persistent El Nino-like conditions, trade wind strength and coastal upwelling were diminished and the shelf was more strongly oxygenated causing a reduction in nutrient supply to the euphotic zone and diminished primary productivity. At the end of the LIA around 1820 AD, however, upwelling intensity increased and enhanced primary productivity. The utilisation of $Si(OH)_4$ by diatoms was very low due to high amounts of dissolved Fe which was remineralised and released from the sediments (high Fe – weaker silicification – weaker utilisation). Between 1820 to 1850 AD the region again experienced periodic stratification events, which resulted in a shift of the diatom assemblage. Although upwelling was not always weak the predominant diatom species in the record for that short period of time reflected the more stratified conditions and a stronger utilisation of $Si(OH)_4$. After 1850 AD present-day conditions were established being characterised by moderate upwelling conditions and nutrient utilisation. El Nino-like conditions have occurred only irregularly and the Peruvian region has been dominated by dry conditions favouring material transport via dust.

6.2 Outlook

One major task of this project was to establish the laboratory and measurement routines for the determination of silicon isotope compositions of waters and sediments at IFM-GEOMAR. Despite the fact that there was close cooperation with international colleagues, in particular with Dr. B. Reynolds and Dr. Gregory de Souza at ETH Zurich, Switzerland, who had several years of experience in Si isotope analyses, substantial analytical problems had to be overcome during the first part of the thesis. This included insufficient chemical yields during ion-chromatographic cleaning of the Si, problems of extracting a pure diatom fraction from the sediments, and most importantly achieving the required analytical precision and accuracy on the MC-ICPMS. Therefore, only one core from

the Peruvian shelf covering the period of time between the last glacial and present could be studied during this thesis. This, however, only represents one local record. In order to obtain more precise estimates of the regional variability of the OMZ it will be necessary to investigate more cores covering the shelf region both latitudinally and in different water dephts. Moreover, direct and detailed comparisons of these results with reconstruction of bottom water oxygen levels from benthic foraminiferal assemblages (as obtained by J. Mallon) and with dissolved nitrate and redox conditions (obtained by N. Glock) from the same cores along the shelf should be conducted.

Studying stable silicon and radiogenic neodymium and strontium isotopes will continue in the second phase of the SFB754 starting in January 2012. As chapter 5 has shown, the direct comparison between the $\delta^{30}Si$ and the $\delta^{15}N$ provides crucial information about nutrient utilisation rates in the past for the detailed reconstruction of environmental factors controlling the diatom productivity and nitrogen cycling. Therefore this approach will be pursued further. The $\delta^{30}Si$ signatures of diatoms will be compared with bulk organic matter $\delta^{15}N$ and with, as a new additional proxy, with diatom-bound organic matter $\delta^{15}N$ in order to estimate the different contributions of the major processes controlling nutrient utilisation and nitrate reduction. This approach is expected to unravel the impacts of varying magnitudes of nitrate reduction related to OMZ strength on the $\delta^{15}N$ signal. The close cooperation and comparison between the water column investigations and the sedimentary reconstructions, which provided unique data sets during the first phase, should continue and be extended.

Another potentially interesting field are $\delta^{30}Si$ measurements of the pore waters, which has not been done so far, but which can provide useful information about remineralisation and other diagenetic effects. The εNd of Fe-Mn coatings, although not providing the expected variability so far, should be studied in low resolution in other sediment cores from different latitudes and water depths to further constrain their potential to identify water mass circulation changes in the Eastern Equatorial Pacific Ocean in the past.

References

Abouchami, W., Galer, S. J. G., & Koschinsky, A. (1999). Pb and Nd isotopes in NE Atlantic Fe–Mn crusts: Proxies for trace metal paleosources and paleocean circulation. *Geochimica et Cosmochimica Acta*, *63*(10), 1489-1505.

Abrantes, F. F., Meggers, H., Nave, S., Bollman, J., Palma, S., Sprengel, C., Henderiks, J., et al. (2002). Fluxes of micro-organisms along a productivity gradient in the Canary Islands region (29°N): Implications for paleoreconstructions. *Deep-Sea Research*, *49*, 3599-3629.

Abrantes, F. F., Lopes, C., Mix, A. C., & Pisias, N. G. (2007). Diatoms in Southeast Pacific surface sediments reflect environmental properties. *Quaternary Science Reviews*, *26*(1-2), 155-169. doi:10.1016/j.quascirev.2006.02.022

Agnihotri, R., Altabet, M. A., Herbert, T. D., & Tierney, J. E. (2008). Subdecadally resolved paleoceanography of the Peru margin during the last two millennia. *Geochemistry Geophysics Geosystems*, *9*(5), 1-15. doi:10.1029/2007GC001744

Albarède, F., Telouk, P., Blichert-Toft, J., Boyet, M., Agranier, A., & Nelson, B. (2004). Precise and accurate isotopic measurements using multiple-collector ICPMS. *Geochimica et Cosmochimica Acta*, *68*(12), 2725-2744. doi:10.1016/j.gca.2003.11.024

Alheit, J., & Niquen, M. (2004). Regime shifts in the Humboldt Current ecosystem. *Progress In Oceanography*, *60*(2-4), 201-222. doi:10.1016/j.pocean.2004.02.006

Alleman, L. Y., Cardinal, D., Cocquyt, C., Plisnier, P.-D., Descy, J.-P., Kimirei, I., Sinyinza, D., et al. (2005). Silicon Isotopic Fractionation in Lake Tanganyika and Its Main Tributaries. *Journal of Great Lakes Research*, *31*(4), 509-519.

Altabet, M. A., & Francois, R. (1994). Sedimentary nitrogen isotopic ratio as a recorder for surface ocean nitrate utilization. *Global Biogeochemical Cycles*, *8*(1), 103-116.

Altabet, M. A., Deuser, W. G., Honjo, S., & Stienen, C. (1991). Seasonal and depth-related changes in the source of sinking particles in the North Atlantic. *Nature*, *354*, 136-139.

Altabet, M. A., Pilskaln, C., Thunell, R., Pride, C. J., Sigman, D. M., Chavez, F. P., & Francois, R. (1999). The nitrogen isotope biogeochemistry of sinking particles from the margin of the Eastern North Pacific. *Deep-Sea Research*, *46*, 655-679.

Alvarez-Salgado, X. A., Nieto-Cid, M., Piedracoba, S., Crespo, B. G., Gago, J., Brea, S., Teixeira, I. G., et al. (2005). Origin and fate of a bloom of Skeletonema costatum during a winter upwelling/downwelling sequence in the Riá de Vigo (NW Spain). *Journal of Marine Research*, *63*, 1127-1149.

Anderson, R. F., Kumar, N., Mortlock, R. A., Froelich, P. N., Kubik, P., Dittrich-Hannen, B., & Suter, M. (1998). Late-Quaternary changes in productivity of the Southern Ocean. *Journal of Marine Systems*, *17*, 497-514.

Armbrust, E. V. (2009). The life of diatoms in the world's oceans. *Nature*, *459*, 185-192. doi:10.1038/nature08057

Arsouze, T., Dutay, J.-C., Lacan, F., & Jeandel, C. (2009). Reconstructing the Nd oceanic cycle using a coupled dynamical – biogeochemical model. *Biogeosciences Discussions*, *6*(3), 5549-5588. doi:10.5194/bgd-6-5549-2009

Ayón, P., Criales-Hernandez, M. I., Schwamborn, R., & Hirche, H.-J. (2008). Zooplankton research off Peru: A review. *Progress In Oceanography*, *79*(2-4), 238-255. doi:10.1016/j.pocean.2008.10.020

Baines, S. B., Twining, B. S., Brzezinski, M. A., Nelson, D. M., & Fisher, N. S. (2010). Causes and biogeochemical implications of regional differences in silicification of marine diatoms. *Global Biogeochemical Cycles*, *24*(4), 1-15. doi:10.1029/2010GB003856

Baker, P. A., Seltzer, G. O., Fritz, S. C., Dunbar, R. B., Grove, M. J., Tapia, P. M., Cross, S. L., et al. (2001). The history of South American tropical precipitation for the past 25,000 years. *Science*, *291*, 640-643. doi:10.1126/science.291.5504.640

Barber, R. T., & Chavez, F. P. (1983). Biological consequences of El Nino. *Science*, *222*, 1203-1210. doi:10.1126/science.222.4629.1203

Barrat, J. A., Keller, F., Amossé, J., Taylor, R. N., Nesbitt, R. W., & Hirata, T. (1996). Determination of Rare Earth Elements in Sixteen Silicate Reference Samples by ICP-MS after Tm Addition and Ion Exchange Separation. *Geostandards Newsletter*, *20*(1), 133-139. doi:10.1111/j.1751-908X.1996.tb00177.x

Basile-Doelsch, I. (2006). Si stable isotopes in the Earth's surface: A review. *Journal of Geochemical Exploration*, *88*(1-3), 252-256. doi:10.1016/j.gexplo.2005.08.050

Bayon, G., German, C. R., Boella, R. M., Milton, J. A., Taylor, R. N., & Nesbitt, R. W. (2002). An improved method for extracting marine sediment fractions and its application to Sr and Nd isotopic analysis. *Chemical Geology*, *187*, 179-199.

Bendix, J. (2000). Precipitation dynamics in Ecuador and northern Peru during the 1991/92 El Nino: a remote sensing perspective. *International Journal of Remote Sensing*, *21*(3), 533-548.

Berger, W. H., Smetacek, V. S., & Wefer, G. (1989). *Productivity of the Ocean: Present and Past* (Life Scien., p. 471). Berlin: John Wiley & Sons.

Beucher, C. P., Brzezinski, M. A., & Jones, J. L. (2008). Sources and biological fractionation of Silicon isotopes in the Eastern Equatorial Pacific. *Geochimica et Cosmochimica Acta*, *72*(13), 3063-3073. doi:10.1016/j.gca.2008.04.021

Beucher, C. P., Brzezinski, M. A., & Jones, J. L. (2011). Mechanisms controlling silicon isotope distribution in the eastern Equatorial Pacific. *Geochimica et Cosmochimica Acta*. doi:10.1016/j.gca.2011.05.024

Bidle, K. D., & Azam, F. (1999). Accelerated dissolution of diatom silica by marine bacterial assemblages. *Nature*, *397*, 508-512.

Bidle, K. D., Manganelli, M., & Azam, F. (2002). Regulation of oceanic silicon and carbon preservation by temperature control on bacteria. *Science*, *298*, 1980-4. doi:10.1126/science.1076076

Bird, B. W., Abbott, M. B., Rodbell, D. T., & Vuille, M. (2011a). Holocene tropical South American hydroclimate revealed from a decadally resolved lake sediment δ18O record. *Earth and Planetary Science Letters*, *310*(3-4), 192-202. doi:10.1016/j.epsl.2011.08.040

Bird, B. W., Abbott, M. B., Vuille, M., Rodbell, D. T., Stansell, N. D., & Rosenmeier, M. F. (2011b). A 2,300-year-long annually resolved record of the South American summer monsoon from the Peruvian Andes. *Proceedings of the National Academy of Sciences*, *108*(21), 8583-8588. doi:10.1073/pnas.1003719108

Bostock, H. C., Opdyke, B. N., & Williams, M. J. M. (2010). Characterising the intermediate depth waters of the Pacific Ocean using $\delta^{13}C$ and other geochemical tracers. *Deep-Sea Research*, *57*(7), 847-859. doi:10.1016/j.dsr. 2010.04.005

Boyle, E. A. (1981). Cadmium, Zinc, Copper, and Barium in Foraminifera tests. *Earth and Planetary Science Letters*, *53*, 11-35.

Boyle, E. A., & Keigwin, L. D. (1985). Comparison of Atlantic and Pacific paleochemical records for the last 215,000 years: changes in deep ocean circulation and chemical inventories. *Earth and Planetary Science Letters*, *76*, 135-150.

Bradtmiller, L. I., Anderson, R. F., Fleisher, M. Q., & Burckle, L. H. (2006). Diatom productivity in the equatorial Pacific Ocean from the last glacial period to the present: A test of the silicic acid leakage hypothesis. *Paleoceanography*, *21*(PA4201), 1-12. doi:10.1029/2006PA001282

Brandes, J. A., Devol, A. H., Yoshinari, T., Jayakumar, D. A., & Naqvi, S. W. A. (1998). Isotopic composition of nitrate in the central Arabian Sea and eastern North Pacific: A tracer for mixing and nitrogen cycles. *Limnology and Oceanography*, *43*(7), 1680-1689.

Brink, K. H., Halpern, D., Huyer, A., & Smith, R. L. (1983). The physical environment of the Peruvian upwelling system. *Progress In Oceanography*, *12*(3), 285-305. doi:10.1016/0079-6611(83)90011-3

Brodie, I., & Kemp, A. E. S. (1994). Variation in biogenic and detrital fluxes and formation of laminae in late Quaternary sediments from the Peruvian coastal upwelling zone. *Marine Geology*, *116*, 385-398.

Broecker, W. S. (2000). Was a change in thermohaline circulation responsible for the Little Ice Age? *Proceedings of the National Academy of Sciences*, *97*(4), 1339-1342.

Bruland, K. W., Rue, E. L., Smith, G. J., & DiTullio, G. R. (2005). Iron, macronutrients and diatom blooms in the Peru upwelling regime: brown and blue waters of Peru. *Marine Chemistry*, *93*(2-4), 81-103. doi:10.1016/j.marchem.2004.06.011

Brzezinski, M. A., Olson, R. J., & Chrisholm, S. W. (1990). Silicon availability and cell-cycle progression in marine diatoms. *Marine ecology progress series*, *67*(1), 83-96.

Brzezinski, M. A., Pride, C. J., Franck, V. M., Sigman, D. M., Sarmiento, J. L., Matsumoto, K., Gruber, N., et al. (2002). A switch from Si(OH)4 to NO3− depletion in the glacial Southern Ocean. *Geophysical Research Letters*, *29*(12), 1-4. doi:10.1029/2001GL014349

Brzezinski, M. A., Baines, S. B., Balch, W. M., Beucher, C. P., Chai, F., Dugdale, R. C., Krause, J. W., et al. (2011). Co-limitation of diatoms by iron and silicic acid in the equatorial Pacific. *Deep-Sea Research*, *58*(3-4), 493-511. doi:10.1016/j.dsr2.2010.08.005

Cardinal, D., Alleman, L. Y., Dehairs, F., Savoye, N., Trull, T. W., & André, L. (2005). Relevance of silicon isotopes to Si-nutrient utilization and Si-source assessment in Antarctic waters. *Global Biogeochemical Cycles*, *19*(2), 1-13. doi:10.1029/2004GB002364

Carré, M., Bentaleb, I., Fontugne, M., & Lavallée, D. (2005). Strong El Niño events during the early Holocene: stable isotope evidence from Peruvian sea shells. *The Holocene*, *15*(1), 42-47. doi:10.1191/0959683605h1782rp

Chavez, F. P. (1995). A comparison of ship and satellite chlorophyll from California and Peru. *Journal of Geophysical Research*, *100*, 855-862.

Chavez, F. P. (2005). Biological consequences of interannual to multidecadal variability. In A. Robinson & K. H. Brink (Eds.), *The Sea, vol. 13* (pp. 643-679). Cambridge: Harvard University Press.

Chavez, F. P., & Barber, R. T. (1987). An estimate of new production in the equatorial Pacific. *Deep-Sea Research*, *34*(7), 1229-1243.

Clement, A. C., Seager, R., & Cane, M. A. (2000). Suppression of El Nino during the mid-Holocene by changes in the Earth's orbit. *Paleoceanography*, *15*(6), 731-737.

Codispoti, L. A., Brandes, J. A., Christensen, J. P., Devol, A. H., Naqvi, S. W. A., Paerl, H. W., & Yoshinari, T. (2001). The oceanic fixed nitrogen and nitrous oxide budgets: Moving targets as we enter the anthropocene? *Scientia Marina*, *65*, 85-105.

Cohen, A. S., O'Nions, R. K., Siegenthaler, R., & Griffin, W. L. (1988). Chronology of the pressure-temperature history recorded by a granulite terrain. *Contributions to Mineralogy and Petrology*, *98*, 303-311.

Cronin, T. M., Dwyer, G. S., Kamiya, T., Schwede, S., & Willard, D. A. (2003). Medieval Warm Period, Little Ice Age and 20th century temperature variability from Chesapeake Bay. *Global and Planetary Change*, *36*(1-2), 17-29. doi:10.1016/S0921-8181(02)00161-3

Czeschel, R., Stramma, L., Schwarzkopf, F. U., Giese, B. S., Funk, A., & Karstensen, J. (2011). Middepth circulation of the eastern tropical South Pacific and its link to the oxygen minimum zone. *Journal of Geophysical Research*, *116*(C01015), 1-13. doi:10.1029/2010JC006565

Dalsgaard, T., Canfield, D. E., Petersen, J., Thamdrup, B., & Acuña-González, J. (2003). N2 production by the anammox reaction in the anoxic water column of Golfo Dulce, Costa Rica. *Nature*, *422*, 606-608. doi:10.1038/nature01526

De La Rocha, C. L. (2003). Silicon isotope fractionation by marine sponges and the reconstruction of the silicon isotope composition of ancient deep water. *Geology*, *31*, 423-426. doi:10.1130/0091-7613(2003)031<0423

De La Rocha, C. L., & Bickle, M. (2005). Sensitivity of silicon isotopes to whole-ocean changes in the silica cycle. *Marine Geology*, *217*(3-4), 267-282. doi:10.1016/j.margeo.2004.11.016

De La Rocha, C. L., Brzezinski, M. A., & De Niro, M. J. (1997). Fractionation of silicon isotopes by marine diatoms during biogenic silica formation. *Geochimica et Cosmochimica Acta*, *61*(23), 5051-5056. doi:10.1016/S0016-7037(97)00300-1

De La Rocha, C. L., Brzezinski, M. A., De Niro, M. J., & Shemesh, A. (1998). Silicon-isotope composition of diatoms as an indicator of past oceanic change. *Nature*, *395*, 680-683.

De La Rocha, C. L., Brzezinski, M. A., & De Niro, M. J. (2000). A first look at the distribution of the stable isotopes of silicon in natural waters. *Geochimica et Cosmochimica Acta*, *64*(14), 2467-2477. doi:10.1016/S0016-7037(00)00373-2

Demarest, M. S., Brzezinski, M. A., & Beucher, C. P. (2009). Fractionation of silicon isotopes during biogenic silica dissolution. *Geochimica et Cosmochimica Acta*, *73*(19), 5572-5583. doi:10.1016/j.gca.2009.06.019

Demarest, M. S., Brzezinski, M. A., Nelson, D. M., Krause, J. W., Jones, J. L., & Beucher, C. P. (2011). Net biogenic silica production and nitrate regeneration determine the strength of the silica pump in the Eastern Equatorial Pacific. *Deep-Sea Research*, *58*(3-4), 462-476. doi:10.1016/j.dsr2.2010.08.007

DeMaster, D. J. (1981). The supply and accumulation of silica in the marine environment. *Geochimica et Cosmochimica Acta*, *45*(10), 1715-1732. doi:10.1016/0016-7037(81)90006-5

DeMaster, D. J. (2002). The accumulation and cycling of biogenic silica in the Southern Ocean: revisiting the marine silica budget. *Deep-Sea Research*, *49*(16), 3155-3167. doi:10.1016/S0967-0645(02)00076-0

De Pol-Holz, R., Ulloa, O., Dezileau, L., Kaiser, J., Lamy, F., & Hebbeln, D. (2006). Melting of the Patagonian Ice Sheet and deglacial perturbations of the nitrogen cycle in the eastern South Pacific. *Geophysical Research Letters*, *33*(4), 3-6. doi:10.1029/2005GL024477

De Pol-Holz, R., Ulloa, O., Lamy, F., Dezileau, L., Sabatier, P., & Hebbeln, D. (2007). Late Quaternary variability of sedimentary nitrogen isotopes in the eastern South Pacific Ocean. *Paleoceanography*, *22*(2), 1-16. doi:10.1029/2006PA001308

De Pol-Holz, R., Robinson, R. S., Hebbeln, D., Sigman, D. M., & Ulloa, O. (2009). Controls on sedimentary nitrogen isotopes along the Chile margin. *Deep-Sea Research*, *56*(16), 1042-1054. doi:10.1016/j.dsr2.2008.09.014

De Vries, T. J., & Schrader, H. (1981). Variations of upwelling/oceanic conditions during the latest Pleistocene through Holocene off the central Peruvian coast: a diatom record. *Marine Micropaleontology*, *6*, 157-167.

Dia, A., Dupré, B., & Allègre, C. J. (1992). Nd isotopes in Indian Ocean sediments used as a tracer of supply to the ocean and circulation paths. *Marine Geology*, *103*, 349-359.

Ding, T., Jiang, S., Wan, D., Li, Y., Li, J., Song, H., Liu, Z., et al. (1996). *Silicon Isotope Geochemistry* (p. 125). Beijing, China: Geological Publishing House.

Ding, T. P., Gao, J. F., Tian, S. H., Wang, H. B., & Li, M. (2011). Silicon isotopic composition of dissolved silicon and suspended particulate matter in the Yellow River, China, with implications for the global silicon cycle. *Geochimica et Cosmochimica Acta*. doi:10.1016/j.gca.2011.07.040

Dixit, S., van Cappellen, P., & van Bennekom, A. J. (2001). Processes controlling solubility of biogenic silica and pore water build-up of silicic acid in marine sediments. *Marine Chemistry*, *73*, 333-352.

Dorbath, L., Cisternas, A., & Dorbath, C. (1990). Assessment of the size of large and great historical earthquakes in Peru. *Bulletin of the Seismological Society of America*, *80*(3), 551-576.

Douthitt, C. B. (1982). The geochemistry of the stable isotopes of silicon. *Geochimica et Cosmochimica Acta*, *46*(8), 1449-1458. doi:10.1016/0016-7037(82)90278-2

Dubois, N., Kienast, M., Kienast, S., Calvert, S. E., François, R., & Anderson, R. F. (2010). Sedimentary opal records in the eastern equatorial Pacific: It is not all about leakage. *Global Biogeochemical Cycles*, *24*(4), 1-15. doi:10.1029/2010GB003821

Dugdale, R. C., & Wilkerson, F. P. (2001). Sources and fates of silicon in the ocean: the role of diatoms in the climate and glacial cycles. *Scientia Marina*, *65*, 141-152.

Dugdale, R. C., Wischmeyer, A. G., Wilkerson, F. P., Barber, R. T., Chai, F., Jiang, M.-S., & Peng, T.-H. (2002). Meridional asymmetry of source nutrients to the equatorial Pacific upwelling ecosystem and its potential impact on ocean–atmosphere CO2 flux; a data and modeling approach. *Deep-Sea Research*, *49*(13-14), 2513-2531. doi:10.1016/S0967-0645(02)00046-2

Dugdale, R. C., Chai, F., Feely, R., Measures, C. I., Parker, A. E., & Wilkerson, F. P. (2011). The regulation of equatorial Pacific new production and pCO2 by silicate-limited diatoms. *Deep-Sea Research*, *58*(3-4), 477-492. doi:10.1016/j.dsr2.2010.08.008

Dullo, W.-C., Rein, B., Wolf, A., Biebow, N., Schaber, K., & Sirocko, F. (2000). Core descriptions and reflectance spectra. *Cruise report SO147 - Peru upwelling, BGR Rep. 0120607-11672/00* (pp. 102-119). Hannover, Germany

Ehlert, C., Frank, M., Haley, B. A., Böniger, U., De Deckker, P., & Gingele, F. X. (2011). Current transport versus continental inputs in the eastern Indian Ocean:

Radiogenic isotope signatures of clay size sediments. *Geochemistry Geophysics Geosystems*, *12, Q06017*(6), 1-17. doi:10.1029/2011GC003544

Elderfield, H., & Sholkovitz, E. R. (1987). Rare earth elements in the pore waters of reducing nearshore sediments. *Earth and Planetary Science Letters*, *82*(3-4), 280-288. doi:10.1016/0012-821X(87)90202-0

Ellwood, M. J., & Hunter, K. A. (1999). Determination of the Zn/Si ratio in diatom opal: a method for the separation, cleaning and dissolution of diatoms. *Marine Chemistry*, *66*(3-4), 149-160. doi:10.1016/S0304-4203(99)00037-7

Estrada, M., & Blasco, D. (1985). Phytoplankton assemblages in coastal upwelling areas. In C. Bas, R. Margalef, & P. Rubies (Eds.), *Simposio Internacional Sobre Las Areas de Afloramiento Mas Importantes del Oeste Africano (Cabo Blanco y Benguela)* (pp. 379-402). Barcelona: Instituto de Investigaciones Pesqueras.

Fagel, N. F., Hillaire-Marcel, C., Humblet, M., Brasseur, R., Weis, D., & Stevenson, R. K. (2004). Nd and Pb isotope signatures of the clay-size fraction of Labrador Sea sediments during the Holocene: Implications for the inception of the modern deep circulation pattern. *Paleoceanography*, *19*, 1-16. doi:10.1029/2003 PA000993

Fedorov, A. V., & Philander, S. G. (2000). Is El Nino changing? *Science*, *288*, 1997-2002. doi:10.1126/science.288.5473.1997

Feldman, G., Clark, D., & Halpern, D. (1984). Satellite Color Observations of phytoplankton distribution in the Eastern Equatorial Pacific during the 1982-1983 El Nino. *Science*, *226*, 1069-1071.

Fiedler, P. C. (2002). Environmental change in the Eastern tropical Pacific Ocean: review of ENSO and decadal variability. *Marine Ecological Process Series*, *224*, 265-283.

Fiedler, P. C., & Talley, L. D. (2006). Hydrography of the eastern tropical Pacific: A review. *Progress In Oceanography*, *69*(2-4), 143-180. doi:10.1016/ j.pocean.2006.03.008

Fitoussi, C., Bourdon, B., Kleine, T., Oberli, F., & Reynolds, B. C. (2009). Si isotope systematics of meteorites and terrestrial peridotites: implications for Mg/Si fractionation in the solar nebula and for Si in the Earth's core. *Earth and Planetary Science Letters*, *287*(1-2), 77-85. doi:10.1016/j.epsl.2009.07.038

Frank, M. (2002). Radiogenic isotopes: Tracers of past ocean circulation and erosional input. *Reviews of Geophysics*, *40*(1), 1-38. doi:10.1029/2000RG000094

Fripiat, F., Cavagna, A.-J., Dehairs, F., de Brauwere, A., André, L., & Cardinal, D. (2011a). Processes controlling the Si-isotopic composition in the Southern Ocean and application for paleoceanography. *Biogeosciences Discussions*, *8*(5), 10155-10185. doi:10.5194/bgd-8-10155-2011

Fripiat, F., Cavagna, A.-J., Savoye, N., Dehairs, F., André, L., & Cardinal, D. (2011b). Isotopic constraints on the Si-biogeochemical cycle of the Antarctic Zone in the Kerguelen area (KEOPS). *Marine Chemistry*, *123*(1-4), 11-22. doi:10.1016/ j.marchem.2010.08.005

Froelich, P. N., Arthur, M. A., Burnett, W. C., Deakin, M., Hensley, V., Jahnke, R., Kaul, L., et al. (1988). Early Diagenesis of Organic Matter in Peru Continental Margin Sediments: Phosphorite Precipitation. *Marine Geology*, *80*, 309-343.

Fuenzalida, R., Schneider, W., Garcés-Vargas, J., Bravo, L., & Lange, C. B. (2009). Vertical and horizontal extension of the oxygen minimum zone in the eastern South Pacific Ocean. *Deep-Sea Research*, *56*(16), 1027-1038. doi:10.1016/j.dsr2.2008.11.001

Garcia, H. E., Locarnini, R. A., Boyer, T. P., Antonov, J. I., Baranova, O. K., Zweng, M. M., & Johnson, D. R. (2010). *World Ocean Atlas 2009 Volume 3: Dissolved Oxygen, Apparent Oxygen Utilization, and Oxygen Saturation*. *World* (S. Levitus., Vol. 3, p. 344). Washington, D.C.: U. S. Government Printing Office.

Garcia, H. E., Locarnini, R. A., Boyer, T. P., Antonov, J. I., Zweng, M. M., Baranova, O. K., & Johnson, D. R. (2010). *World Ocean Atlas 2009, Volume 4: Nutrients (phosphate, nitrate, and silicate)*. *World* (S. Levitus., Vol. 4, p. 398). Washington, D.C.: U. S. Government Printing Office.

Georg, R. B., Reynolds, B. C., Frank, M., & Halliday, A. N. (2006). Mechanisms controlling the silicon isotopic compositions of river waters. *Earth and Planetary Science Letters*, *249*(3-4), 290-306. doi:10.1016/j.epsl.2006.07.006

Georg, R. B., Reynolds, B. C., Frank, M., & Halliday, A. N. (2006). New sample preparation techniques for the determination of Si isotopic compositions using MC-ICPMS. *Chemical Geology*, *235*(1-2), 95-104. doi:10.1016/j.chemgeo.2006.06.006

Georg, R. B., Zhu, C., Reynolds, B. C., & Halliday, A. N. (2009). Stable silicon isotopes of groundwater, feldspars, and clay coatings in the Navajo Sandstone aquifer, Black Mesa, Arizona, USA. *Geochimica et Cosmochimica Acta*, *73*(8), 2229-2241. doi:10.1016/j.gca.2009.02.005

German, C. R., Klinkhammer, G. P., Edmond, J. M., Mitra, A., & Elderfield, H. (1990). Hydrothermal scavenging of rare-earth elements in the ocean. *Nature*, *345*, 516-518.

Goldstein, S. L., & Hemming, S. R. (2003). Long-lived Isotopic Tracers in Oceanography, Paleoceanography and Ice Sheet Dynamics. *Treatise on Geochemistry*, *6*, 453-489.

Goldstein, S. L., O'Nions, R. K., & Hamilton, P. J. (1984). A Sm - Nd isotopic study of atmospheric dusts and particulates from major river systems. *Earth and Planetary Science Letters*, *70*, 221-236.

Graham, N. E., Hughes, M. K., Ammann, C. M., Cobb, K. M., Hoerling, M. P., Kennett, D. J., Kennett, J. P., et al. (2007). Tropical Pacific – mid-latitude teleconnections in medieval times. *Climatic Change*, *83*(1-2), 241-285. doi:10.1007/s10584-007-9239-2

Graham, N. E., Ammann, C. M., Fleitmann, D., Cobb, K. M., & Luterbacher, J. (2010). Support for global climate reorganization during the "Medieval Climate Anomaly." *Climate Dynamics*, *37*(5-6), 1217-1245. doi:10.1007/s00382-010-0914-z

Grasse, P., Stichel, T., Stumpf, R., Stramma, L., & Frank, M. (2011). The Distribution of Neodymium Isotopes and Concentrations in the Eastern Equatorial Pacific: Water Mass Advection versus Particle Exchange. Under Review in *Earth and Planetary Science Letters.*

Grousset, F. E., Biscaye, P. E., Zindler, A., Prospero, J., & Chester, R. (1988). Neodymium isotopes as tracers in marine sediments and aerosols: North Atlantic. *Earth and Planetary Science Letters*, *87*(4), 367-378. doi:10.1016/0012-821X(88)90001-5

Grove, J. M. (2001). The initiation of the "Little Ice Age" in regions round the North Atlantic. *Climatic Change*, *48*, 53-82.

Gunther, E. R. (1936). A report on oceanographic investigations in the Peru Coastal Current. *Discovery Report*, *13*, 107-276.

Gutiérrez, D., Sifeddine, A., Reyss, J. L., Vargas, G., Velazco, F., Salvatteci, R., Ferreira, V., et al. (2006). Anoxic sediments off Central Peru record interannual to multidecadal changes of climate and upwelling ecosystem during the last two centuries. *Advances in Geosciences*, *6*, 119-125. doi:10.5194/adgeo-6-119-2006

Gutiérrez, D., Enriquez, E., Purca, S., Quipuzcoa, L., Marquina, R., Flores, G., & Graco, M. (2008). Oxygenation episodes on the continental shelf of central Peru: Remote forcing and benthic ecosystem response. *Progress In Oceanography*, *79*(2-4), 177-189. doi:10.1016/j.pocean.2008.10.025

Gutiérrez, D., Sifeddine, A., Field, D. B., Ortlieb, L., Vargas, G., Chavez, F. P., Velazco, F., et al. (2009). Rapid reorganization in ocean biogeochemistry off Peru towards the end of the Little Ice Age. *Biogeosciences*, *6*, 835-848. doi:10.5194/bg-6-835-2009

Gutjahr, M., Frank, M., Stirling, C. H., Klemm, V., van De Flierdt, T., & Halliday, A. N. (2007). Reliable extraction of a deepwater trace metal isotope signal from Fe–Mn oxyhydroxide coatings of marine sediments. *Chemical Geology*, *242*(3-4), 351-370. doi:10.1016/j.chemgeo.2007.03.021

Gutjahr, M., Frank, M., Stirling, C. H., Keigwin, L. D., & Halliday, A. N. (2008). Tracing the Nd isotope evolution of North Atlantic Deep and Intermediate Waters in the western North Atlantic since the Last Glacial Maximum from Blake Ridge sediments. *Earth and Planetary Science Letters*, *266*(1-2), 61-77. doi:10.1016/j.epsl.2007.10.037

Haley, B. A., Klinkhammer, G. P., & McManus, J. (2004). Rare earth elements in pore waters of marine sediments. *Geochimica et Cosmochimica Acta*, *68*(6), 1265-1279. doi:10.1016/j.gca.2003.09.012

Hansen, H. P., & Koroleff, F. (1999). Determination of nutrients. In K. Grasshoff, K. Kremling, & M. Erhardt (Eds.), *Methods of Seawater Analysis* (3rd ed., pp. 159-228). Wiley VHC.

Haug, G. H., Hughen, K. A., Sigman, D. M., Peterson, L. C., & Röhl, U. (2001). Southward migration of the intertropical convergence zone through the Holocene. *Science*, *293*, 1304-1308. doi:10.1126/science.1059725

Hendry, K. R., Georg, R. B., Rickaby, R. E. M., Robinson, L. F., & Halliday, A. N. (2010). Deep ocean nutrients during the Last Glacial Maximum deduced from sponge silicon isotopic compositions. *Earth and Planetary Science Letters*, *292*(3-4), 290-300. doi:10.1016/j.epsl.2010.02.005

Horn, M. G., Robinson, R. S., Rynearson, T. a, & Sigman, D. M. (2011). Nitrogen isotopic relationship between diatom-bound and bulk organic matter of cultured polar diatoms. *Paleoceanography*, *26*(PA3208), 1-12. doi:10.1029/2010PA002080

Horwitz, E. P., Chiarizia, R., & Dietz, M. L. (1992). A novel strontium-selective extraction chromatographic resin. *Solvent Extraction and Ion Exchange*, *10*(2), 313-336. doi:10.1080/07366299208918107

Hurd, D. C. (1973). Interactions of biogenic opal, sediment and seawater in the Central Equatorial Pacific. *Geochimica et Cosmochimica Acta*, *37*(10), 2257-2282. doi:10.1016/0016-7037(73)90103-8

Hutchins, D. A., & Bruland, K. W. (1998). Iron-limited diatom growth and Si:N uptake ratios in a coastal upwelling regime. *Nature*, *393*, 561-564.

Hutchins, D. A., Hare, C. E., Weaver, R. S., Zhang, Y., Firme, G. F., DiTullio, G. R., Alm, M. B., et al. (2002). Phytoplankton iron limitation in the Humboldt Current and Peru Upwelling. *Limnology and Oceanography*, *47*(4), 997-1011. doi:10.4319/lo.2002.47.4.0997

Huyer, A., Smith, R. L., & Paluszkiewicz, T. (1987). Coastal Upwelling off Peru During Normal and El Niño Times, 1981–1984. *Journal of Geophysical Research*, *92*(C13), 14297-14307. doi:10.1029/JC092iC13p14297

Ingall, E., & Jahnke, R. (1994). Evidence for enhanced phosphorus regeneration from marine sediments overlain by oxygen depleted waters. *Geochimica et Cosmochimica Acta*, *58*(11), 2571-2575.

Jacobsen, S. B., & Wasserburg, G. J. (1980). Sm-Nd Isotopic Evolution of Chondrites. *Earth and Planetary Science Letters*, *50*, 139-155.

Jeandel, C., Arsouze, T., Lacan, F., Techine, P., & Dutay, J.-C. (2007). Isotopic Nd compositions and concentrations of the lithogenic inputs into the ocean: A compilation, with an emphasis on the margins. *Chemical Geology*, *239*(1-2), 156-164. doi:10.1016/j.chemgeo.2006.11.013

Karl, D. M., & Tien, G. (1992). Magic: A sensitive and Precise Method for Measuring Dissolved Phosphorus in Aquatic Environments. *Limnology and Oceanography*, *37*(1), 105-116.

Karstensen, J., & Ulloa, O. (2008). The Peru-Chile Current System. *Encyclopedia of Ocean Sciences - 2nd online edition*.

Karstensen, J., Stramma, L., & Visbeck, M. (2008). Oxygen minimum zones in the eastern tropical Atlantic and Pacific oceans. *Progress In Oceanography*, *77*(4), 331-350. doi:10.1016/j.pocean.2007.05.009

Kawabe, M., & Fujio, S. (2010). Pacific Ocean Circulation Based on Observation. *Journal of Oceanography*, *66*, 389-403.

Kessler, W. S. (2006). The circulation of the eastern tropical Pacific: A review. *Progress In Oceanography*, *69*(2-4), 181-217. doi:10.1016/j.pocean.2006.03.009

Klevenz, V., Vance, D., Schmidt, D., & Mezger, K. (2008). Neodymium isotopes in benthic foraminifera: Core-top systematics and a down-core record from the Neogene south Atlantic. *Earth and Planetary Science Letters*, *265*(3-4), 571-587. doi:10.1016/j.epsl.2007.10.053

Koning, E., van Iperen, J. M., van Raaphorst, W., Helder, W., Brummer, G. A., & van Weering, T. C. E. (2001). Selective preservation of upwelling-indicating diatoms in sediments off Somalia, NW Indian Ocean. *Deep-Sea Research*, *48*, 2473-2495.

Koutavas, A., & Lynch-Stieglitz, J. (2004). Variability of the marine ITCZ over the eastern Pacific during the pastn 30,000 years - regional perspective and global context. *Advances in Global Change Research*, *21*(Section B), 347-369. doi:10.1007/978-1-4020-2944-8_12

Kraft., S., Hathorne, E., Frank, M., & Weldeab, S. (2011). Influence of different cleaning methods on seawater εNd extracted from planktonic foraminifera, in preparation.

Lacan, F., & Jeandel, C. (2001). Tracing Papua New Guinea imprint on the central Equatorial Pacific Ocean using neodymium isotopic compositions and Rare Earth Element patterns. *Earth and Planetary Science Letters*, *186*(3-4), 497-512. doi:10.1016/S0012-821X(01)00263-1

Lacan, F., & Jeandel, C. (2005). Neodymium isotopes as a new tool for quantifying exchange fluxes at the continent–ocean interface. *Earth and Planetary Science Letters*, *232*(3-4), 245-257. doi:10.1016/j.epsl.2005.01.004

Lamb, H. H. (1965). The early Medieval Warm Epoch and its sequel. *Palaeogeography, Palaeoclimatology, Palaeoecology*, *1*, 13-37.

Landing, W. M., & Bruland, K. W. (1987). The contrasting biogeochemistry of iron and manganese in the Pacific Ocean. *Geochimica et Cosmochimica Acta*, *51*, 29-43.

Le Fèvre, B., & Pin, C. (2005). A straightforward separation scheme for concomitant Lu–Hf and Sm–Nd isotope ratio and isotope dilution analysis. *Analytica Chimica Acta*, *543*(1-2), 209-221. doi:10.1016/j.aca.2005.04.044

Lewin, J. C. (1961). The dissolution of silica from diatom walls. *Geochimica et Cosmochimica Acta*, *21*(104), 182-198.

Liu, K.-K., & Kaplan, I. R. (1989). The eastern tropical Pacific as a source of 15N-enriched nitrate in seawater off southern Califomia. *Limnology and Oceanography*, *34*(5), 820-830.

Loubere, P., Richaud, M., Liu, Z., & Mekik, F. (2003). Oceanic conditions in the eastern equatorial Pacific during the onset of ENSO in the Holocene. *Quaternary Research*, *60*(2), 142-148. doi:10.1016/S0033-5894(03)00092-9

Loubere, P., Fariduddin, M., & Richaud, M. (2011). Glacial marine nutrient and carbon redistribution: Evidence from the tropical ocean. *Geochemistry Geophysics Geosystems*, *12*(8, Q08013), 1-16. doi:10.1029/2011GC003546

Lukas, R. (1986). The termination of the Equatorial Undercurrent in the eastern Pacific. *Progress In Oceanography*, *16*(2), 63-90. doi:10.1016/0079-6611(86)90007-8

Makou, M. C., Eglinton, T. I., Oppo, D. W., & Hughen, K. A. (2010). Postglacial changes in El Nino and La Nina behavior. *Geology*, *38*(1), 43-46. doi:10.1130/G30366.1

Mann, M. E., Cane, M. A., Zebiak, S. E., & Clement, A. C. (2005). Volcanic and Solar Forcing of the Tropical Pacific over the Past 1000 Years. *Journal of Climate*, *18*, 447-456.

Mann, M. E., Zhang, Z., Rutherford, S., Bradley, R. S., Hughes, M. K., Shindell, D., Ammann, C. M., et al. (2009). Global signatures and dynamical origins of the Little Ice Age and Medieval Climate Anomaly. *Science*, *326*, 1256-1260. doi:10.1126/science.1177303

Mantua, N. J., & Hare, S. R. (2002). The Pacific Decadal Oscillation. *Journal of Oceanography*, *58*, 35-44.

Martin, E. E., & Scher, H. D. (2004). Preservation of seawater Sr and Nd isotopes in fossil fish teeth: bad news and good news. *Earth and Planetary Science Letters*, *220*(1-2), 25-39. doi:10.1016/S0012-821X(04)00030-5

Matsumoto, K., & Sarmiento, J. L. (2008). A corollary to the silicic acid leakage hypothesis. *Paleoceanography*, *23*(PA2203). doi:10.1029/2007PA001515

McGee, D., Marcantonio, F., & Lynch-Stieglitz, J. (2007). Deglacial changes in dust flux in the eastern equatorial Pacific. *Earth and Planetary Science Letters*, *257*(1-2), 215-230. doi:10.1016/j.epsl.2007.02.033

McManus, J., Berelson, W. M., Coale, K. H., Johnson, K. S., & Kilgore, T. E. (1997). Phosphorus regeneration in continental margin sediments. *Geochimica et Cosmochimica Acta*, *61*(14), 2891-2907.

Milligan, A. J., Varela, D. E., Brzezinski, M. A., & Morel, F. M. M. (2004). Dynamics of silicon metabolism and silicon isotopic discrimination in a marine diatom as a function of pCO2. *Limnology and Oceanography*, *49*(2), 322-329. doi:10.4319/lo.2004.49.2.0322

Mohtadi, M., Rossel, P., Lange, C. B., Pantoja, S., Böning, P., Repeta, D. J., Grunwald, M., et al. (2008). Deglacial pattern of circulation and marine productivity in the upwelling region off central-south Chile. *Earth and Planetary Science Letters*, *272*(1-2), 221-230. doi:10.1016/j.epsl.2008.04.043

Molina-Cruz, A. (1977). The Relation of the Southern Trade Winds to Upwelling Processes during the Last 75,000 Years. *Quaternary Research*, *8*, 324-338.

Mollier-Vogel, E., Ryabenko, E., Martinez, P., Wallace, D. W., Altabet, M. A., Schneider, R. (2011). Nitrogen isotope gradients off Peru and Ecuador related to

upwelling, productivity, nutrient uptake and oxygen deficiency. *Deep-Sea Research*. in progress.

Montes, I., Colas, F., Capet, X., & Schneider, W. (2010). On the pathways of the equatorial subsurface currents in the eastern equatorial Pacific and their contributions to the Peru-Chile Undercurrent. *Journal of Geophysical Research*, *115*(C9), 1-16. doi:10.1029/2009JC005710

Moore, J. K., Doney, S. C., Glover, D. M., & Fung, I. Y. (2002). Iron cycling and nutrient-limitation patterns in surface waters of the World Ocean. *Deep-Sea Research*, *49*, 463-507.

Moore, J. K., Doney, S. C., & Lindsay, K. (2004). Upper ocean ecosystem dynamics and iron cycling in a global three-dimensional model. *Global Biogeochemical Cycles*, *18*(4), 1-21. doi:10.1029/2004GB002220

Morales, C. E., Hormazábal, S. E., & Blanco, J. L. (1999). Interannual variability in the mesoscale distribution of the depth of the upper boundary of the oxygen minimum layer off northern Chile (18-24°S): Implications for the pelagic system and biogeochemical cycling. *Journal of Marine Research*, *57*, 909-932.

Morel, F. M. M., & Price, N. M. (2003). The biogeochemical cycles of trace metals in the oceans. *Science*, *300*, 944-947. doi:10.1126/science.1083545

Morley, D. W., Leng, M. J., Mackay, A. W., Sloane, H. J., Rioual, P., & Battarbee, R. W. (2004). Cleaning of lake sediment samples for diatom oxygen isotope analysis. *Journal of Paleolimnology*, *31*(3), 391-401. doi:10.1023/B:JOPL.0000021854.70714.6b

Mortlock, R. A., & Froelich, P. N. (1989). A simple method for the rapid determination of biogenic opal in pelagic marine sediments. *Deep-Sea Research*, *36*(9), 1415-1426.

Müller, P. J., & Schneider, R. (1993). An automated leaching method for the determination of opal in sediments and particulate matter. *Deep-Sea Research*, *40*(3), 425-444. doi:10.1016/0967-0637(93)90140-X

Munoz, P., Lange, C. B., Gutiérrez, D., Hebbeln, D., Salamanca, M. A., Dezileau, L., Reyss, J. L., et al. (2004). Recent sedimentation and mass accumulation rates based on 210Pb along the Peru–Chile continental margin. *Deep-Sea Research*, *51*(20-21), 2523-2541. doi:10.1016/j.dsr2.2004.08.015

Nelson, D. M., & Goering, J. J. (1977). Near-surface silica dissolution in the upwelling region off northwest Africa. *Deep-Sea Research*, *24*(1), 65-73. doi:10.1016/0146-6291(77)90542-2

Nelson, D. M., Tréguer, P., Brzezinski, M. A., Leynaert, A., & Quéguiner, B. (1995). Production and dissolution of biogenic silica in the ocean: Revised global estimates, comparison with regional data and relationship to biogenic sedimentation. *Global Biogeochemical Cycles*, *9*(3), 359-372.

Newton, A., Thunell, R., & Stott, L. (2006). Climate and hydrographic variability in the Indo-Pacific Warm Pool during the last millennium. *Geophysical Research Letters*, *33*(19), 1-5. doi:10.1029/2006GL027234

Noffke, A., Hensen, C., Sommer, S., Scholz, F., Bohlen, L., Mosch, T., & Wallmann, K. (2011). Benthic iron and phosphorus fluxes across the Peruvian Oxygen minimum zone. *submitted*.

Nozaki, Y., & Yamamoto, Y. (2001). Radium 228 based nitrate fluxes in the eastern Indian OCean and the South china Sea and a silicon-induced "alkalinity pump" hypothesis. *Global Biogeochemical Cycles*, *15*(3), 555-567.

Palmer, M. R., & Edmond, J. M. (1989). The strontium isotope budget of the modern ocean. *Earth and Planetary Science Letters*, *92*, 11-26.

Pennington, J. T., Mahoney, K., Kuwahara, V. S., Kolber, D. D., Calienes, R., & Chavez, F. P. (2006). Primary production in the eastern tropical Pacific: A review. *Progress In Oceanography*, *69*(2-4), 285-317. doi:10.1016/j.pocean.2006.03.012

Penven, P., Echevin, V., Pasapera, J., Colas, F., & Tam, J. (2005). Average circulation, seasonal cycle, and mesoscale dynamics of the Peru Current System: A modeling approach. *Journal of Geophysical Research*, *110*(C10021), 1-21. doi:10.1029/2005JC002945

Philander, S. G. (1999). A review of tropical ocean – atmosphere interactions. *Tellus*, *51*(A-B), 71-90.

Pichevin, L. E., Reynolds, B. C., Ganeshram, R. S., Cacho, I., Pena, L. D., Keefe, K., & Ellam, R. M. (2009). Enhanced carbon pump inferred from relaxation of nutrient limitation in the glacial ocean. *Nature*, *459*, 1114-1117. doi:10.1038/nature08101

Piepgras, D. J., & Jacobsen, S. B. (1988). The isotopic composition of neodymium in the North Pacific. *Geochimica et Cosmochimica Acta*, *52*, 1373-1381.

Rabatel, A., Francou, B., Jomelli, V., Naveau, P., & Grancher, D. (2008). A chronology of the Little Ice Age in the tropical Andes of Bolivia (16°S) and its implications for climate reconstruction. *Quaternary Research*, *70*(2), 198-212. doi:10.1016/j.yqres.2008.02.012

Ragueneau, O., Tréguer, P., Leynaert, A., Anderson, R. F., Brzezinski, M. A., DeMaster, D. J., Dugdale, R. C., et al. (2000). A review of the Si cycle in the modern ocean: recent progress and missing gaps in the application of biogenic opal as a paleoproductivity proxy. *Global and Planetary Change*, *26*(4), 317-365. doi:10.1016/S0921-8181(00)00052-7

Ragueneau, O., Savoye, N., Del Amo, Y., Cotten, J., Tardiveau, B., & Leynaert, A. (2005). A new method for the measurement of biogenic silica in suspended matter of coastal waters: using Si:Al ratios to correct for the mineral interference. *Continental Shelf Research*, *25*(5-6), 697-710. doi:10.1016/j.csr.2004.09.017

Ravelo, A. C., & Andreasen, D. H. (2000). Enhanced circulation during a warm period. *Geophysical Research Letters*, *27*(7), 1001-1004.

Raymo, M. E., Hodell, D. A., & Jansen, E. (1992). Response of Deep-Ocean Circulation to Initiation of Northern Hemisphere Glaciation (3-2Ma). *Paleoceanography*, *7*(5), 645-672.

Rein, B., Lückge, A., & Sirocko, F. (2004). A major Holocene ENSO anomaly during the Medieval period. *Geophysical Research Letters*, *31*(17), 2-5. doi:10.1029/2004GL020161

Rein, B., Lückge, A., Reinhardt, L., Sirocko, F., Wolf, A., & Dullo, W.-C. (2005). El Niño variability off Peru during the last 20,000 years. *Paleoceanography*, *20*(4), 1-18. doi:10.1029/2004PA001099

Reinhardt, L., Kudrass, H., Lückge, A., Wiedicke, M., Wunderlich, J., & Wendt, G. (2002). High-resolution sediment echosounding off Peru: Late Quaternary depositional sequences and sedimentary structures of a current-dominated shelf. *Marine Geophysical Researches*, *23*(1980), 335-351.

Reuter, J., Stott, L., Khider, D., Sinha, A., Cheng, H., & Edwards, R. L. (2009). A new perspective on the hydroclimate variability in northern South America during the Little Ice Age. *Geophysical Research Letters*, *36*(21), 1-5. doi:10.1029/2009GL041051

Reynolds, B. C., Frank, M., & Halliday, A. N. (2006). Silicon isotope fractionation during nutrient utilization in the North Pacific. *Earth and Planetary Science Letters*, *244*(1-2), 431-443. doi:10.1016/j.epsl.2006.02.002

Reynolds, B. C., Aggarwal, J., André, L., Baxter, D. C., Beucher, C. P., Brzezinski, M. A., Engström, E., et al. (2007). An inter-laboratory comparison of Si isotope reference materials. *Journal of Analytical Atomic Spectrometry*, *22*(5), 561-568. doi:10.1039/b616755a

Reynolds, B. C., Frank, M., & Halliday, A. N. (2008). Evidence for a major change in silicon cycling in the subarctic North Pacific at 2.73 Ma. *Paleoceanography*, *23*(4, PA4219), 1-10. doi:10.1029/2007PA001563

Rodbell, D. T., Seltzer, G. O., Anderson, D. M., Abbott, M. B., Enfield, D. B., & Newman, J. H. (1999). An ~15,000-Year Record of El Nino–Driven Alluviation in Southwestern Ecuador. *Science*, *283*, 516-520.

Rojas de Mendiola, B. (1981). Seasonal phytoplankton distribution along the Peru coast. In F. Richards (Ed.), *Coastal Upwelling* (pp. 345-356). Washington, D.C.: American Geophysical Union.

Romero, O. E., Hebbeln, D., & Wefer, G. (2001). Temporal and spatial variability in export production in the SE Pacific Ocean: evidence from siliceous plankton fluxes and surface sediment assemblages. *Deep-Sea Research*, *48*(12), 2673-2697. doi:10.1016/S0967-0637(01)00037-1

Rossel, F., & Cadier, E. (2009). El Nino and prediction of anomalous monthly rainfalls in Ecuador. *Hydrological Processes*, *23*, 3253- 3260. doi:10.1002/hyp

Rutberg, R. L., Hemming, S. R., & Goldstein, S. L. (2000). Reduced North Atlantic Deep Water flux to the glacial Southern Ocean inferred from neodymium isotope ratios. *Nature*, *405*, 935-938. doi:10.1038/35016049

Ryabenko, E. (2011). *Nitrogen isotopes in the Atlantic and Pacific Oxygen Minimum Zones*. PhD thesis, Christian-Albrechts-University Kiel. pp. 130.

Sandweiss, D. H., Maasch, K. A., Burger, R. L., Richardson, J. B., Rollins, H. B., Clement, A., Maasch, K. A., et al. (2001). Variation in Holocene El Nino frequencies: Climate records and cultural consequences in ancient Peru. *Geology*, *29*, 603-606. doi:10.1130/0091-7613(2001)029<0603

Sar, E. A., Sunesen, I., & Fernández, P. V. (2007). Marine diatoms from Buenos Aires coastal waters (Argentina).II. Thalassionemataceae and Rhaphoneidaceae. *Revista Chilena de Historia Natural*, *80*, 63-80.

Sarbas, B., & Nohl, U. (2009). The GEOROC database - A decade of "online geochemistry." *Geochimica et Cosmochimica Acta*, *73*(13), A1158. (http://georoc.mpch-mainz.gwdg.de/georoc/).

Sarmiento, J. L., Gruber, N., Brzezinski, M. A., & Dunne, J. P. (2004). High-latitude controls of thermocline nutrients and low latitude biological productivity. *Nature*, *427*, 56-60. doi:10.1038/nature02204.1.

Sarthou, G., Timmermans, K. R., Blain, S., & Tréguer, P. (2005). Growth physiology and fate of diatoms in the ocean: a review. *Journal of Sea Research*, *53*(1-2), 25-42. doi:10.1016/j.seares.2004.01.007

Savage, P. S., Georg, R. B., Armytage, R. M. G., Williams, H. M., & Halliday, A. N. (2010). Silicon isotope homogeneity in the mantle. *Earth and Planetary Science Letters*, *295*(1-2), 139-146. doi:10.1016/j.epsl.2010.03.035

Scheidegger, K. F., & Krissek, L. A. (1982). Dispersal and deposition of eolian and fluvial sediments off Peru and northern Chile. *Geological Society Of America Bulletin*, *93*(2), 150-162. doi:10.1130/0016-7606(1982)93<150

Schrader, H. (1992). Coastal upwelling and atmospheric CO2 changes over the last 400,000 years: Peru. *Marine Geology*, *107*(4), 239-248. doi:10.1016/0025-3227(92)90074-R

Schrader, H., & Sorknes, R. (1991). Peruvian coastal upwelling: Late Quaternary productivity changes revealed by diatoms. *Marine Geology*, *97*, 233-249.

Shemesh, A., Mortlock, R. A., Smith, R. J., & Froelich, P. N. (1988). Determination of Ge/Si in marine siliceous microfossils: Separation, cleaning and dissolution of diatoms and radiolaria. *Marine Chemistry*, *25*(4), 305-323. doi:10.1016/0304-4203(88)90113-2

Siegenthaler, U., Stocker, T. F., Monnin, E., Lüthi, D., Schwander, J., Stauffer, B., Raynaud, D., et al. (2005). Stable carbon cycle-climate relationship during the Late Pleistocene. *Science*, *310*, 1313-1317. doi:10.1126/science.1120130

Sifeddine, A., Gutiérrez, D., Ortlieb, L., Boucher, H., Velazco, F., Field, D. B., Vargas, G., et al. (2008). Laminated sediments from the central Peruvian continental slope: A 500 year record of upwelling system productivity, terrestrial runoff and redox conditions. *Progress In Oceanography*, *79*(2-4), 190-197. doi:10.1016/j.pocean.2008.10.024

Sims, P. A., Mann, D. G., & Medlin, L. K. (2006). Evolution of the diatoms: insights from fossil, biological and molecular data. *Phycologia*, *45*(4), 361-402. doi:10.2216/05-22.1

Strub, P. T., Mesias, J. M., Montecino, V., Rutlland, J., & Salinas, S. (1998). Coastal Ocean Circulation off western South America. In A. R. Robinson & K. H. Brink (Eds.), *The Sea, vol. 11* (pp. 273-314). Holboken, N. J.: John Wiley.

Stumpf, R., Frank, M., Schönfeld, J., & Haley, B. A. (2010). Late Quaternary variability of Mediterranean Outflow Water from radiogenic Nd and Pb isotopes. *Quaternary Science Reviews*, *29*(19-20), 2462-2472. doi:10.1016/j.quascirev.2010.06.021

Stumpf, R., Frank, M., Schönfeld, J., & Haley, B. A. (2011). Climatically driven changes in sediment supply on the SW Iberian shelf since the Last Glacial Maximum. *Earth and Planetary Science Letters*, *312*(1-2), 80-90. doi:10.1016/j.epsl.2011.10.002

Sunda, W. G., & Huntsman, S. A. (1995). Iron uptake and growth limitation in oceanic and coastal phytoplankton. *Marine Chemistry*, *50*(1-4), 189-206. doi:10.1016/0304-4203(95)00035-P

Sunesen, I., Hernández-Becerril, D. U., & Sar, E. A. (2008). Marine diatoms from Buenos Aires coastal waters (Argentina). V. Species of the genus Chaetoceros. *Revista de Biologia Marina y Oceanografia*, *43*(2), 303-326.

Tachikawa, K., Jeandel, C., & Roy-Barman, M. (1999). A new approach to the Nd residence time in the ocean: the role of atmospheric inputs. *Earth and Planetary Science Letters*, *170*(4), 433-446. doi:10.1016/S0012-821X(99)00127-2

Tachikawa, K., Roy-Barman, M., Michard, A., Thouron, D., Yeghicheyan, D., & Jeandel, C. (2004). Neodymium isotopes in the Mediterranean Sea: comparison between seawater and sediment signals. *Geochimica et Cosmochimica Acta*, *68*(14), 3095-3106. doi:10.1016/j.gca.2004.01.024

Takeda, S. (1998). Influence of iron availability on nutrient consumption ratio of diatoms in oceanic waters. *Nature*, *393*, 1-4.

Talley, L. D. (1993). Distribution and Formation of North Pacific Intermediate Water. *Journal of Physical Oceanography*, *23*, 517-537.

Talley, L. D. (1999). Some aspects of ocean heat transport by the shallow intermediate and deep overturning circulations. *Mechanisms of Global Climate Change at Millenial Time Scales* (Vol. 112, p. 26). American Geophysical Union.

Tanaka, T., Togashi, S., Kamioka, H., Amakawa, H., Kagami, H., Hamamoto, T., Yuhara, M., et al. (2000). JNdi-1: a neodymium isotopic reference in consistency with LaJolla neodymium. *Chemical Geology*, *168*(3-4), 279-281. doi:10.1016/S0009-2541(00)00198-4

Thiede, J., & Suess, E. (1983). *Coastal Upwelling: Its Sediment Record* (p. 610). New York: Plenum Publishing Corporation.

Thomas, A. C., Carr, M.-E., & Strub, P. T. (2001). Chlorophyll variability in eastern boundary currents. *Geophysical Research Letters*, *28*(18), 3421-3424.

Toggweiler, J. R., Dixon, K., & Broecker, W. S. (1991). The Peru Upwelling and the Ventilation of the South Pacific Thermocline. *Journal of Geophysical Research*, *96*(C11), 20467-20497. doi:10.1029/91JC02063

Tréguer, P., Nelson, D. M., Van Bennekom, A. J., DeMaster, D. J., Leynaert, A., & Quéguiner, B. (1995). The silica balance in the world ocean: a reestimate. *Science*, *268*, 375-9. doi:10.1126/science.268.5209.375

Tudhope, A. W., Chilcott, C. P., McCulloch, M. T., Cook, E. R., Chappell, J., Ellam, R. M., Lea, D. W., et al. (2001). Variability in the El Niño-Southern Oscillation through a glacial-interglacial cycle. *Science*, *291*, 1511-1517. doi:10.1126/science.1057969

Tütken, T., Eisenhauer, A., Wiegand, B., & Hansen, B. T. (2002). Glacial-interglacial cycles in Sr and Nd isotopic composition of Arctic marine sediments triggered by the Svalbard/Barents Sea ice sheet. *Marine Geology*, *182*, 351-372.

Unkel, I., Kadereit, A., Mächtle, B., Eitel, B., Kromer, B., Wagner, G., & Wacker, L. (2007). Dating methods and geomorphic evidence of palaeoenvironmental changes at the eastern margin of the South Peruvian coastal desert (14°30′S) before and during the Little Ice Age. *Quaternary International*, *175*(1), 3-28. doi:10.1016/j.quaint.2007.03.006

Valdés, J., Ortlieb, L., Gutiérrez, D., Marinovic, Luis, Vargas, G., & Sifeddine, A. (2008). 250 years of sardine and anchovy scale deposition record in Mejillones Bay, northern Chile. *Progress In Oceanography*, *79*(2-4), 198-207. doi:10.1016/j.pocean.2008.10.002

van Bennekom, A. J., Berger, G. W., van der Gaast, S. J., & de Vries, R. T. P. (1988). Primary Productivity and the Silica Cycle in the Southern Ocean (Atlantic sector). *Palaeogeography, Palaeoclimatology, Palaeoecology*, *67*(1-2), 19-30. doi:10.1016/0031-0182(88)90120-4

van Bennekom, A. J., Jansen, J. H. F., van der Gaast, S. J., van Iperen, J. M., & Pieters, J. (1989). Aluminium-rich opal: an intermediate in the preservation of biogenic silica in the Zaire (Congo) deep-sea fan. *Deep-Sea Research*, *36*(2), 173-190. doi:10.1016/0198-0149(89)90132-5

van Cappellen, P., & Qiu, L. (1997). Biogenic silica dissolution in sediments of the Southern Ocean. I. Solubility. *Deep-Sea Research*, *44*(5), 1109-1128. doi:10.1016/S0967-0645(96)00113-0

van den Boorn, S. H. J. M., Vroon, P. Z., van Belle, C. C., van der Wagt, B., Schwieters, J., & van Bergen, M. J. (2006). Determination of silicon isotope ratios in silicate materials by high-resolution MC-ICP-MS using a sodium hydroxide sample digestion method. *Journal of Analytical Atomic Spectrometry*, *21*(8), 734. doi:10.1039/b600933f

Vanhaecke, F., & Moens, L. (2004). Overcoming spectral overlap in isotopic analysis via single- and multi-collector ICP-mass spectrometry. *Analytical and Bioanalytical Chemistry*, *378*(2), 232-240. doi:10.1007/s00216-003-2175-8

Vance, D., & Burton, K. W. (1999). Neodymium isotopes in planktonic foraminifera: a record of the response of continental weathering and ocean circulation rates

to climate change. *Earth and Planetary Science Letters*, *173*(4), 365-379. doi:10.1016/S0012-821X(99)00244-7

Vance, D., Scrivner, A. E., Beney, P., Staubwasser, M., Henderson, G. M., & Slowey, N. C. (2004). The use of foraminifera as a record of the past neodymium isotope composition of seawater. *Paleoceanography*, *19*(2), 1-17. doi:10.1029/2003PA000957

Varela, D. E., Pride, C. J., & Brzezinski, M. A. (2004). Biological fractionation of silicon isotopes in Southern Ocean surface waters. *Global Biogeochemical Cycles*, *18*(1), 1-8. doi:10.1029/2003GB002140

Vargas, G., Rutllant, J. A., & Ortlieb, L. (2006). ENSO tropical–extratropical climate teleconnections and mechanisms for Holocene debris flows along the hyperarid coast of western South America (17°–24°S). *Earth and Planetary Science Letters*, *249*(3-4), 467-483. doi:10.1016/j.epsl.2006.07.022

Vargas, G., Pantoja, S., Rutllant, J. A., Lange, C. B., & Ortlieb, L. (2007). Enhancement of coastal upwelling and interdecadal ENSO-like variability in the Peru-Chile Current since late 19th century. *Geophysical Research Letters*, *34*(13), 1-6. doi:10.1029/2006GL028812

Veizer, J., Ala, D., Azmy, K., Bruckschen, P., Buhl, D., Bruhn, F., Carden, G. A. F., et al. (1999). $^{87}Sr/^{86}Sr$, $d^{13}C$ and $d^{18}O$ evolution of Phanerozoic seawater. *Chemical Geology*, *161*, 59-88.

Vuille, M., Francou, B., Wagnon, P., Juen, I., Kaser, G., Mark, B. G., & Bradley, R. S. (2008). Climate change and tropical Andean glaciers: Past, present and future. *Earth-Science Reviews*, *89*(3-4), 79-96. doi:10.1016/j.earscirev.2008.04.002

Wada, E., & Hattori, A. (1978). Nitrogen isotope effects in the assimilation of inorganic nitrogenous compounds by marine diatoms. *Geomicrobiology Journal*, *1*(1), 85-101. doi:10.1080/01490457809377725

Wang, O., Fukumori, I., Lee, T., & Cheng, B. (2004). On the cause of eastern equatorial Pacific Ocean T-S variations associated with El Niño. *Geophysical Research Letters*, *31*(15), 1-5. doi:10.1029/2004GL020188

Waylen, P. R., & Caviedes, C. N. (1984). El Nino and annual floods on the North Peruvian littoral. *Journal of Hydrology*, *89*, 141-156. doi:10.2307/214939

Westbroek, P., Brown, C. W., van Bleijswijk, J., Brownlee, C., Brummer, G. J., Conte, M., Egge, J., et al. (1993). A model system approach to biological forcing. the example of Emiliania huxleyi. *Global and Planetary Change*, *8*, 27-46.

Wijffels, S. E., Toole, J. M., Bryden, H. L., Fine, R. a, Jenkins, W. J., & Bullister, J. L. (1996). The water masses and circulation at 10°N in the Pacific. *Deep-Sea Research*, *43*(4), 501-544. doi:10.1016/0967-0637(96)00006-4

Wilken, S., Hoffmann, B., Hersch, N., Kirchgessner, N., Dieluweit, S., Rubner, W., Hoffmann, L. J., et al. (2011). Diatom frustules show increased mechanical strength and altered valve morphology under iron limitation. *Limnology and Oceanography*, *56*(4), 1399-1410. doi:10.4319/lo.2011.56.4.1399

Wille, M., Sutton, J., Ellwood, M. J., Sambridge, M., Maher, W. A., Eggins, S., & Kelly, M. (2010). Silicon isotopic fractionation in marine sponges: A new model for understanding silicon isotopic variations in sponges. *Earth and Planetary Science Letters*, *292*(3-4), 281-289. doi:10.1016/j.epsl.2010.01.036

Winkler, L. W. (1888). Die Bestimmung des im Wasser gelösten Sauerstoffs. *Berichte der Deutschen Chemischen Gesellschaft*, *21*, 2843-2855.

Wischmeyer, A. G., De La Rocha, C. L., Maier-Reimer, E., & Wolf-Gladrow, D. A. (2003). Control mechanisms for the oceanic distribution of silicon isotopes. *Global Biogeochemical Cycles*, *17*(3), 1-12. doi:10.1029/2002GB002022

Wolf, A. (2002). *Zeitliche Variationen im peruanischen Küstenauftrieb seit dem Letzten Glazialen Maximum – Steuerung durch globale Klimadynamik*. PhD thesis, Christian-Albrechts University Kiel. pp. 115

Wyrtki, K., & Wenzel, J. (1984). Possible gyre-gyre interaction in the Pacific Ocean. *Nature*, *309*, 538-540.

Appendix

Table A.1: Seawater oxygen and $Si(OH)_4$ concentrations and $\delta^{30}Si_{Si(OH)4}$ data from the RV Meteor cruises M77/3 and 4, collected in January and February 2009. $2\sigma_{(sd)}$ represents the external reproducibilities of repeated sample measurements.

Station	Latitude	Longitude	water depth [m]	Oxygen [µmol/kg]	$Si(OH)_4$ [µmol/kg]	$\delta^{30}Si$ [‰]	$2\sigma_{(sd)}$
120	3° 35.4' S	80° 57.0' W	2.4	227.86	2.80	2.61	0.28
			4.7	227.77	2.87	-	-
			10.1	221.53	2.99	-	-
			20.5	185.57	12.40	-	-
			30.1	116.71	14.95	1.75	0.15
			40.2	35.13	16.62	-	-
			49.9	46.38	15.60	-	-
			59.6	59.16	15.54	1.58	0.07
			80.4	58.31	15.54	1.76	0.11
			101.6	54.49	15.93	1.32	0.33
			120.7	35.87	18.98	-	-
			151.2	47.16	18.37	-	-
			151.6	48.93	18.39	-	-
			160.3	51.28	18.29	-	-
			170.3	50.32	18.79	-	-
			180.4	46.76	19.18	-	-
			217.4	20.29	22.43	1.49	0.29
122	6° 00.0' S	81° 15.6' W	1.9	118.82	8.97	1.86	0.09
			5.7	113.89	10.62	-	-
			10.5	46.24	14.26	1.87	0.19
			19.9	5.11	16.82	1.38	0.18
			30.2	5.11	17.21	-	-
			40.8	7.09	17.80	1.36	0.24
			51.7	7.18	18.00	-	-
			60.6	6.23	18.88	-	-
			69.7	5.94	20.36	-	-
			80.2	4.90	21.15	1.48	0.14
			90.5	4.64	21.15	-	-
			100.4	4.37	21.44	-	-
			125.5	3.13	21.93	-	-
			150.0	3.17	22.81	-	-
			174.5	3.12	25.18	1.30	0.18
			198.1	3.13	26.36	-	-
			203.2	3.20	26.16	-	-
806	8° 00.0' S	79° 50.4' W	1.5	212.83	6.25	2.03	0.22
			9.7	155.43	6.95	-	-
			20.8	10.72	12.16	-	-
			30.2	6.10	14.24	1.64	0.28
			41.0	8.73	16.68	-	-
			50.2	10.56	17.37	-	-
			60.4	10.59	17.72	1.67	0.20
			70.6	10.43	17.72	-	-

Table A.1: continued

Station	Latitude	Longitude	water depth [m]	Oxygen [µmol/kg]	$Si(OH)_4$ [µmol/kg]	$\delta^{30}Si$ [‰]	$2\sigma_{(sd)}$
806	8° 00.0' S	79° 50.4' W	81.2	9.09	18.41	-	-
			90.2	8.39	18.76	1.62	0.28
			100.2	6.70	18.07	-	-
			110.3	5.85	19.80	-	-
			120.0	3.59	24.67	1.49	0.21
			129.7	2.02	30.23	-	-
			141.0	2.12	30.92	1.58	0.35
807	10° 00.0' S	78° 22.8' W	2.0	65.53	9.73	1.96	0.11
			10.8	6.00	16.68	-	-
			20.5	1.84	18.76	-	-
			29.8	1.90	20.85	1.52	0.20
			39.9	1.89	23.28	-	-
			49.6	1.91	26.06	-	-
			60.2	1.97	26.06	1.26	0.18
			70.9	1.96	30.58	-	-
			79.7	1.96	31.97	-	-
			90.1	2.03	32.31	1.18	0.16
			99.5	2.05	32.31	-	-
			110.0	2.00	32.66	1.11	0.16
19	12° 21.6' S	77° 00.0' W	2.3	191.39	17.72	1.83	0.23
			2.7	184.47	21.20	-	-
			10.4	2.08	-	1.63	0.20
			21.7	1.84	33.70	-	-
			32.0	1.84	33.36	-	-
			39.9	2.01	-	1.16	0.20
			42.2	1.86	40.65	-	-
			51.7	1.87	39.26	-	-
			60.2	1.98	-	1.42	0.19
			62.1	1.93	37.53	-	-
			72.1	1.97	38.91	-	-
			79.5	2.02	-	1.47	0.16
			82.4	1.94	38.91	-	-
			92.0	2.02	40.65	-	-
			97.5	2.04	41.69	1.06	0.17
77	14° 00.0' S	76° 30.6' W	2.0	83.46	17.54	1.71	0.31
			10.0	12.00	17.54	1.84	0.26
			19.2	2.64	23.92	1.57	0.29
			50.8	2.70	-	1.36	0.34
			51.2	2.72	38.28	-	-
			150.4	2.91	32.70	1.68	0.29
			196.7	2.97	29.55	1.71	0.29
34	16° 00.0' S	74° 10.8' W	2.1	165.82	3.82	2.66	0.48
			11.1	158.44	4.52	-	-
			20.0	132.15	7.30	1.90	0.30
			29.9	58.64	12.51	-	-
			40.1	38.72	15.29	1.69	0.40
			50.1	25.27	20.85	-	-
			60.2	7.72	23.98	1.75	0.22
			70.6	2.53	25.37	-	-
			80.1	2.42	26.76	1.63	0.18

Table A.1: continued

Station	Latitude	Longitude	water depth [m]	Oxygen [µmol/kg]	$Si(OH)_4$ [µmol/kg]	$\delta^{30}Si$ [‰]	$2\sigma_{(sd)}$
34	16° 00.0' S	74° 10.8' W	90.4	2.12	27.80	-	-
			100.1	2.16	29.88	-	-
			116.9	2.35	31.62	1.26	0.22
			117.3	2.32	31.97	-	-
43	17° 18.0' S	71° 54.0'W	3.9	238.46	2.14	2.81	0.33
			9.9	234.36	2.60	-	-
			20.8	149.15	5.27	2.40	0.16
			30.1	81.91	10.36	-	-
			40.0	15.15	19.33	1.49	0.18
			50.0	8.54	22.57	-	-
			60.7	3.21	26.74	1.30	0.28
			70.3	2.17	31.01	-	-
			80.5	2.14	32.40	-	-
			90.3	2.15	23.07	-	-
			97.8	2.18	30.80	-	-
			121.0	2.28	31.23	-	-
			121.3	2.23	31.05	1.36	0.25

Table A.2: Concentrations of $bSiO_2$ (wt%), Al/Si (mmol/mol) and Ti/Si ratios (µmol/mol) and $\delta^{30}Si$ (‰) data for bulk $bSiO_2$ and hand-picked diatoms from surface samples from the Peruvian shelf. $2\sigma_{(sd)}$ represents the external reproducibilities of repeated sample measurements.

Station	Latitude	Longitude	Depth [m]	$bSiO_2$ [wt%]	$\delta^{30}Si_{bSiO2}$ [‰]	$2\sigma_{(sd)}$	Al/Si [mmol/mol]	Ti/Si [µmol/mol]	$\delta^{30}Si_{diatom}$ [‰]	$2\sigma_{(sd)}$
M77/2-076	00° 05.5' N	80° 33.4' W	290	2.81	0.75	0.29	9	69	1.77	0.10
M77/2-067	01° 45.1' S	82° 37.5' W	2075	7.15	0.58	0.09	-	-	-	-
M77/2-062	02° 30.0' S	81° 14.7' W	1678	5.11	-	-	-	-	1.47	0.23
M77/2-071	02° 50.0' S	80° 50.7' W	100	2.39	-0.43	0.29	189	54	-	-
M77/2-070	03° 07.0' S	80° 38.8' W	59	0.24	-0.10	0.13	235	125	-	-
M77/2-060	03° 51.1' S	81° 15.5' W	701	4.28	0.53	0.22	-	-	1.82	0.40
M77/2-052	05° 29.0' S	81° 27.0' W	1252	8.58	0.76	0.10	80	84	1.95	0.13
M77/2-053	05° 28.9' S	81° 34.0' W	2607	11.52	0.89	0.21	24	31	-	-
M77/2-047	07° 52.0' S	80° 31.4' W	625	3.85	0.28	0.19	61	59	-	-
M77/2-050	08° 01.0' S	80° 30.1' W	1013	7.44	0.78	0.25	-	-	1.61	0.17
M77/2-028	09° 17.7' S	79° 53.9' W	1105	5.01	0.30	0.10	31	42	-	-
M77/2-029	09° 17.7' S	79° 37.1' W	437	4.64	0.46	0.29	45	40	-	-
M77/2-026	10° 45.1' S	78° 28.4' W	424	3.62	0.10	0.14	44	44	-	-
M77/2-022	10° 53.2' S	78° 46.4' W	1923	4.66	0.52	0.10	45	33	-	-
M77/1-450	11° 00.0' S	78° 10.0' W	319	13.86	0.90	0.17	10	42	-	-
M77/1-460	11° 00.0' S	78° 35.2' W	1245	1.50	-0.10	0.29	44	38	-	-
M77/1-462	11° 00.0' S	78° 44.7' W	2020	5.00	-	-	-	-	0.75	0.05
M77/1-469	11° 00.1' S	77° 56.6' W	145	17.62	1.03	0.15	22	54	1.05	0.38
M77/1-543	11° 00.0' S	77° 47.4' W	77	12.88	0.85	0.15	8	33	-	-
M77/2-005	12° 05.7' S	77° 40.1`W	214	10.94	0.95	0.10	1	96	-	-
M77/1-620	12° 18.6' S	77° 19.2' W	150	17.65	0.92	0.18	2	45	-	-

Table A.2: continued

Station	Latitude	Longitude	Depth [m]	$bSiO_2$ [wt%]	$\delta^{30}Si_{bSiO2}$ [‰]	$2\sigma_{(sd)}$	Al/Si [mmol/mol]	Ti/Si [µmol/mol]	$\delta^{30}Si_{diatom}$ [‰]	$2\sigma_{(sd)}$
M77/1-623	12° 38.2' S	77° 34.6' W	1085	5.85	0.61	0.13	15	59	0.61	0.20
M77/2-002	15° 04.8' S	75° 44.0`W	290	20.55	1.07	0.22	10	47	0.99	0.15
M77/1-420	15° 11.4' S	75° 34.9' W	516	17.31	1.07	0.13	24	41	1.87	0.10
M77/1-396	17° 26.0' S	71° 51.4' W	299	6.06	0.95	0.29	28	103	-	-
M77/1-403	17° 26.0' S	71° 51.4' W	296	2.39	-0.98	0.21	45	84	-	-
M77/1-407	17° 34.4' S	71° 56.0' W	788	2.75	0.17	0.15	41	78	-	-
M77/1-411	17° 47.2' S	72° 44.7' W	2167	5.39	0.52	0.16	56	64	0.58	0.25

Table A.3: Surface sediment $^{87}Sr/^{86}Sr$, $^{143}Nd/^{144}Nd$ and εNd from Fe-Mn coatings, detrital material and benthic foraminifers. $2\sigma_{(sd)}$ represents the external reproducibilities of repeated standard measurements.

Station	Latitude	Longitude	Depth [m]	$^{87}Sr/^{86}Sr$ coating	$2\sigma_{(sd)}$	$^{143}Nd/^{144}Nd$ coating	εNd coating	$2\sigma_{(sd)}$	$^{87}Sr/^{86}Sr$ detritus	$2\sigma_{(sd)}$	$^{143}Nd/^{144}Nd$ detritus	εNd detritus	$2\sigma_{(sd)}$	$^{143}Nd/^{144}Nd$ foram	εNd foram	$2\sigma_{(sd)}$
M771-398	17°28.1' S	71°52.4' W	496	0.708920	3.2E-05	0.512408	-4.5	0.3	0.707180	1.5E-05	0.512315	-6.3	0.1	-	-	-
M771-403	17°26.0' S	71°51.4' W	296	0.709129	3.2E-05	0.512425	-4.2	0.5	0.707827	1.5E-05	0.512328	-6.0	0.1	-	-	-
M771-409	17°38.4' S	71°58.3' W	920	0.708844	3.2E-05	0.512416	-4.3	0.3	0.707408	1.5E-05	0.512324	-6.1	0.1	-	-	-
M771-420	15°11.4' S	75°34.9' W	516	0.709160	1.4E-05	0.512550	-1.7	0.3	0.707958	1.4E-05	0.512501	-2.7	0.3	0.512564	-1.4	0.4
M771-457	11°00.1' S	78°19.3' W	467	-	-	-	-	-	-	-	-	-	-	0.512628	-0.2	0.4
M771-458	11°00.0' S	78°25.6' W	698	0.709092	3.2E-05	0.512555	-1.6	1.0	0.707634	1.5E-05	0.512458	-3.5	0.1	0.512522	-2.3	0.7
M771-487	11°00.0' S	78°23.2' W	579	-	-	-	-	-	-	-	-	-	-	0.512595	-0.8	0.4
M771-519	11°00.0' S	78°16.3' W	410	-	-	-	-	-	-	-	-	-	-	0.512698	1.2	0.4
M771-520	11°00.0' S	78°01.9' W	196	0.709030	3.2E-05	0.512566	-1.4	0.5	0.708589	1.5E-05	0.512357	-5.5	0.1	-	-	-
M771-554	10°26.4' S	78°54.7' W	522	-	-	-	-	-	-	-	-	-	-	0.512563	-1.5	0.4
M771-590	11°15.1' S	78°16.4' W	547	-	-	-	-	-	-	-	-	-	-	0.512616	-0.4	0.4

Table A.3: continued

Station	Latitude	Longitude	Depth [m]	$^{87}Sr/^{86}Sr$ coating	$2\sigma_{(sd)}$	$^{143}Nd/^{144}Nd$ coating	εNd coating	$2\sigma_{(sd)}$	$^{87}Sr/^{86}Sr$ detritus	$2\sigma_{(sd)}$	$^{143}Nd/^{144}Nd$ detritus	εNd detritus	$2\sigma_{(sd)}$	$^{143}Nd/^{144}Nd$ foram	εNd foram	$2\sigma_{(sd)}$
M771-602	11°16.0' S	78°18.4' W	618	0.709124	3.2E-05	0.512554	-1.6	1.0	0.707777	1.5E-05	0.512470	-3.3	0.1	0.512512	-2.5	0.7
M771-608	12°32.6' S	77°30.5' W	584	-	-	-	-	-	-	-	-	-	-	0.512556	-1.6	0.4
M771-611	12°29.5' S	77°28.0' W	417	-	-	-	-	-	-	-	-	-	-	0.512587	-1.0	0.4
M771-620	12°18.6' S	77°19.2' W	150	0.709001	1.4E-05	0.512569	-1.3	0.3	0.707487	1.4E-05	0.512475	-3.2	0.3	-	-	-
M772-002	15°04.8' S	75°44.0`W	290	0.709100	1.4E-05	0.512570	-1.3	0.3	0.708073	1.4E-05	0.512473	-3.2	0.3	-	-	-
M772-022	10°53.2' S	78°46.4' W	1923	0.708998	3.2E-05	0.512563	-1.5	0.3	0.707169	1.5E-05	0.512442	-3.8	0.1	-	-	-
M772-026	10°45.1' S	78°28.4' W	425	-	-	-	-	-	-	-	-	-	-	0.512542	-1.9	0.4
M772-028	09°17.7' S	79°53.9' W	1105	0.709037	3.2E-05	0.512579	-1.1	0.3	0.707777	1.5E-05	0.512384	-5.0	0.1	-	-	-
M772-029	09°17.7' S	79°37.1' W	433	-	-	-	-	-	-	-	-	-	-	0.512585	-1.0	0.4
M772-031	09°03.0' S	79°26.9' W	114	0.709111	3.2E-05	0.512578	-1.2	0.3	0.705873	1.5E-05	0.512508	-2.5	0.1	0.512558	-1.6	0.7
M772-047	07°52.0' S	80°31.4' W	625	0.709102	3.2E-05	0.512578	-1.2	0.3	0.707975	1.5E-05	0.512396	-4.7	0.1	0.512567	-1.4	0.7
M772-052	05°29.0' S	81°27.0' W	1255	-	-	-	-	-	-	-	-	-	-	0.512578	-1.2	0.7
M772-053	05°28.9' S	81°34.0' W	2607	0.708990	3.2E-05	0.512582	-1.1	0.3	0.710374	1.5E-05	0.512320	-6.2	0.1	-	-	-
M772-054	05°29.0' S	81°18.4' W	297	0.708788	3.2E-05	0.512598	-0.8	0.3	0.710489	1.5E-05	0.512333	-5.9	0.1	-	-	-
M772-056	03°45.0' S	81°07.3' W	350	0.708847	3.2E-05	0.512638	0.0	0.3	0.708117	1.5E-05	0.512429	-4.1	0.1	0.512613	-0.5	0.7
M772-064	01°53.5' S	81°11.8' W	529	-	-	-	-	-	-	-	-	-	-	0.512753	2.2	0.4
M772-065	01°57.0' S	81°07.2' W	206	0.708816	3.2E-05	-	-	-	0.706146	1.5E-05	0.512637	0.0	0.1	0.512688	1.0	0.7
M772-067	01°45.1' S	82°37.5' W	2075	0.709077	3.2E-05	0.512679	0.8	1.0	0.708736	1.5E-05	0.512527	-2.2	0.1	-	-	-
M772-069	03°16.0' S	80°56.9' W	339	0.708916	1.4E-05	0.512731	1.8	0.3	0.705084	1.5E-05	0.512582	-1.1	0.1	0.512720	1.6	0.7
M772-072	02°49.0' S	81°00.5' W	425	-	-	-	-	-	-	-	-	-	-	0.512716	1.5	0.4

Table A.4: Downcore records of core SO147-106KL for $\delta^{30}Si$ ($bSiO_2$ and picked diatoms) (‰), $^{87}Sr/^{86}Sr$, $^{143}Nd/^{144}Nd$ and εNd (Fe-Mn coatings and detrital material). $2\sigma_{(sd)}$ represents the external reproducibilities of repeated standard measurements.

age [call. yr BP]	$\delta^{30}Si_{bSiO2}$ [‰]	$2\sigma_{(sd)}$	$\delta^{30}Si_{diatom}$ [‰]	$2\sigma_{(sd)}$	$^{87}Sr/^{86}Sr_{coating}$	$2\sigma_{(sd)}$	$^{143}Nd/^{144}Nd_{coating}$	$\varepsilon Nd_{coating}$	$2\sigma_{(sd)}$	$^{87}Sr/^{86}Sr_{detritus}$	$2\sigma_{(sd)}$	$^{143}Nd/^{144}Nd_{detritus}$	$\varepsilon Nd_{detritus}$	$2\sigma_{(sd)}$
1169	-	-	1.38	0.11	0.709082	1.4E-05	0.512572	-1.3	0.3	0.708485	1.4E-05	0.512406	-4.5	0.3
1175	0.91	0.10	-	-	-	-	-	-	-	-	-	-	-	-
1334	1.11	0.21	-	-	-	-	-	-	-	-	-	-	-	-
1370	-	-	-	-	0.709128	1.4E-05	0.512585	-1.0	0.3	-	-	-	-	-
1388	0.94	0.18	-	-	-	-		-	-	-	-	-	-	-
1466	-	-	-	-	0.709117	1.4E-05	0.512583	-1.1	0.3	0.707750	1.4E-05	0.512451	-3.6	0.3
dupl.	-	-	-	-	0.709160	1.4E-05	0.512539	-1.9	0.3	-	-	-	-	-
1560	-	-	0.89	0.17	-	-	-	-	-	-	-	-	-	-
1578	1.10	0.10	-	-	-	-	-	-	-	-	-	-	-	-
1701	1.01	0.22	-	-	-	-	-	-	-	-	-	-	-	-
1725	-	-	-	-	0.709071	1.4E-05	0.512578	-1.2	0.3	-	-	-	-	-
1839	-	-	-	-	0.709125	1.4E-05	0.512604	-0.7	0.3	0.707292	1.4E-05	0.512487	-2.9	0.3
1860	1.26	0.24	-	-	-	-	-	-	-	-	-	-	-	-
2006	-	-	-	-	0.709132	1.4E-05	0.512576	-1.2	0.3	-	-	-	-	-
2449	0.80	0.13	-	-	-	-	-	-	-	-	-	-	-	-
3089	0.72	0.11	-	-	-	-	-	-	-	-	-	-	-	-
3130	-	-	0.83	0.10	0.709146	1.4E-05	0.512576	-1.2	0.3	0.706663	1.4E-05	0.512518	-2.3	0.3
3424	-	-	0.51	0.13	-	-	-	-	-	-	-	-	-	-
3470	0.83	0.18	-	-	-	-	-	-	-	-	-	-	-	-
3795	-	-	0.62	0.07	0.709149	1.4E-05	0.512541	-1.9	0.3	0.706719	1.4E-05	0.512521	-2.3	0.3
4182	-	-	-	-	0.709142	1.4E-05	0.512552	-1.7	0.3	-	-	-	-	-
dupl.	-	-	-	-	0.709150	1.4E-05	0.512558	-1.6	0.3	-	-	-	-	-
4407	-	-	-	-	0.709138	1.4E-05	0.512560	-1.5	0.3	0.706469	1.4E-05	0.512566	-1.4	0.3
4828	0.81	0.27	-	-	-	-	-	-	-	-	-	-	-	-
5943	-	-	0.42	0.22	-	-	-	-	-	-	-	-	-	-
8312	-	-	-	-	0.709168	1.4E-05	0.512564	-1.4	0.5	0.707013	1.4E-05	0.512548	-1.7	0.3
8370	0.39	0.24	-	-	-	-	-	-	-	-	-	-	-	-
8928	-	-	1.15	0.21	0.709158	1.4E-05	0.512590	-0.9	0.5	-	-	-	-	-
8950	-	-	-	-	0.709162	1.4E-05	0.512561	-1.5	0.5	0.707012	1.4E-05	0.512572	-1.3	0.3
9108	1.10	0.09	-	-	-	-	-	-	-	-	-	-	-	-
9170	-	-	-	-	0.709165	1.4E-05	0.512553	-1.7	0.5	0.706989	1.4E-05	0.512564	-1.5	0.3

Table A.4: continued

age [call. yr BP]	$\delta^{30}Si_{bSiO2}$ [‰]	$2\sigma_{(sd)}$	$\delta^{30}Si_{diatom}$ [‰]	$2\sigma_{(sd)}$	$^{87}Sr/^{86}Sr_{coating}$	$2\sigma_{(sd)}$	$^{143}Nd/^{144}Nd_{coating}$	$\varepsilon Nd_{coating}$	$2\sigma_{(sd)}$	$^{87}Sr/^{86}Sr_{detritus}$	$2\sigma_{(sd)}$	$^{143}Nd/^{144}Nd_{detritus}$	$\varepsilon Nd_{detritus}$	$2\sigma_{(sd)}$
9263	-	-	1.22	0.16	0.709155	1.4E-05	0.512561	-1.5	0.5	-	-	-	-	-
9276	1.01	0.28	-	-	-	-	-	-	-	-	-	-	-	-
9487	-	-	-	-	0.709168	1.4E-05	0.512560	-1.5	0.5	-	-	-	-	-
dupl.	-	-	-	-	-	-	0.512551	-1.7	0.5	-	-	-	-	-
9504	0.72	0.27	-	-	-	-	-	-	-	-	-	-	-	-
9523	-	-	-	-	0.709157	2.6E-05	0.512580	-1.1	0.5	0.707162	1.4E-05	0.512527	-2.2	0.3
9731	0.67	0.14	-	-	-	-	-	-	-	-	-	-	-	-
9796	-	-	-	-	0.709159	2.6E-05	0.512546	-1.8	0.5	0.707324	1.4E-05	0.512514	-2.4	0.3
9896	0.46	0.30	-	-	-	-	-	-	-	-	-	-	-	-
10183	-	-	-	-	0.709181	2.6E-05	0.512586	-1.0	0.5	-	-	-	-	-
10206	-	-	1.30	0.08	0.709163	2.6E-05	0.512571	-1.3	0.5	0.706966	1.4E-05	0.512509	-2.5	0.3
10323	0.38	0.14	-	-	-	-	-	-	-	-	-	-	-	-
10799	0.84	0.10	-	-	-	-	-	-	-	-	-	-	-	-
10805	-	-	-	-	0.709141	2.6E-05	0.512565	-1.4	0.5	0.707154	1.4E-05	0.512532	-2.1	0.3
11274	0.33	0.13	-	-	-	-	-	-	-	-	-	-	-	-
11613	-	-	-	-	0.709148	2.6E-05	0.512568	-1.4	0.3	0.706571	1.5E-05	0.512545	-1.8	0.3
11822	0.44	0.14	-	-	-	-	-	-	-	-	-	-	-	-
12405	0.88	0.15	-	-	-	-	-	-	-	-	-	-	-	-
12474	-	-	-	-	0.709117	2.6E-05	0.512542	-1.9	0.3	0.706476	1.5E-05	0.512556	-1.6	0.3
13257	0.41	0.18	-	-	-	-	-	-	-	-	-	-	-	-
13789	-	-	0.83	0.09	0.709136	2.6E-05	0.512560	-1.5	0.5	0.706507	1.5E-05	0.512571	-1.3	0.3
14009	0.53	0.12	-	-	-	-	-	-	-	-	-	-	-	-
14153	-	-	0.58	0.16	0.709119	2.6E-05	0.512569	-1.3	0.3	0.706203	1.5E-05	0.512597	-0.8	0.3
14441	0.51	0.10	-	-	-	-	-	-	-	-	-	-	-	-
14932	0.79	0.10	-	-	-	-	-	-	-	-	-	-	-	-
15410	-	-	-	-	0.709096	2.6E-05	0.512546	-1.8	0.3	0.706442	1.5E-05	0.512547	-1.8	0.3
dupl.	-	-	-	-	0.709105	1.5E-05	0.512529	-2.1	0.3	-	-	-	-	-
15506	0.63	0.21	-	-	-	-	-	-	-	-	-	-	-	-
16030	0.98	0.19	-	-	-	-	-	-	-	-	-	-	-	-
16274	-	-	-	-	0.709117	2.6E-05	0.512572	-1.3	0.3	0.706408	1.5E-05	0.512567	-1.4	0.3
18802	0.35	0.14	-	-	-	-	-	-	-	-	-	-	-	-
19630	-	-	-	-	0.709123	2.6E-05	0.512550	-1.7	0.5	0.706283	1.5E-05	0.512604	-0.7	0.3

Table A.5: Nearshore water column dissolved εNd values. $2\sigma_{(sd)}$ represents the external reproducibilities of repeated standard measurements.

Station	Latitude	Longitude	Bottom Depth [m]	Depth [m]	εNd	$2\sigma_{(sd)}$	Reference
152	0°	85°50' W	2907	3	0.6	0.1	Grasse et al., unpublished, 2011
				90	-1.8	0.1	
117	3°35' S	82°00' W	4084	2	-1.5	0.2	Grasse et al., unpublished, 2011
				150	-2.3	0.1	
				398	-2.8	0.1	
				1487	-3.2	0.8	
				2473	-3.9	0.2	
				3453	-3.7	0.2	
125	6°00' S	82°00' W	5173	100	-2.3	0.4	this study
806	8°00' S	79°51' W	138	3	-4.6	0.2	this study
				80	-1.0	0.4	
2	10°00' S	80°00' W	6296	2	-2.7	0.3	Grasse et al., unpublished, 2011
				101	-1.7	0.3	
				498	-2.1	0.1	
				991	-2.3	0.1	
807	10°00' S	78°23' W	111	3	-1.5	0.6	this study
				106	-4.2	0.5	
810	10°00' S	78°48' W	151	3	-5.7	0.3	this study
812	10°00' S	79°08' W	331	300	-2.8	0.3	this study
78	14°00' S	77°03' W	3026	2	-2.6	0.4	Grasse et al., unpublished, 2011
				199	-2.3	0.4	
				498	-2.5	0.4	
				1999	-3.2	0.3	
				2498	-4.7	0.3	
				2986	-3.6	0.3	
30	16°00' S	75°33' W	6165	3	-3.4	0.4	Grasse et al., unpublished, 2011
				501	-2.9	0.5	
				1011	-3.4	0.4	
				3549	-4.3	0.5	
				4571	-4.9	0.5	
				5494	-4.5	0.5	
34	16°00' S	74°11' W	116	3	-3.9	0.3	this study
				111	-3.4	0.6	

Table A.6: Downcore records of core M77/1-470 for $bSiO_2$ concentrations (wt%), $\delta^{30}Si_{opal}$ (‰), $^{143}Nd/^{144}Nd$, εNd and $^{87}Sr/^{86}Sr$ (Fe-Mn coatings and detrital material). $2\sigma_{(sd)}$ represents the external reproducibilities of repeated sample (Si) and standard (Nd, Sr) measurements.

depth [cm]	$bSiO_2$ [wt%]	$\delta^{30}Si_{opal}$ [‰]	$2\sigma_{(sd)}$	$^{143}Nd/^{144}Nd_{detritus}$	$\varepsilon Nd_{detritus}$	$2\sigma_{(sd)}$	$^{87}Sr/^{86}Sr_{detritus}$	$2\sigma_{(sd)}$	$^{143}Nd/^{144}Nd_{coating}$	$\varepsilon Nd_{coating}$	$2\sigma_{(sd)}$	$^{87}Sr/^{86}Sr_{coating}$	$2\sigma_{(sd)}$
0.5	-	1.03	0.15	-	-	-	-	-	-	-	-	-	-
1.5	18.8	-	-	-	-	-	-	-	0.512539	-1.9	0.3	0.709030	2.6E-05
3.5	18.6	0.93	0.08	0.512369	-5.2	0.3	0.709315	1.5E-05	0.512551	-1.7	0.3	0.708971	2.6E-05
5.5	22.2	-	-	0.512381	-5.0	0.3	0.709356	1.5E-05	0.512546	-1.8	0.3	0.709080	2.6E-05
9	16.9	0.96	0.09	0.512398	-4.7	0.3	0.708822	1.5E-05	0.512556	-1.6	0.3	0.709099	2.6E-05
11	16.3	-	-	-	-	-	-	-	0.512526	-2.2	0.3	0.709121	2.6E-05
15	17.2	-	-	0.512383	-5.0	0.3	0.708737	1.5E-05	0.512521	-2.3	0.3	0.709112	2.6E-05
16	-	0.96	0.07	-	-	-	-	-	-	-	-	-	-
19	19.5	-	-	0.512386	-4.9	0.3	0.708552	1.5E-05	0.512559	-1.5	0.3	0.709094	2.6E-05
20	19.8	1.05	0.10	0.512410	-4.5	0.3	0.708412	8.0E-06	0.512571	-1.3	0.3	0.708748	8.0E-06
23	18.8	-	-	0.512393	-4.8	0.3	0.708720	1.5E-05	0.512547	-1.8	0.3	0.709153	2.6E-05
24	-	1.15	0.13	-	-	-	-	-	-	-	-	-	-
25	15.9	-	-	-	-	-	-	-	0.512539	-1.9	0.3	0.709132	2.6E-05
26	19.3	-	-	0.512387	-4.9	0.3	0.707482	8.0E-06	-	-	-	0.708973	8.0E-06
27	18.9	-	-	0.512397	-4.7	0.3	0.707555	1.5E-05	0.512542	-1.9	0.3	0.709130	2.6E-05
28	-	1.00	0.14	-	-	-	-	-	-	-	-	-	-
29	26.9	-	-	0.512452	-3.6	0.3	0.706549	1.5E-05	0.512538	-2.0	0.3	0.709136	2.6E-05
32	14.0	0.55	0.17	0.512442	-3.8	0.3	0.706763	1.5E-05	0.512523	-2.3	0.3	0.709140	2.6E-05
dupl.	10.1	-	-	0.512445	-3.8	0.3	0.706469	8.0E-06	0.512564	-1.4	0.3	0.708935	5.0E-06
36	14.4	1.10	0.15	0.512419	-4.3	0.3	0.706767	8.0E-06	0.512574	-1.2	0.3	0.708727	8.0E-06
40	12.3	0.79	0.11	0.512408	-4.5	0.3	0.706964	8.0E-06	0.512565	-1.4	0.3	0.708928	8.0E-06
44	15.0	0.91	0.18	0.512421	-4.2	0.3	0.707057	8.0E-06	0.512572	-1.3	0.3	0.708745	5.0E-06
48	-	0.75	0.05	-	-	-	-	-	-	-	-	-	-
48.5	-	-	-	0.512395	-4.7	0.3	0.707816	8.0E-06	0.512564	-1.4	0.3	0.708847	5.0E-06

Table A.7: Downcore records of core B0405-6 for $bSiO_2$ concentrations (wt%), $\delta^{30}Si_{opal}$ (‰), $^{143}Nd/^{144}Nd$, εNd and $^{87}Sr/^{86}Sr$ of the detrital material. $2\sigma_{(sd)}$ represents the external reproducibilities of repeated sample (Si) and standard (Nd, Sr) measurements.

age [yr AD]	$bSiO_2$ [wt%]	$\delta^{30}Si_{opal}$ [‰]	$2\sigma_{(sd)}$	$^{143}Nd/^{144}Nd_{detritus}$	$\varepsilon Nd_{detritus}$	$2\sigma_{(sd)}$	$^{87}Sr/^{86}Sr_{detritus}$	$2\sigma_{(sd)}$
1950	21.7	0.91	0.15	0.512507	-2.6	0.1	0.708372	8.0E-06
1925	21.0	0.83	0.15	0.512460	-3.5	0.3	0.707923	8.0E-06
1903	18.9	0.62	0.10	0.512487	-2.9	0.3	0.707715	8.0E-06
1857	34.4	1.02	0.16	0.512471	-3.3	0.3	0.707829	8.0E-06
dupl.	37.7	1.22	0.14	0.512481	-3.1	0.1	0.707736	8.0E-06
1818	12.6	0.56	0.15	0.512468	-3.3	0.3	0.707702	8.0E-06
1793	15.8	0.82	0.14	0.512446	-3.7	0.3	0.707265	8.0E-06
1761	13.5	0.71	0.16	0.512627	-0.2	0.3	0.707296	8.0E-06
1698	17.3	0.73	0.09	0.512462	-3.4	0.3	0.707278	8.0E-06
1564	20.8	0.81	0.12	0.512467	-3.3	0.3	0.707281	8.0E-06
1475	17.1	0.77	0.04	0.512427	-4.1	0.3	0.707959	8.0E-06
1370	34.2	0.80	0.23	0.512509	-2.5	0.3	0.707111	8.0E-06